Universitat Politècnica de València

Departamento de Comunicaciones

Doctoral Thesis

New Wide-Band Capacitive Filter Structures in Rectangular Waveguide Technology With Enhanced Out-of-Band Response

Joaquin Francisco Valencia Sullca

Co-directors

Dr. Vicente E. Boria Esbert (Universitat Politècnica de València)

Dr. Santiago Cogollos Borrás (Universitat Politècnica de València)

Dr. Marco Guglielmi (Universitat Politècnica de València)

Tesis Doctoral presentada al Departamento de Comunicaciones,
en el cumplimiento parcial de los requisitos para obtener:
Título de Doctor en Ingeniería de Telecomunicación
por la Universitat Politècnica de València

Fecha: 10 de Noviembre 2021, Valencia

Agradecimientos

Quiero aprovechar esta página para dedicar unas palabras a todas aquellas personas sin las cuales no hubiera sido posible la realización de la presente tesis doctoral.

En primer lugar, quisiera expresar mi agradecimiento a mis directores de la tesis doctoral. Vicente, Santiago y Marco: gracias por su inestimable ayuda, apoyo y experiencia para la realización de la tesis. En estos años he aprendido mucho de vosotros, gracias por su paciencia y conocimiento en esta etapa, los cuales me han permitido afrontar y superar los diferentes obstáculos que han surgido en el desarrollo de la tesis. Asimismo, gracias a vosotros he podido aprender, familiarizarme y especializarme en los diferentes campos del conocimiento que han sido parte del desarrollo de la tesis doctoral, sin su apoyo nada de esto hubiera sido posible. Finalmente, me llena de alegría haber trabajado con vosotros, muchas gracias por todo.

Mi segundo agradecimiento, es para toda mi familia, en especial a mi madre, padre, hermanas y hermanos gracias por su paciencia, confianza, apoyo y afecto en estos años para la culminación de la tesis. Vosotros siempre me habéis inspirado para seguir adelante, a pesar de las dificultades que se me han presentado, siempre han estado a mi lado para apoyarme y guiarme, todo esto va por vosotros. Asimismo, muchas gracias a todos mis familiares que han sido de gran apoyo por sus consejos en cada etapa de mi vida.

También me gustaría agradecer a todo el equipo del GAM y VSC por su ayuda en la realización de las diferentes actividades de investigación, que me han permitido enriquecer mis conocimientos.

Por último, me gustaría agradecer a mis amigas y amigos por su comprensión, aliento, confianza y apoyo para la culminación de este documento.

Resumen

La presente tesis doctoral tiene como objetivo fundamental desarrollar nuevas estructuras capacitivas de filtrado en guía de ondas rectangular que sean capaces de proporcionar mayores ancho de banda en la banda de paso y, al mismo tiempo, mejorar la respuesta fuera de banda. Estas nuevas estructuras guiadas han sido pensadas para ofrecer nuevas soluciones tecnológicas para los filtros de microondas de alta frecuencia, con una variedad de diferentes funciones de transferencia, abordando específicamente las necesidades de los futuros sistemas de telecomunicaciones para aplicaciones terrestres y espaciales.

En este contexto, por lo tanto, discutimos en este documento el estudio, diseño y fabricación de varios tipos de filtros de microondas en guía de ondas rectangular que muestran una mejora significativa con respecto al estado del arte. Las soluciones que discutimos se obtienen introduciendo modificaciones simples en la estructura de los filtros de microondas clásicos. Varias técnicas que emplean iris híbridos, resonadores con salto de impedancia, configuración en escalera y uniones T en plano E con conexiones en corto-circuito o manifold, se utilizan con éxito para cumplir con las exigentes especificaciones de los futuros sistemas para aplicaciones terrestres y espaciales. Además, un desafío actual adicional al que se enfrentan todos los diseñadores de equipos y componentes de microondas es la necesidad de reducir tanto su tamaño físico como su masa (o peso). Para abordar este problema, discutimos en este documento el uso de aperturas resonantes en guías de ondas rectangulares, presentando una nueva familia de filtros que se pueden usar para implementar funciones complejas de transferencia de banda única y banda doble con una reducción significativa de tamaño y masa.

En los siguientes capítulos de esta tesis doctoral, cada tema se analiza en detalle, incluyendo las formulaciones teóricas básicas, los procedimientos de diseño, los resultados de las simulaciones electromagnéticas de onda completa, las consideraciones de fabricación y el rendimiento medido de una serie de prototipos. En todos los casos se ha encontrado

una excelente concordancia entre las mediciones y las simulaciones realizadas, validando así completamente tanto las estructuras novedosas propuestas como sus procedimientos de diseño.

Resum

La present tesi doctoral té com a objectiu fonamental el desenvolupament de noves estructures capacitives de filtrat en guia d'ones rectangular que siguen capaços de proporcionar major ample de banda en la banda de pas i millorar, al mateix temps, la resposta fora de banda. Aquestes noves estructures guiades han sigut pensades per a oferir noves solucions tecnològiques per a filtres de microones d'alta freqüència, amb una varietat de diferents funcions de transferència, abordant específicament les necessitats dels futurs sistemes de telecomunicacions per a aplicacions terrestres i espacials.

En aquest context, per tant, discutim en aquest document l'estudi, disseny i fabricació de diversos tipus de filtres de microones en guia d'ones rectangular que mostren una millora significativa respecte a l'estat de l'art. Les solucions que discutim s'obtenen introduint modificacions simples en l'estructura dels filtres de microones clàssics. Diverses tècniques que fan ús d'iris híbrids, ressonadors amb salt d'impedància, configuració en escala i unions T en plànol E amb connexions en curtcircuit o col·lector, s'utilitzen amb èxit per a complir amb les exigents especificacions dels sistemes futurs per a aplicacions terrestres i espacials. A més, un desafiament actual addicional al qual s'enfronten tots els dissenyadors d'equips i components de microones és la necessitat de reduir tant la seua grandària física com la seua massa (o pes). Per a abordar aquest problema, discutim en aquest document l'ús d'obertures ressonants en guies d'ones rectangulars, presentant una nova família de filtres que es poden usar per a implementar funcions complexes de transferència de banda única i doble banda amb una reducció significativa de grandària i massa.

En els següents capítols d'aquesta tesi doctoral, cada tema s'analitza detalladament, incloent les formulacions teòriques bàsiques, els procediments de disseny, els resultats de les simulacions electromagnètiques d'ona completa, les consideracions de fabricació i el rendiment mesurat d'una sèrie de prototips. En tots els casos s'ha trobat una excel·lent

concordança entre el mesurament i les simulacions realitzades, validant així completament tant les estructures noves propostes com els seus procediments de disseny.

Abstract

The main objective of this doctoral thesis is the development of new capacitive filtering structures in rectangular waveguide that are able to provide wide bandwidths in the passband and improve, at the same time, the out-of-band response. These new guided structures have been developed in order to offer new technological solutions for high-frequency microwave filters, with a variety of different transfer functions, addressing specifically the needs of future telecommunication systems for both ground and space applications.

In this context, therefore, we discuss in this document the study, design and manufacture of several types of microwave filter in rectangular waveguide that show a significant improvement with respect to the state-of-the-art. The new solutions that we propose are obtained by introducing simple modifications in the structure of classic microwave filters. Several techniques based on hybrid irises, stepped impedance resonators, staircase configuration and E-plane T-junctions with shorted stubs or manifold connections, are successfully used in order to meet the very demanding specifications of future systems for both ground and space applications. Furthermore, an additional current challenge faced by all designers of microwave components is the need to reduce both their physical size and mass (or weight). To address this issue, we discuss in this document the use of resonant apertures in rectangular waveguide, introducing a new family of filters which can be used to implement complex single and dual-band transfer functions with significant size and mass reduction.

In the following chapters of this doctoral thesis, each subject is discussed in detail including the basic theoretical formulations, design procedures, the results of full-wave electromagnetic simulations, manufacturing considerations, and the measured performance of a number of prototypes. Excellent agreement is found in all cases between measurement and simulations, thereby fully validating both the novel structures discussed and their design procedures.

Contents

Resumen v

Resum vii

Abstract ix

Contents 1

Figure List 7

Table List 27

Acronyms 29

1 Introduction 31

1.1 Motivation and Objectives 31

2 State of the Art 33

2.1 Microwave Filters 35

2.1.1 Hybrid and Wide-Band Filtering Structures 38

2.2 Rectangular Waveguide Filters 40

2.2.1 Inductive Band-Pass Filters 41

2.2.2 Improved Inductive Filters 43

2.2.3 Improving Filter Selectivity . . . 50
2.2.4 Resonant Apertures . . . 54
2.3 Design of Wide-band Microwave Filters . . . 59

3 Hybrid Filters and Stepped Impedance Resonators 65

3.1 Wideband Filters Specifications . . . 66
3.2 Filter Design Procedure . . . 66
3.3 Hybrid Filters . . . 68
3.3.1 Classical Filters . . . 69
3.3.2 Hybrid Filters . . . 70
3.3.3 Optimal Hybrid Filters . . . 72
3.4 Changing Resonator Width . . . 76
3.4.1 Inductive Filters . . . 76
3.4.2 Capacitive Filters . . . 79
3.5 Design of Wideband SIR Filters . . . 81
3.5.1 Basic SIR . . . 81
3.5.2 Inductive SIR Filter . . . 83
3.5.3 Capacitive SIR Filter . . . 83
3.5.4 Hybrid SIR Filter . . . 88
3.6 High-Accuracy Wideband Hybrid SIR Filter . . . 90
3.6.1 LA The Design Procedure . . . 91
3.6.2 The HA Prototype . . . 91
3.6.3 Measurements . . . 94
3.6.4 Inverse ASM . . . 96
3.7 Tolerance Analysis . . . 98
3.8 High Power Analysis . . . 99
3.9 Higher Order Modes Analysis . . . 101
3.10 Conclusions . . . 105

4 Advanced Topologies for Wideband Hybrid SIR Filters in Rectangular Waveguide 107

4.1 Wideband Hybrid SIR Filters Specifications . . . 108
4.2 Changing the Offset of the Irises . . . 108
4.2.1 Inductive Irises . . . 108
4.2.2 Capacitive Irises . . . 110
4.2.3 Hybrid SIR Filters . . . 110
4.3 Changing the Position of the SIRs . . . 113
4.4 Hybrid SIR Filter With Tuning Screws . . . 116

4.5 HA Design With Body and Cover . . . 117
4.5.1 The Prototype . . . 117
4.5.2 Measurements . . . 120
4.6 Compact Hybrid SIR Filter Design . . . 122
4.6.1 The HA Design . . . 124
4.6.2 Measurements . . . 126
4.7 Tolerance Analysis . . . 130
4.8 High Power Analysis . . . 131
4.9 Higher Order Modes Analysis . . . 133
4.10 Conclusions . . . 137

5 Hybrid Wideband Staircase Filters in Rectangular Waveguide 139

5.1 Hybrid Wideband Filter Specifications . . . 140
5.2 Hybrid Staircase Filters . . . 140
5.2.1 Basic Staircase . . . 141
5.2.2 Inductive Staircase Filters . . . 141
5.2.3 Capacitive Staircase Filters . . . 149
5.2.4 Hybrid Staircase Filters . . . 154
5.2.4.1 Staircase 1 . . . 156
5.2.4.2 Staircase 2 . . . 158
5.2.4.3 Staircase 3 . . . 158
5.2.4.4 Staircase 4 . . . 163
5.2.4.5 Comparative Discussion . . . 165
5.3 E-Plane T-Junction Manifold Connection . . . 165
5.3.1 Basic Manifold Structure . . . 167
5.3.2 Capacitive Manifold Filter . . . 169
5.3.3 Hybrid Manifold Filter . . . 169
5.3.4 Hybrid Staircase Manifold Filter . . . 171
5.4 E-Plane Folded Hybrid Filter . . . 176
5.4.1 Basic E-Plane Folded Structure . . . 177
5.4.2 E-Plane Folded Hybrid Staircase Manifold Filter . . . 177
5.5 The Prototype . . . 187
5.5.1 Yield Analysis . . . 193
5.5.2 High Power Analysis . . . 194
5.5.3 Measurements . . . 195
5.6 High Order Modes Effects . . . 197
5.6.1 H-Plane Transformer . . . 201
5.6.2 Changing Central Resonator Width . . . 203
5.7 Conclusions . . . 210

6 Dual-Band Filters in Rectangular Waveguide Using Resonant Apertures 211

6.1 Capacitive Reference Filter 212
6.2 Basic Resonant Aperture 214
6.3 Design Procedure for Dual-Band RA Filters 219
6.4 Dual-Band RA Filter Design Example 220
6.4.1 Capacitibe Stubs 221
6.4.2 Staircase Filter 223
6.4.3 Staircase Filter With TZs 227
6.5 The First Prototype 229
6.5.1 Measurements 232
6.6 The Second Prototype 235
6.6.1 Measurements 237
6.7 Tolerance Analysis 241
6.8 High Power Analysis 241
6.9 Higher Order Modes Analysis 245
6.10 Conclusions 248

7 Wideband Filters in Rectangular Waveguide Using Resonant Apertures 249

7.1 Extended Bandpass RA Filter 250
7.2 Design Procedure of Extended Bandpass RA Filter 250
7.2.1 Extended Bandpass RA Reference Filter 254
7.2.2 Capacitibe Stubs 254
7.2.3 Staircase Filter 256
7.2.4 Staircase Filter With TZs 258
7.3 Extended Bandpass RA Prototype 260
7.3.1 Measurements 264
7.4 Yield Analysis 266
7.5 High Power Analysis 267
7.6 Higher Order Mode Analysis 268
7.7 Conclusions 270

8 Conclusions and Future Work 271

8.1 Conclusions 271
8.2 Future work 273

A Manufacturing Plans With Solid Works **275**

A.1 Objective . . . 275
A.2 Detailed Steps of the 3D Plans . . . 275
A.2.1 Converting File Format . . . 276
A.2.2 Designing the Outer Body . . . 276
A.2.3 Creating the Inside of the Filter . . . 276
A.2.4 Input and Output Waveguide Flanges . . . 276
A.2.5 Fixing Screws . . . 277
A.2.6 Alignment Pins . . . 277
A.2.7 Real Tuning Screws . . . 278
A.2.8 Body and Cover . . . 278
A.2.9 Pressure Wells . . . 278
A.2.10 Assembly of the Body and Cover . . . 279
A.2.11 Generate Drawings . . . 279
A.3 3D Manufacturing Plans of the Filters . . . 279

B Publications **287**

B.1 Journal Publications . . . 287
B.2 Conference Publications . . . 287

Bibliography **289**

Figure List

2.1 Scenario with emerging applications of future satellites. 33

2.2 Satellite communication subsystem block diagram. 34

2.3 Satellite receiver block diagram. 35

2.4 Multiplexing scheme in a satellite system. 36

2.5 Examples of implementations of microwave filters. 37

2.6 Cascaded low-pass and band-stop filters. 41

2.7 Bandpass filter in rectangular waveguide with inductive irises. 42

2.8 Cavity used to exploit the interaction between TE_{10} and TE_{30} modes. . 43

2.9 Six-pole evanescent inductive filter loaded with rectangular dielectric posts. 44

2.10 Inductive filter with change of resonator widths and iris thicknesses. . . 44

2.11 Implementation of a SIR resonator. 45

2.12 Simulated magnetic field distributions of TE_{101}, TE_{102}, and TE_{201} modes. 46

2.13 Waveguide structure of the inductive staircase filter. 47

2.14 Implementation of the high-power rectangular waveguide band pass filter with capacitive coupling iris (CIRWBPF). 48

2.15 Side view of a filter inverter realized as a low-pass structure with capacitive irises. 49

2.16 Configurations of inductive filter cavities for generating TZs. 51

2.17 An alternative waveguide implementation of a trisection. 51

2.18 Basic building block with the capacitive coupling scheme and the E-plane stub. 52

2.19 Geometry of the basic triplet block and routing scheme. Solid lines indicate direct couplings whereas dashed lines refer to cross-couplings. . 52

2.20 Geometries of the trisections that provide TZs below the pass-band using a classical capacitive window as cross-coupling. 53

2.21 Geometry of a capacitive obstacle including one stub. 53

2.22 Left: Dimensions of a resonant iris. Center: Location of the iris in the waveguide. Right: Lumped-element equivalent circuit of a resonant iris. 54

2.23 Geometry of asymmetric-iris coupled-cavity filters. 55

2.24 Structure of a TM_{110} mode in-line filter that uses bypass couplings of non-resonating $TE_{10/01}$ modes. 56

2.25 Implementation of non-centered resonant irises filter. 56

2.26 Implementation of multi-aperture waveguide iris. 57

2.27 Structure of filter with resonating irises and shorting stubs. 58

2.28 Lumped-element ladder network for a lowpass filter prototype with a shunt capacitor as the first element. 59

2.29 Lowpass prototype filter with admittance inverters. 60

2.30 Lumped band-pass prototype filter with admittance inverters. 61

2.31 Distributed band-pass prototype filter with admittance inverters. 61

2.32 Generalized equivalent circuit for a band-pass filter circuit with admittance inverters. 62

2.33 Tolerance analysis of an inductive filter. 63

2.34 Higher power analysis of an in-line interdigital filter. 64

3.1 Typical irises in a rectangular waveguide (front view). Left: centered inductive iris of width w. Right: centered capacitive iris of height h. . . 68

3.2 Structure of a four-pole inductive filter. 69

3.3 Structure of a four-pole capacitive filter. 69

3.4 Simulated performance of the four-pole inductive filter (4-P Ind Filter) and four-pole capacitive filter (4-P Cap Filter). 70

3.5 Structure of the four-pole hybrid filter with an inductive iris in the center section. 71

3.6 Structure of the four-pole hybrid filter with inductive irises in the first and last couplings. 71

3.7 Simulated performance of the four-pole hybrid filters with an inductive iris in the center section (4-P Hyb Filter I) and inductive irises in the first and last couplings (4-P Hyb Filter II). 72

3.8 Structure of the eight-pole inductive filter. 73

3.9 Structure of the eight-pole capacitive filter. 73

3.10 Simulated performance of the eight-pole inductive filter (8-P Ind Filter) and eight-pole capacitive filter (8-P Cap Filter). 74

3.11 Structure of the eight-pole hybrid filter with three inductive coupling windows in the center section. 75

3.12 Structure of the eight-pole hybrid filter with two inductive irises in the first and last coupling sections. 75

3.13 Simulated performance of the eight-pole hybrid filters with three inductive irises in the center section (8-P Hyb Filter I), and two inductive irises in the first and last coupling sections (8-P Hyb Filter II). 76

3.14 Structure of the inductive filter with widths that decrease as we approach the center of the structure. 77

3.15 Simulated performance of the inductive filter (Ind Ref Filter) and inductive filter with widths that decrease as we approach the center of the structure (Ind W Filter I). 77

3.16 Structure of the inductive filter with widths that increase as we approach the center of the structure. 78

3.17 Simulated performance of the inductive filter (Ind Ref Filter) and inductive filter with widths that increase as we approach the center of the structure (Ind W Filter II). 78

3.18 Structure of the capacitive filter with widths that decrease as we approach the center of the structure. 79

3.19 Simulated performance of the capacitive filter (Cap Ref Filter) and capacitive filter with widths decreasing as we approach the center of the structure (Cap W Filter I). 80

3.20 Structure of the capacitive filter with widths that increase as we approach the center of the structure. 80

3.21 Simulated performance of the capacitive filter (Cap Ref Filter) and capacitive filter with widths increasing as we approach the center of the structure (Cap W Filter II). 81

3.22 Geometry (side view) of a basic SIR with capacitive input and output couplings. 82

3.23 Simulated performance of the capacitive four-pole filter with several SIR implementations. 83

3.24 Structure of the inductive filter with SIRs of dimensions $H_1 = 10.16$ mm, $H_2 = 6.0$ mm and $L_2 = 5.0$ mm. 84

3.25 Simulated performance of the inductive reference filter (Ind Ref Filter) and inductive filter with SIRs (Ind SIR Filter). 84

3.26 Structure of the capacitive filter with SIRs of dimensions $H_1 = 10.16$ mm, $H_2 = 6.0$ mm and $L_2 = 5.0$ mm. 85

3.27 Simulated performance of the capacitive reference filter (Cap Ref Filter) and the first capacitive filter with SIRs (Cap SIR Filter I). 85

3.28 Structure of the capacitive filter with SIRs of dimensions $H_1 = 8.0$ mm, $H_2 = 4.0$ mm and $L_2 = 5.0$ mm. 86

3.29 Simulated performance of the first capacitive filter with SIRs (Cap SIR Filter I) and the second capacitive filter with SIRs (Cap SIR Filter II). 87

3.30 Simulated performance of the capacitive reference filter (Cap Ref Filter), capa-citive filter with widths that decrease as we approach the center of the structure (Cap W Filter) and capacitive filter with SIRs (Cap SIR Filter). 87

3.31 Structure of the hybrid filter with SIRs of dimensions $H_1 = 10.16$ mm, $H_2 = 6.0$ mm and $L_2 = 5.0$ mm. 88

3.32 Simulated performance of the hybrid reference filter (Hyb Ref Filter) and the first hybrid filter with SIRs (Hyb SIR Filter I). 89

3.33 Structure of the hybrid filter with SIRs $H_1 = 8.0$ mm, $H_2 = 4.0$ mm and $L_2 = 5.0$ mm. 89

3.34 Simulated performance of the first hybrid filter with SIRs (Hyb SIR Filter I) and the second hybrid filter with SIRs (Hyb SIR Filter II). . . 90

3.35 Structure of the in-line wideband hybrid SIR filter designed with a radius equal to r =1.0 mm. 92

3.36 Simulated performance of the in-line hybrid SIR filter using FEST3D and CST. 94

3.37 Manufactured prototype in aluminum of the in-line hybrid SIR filter (no silver plating). 94

3.38 Measurement of the in-band performance of the filter compared with the EM simulation (CST). 95

3.39 Measurement of the out-of-band performance of the filter compared with the EM simulation (CST). 96

3.40 Inverse ASM in-band performance compared with the measurement of the in-band performance. 97

3.41 Inverse ASM out-of-band performance compared with the measurement of the out-of-band performance. 99

3.42 Tolerance analysis of the in-line hybrid SIR filter. 100

3.43 Multipactor results (electron evolution) for the capacitive window of height h_3 at 11.75 GHz of the in-line hybrid SIR filter. 101

3.44 Simulated performance of the in-line hybrid SIR filter for the higher order mode TE_{20} using FEST3D and CST. 102

3.45 Simulated performance of the in-line hybrid SIR filter for the higher order mode TE_{01} using CST. 103

3.46 Simulated performance of the in-line hybrid SIR filter for the higher order modes TE_{11} and TM_{11} using CST. 103

3.47 Simulated performance of the in-line hybrid SIR filter for the higher order mode TE_{30} using CST. 104

3.48 Simulated performance of the in-line hybrid SIR filter for the higher order modes TE_{21} and TM_{21} using CST. 104

4.1 Structure of a filter with an offset in the position of the inductive irises. 109

4.2 Simulated performance of the inductive filter (Ind Ref Filter) and the inductive filter with an offset in the position of the inductive irises (Ind Offset Filter). 109

4.3 Structure of a filter with an offset in the position of the capacitive irises. 110

4.4 Simulated performance of the capacitive filter (Cap Ref Filter) and the capacitive filter with an offset in the position of the capacitive irises (Cap Offset Filter). 111

4.5 Structure of the first hybrid SIR filter with an offset in the position of the irises. 111

4.6 Simulated performance of the hybrid SIR filter (Hyb SIR Ref Filter) and the first hybrid SIR filter with an offset in the position of the irises (Hyb SIR O Filter I). 112

4.7 Structure of the second hybrid SIR filter with an offset only in the position of the capacitive irises. 112

4.8 Simulated performance of the first hybrid SIR filter (Hyb SIR O Filter I) and the second hybrid SIR filter (Hyb SIR O Filter II) with an offset only in the position of the capacitive irises. 113

4.9 Structure of the first hybrid SIR filter with an offset in both capacitive irises and SIRs. 114

4.10 Simulated performance of the second hybrid SIR filter with an offset in the position of the capacitive irises (Hyb SIR O Filter II) and the first hybrid SIR filter with an offset in both capacitive irises and SIRs (Hyb SIR O-S Filter I). 114

4.11 Structure of the second hybrid SIR filter with an offset in both capacitive irises and SIRs. 115

4.12 Simulated performance of the first hybrid SIR filter with an offset in both capacitive irises and SIRs (Hyb SIR O-S Filter I) and the second hybrid SIR filter with the modifications in the SIRs (Hyb SIR O-S Filter II). 115

4.13 Structure of the hybrid SIR filter with an offset in both capacitive irises and SIRs and, at the same time, with tuning screws. 116

4.14 Simulated performance of the second hybrid SIR filter with an offset in both capacitive irises and SIRs (Hyb SIR O-S Filter II) and the same filter with screws (Hyb SIR O-S TS Filter). 117

4.15 Structure of the in-line hybrid SIR filter designed with rounded corners (r =1.0 mm), and tuning screws of radius r =0.9 mm. 118

4.16 Simulated performance of the in-line hybrid SIR filter with tuning screws using both FEST3D and CST software tools. 118

4.17 Simulated performance of the in-line hybrid SIR filter (Inline SIR Filter), and inline hybrid filter with body and cover (Screw SIR Filter) using CST. 120

4.18 Manufactured prototype in aluminum of the in-line hybrid SIR filter with body and cover (no silver plating). 121

4.19 Measurement of the in-band performance of the filter with body and cover compared with the EM simulation (CST). 121

4.20 Measurement of the out-of-band performance of the filter with body and cover compared with the EM simulation (CST). 122

4.21 Structure of the first E-plane folded hybrid SIR filter. 123

4.22 Simulated performance of the in-line hybrid SIR filter (Hyb SIR Ref Filter) and the first E-plane folded hybrid SIR filter (Fol Hyb SIR Filter I). 123

4.23 Structure of the second E-plane folded hybrid SIR filter. 124

4.24 Simulated performance of the first E-plane folded hybrid SIR filter (Fol Hyb SIR Filter I) and the second E-plane folded hybrid SIR filter (Fol Hyb SIR Filter II). 125

4.25 Structure of the E-plane folded hybrid SIR filter designed with a radius equal to r =1.0 mm. 125

4.26 Simulated performance of the E-plane folded hybrid SIR filter using FEST3D and CST. 126

4.27 Simulated performance of the in-line hybrid SIR filter (Inline SIR Filter), and the E-plane folded hybrid SIR filter (Folded SIR Filter) using CST. 127

4.28 Manufactured prototype in aluminum of the E-plane folded hybrid SIR filter (no silver plating). 127

4.29 Measurement and simulated results (with CST) of the in-band performance of the E-plane folded hybrid SIR filter. 129

4.30 Measurement and simulated results (with CST) of the out-of-band performance of the E-plane folded hybrid SIR filter with the EM simulation (CST). 130

4.31 Tolerance analysis of the in-line hybrid SIR filter with body and cover. 131

4.32 Tolerance analysis of the E-plane folded hybrid SIR filter. 132

4.33 Multipactor results (electron evolution) for the capacitive window of height h_3 at 11.75 GHz of the in-line hybrid SIR filter with tuning screws. 132

4.34 Multipactor results (electron evolution) for the capacitive window of height h_3 at 11.75 GHz of the E-plane folded hybrid SIR filter. 134

4.35 Simulated performance of the in-line hybrid SIR filter with body and cover for the higher order mode TE_{20} using FEST3D and CST. 134

4.36 Simulated performance of the in-line hybrid SIR filter with body and cover for the higher order mode TE_{30} using CST. 135

4.37 Simulated performance of the E-plane folded hybrid SIR filter for the higher order mode TE_{20} using FEST3D and CST. 136

4.38 Simulated performance of the E-plane folded hybrid SIR filter for the higher order mode TE_{30} using CST. 136

5.1 The resonant modes of a rectangular waveguide cavity. 141

5.2 Geometry of a resonator coupled with inductive couplings in the front and end walls (top view). 142

5.3 Geometry of a staircase resonator with inductive couplings (top view). . 142

5.4 Structure of the four-pole inductive filter with $BW = 300$ MHz. 143

5.5 Structure of the four-pole inductive staircase filter with $BW = 300$ MHz. 143

5.6 Simulated performance of the four-pole inductive reference filter (4-P Ind Ref Filter) and four-pole inductive staircase filter (4-P Ind Stair Filter I) with $BW = 300$ MHz. 144

5.7 Structure of the four-pole inductive staircase filter, changing the width of the resonators, with $BW = 300$ MHz. 145

5.8 Simulated performance of the four-pole inductive staircase filter (4-P Ind Stair Filter I) and four-pole inductive staircase filter, changing the width of the resonators (4-P Ind Stair Filter II), with $BW = 300$ MHz. 145

5.9 Structure of the four-pole inductive staircase filter, changing the width of the resonators and applying an offset in the central inductive coupling, with $BW = 300$ MHz. 145

5.10 Simulated performance of the four-pole inductive reference filter (4-P Ind Ref Filter) and the four-pole inductive staircase filter changing the width of the resonators and applying an offset in the central inductive coupling (4-P Ind Stair Filter III), with $BW = 300$ MHz. 146

5.11 Structure of the eight-pole inductive filter with $BW = 720$ MHz. 147

5.12 Structure of the eight-pole inductive staircase filter with $BW = 720$ MHz. 147

5.13 Simulated performance of the eight-pole inductive reference filter (8-P Ind Ref Filter) and eight-pole inductive staircase filter (8-P Ind Stair Filter) with $BW = 720$ MHz. 147

5.14 Structure of the eight-pole inductive filter with $BW = 1410$ MHz. . . . 148

5.15 Structure of the eight-pole inductive staircase filter with $BW = 1410$ MHz. 148

5.16 Simulated performance of the eight-pole inductive reference filter (8-P Ind Ref BW Filter) and eight-pole inductive staircase filter (8-P Ind Stair BW Filter) with $BW = 1410$ MHz. 149

5.17 Geometry of a resonator coupled with capacitive couplings in the front and end walls (side view). 150

5.18 Geometry of a staircase resonator with capacitive couplings (side view). 150

5.19 Structure of the four-pole capacitive filter with $BW = 720$ MHz. 150

5.20 Structure of the four-pole capacitive staircase filter with $BW = 720$ MHz. 151

5.21 Simulated performance of the four-pole capacitive reference filter (4-P Cap Ref Filter) and capacitive staircase filter (4-P Cap Stair Filter) with $BW = 720$ MHz. 152

5.22 Structure of the eight-pole capacitive filter with $BW = 1410$ MHz. . . . 152

5.23 Structure of the eight-pole capacitive staircase filter with $BW = 1410$ MHz. 153

5.24 Simulated performance of the eight-pole capacitive reference filter (8-P Cap Ref Filter) and capacitive staircase filter (8-P Cap Stair Filter) with $BW = 1410$ MHz. 153

5.25 Structure of the hybrid (reference) eight-pole filter with $BW = 1410$ MHz. 154

5.26 Geometry of the first three-resonator arrangement of the first staircase confi-guration with the capacitive coupling apertures located at $l_{s_1} = l_1/4$ and $l_{s_2} = 3l_2/4$, respectively, from the resonator input. 156

5.27 Simulated performance of the hybrid reference filter (Hybrid) and hybrid staircase filter with the topologies 1 (Topo 1) and 2 (Topo 2) for the first staircase configuration. 157

5.28 Simulated performance of the hybrid reference filter (Hybrid) and hybrid staircase filter with the topologies 3 (Topo 3) and 4 (Topo 4) for the first staircase configuration. 157

5.29 Structure of the hybrid staircase filter of the first staircase configuration with the topology 4. 158

5.30 Geometry of the three-resonator arrangement of the second staircase configuration with the capacitive coupling apertures located at $l_{s_1} = l_1/4$, $l_{s_2} = 3l_2/4$ and $l_{s_3} = l_3/4$, respectively, from the resonator input. . 159

5.31 Simulated performance of the hybrid reference filter (Hybrid) and hybrid staircase filter with the topologies 1 (Topo 1) and 2 (Topo 2) for the second staircase configuration. 159

5.32 Simulated performance of the hybrid reference filter (Hybrid) and hybrid staircase filter with the topologies 3 (Topo 3) and 4 (Topo 4) for the second staircase configuration. 160

5.33 Structure of the hybrid staircase filter of the second staircase configuration with the topology 4. 160

5.34 Geometry of the three-resonator arrangement of the third staircase configuration with the capacitive coupling apertures located at $l_{s_1} = l_1/4$, $l_{s_{2a}} = l_2/4$, $l_{s_{2b}} = 3l_2/4$ and $l_{s_3} = l_3/4$, respectively, from the resonator input. 161

5.35 Simulated performance of the hybrid reference filter (Hybrid) and hybrid staircase filter with the topologies 1 (Topo 1) and 2 (Topo 2) for the third staircase configuration. 161

5.36 Simulated performance of the hybrid reference filter (Hybrid) and hybrid staircase filter with the topologies 3 (Topo 3) and 4 (Topo 4) for the third staircase configuration. 162

5.37 Structure of the hybrid staircase filter of the third staircase configuration with the topology 4. 162

5.38 Geometry of the three-resonator arrangement of the fourth staircase configuration with the capacitive coupling apertures located at $l_{s_1} = l_1/4$, $l_{s_{2a}} = l_2/4$ and $l_{s_{2b}} = 3l_2/4$, respectively, from the resonator input. 163

5.39 Simulated performance of the hybrid reference filter (Hybrid) and hybrid staircase filter with the topologies 1 (Topo 1) and 2 (Topo 2) for the fourth staircase configuration. 164

5.40 Simulated performance of the hybrid reference filter (Hybrid) and hybrid staircase filter with the topologies 3 (Topo 3) and 4 (Topo 4) for the fourth staircase configuration. 164

5.41 Structure of the hybrid staircase filter of the fourth staircase configuration with the topology 4. 165

5.42 Simulated performance of the hybrid staircase filter with the topology 4 of the first configuration (Stair 1 Topo 4) and second configuration (Stair 2 Topo 4). 166

5.43 Simulated performance of the hybrid staircase filter with the topology 4 of the third configuration (Stair 3 Topo 4) and fourth configuration (Stair 4 Topo 4). 166

5.44 Geometry of a simple E-plane manifold connection. 167

5.45 Simulated performance of the E-plane manifold connection with a stub of length $l_m = \lambda/2 - b/2$. 167

5.46 Geometry of the E-plane T-junction in the input (or output) port of a rectangular waveguide filter with capacitive couplings. 168

5.47 Structure of the capacitive filter with manifold input-output connections. 169

5.48 Simulated performance of the capacitive filter (Cap Ref Filter) and capacitive filter with manifold connections (Cap Man Filter). 170

5.49 Structure of the hybrid filter with manifold input-output connections. . 170

5.50 Simulated performance of the hybrid filter (Hyb Ref Filter) and hybrid filter with manifold connections (Hyb Man Filter). 171

5.51 Structure of the hybrid staircase filter of the first staircase configuration with the topology 4 and manifold input-output connections. 172

5.52 Simulated performance of the hybrid staircase filter (Stair 1 Topo 4) and hybrid staircase filter with manifold connections (Filter 1). 172

5.53 Structure of the hybrid staircase filter of the second staircase configuration with the topology 4 and manifold input-output connections. . . . 173

5.54 Simulated performance of the hybrid staircase filter (Stair 2 Topo 4) and hybrid staircase filter with manifold connections (Filter 2). 174

5.55 Structure of the hybrid staircase filter of the third staircase configuration with the topology 4 and manifold input-output connections. 174

5.56 Simulated performance of the hybrid staircase filter (Stair 3 Topo 4) and hybrid staircase filter with manifold connections (Filter 3). 175

5.57 Structure of the hybrid staircase filter of the fourth staircase configuration with the topology 4 and manifold input-output connections. 175

5.58 Simulated performance of the hybrid staircase filter (Stair 4 Topo 4) and hybrid staircase filter with manifold connections (Filter 4). 176

5.59 Geometry of the central section of the in-line filter with inductive couplings and of the E-plane folded configurations 1 to 3 (side view). . . . 178

5.60 Geometry of the central section of the E-plane folded configurations 4 to 7 (side view). 179

5.61 Structure of the hybrid staircase filter with manifold inputs, and folded central section (Folded 1 configuration). 180

5.62 Simulated performance of the hybrid staircase filter with manifold connections (Filter 2) compared to the performance of the Filter 2 with folding option 1 (Folded 1). 180

5.63 Structure of the hybrid staircase filter with manifold inputs, and folded central section (Folded 2 configuration). 181

5.64 Simulated performance of the hybrid staircase filter with manifold connections (Filter 2) compared to the performance of the Filter 2 with folding option 2 (Folded 2). 181

5.65 Structure of the hybrid staircase filter with manifold inputs, and folded central section (Folded 3 configuration). 182

5.66 Simulated performance of the hybrid staircase filter with manifold connections (Filter 2) compared to the performance of the Filter 2 with folding option 3 (Folded 3). 182

5.67 Structure of the hybrid staircase filter with manifold inputs, and folded central section (Folded 4 configuration). 183

5.68 Simulated performance of the hybrid staircase filter with manifold connections (Filter 2) compared to the performance of the Filter 2 with folding option 4 (Folded 4). 183

5.69 Structure of the hybrid staircase filter with manifold inputs, and folded central section (Folded 5 configuration). 184

5.70 Simulated performance of the hybrid staircase filter with manifold connections (Filter 2) compared to the performance of the Filter 2 with folding option 5 (Folded 5). 184

5.71 Structure of the hybrid staircase filter with manifold inputs, and folded central section (Folded 6 configuration). 185

5.72 Simulated performance of the hybrid staircase filter with manifold connections (Filter 2) compared to the performance of the Filter 2 with folding option 6 (Folded 6). 185

5.73 Structure of the hybrid staircase filter with manifold inputs, and folded central section (Folded 7 configuration). 186

5.74 Simulated performance of the hybrid staircase filter with manifold connections (Filter 2) compared to the performance of the Filter 2 with folding option 7 (Folded 7). 186

5.75 Structure of the hybrid staircase filter with manifold inputs and folded central section (Folded 5 configuration), designed with sharp concave corners. 187

5.76 Structure of the hybrid staircase filter with manifold inputs and folded central section (Folded 5 configuration), designed with a radius equal to $r = 1.1$ mm. 188

5.77 Simulated performance of the hybrid staircase filter with manifold inputs and folded central section (Folded 5 configuration), using FEST3D LA and CST. 188

5.78 Simulated performance of the hybrid staircase filter with manifold inputs and folded central section (Folded 5 configuration), using FEST3D HA and CST. 189

5.79 Simulated performance of the E-plane folded hybrid SIR filter (Fol SIR Filter), and the E-plane folded hybrid staircase filter with manifold connections (Fol Stair Filter) using CST. 190

5.80 Tolerance analysis of the considered E-plane folded hybrid staircase filter with manifold connections (Folded 5). 193

5.81 Multipactor simulation with discharges for the capacitive window (b_3) of Folded 5 filter at 11.73 GHz. 195

5.82 Manufactured prototype in aluminum of the E-plane folded hybrid staircase filter with manifold connections (Folded 5), without silver plating. 196

5.83 Measurement of the in-band performance of Folded 5 filter compared with the EM simulation (CST). 196

5.84 Measurement of the out-of-band performance of Folded 5 filter compared with the EM simulation (CST). 197

5.85 Simulated performance of the hybrid staircase filter with manifold inputs and folded central section (Folded 5), for the higher order mode TE_{20} using FEST3D and CST. 198

5.86 Simulated performance of the hybrid staircase filter with manifold inputs and folded central section (Folded 5), for the higher order mode TE_{01} using CST. 199

5.87 Simulated performance of the hybrid staircase filter with manifold inputs and folded central section (Folded 5), for the higher order modes TE_{11} and TM_{11} using CST. 199

5.88 Simulated performance of the hybrid staircase filter with manifold inputs and folded central section (Folded 5), for the higher order mode TE_{30} using CST. 200

5.89 Simulated performance of the hybrid staircase filter with manifold inputs and folded central section (Folded 5), for the higher order modes TE_{21} and TM_{21} using CST. 200

5.90 Structure of the H-plane transformer composed of rectangular waveguide sections of smaller width. 202

5.91 Simulated performance (using CST) of our filter with TE_{20} excitation (TE_{20} CST) compared to the performance of the filter plus the high-pass device (TE_{20} Device). 204

5.92 Simulated performance (using CST) of our filter with TE_{30} excitation (TE_{30} CST) compared to the performance of the filter plus the high-pass device (TE_{30} Device). 204

5.93 Structure of the hybrid staircase filter with manifold inputs and folded central section (Folded 5), designed with sharp concave corners and reducing the width of the central resonators. 205

5.94 Structure of the hybrid staircase filter with manifold inputs and folded central section (Folded 5), designed with a radius equal to $r = 1.1$ mm and reducing the width of the central resonators. 205

5.95 Simulated performance of the structures in Fig. 5.93 and Fig. 5.94 (reducing the widths of the central resonators) using FEST3D HA and CST. 206

5.96 Simulated performance (using CST) of the filter in Fig. 5.76 with TE_{20} excitation (TE_{20} CST I), compared to the performance of the filter in Fig. 5.94 reducing the widths of the central resonators (TE_{20} CST II). . 207

5.97 Simulated performance (using CST) of the filter in Fig. 5.76 with TE_{30} excitation (TE_{30} CST I), compared to the performance of the filter in Fig. 5.94 reducing the widths of the central resonators (TE_{30} CST II). . 207

6.1 Structure of the reference capacitive filter. 213

6.2 Simulated performance of the reference capacitive filter. 213

6.3 Typical irises in a rectangular waveguide (front view). Left: centered inductive iris of width a_1. Right: centered capacitive iris of height b_1. . 214

6.4 Resonant aperture in a rectangular waveguide (front view). The aperture is centered and has width a_1 and height b_1. 215

6.5 Geometry of a resonant aperture in a WR-90 waveguide. 215

6.6 Simulated performance of the resonant aperture, changing a_1 from 22.86 mm to 19.25 mm. 216

6.7 Simulated performance of the resonant aperture ($a_1 = 21.50$ mm), changing h from 10.16 mm to 7.50 mm. 216

6.8 Simulated performance of the resonant aperture ($a_1 = 20.00$ mm), changing h from 10.16 mm to 13.50 mm. 217

6.9 Simulated performance of the resonant aperture ($a_1 = 20.00$ mm, $h = 12.50$ mm), changing b_1 from 3.5 mm to 2.0 mm. 218

6.10 Simulated performance of the resonant aperture ($a_1 = 20.00$ mm, $h = 12.50$ mm), changing t from 2.0 mm to 0.5 mm. 218

6.11 Circuital model of the dual-band RA filter. 220

6.12 Structure of the dual-band RA filter. 221

6.13 Simulated performance of the dual-band RA filter (DB RA Filter). . . . 222

6.14 Geometry of a resonator coupled with capacitive couplings in the front and end walls, and capacitive stubs (l_{s_1} and l_{s_2}) in the input of the resonator (side view). 222

6.15 Structure of the dual-band RA filter with capacitive stubs before the input and output RAs. 223

6.16 Simulated performance of the dual-band RA filter with capacitive stubs before the input and output RAs (DB RA TZ Filter). 224

6.17 Geometry of the basic (three-resonator) staircase configuration with the capacitive coupling apertures located at $l_{s_1} = 3l_1/4$, $l_{s_{2a}} = l_2/4$, $l_{s_{2b}} = 3l_2/4$ and $l_{s_{3a}} = l_3/4$ respectively, from the resonator input. . . . 225

6.18 Structure of the capacitive staircase filter. 225

6.19 Simulated performance of the reference capacitive filter (Cap Ref Filter) and the capacitive staircase filter (Cap Stair Filter). 226

6.20 Structure of the dual-band RA staircase filter. 226

6.21 Simulated performance of the dual-band RA staircase filter (DB RA Stair Filter). 227

6.22 Structure of the dual-band RA staircase filter with capacitive stubs before the input and output RAs. 228

6.23 Simulated performance of the dual-band RA staircase filter with capacitive stubs before the input and output RAs (DB RA Stair TZ Filter). . 228

6.24 Simulated performance of the optimized dual-band RA staircase filter with capacitive stubs before the input and output RAs (DB RA Stair TZ Filter). 229

6.25 Structure of the first dual-band RA staircase filter with capacitive stubs before the input and output RAs. 230

6.26 Simulated performance of the dual-band RA staircase filter with capacitive stubs before the input and output RAs (DB RA Stair TZ Filter I). 231

6.27 Structure of the first dual-band RA staircase filter with capacitive stubs before the input and output RAs of the filter (DB RA Stair TZ Filter I), designed with a radius equal to $r = 1.1$ mm in the distributed resonators. 231

6.28 Full-wave simulated performance of the structure in Fig. 6.27 with rounded corners obtained using FEST3D and CST. 232

6.29 Manufactured prototype in aluminum of the first dual-band RA staircase filter (no silver plating). 233

6.30 Measurement of the in-band performance compared with the EM simulation results (CST). 233

6.31 Measurement of the out-of-band performance compared with the EM simulation results (CST). 235

6.32 Structure of the second dual-band RA staircase filter with capacitive stubs before the input and output RAs. 236

6.33 Simulated performance of the dual-band RA staircase filter with capacitive stubs before the input and output irises of the filter (DB RA Stair TZ Filter II). 236

6.34 Structure of the second dual-band RA staircase filter with capacitive stubs before the input and output RAs of the filter (DB RA Stair TZ Filter II), designed with radius equal to $r_1 = 1.1$ mm in the distributed resonators and $r_2 = 1.0$ mm in the capacitive stubs, respectively. 237

6.35 Full-wave simulated performance of the structure in Fig. 6.34 with rounded corners obtained using FEST3D and CST. 238

6.36 Manufactured prototype in aluminum of the second dual-band RA staircase filter (no silver plating). 238

6.37 Measurement of the in-band performance compared with the EM simulation results (CST). 240

6.38 Measurement of the out-of-band performance compared with the EM simulation results (CST). 240

6.39 Tolerance analysis of the first dual-band RA filter. 242

6.40 Tolerance analysis of the second dual-band RA filter. 242

6.41 Multipactor simulation with discharges for the resonant aperture RA_3 at 6.98 GHz of the first dual-band RA filter. 244

6.42 Multipactor simulation with discharges for the resonant aperture RA_3 at 6.97 GHz of the second dual-band RA filter. 244

6.43 Structure of the H-plane transformer composed of rectangular waveguide sections of smaller width. 246

6.44 Simulated performance (using CST) of the first dual-band RA filter with TE_{20} excitation (TE_{20} CST I) compared to the performance of the filter plus high-pass device (TE_{20} Device). 247

6.45 Simulated performance (using CST) of the second dual-band RA filter with TE_{20} excitation (TE_{20} CST II) compared to the performance of the filter plus high-pass device (TE_{20} Device). 247

7.1 Circuital model of the extended bandpass RA filter. 252

7.2 Circuital model based on a $\prod$ configuration. 253

7.3 Structure of the extended bandpass RA filter. 254

7.4 Simulated performance of the extended bandpass RA filter (EB RA Filter). 255

7.5 Structure of the extended bandpass RA filter with four capacitive stubs between all the RAs. 255

7.6 Simulated performance of the extended bandpass RA filter (EB RA Filter) and the EB RA Filter with four capacitive stubs between all the RAs (EB RA TZ Filter). 256

7.7 Structure of the extended bandpass RA staircase filter. 257

7.8 Simulated performance of the extended bandpass RA filter (EB RA Filter) and the EB RA Filter with the staircase configuration (EB RA Stair Filter I). 257

7.9 Simulated performance of the extended bandpass RA filter with the staircase configuration (EB RA Stair Filter I) and the EB RA Stair Filter I with the optimized change of the RAs location (EB RA Stair Filter II). 258

7.10 Structure of the extended bandpass RA staircase filter with two stubs both before and after of the input and output RAs. 259

7.11 Simulated performance of the extended bandpass RA staircase filter (EB RA Stair Filter II) and the EB RA Stair Filter II with two stubs both before and after of the input and output RAs (EB RA Stair TZ Filter). 259

7.12 Simulated performance of the extended bandpass RA filter (EB RA Filter) and the EB RA Stair Filter II with two stubs both before and after of the input and output RAs (EB RA Stair TZ Filter). 260

7.13 Simulated performance, in a wider frequency range (from 6.5 to 13 GHz), of the EB RA Filter (EB RA Filter I) and the EB RA Stair TZ Filter (EB RA Filter II). 261

7.14 Structure of the extended bandpass RA filter with two stubs both before and after of the input and output RAs (EB RA Stair TZ Filter), designed with a radius equal to $r = 1.1$ mm in the distributed resonators. 262

7.15 Simulated performance of the extended bandpass RA filter with two stubs both before and after of the input and output RAs (EB RA Stair TZ Filter) using FEST3D and CST. 262

7.16 Manufactured extended bandpass RA prototype in aluminum (no silver plating). 264

7.17 Measurement of the in-band performance of the extended bandpass RA filter compared with the EM simulation (CST). 265

7.18 Measurement of the out-of-band performance of the extended bandpass RA filter compared with the EM simulation (CST). 265

7.19 Measurement of the out-of-band performance of the extended bandpass RA filter compared with the EM simulation (CST) including losses (due to the finite conductivity of the aluminum). 266

7.20 Tolerance analysis of the extended bandpass RA filter. 267

7.21 Multipactor simulation with discharges for the resonant aperture RA_2 at 6.81 GHz of the extended bandpass RA filter. 268

7.22 Simulated performance of the EB RA Filter (EB RA Filter III) and the EB RA Stair TZ Filter (EB RA Filter IV). 269

7.23 Simulated performance (using CST) of the extended bandpass RA filter with TE_{20} excitation (TE_{20} CST) compared to the performance of the filter plus high-pass device (TE_{20} Device). 270

A.1 Structure of the flanges for WR-90. 277
A.2 3D plans of the in-line hybrid SIR filter. 280
A.3 3D plans of the in-line screw hybrid SIR filter. 281
A.4 3D plans of the E-plane folded hybrid SIR filter. 282
A.5 3D plans of the E-plane folded hybrid staircase filter. 283
A.6 3D plans of the first dual-band RA staircase filter. 284
A.7 3D plans of the second dual-band RA staircase filter. 285
A.8 3D plans of the extended bandpass RA staircase filter. 286

Table List

3.1 Physical dimensions for the in-line hybrid SIR filter. 93

3.2 Errors of the measures of the fabricated structure and inverse ASM. . . 97

3.3 Errors of the measures of the fabricated structure and inverse ASM. . . 98

3.4 Tolerance analysis of the fabricated structure. 98

3.5 High power analysis of the in-line hybrid SIR filter. 100

3.6 Cut-off frequencies of higher order modes exciting the in-line inline hybrid SIR filter. 102

4.1 Physical dimensions for the hybrid SIR filter with body and cover. . . . 119

4.2 Physical dimensions for the E-plane folded hybrid SIR filter. 128

4.3 Tolerance analysis of the structures that we have fabricated. 130

4.4 High power analysis of the in-line hybrid SIR filter with tuning screws. 133

4.5 High power analysis of the E-plane folded hybrid SIR filter. 133

5.1 Position of the first three resonators for each staircase configuration. . . 155

5.2 Location of the capacitive irises for each topology. 155

5.3 Position of the fourth resonator, and of the first and second inductive irises, in the central section for each folding configuration. 177

5.4 Physical dimensions (manifold T-junctions and coupling windows) for the E-plane folded hybrid staircase filter with manifold connections. . . 191

5.5 Physical dimensions (resonators) for the E-plane folded hybrid staircase filter with manifold connections. 192

5.6 Results of the tolerance analysis. 193

5.7 High power analysis of the the considered E-plane folded hybrid staircase filter with manifold connections (Folded 5). 194

5.8 The higher order modes cut-off frequencies of the Folded 5 filter. 198

5.9 Physical dimensions for the high-pass filter. 202

5.10 Physical dimensions (manifold T-junctions and coupling windows) for the new E-plane folded hybrid staircase filter with manifold connections, and reducing the width of the central resonators. 208

5.11 Physical dimensions (resonators) for the new E-plane folded hybrid staircase filter with manifold connections, and reducing the width of the central resonators. 209

6.1 Physical dimensions for the first DB RA Staircase Filter I with two stubs before of the RAs. 234

6.2 Physical dimensions for the second DB RA Staircase Filter II with two stubs before of the RAs. 239

6.3 Results of the tolerance analysis for the dual-band RA filters. 241

6.4 High power analysis of the first dual-band RA filter. 243

6.5 High power analysis of the second dual-band RA filter. 243

6.6 The higher order modes cut-off frequencies. 245

6.7 Physical dimensions for the high-pass filter. 246

7.1 Physical dimensions for the EB RA Stair TZ Filter. 263

7.2 Results of the tolerance analysis for the extended bandpass RA filter. . 266

7.3 High power analysis of the extended bandpass RA filter. 268

Acronyms

ASM	Aggressive Space Mapping
CST	CST Microwave Studio
EM	Electromagnetic
FEST3D	3D Full-Wave EM Software Tool
HA	High-Accuracy
HFSS	High-Frequency Structure Simulator
IL	Insertion Loss
LA	Low-Accuracy
RA	Resonant Aperture
RL	Return Loss
SIR	Stepped Impedance Resonator
TZ	Transmission Zero
UIR	Uniform Impedance Resonator
VNA	Vector Network Analyzer

Chapter 1

Introduction

1.1 Motivation and Objectives

Waveguide technology is especially suitable for a wide variety of payloads in the microwave and millimeter-wave frequency bands for both ground and space applications. In particular, the use of filters to select specific portions or segments of the radiofrequency spectrum (or channels) is of paramount importance for all telecommunication and earth observation systems. For this reason, the development of new, more advanced microwave and millimeter wave filtering structures has motivated in the last fifty years a very significant research effort. Furthermore, the current evolution trends require the implementation of microwave filters with ever increasing demands on both electrical and mechanical specifications.

In this context, therefore, the research work described in this doctoral thesis includes several lines of investigations. The overarching objective is to introduce new topologies that can be used to implement filters with pass-bands that are as wide as possible while, at the same time, achieving significant improvements in the out-of-band response with respect to classical solutions [1].

To this end, one of the structures that we propose in this work is based on the simultaneous use of inductive and capacitive irises for the design of waveguide filters to take effectively advantage of the specific characteristics offered by both topologies [2], [3].

Another line of investigation is to study the possibility of replacing resonant cavities of uniform heights with structures based on waveguide sections of different height. This is, in fact, equivalent to building resonators cascading waveguides of different characteristic

impedance, also known as stepped impedance resonators (SIRs) [4]. This is motivated by the well-known fact that SIRs can provide a higher rejection by decreasing the level of the spurious responses, or shifting them far away from the useful filter pass-band.

Another approach that is discussed to improve the out-of-band response of filters is the staircase configuration [5]. This topology is based on arranging the coupling windows in a particular configuration with the objective of reducing the coupling of higher-order resonances between adjacent resonators. In addition, another approach that is discussed is the use of E-plane T-junctions with shorted stubs or manifold connections [6] to introduce transmission zeros in the filter transfer function. Additionally, E-plane folded structures are also explored with the objective of further improving the filtering performance.

In addition to the above, a further novel concept is also introduced in this research work, namely, the double use of coupling apertures as resonant apertures (RAs) and impedance inverters, with the objective of creating new families of compact dual-band and wide-band microwave filters in rectangular waveguide [7].

It is important to mention that all of the solutions proposed in this thesis are first discussed theoretically, the resulting waveguide structures are then simulated and optimized with full-wave EM simulators of proven accuracy. After that, they are manufactured and tested always obtaining an excellent agreement between simulations and measurements.

Chapter 2

State of the Art

As already discussed, the objective of this doctoral thesis is to propose new technological solutions for the implementation of microwave and millimeter-wave filters for both ground and space applications, with particular emphasis on satellite payloads. In this context, therefore it is interesting to briefly review some of the space systems that are currently under development, as shown in Fig. 2.1.

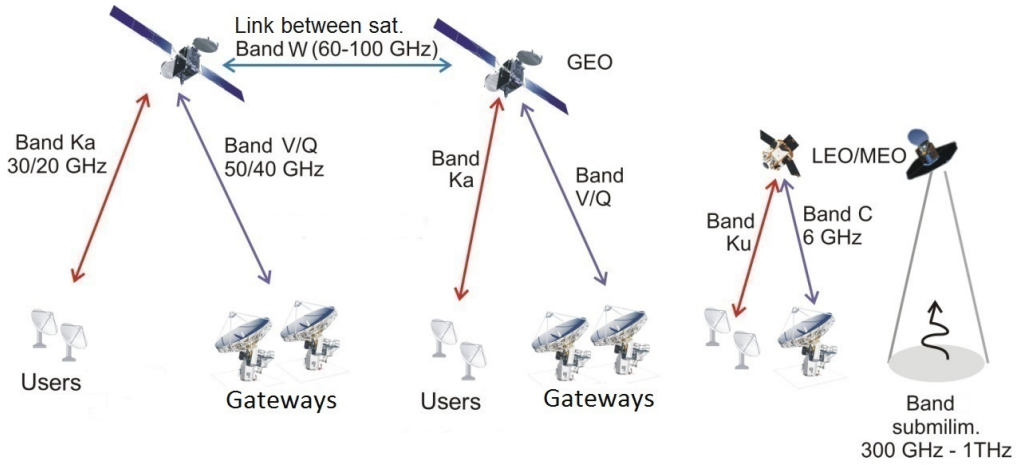

Figure 2.1: Scenario with emerging applications of future satellites.

The increasing demand for wide-band communication services using geostationary satellites has recently motivated the design of microwave filters with wider bandwidths, increased selectivity and wider spurious-free performance. A typical diagram of a communication subsystem of a satellite repeater is shown in Fig. 2.2 [6].

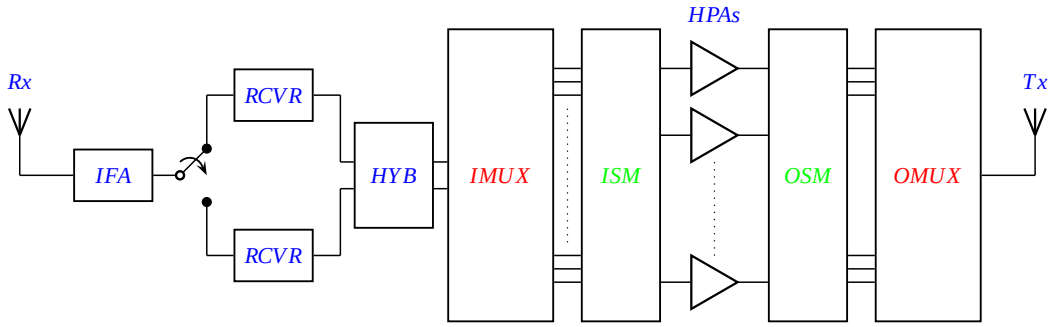

Figure 2.2: Satellite communication subsystem block diagram.

The block diagram of Fig. 2.2 is composed of the following components:

- A receive antenna (Rx) that is connected to an IFA (Input Filter Assembly). The IFA is composed of a wide-band filter, followed by a redundant low-noise receiver (RCVR).
- Next, the signal is channelized into an input multiplexing network (IMUX) in order to divide the frequency plan into the individual RF channels (transponders).
- The traffic flow from one transponder to another is provided by the input and output switch matrices (ISM and OSM).
- The HPAs (High-Power Amplifiers) are necessary to raise the power levels of the RF signals before they are transmitted back to earth.
- The output multiplexer (OMUX) network is used to recombine each RF channel after amplification. Finally, the wide-band signal generated by the OMUX is fed to the transmit antenna (Tx).

To better understand the receiver section in the diagram displayed in Fig. 2.2, we now show in Fig. 2.3 a more detailed block diagram [6]. The components are:

- The IFA consists of a wide-band input receive filter that selects only the signals in the allocated frequency spectrum.
- Next, the signals are fed to the LNA (low-noise amplifier).
- To minimize the interference between the transmit and receive frequencies a frequency down-converter is required. It is composed of a mixer-local oscillator (LO) assembly.
- Before the channelization and final amplification of the signals, a driver amplifier (DAMP) is required in order to achieve the required power levels.
- Finally, the two redundant paths are combined with a 3 dB hybrid.

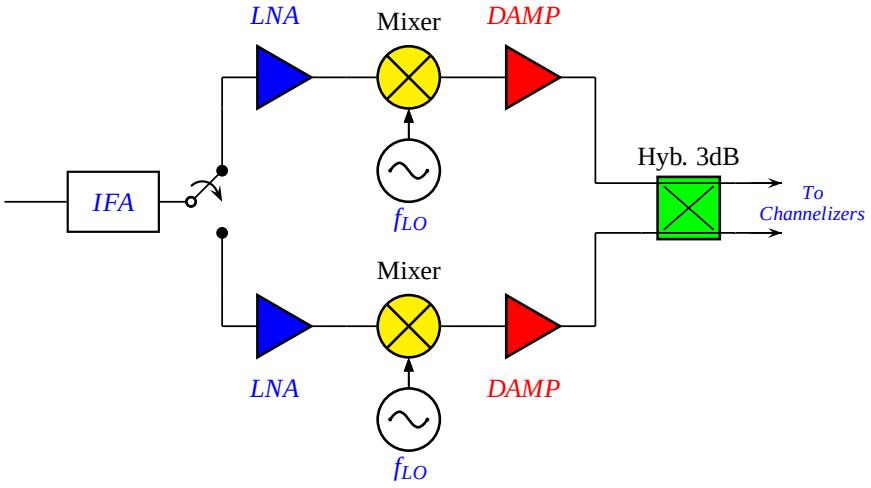

Figure 2.3: Satellite receiver block diagram.

An output multiplexing network is then used to combine the outputs of the various high-power channel amplifiers into a single RF signal that is re-transmitted with a common antenna. Fig. 2.4 shows the multiplexing scheme of a contiguous band multiplexer in a satellite system [6]. This scheme consists of a number of bandpass filters that are connected to a common manifold (block M in Fig. 2.4). The output of each filter corresponds to a transponder channel that accepts the amplified signal within the passband and rejects the frequencies of the other transponders. The next device is a wide-band harmonic filter, which is required to limit the potential interference with other systems.

The main advantage of this scheme is that allows a simpler beamforming network with the objective to simplify the optimization of the antenna. In addition to the sharper amplitude characteristics, this scheme allows to reduce the effect of multipath in the satellite, which results into an improvement of the communication channel characteristics.

As shown above, therefore, microwave filters are key components of all communication satellite payloads.

2.1 Microwave Filters

As briefly discussed in the previous section, microwave filters are indeed among the most important components for all telecommunication and earth observation satellite payloads. This has, in turn, motivated, up to the current days, a very significant amount of research. This interest is clearly demonstrated by the very large number of contributions that can be found in the technical literature. An excellent review of both filter structures and dedicated design procedures can be found in [8] and [9].

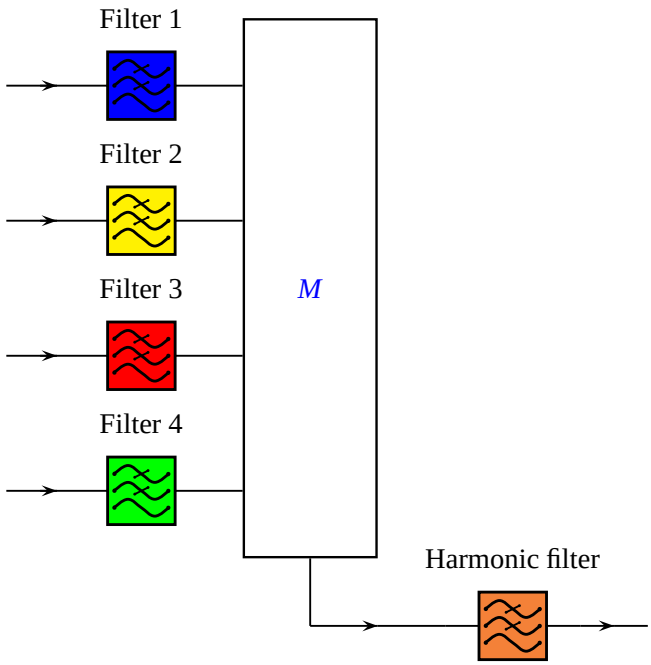

Figure 2.4: Multiplexing scheme in a satellite system.

As the advancement of the state-of-the-art of microwave filters is the overarching objective of the research described in this doctoral thesis, we find it appropriate to outline in this chapter some of the most recent developments in the area.

Microwave filters can be implemented in many different technologies such as planar, coaxial or metallic waveguide, just to mention a few of them [10], [11] and [12]. Fig. 2.5 shows different examples of implementations of microwave filters, namely:

- Fig. 2.5 (a) shows the structure of a low-pass corrugated waveguide filter in rectangular waveguide [12].
- Fig. 2.5 (b) shows a planar filter based on hybrid microstrip and coplanar waveguide [13].
- Fig. 2.5 (c) shows the manufactured prototype of a band-pass inductive waveguide filter [14].
- Fig. 2.5 (d) shows the manufactured prototype of a dual-mode filter in circular waveguide technology [14].
- Fig. 2.5 (e) shows the structure of a coaxial diplexer with combline resonators coupled by small lateral apertures [12].
- Fig. 2.5 (f) shows the structure of a compact triple-band bandpass filters based on rectangular waveguide resonators [15].

(a) Low-pass corrugated waveguide filter.

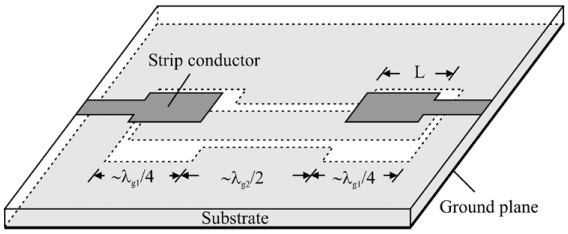

(b) Planar filter.

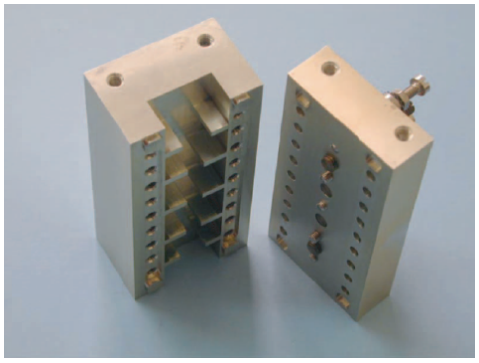

(c) Inductive waveguide filter.

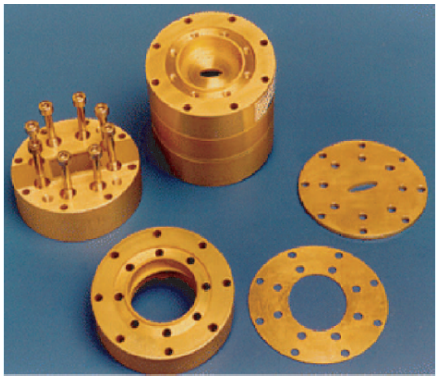

(d) Dual-mode filter in circular waveguide.

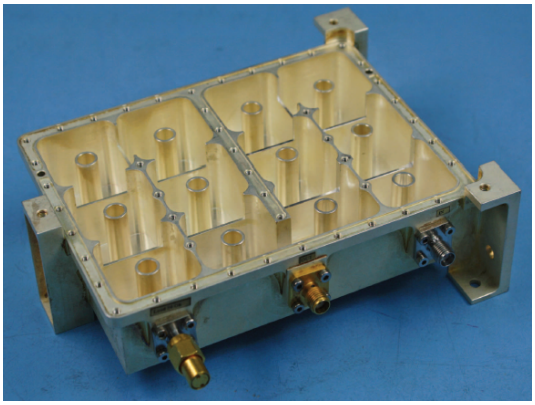

(e) Coaxial diplexer with combline resonators.

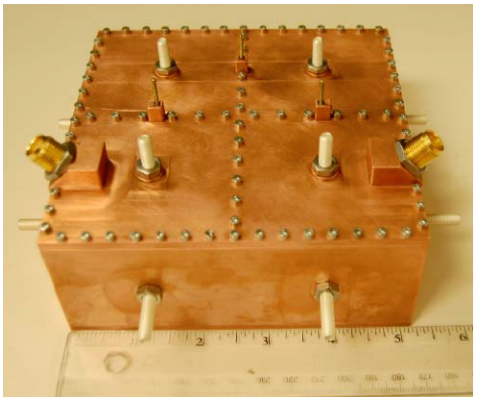

(f) Triple-band waveguide filter.

Figure 2.5: Examples of implementations of microwave filters.

Furthermore, it is important to note that, in addition to the bandpass performance, the out-of-band performance is also a key parameter for all microwave filters. This is particularly relevant for filters implemented with coupled resonator structures based on lengths of uniform waveguide. This is because the resonators, in addition to producing the wanted resonance at the filter center frequency, generally produce also a number of unwanted (or spurious) resonances corresponding to the harmonics of the basic resonance. The spurious resonances can then result into additional unwanted pass-band regions above the desired pass-band, thus degrading the out-of-band performance of the filter.

2.1.1 Hybrid and Wide-Band Filtering Structures

A number of different approaches have indeed been proposed in the past to overcome this key aspect of the out-of-band performance of coupled resonator filters. For instance, one of the first techniques developed in the 1990s is the use of *hybrid* filtering structures, which are based on the use of mixed lumped and distributed resonators [16]. The basic idea of hybrid structures is simple. The filter is composed of different types of resonators with harmonic responses that do not coincide in frequency. This, in turn, produces an important improvement in the out-of-band performance. A number of different hybrid filter implementations has also been discussed in the technical literature. For instance, a new configuration of a dielectric loaded cavity filter that uses the TE_{01} and HE_{11} modes to improve the out-of-band performance has been proposed in [17] and [18].

Another hybrid approach has been proposed in [19], where a combline filter has been designed based on mixed capacitive and inductive couplings, in order to generate transmission zeros near the pass band with the objective of improving the selectivity. Also, in [20] a folded rectangular waveguide filter has been designed with mixed capacitive and inductive irises in order to implement transmission zeros in the out-of-band response.

Furthermore, a novel mixed resonator filter configuration has also been discussed in [21], where the structure is based on a combination of combline resonators and the HE_{11} mode of a dielectric resonator, with the objective to improve the spurious response. Yet another example has been proposed in [22], where mixed electric and magnetic couplings between the resonators are used in order to generate transmission zeros near the filter pass-band, thus enhancing the selectivity. Also, in [23], a novel hybrid structure based on the combination of a substrate integrated waveguide (SIW) and coplanar waveguide (CPW) has been proposed with the advantages of improving both the in-band and the out-of-band responses.

More recently, several papers have discussed improvements of both the pass-band and the out-of-band performance of a filter using mixed-mode and hybrid structures. For instance, a pseudo-elliptic filter based on mixed-mode resonators, namely, the TE_{101}

cavity mode and the $TE_{01\delta}$ dielectric mode have been proposed in [24] and [25]. Also, a novel hybrid bandpass filter has been proposed in [26], where the structure is based on coaxial resonators and an evanescent mode waveguide loaded with posts, thereby obtaining an important improvement of the out-of-band response and, at the same time, an enhancement of the filter selectivity.

Other examples of hybrid structures have also been reported. For instance, a compact bandpass filter based on the using quarter-mode substrate integrated waveguide (QMSIW) cavities with mixed couplings, and another with coplanar waveguide (CPW) have been proposed in [27] and [28], respectively. Yet other approaches based on the use of lumped elements have been proposed in [29] and [30], with the objective of obtaining an important improvement in both the pass-band and the out-of-band responses.

In this context, it is interesting to note that many contributions can be found in the technical literature describing wide-band filters in planar technology. For instance. a novel ultra-wideband (UWB) bandpass filter (BPF) which uses a hybrid microstrip and coplanar waveguide (CPW) structure is described in [13]. Also, a compact ultra-wideband bandpass filter, based on a microstrip and coplanar waveguide (CPW) structure, has been proposed in [31].

Many additional examples of hybrid structures can also be found in the technical literature for wide-band filter implementations in planar technology. For instance, a highly selective wide-band bandpass filter has been proposed in [32], where the structure is based on the combination of microstrip and CPW sections.

However, the structures in planar technology have the following well-known limitations:

- High insertion loss.
- Limited out-of-band rejection at high frequencies.
- Low power-handling capabilities.

On the other hand, a significantly smaller number of contributions can be found in the technical literature discussing wide-band filters in rectangular waveguide technology. For instance, a filter with wide pass-band that covers the frequency range of 40-60 GHz has been proposed in [33]. However, the resulting structure is rather long, since it is based on the cascaded connection of an inductive bandpass filter and a capacitive low-pass filter.

Furthermore, in [34] a rectangular waveguide band-pass filter has been designed with reduced sensitivity to fabrication tolerances for Q-band payloads. Also, a stepped-impedance band-pass filter in rectangular waveguide with an improved selectivity has been proposed in [35]. However, the resulting structures are rather long.

In this context, therefore, and as already discussed, the main objective of this thesis is to introduce novel structures for the implementation of wide-band bandpass filters in rectangular waveguide. We find it therefore appropriate to discuss in the next section the state-of-the-art of rectangular waveguide filters.

2.2 Rectangular Waveguide Filters

One of the oldest areas of research in the microwave field is indeed the study, analysis and design of microwave filtering structures in rectangular waveguide. In this context, several methodologies and sets of formulas have indeed been developed since the very early days of microwaves. For wide-band filters, for instance, the most traditional design procedure is to view the filter as a low-pass structure [36] and [37]. Many other procedures have also been developed for narrow-band filters using lumped-element networks [38]-[42].

Independently from which design procedure we follow, however, the design of microwave filters always starts with a set of specifications. The specifications usually cover both the electrical performance and other physical or environmental requirements. Typical electrical requirements are:

- Center frequency and bandwidth
- In-band Return Loss level
- Near-band selectivity
- Out-of-band rejection
- High-power capability

Typical physical requirements are:

- Hardware size and mass
- Resistance to vibrations
- Good temperature behavior
- Specified maximum outgassing

In this context, one of the most challenging requirements that needs to be addressed for all filters in general, and for filters in rectangular waveguide technology in particular, is the out-of-band performance. The reason for this is that a length of rectangular waveguide generally has a frequency response that is periodic. As a consequence, in addition to the desired pass-band (usually located at the lowest frequency), they also exhibit additional undesired band-pass regions at higher frequencies. The higher pass-bands are normally considered spurious responses that need to be (ideally) eliminated. Another equally important requirement is the near-band selectivity. This parameter has a direct effect on the efficiency of the spectrum utilization. As a consequence, the near-band selectivity is

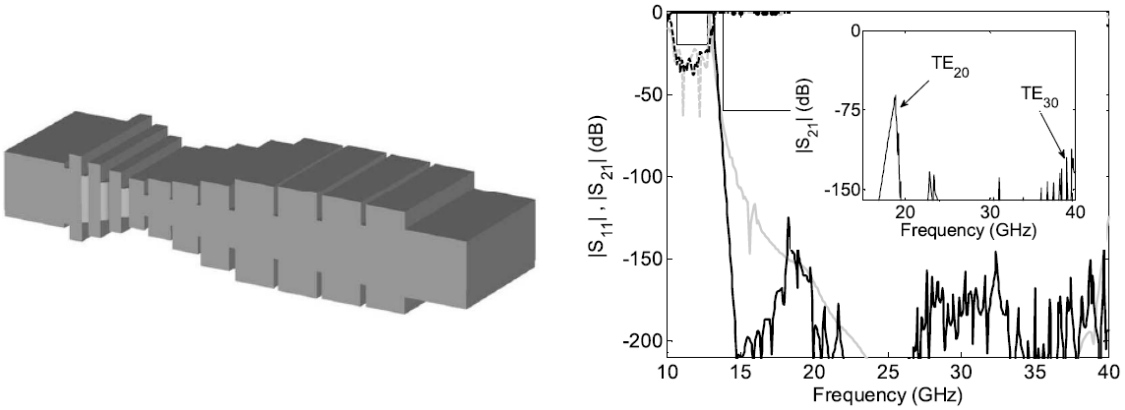

(a) Structure of the chirped filter.

(b) Simulated performance of the filter.

Figure 2.6: Cascaded low-pass and band-stop filters.

very often a critical parameter.

For wide-band filters, satisfying a the same time the near-band requirements and the out-of-band performance is normally a particularly challenging issue.

Many approaches have indeed been developed in the past to overcome this problem. The simplest and most traditional solution is to cascade a low-pass filter with a band-stop filter, as shown in Fig. 2.6, with the objective of obtaining good near-band selectivity and suppress, at the same time, all the spurious responses with a stop-band filter, as discussed, for instance, in [43] and [44]. This is indeed an effective solution but the resulting structure can have a very significant size and mass.

2.2.1 Inductive Band-Pass Filters

In rectangular waveguide technology, band-pass filters have traditionally been implemented using lengths of waveguides as resonators, and inductive posts or irises as coupling elements (or impedance inverters) [1]. An example of this classic topology is shown in Fig. 2.7 [14].

The structure in Fig. 2.7 is very simple, and it is indeed one of the most common implementation of band-pass filters in rectangular waveguide. Furthermore, this type of filter has very good rejection levels below the filter pass-band. The near-band rejection levels can also be achieved increasing the order of the filter. However, due to the periodic nature of the behavior of waveguide resonators, the response of these filters usually show significant unwanted spurious responses above the intended filter pass-band. Unfortunately, the spurious responses become stronger as the filter bandwidth is increased. As a consequence, this type of filter is usually recommended only for narrow-band applica-

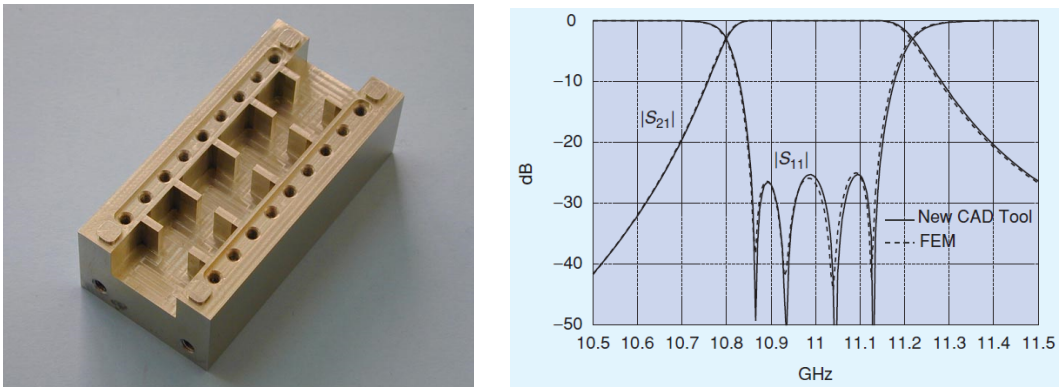

(a) Structure of the inductive filter.

(b) Simulated performance of the filter.

Figure 2.7: Bandpass filter in rectangular waveguide with inductive irises.

tions [1].

Examples of filters with inductive irises in rectangular waveguide are discussed, for instance, in [45] and [46], for narrow to fairly wide bandwidth applications. The main advantages offered by this type of filters are:

- The design is very well established.
- The fabrication cost can be very low.
- The high power capability is excellent.

However, as already anticipated, for wide-band implementations, inductive filter structures can exhibit a number of shortcomings, in particular:

- The presence of spurious responses due to the behavior of the basic resonators.
- Wide-band design require strong input couplings that are difficult to implement with narrow inductive windows. The use of wider inductive windows helps to degrade the out-of-band response.
- The behavior of an iris is frequency dependent. Using irises to implement inverters (usually frequency independent) in practice, may produce an added difficulty in the design process (non-existent in narrow-band designs).

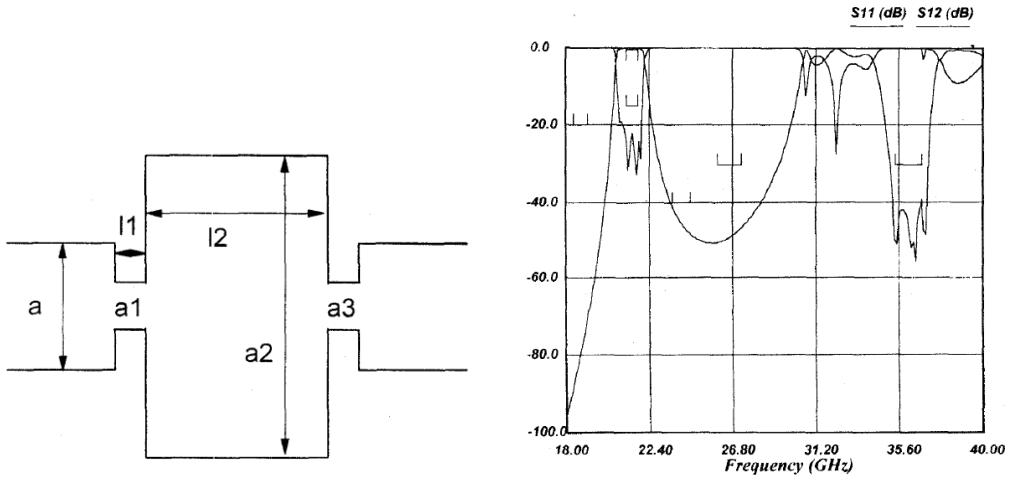

(a) Structure of the cavity.

(b) Simulated performance of the filter.

Figure 2.8: Cavity used to exploit the interaction between TE_{10} and TE_{30} modes.

2.2.2 Improved Inductive Filters

A very large number of different techniques have indeed been reported in the technical literature with the objective of improving the out-of-band response of inductive filters in rectangular waveguide. A solution based on integrating band-pass and band-reject filters in rectangular waveguide has been, for instance, proposed in [47]. The objective is to reduce, or to eliminate, the second harmonic of the filter exploiting the interaction between the fundamental TE_{10} mode within each filter cavity with the higher TE_{30} mode generated at the coupling apertures, as shown in Fig. 2.8. Also, an inductive evanescent-mode filter with dielectric resonators has been proposed in [48], in order to obtain a good spurious-free band, as shown in Fig. 2.9.

Another approach is the well-known technique of changing the width of the resonators, as discussed in [49] and [50], with the objective of improving the out-of-band performance. In another contribution, a rectangular waveguide band-pass filter has been proposed [51], where an important improvement of the stop-band performance is obtained changing the width of each resonator together with the offsets between adjacent resonant cavities. In addition, a non-uniform inductive filter with different resonator widths has also been proposed in [52], with the objective of improving the spurious-free stop-band, as shown in Fig. 2.10.

Additionally, a novel rectangular waveguide band-pass filter structure has been proposed in [53], where capacitively-loaded resonators are used in order to avoid spurious responses thereby obtaining an important stop-band suppression. Furthermore, an inductive waveguide band-pass filter has been proposed in [54], using inductive irises of different

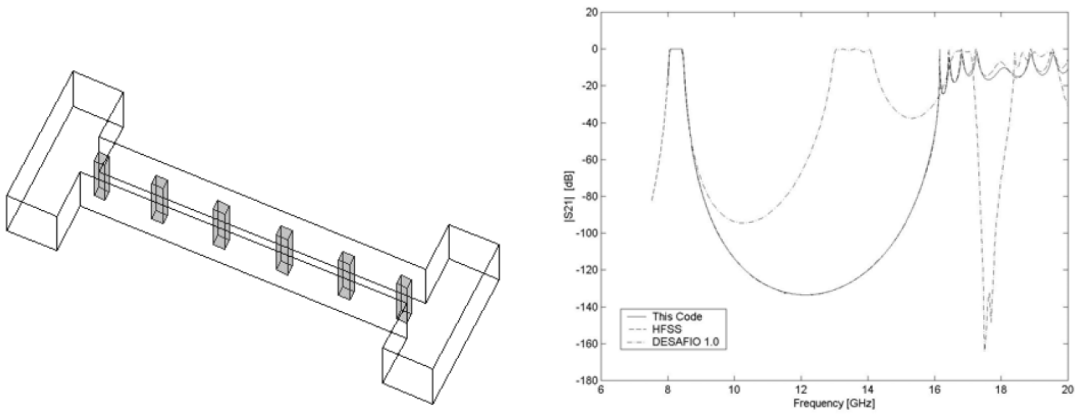

(a) Structure of the filter. (b) Simulated performance of the filter.

Figure 2.9: Six-pole evanescent inductive filter loaded with rectangular dielectric posts.

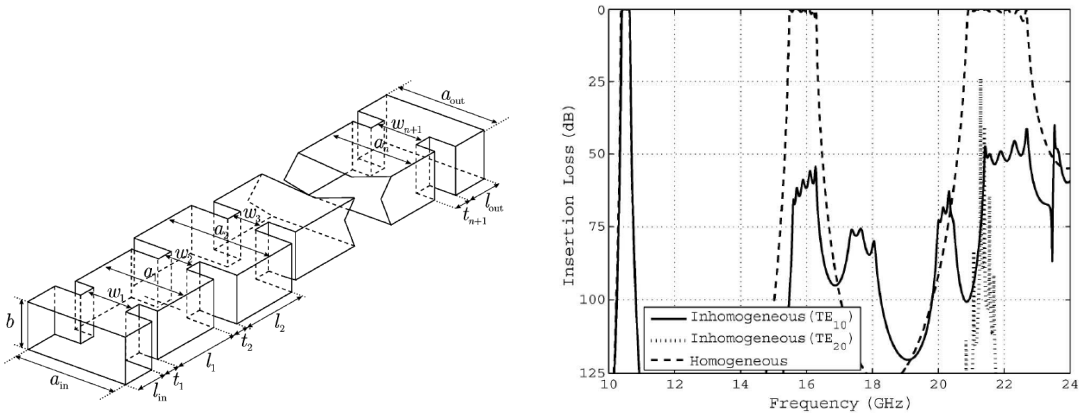

(a) Structure of the filter. (b) Simulated performance of the filter.

Figure 2.10: Inductive filter with change of resonator widths and iris thicknesses.

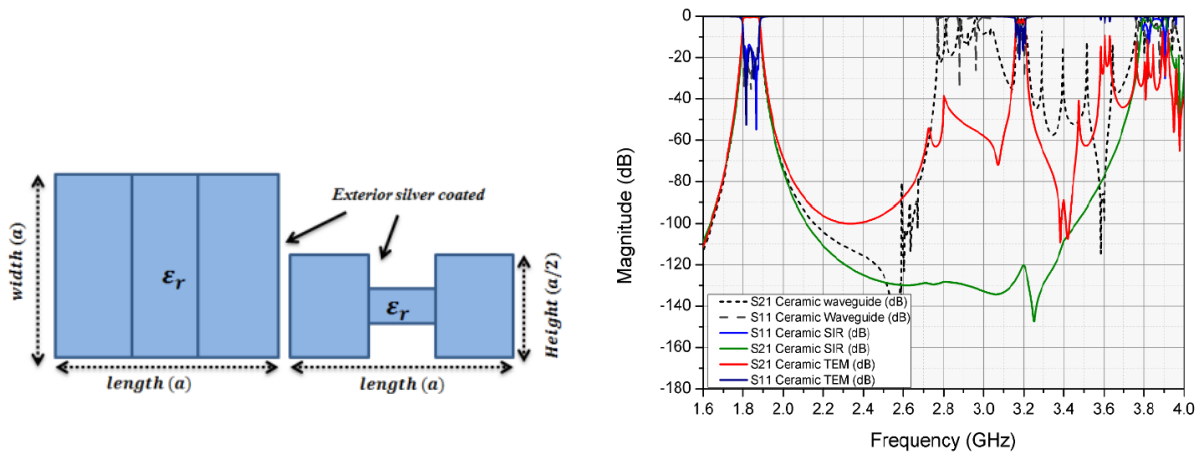

(a) Structure of the SIR.

(b) Simulated performance of the filter.

Figure 2.11: Implementation of a SIR resonator.

thicknesses, and resonators of different widths, in order to reduce the first harmonic pass-band, and further increase the level of spurious rejection.

Moreover, integrated ceramic waveguide filters have been proposed in [55] and [56]. The structures are based on non-uniform width ceramic waveguide resonators and evanescent mode ceramic resonators, in order to improve the spurious performance. Additionally, a filter based on a waveguide loaded with dielectrics of different width has been proposed in [57], always with the objective of obtaining an improved spurious-free response.

One more very effective approach to improve the stop-band performance of microwave filters is to use resonators composed of a number of waveguide sections with different characteristic impedance. These are the so-called stepped impedance resonators (SIRs). In [4], for instance, rectangular waveguide band-pass filters have been designed using SIRs in empty waveguides coupled through symmetric inductive irises. Also, in [58] integrated ceramic waveguide filters coupled through inductive posts have been designed with SIRs, as shown in Fig. 2.11. Both approaches provide a very good stop-band performance with a wide spurious-free frequency range above the pass-band.

More recently, a new technique for rectangular waveguide inductive band-pass filters has been proposed in [5], using a particular arrangement of the coupling windows that attenuates the coupling between harmonic resonances and improves the out-of-band response. The energy coupling between one resonator and the next one in inductive filters is implemented coupling the magnetic field from one resonator to the other. To understand the basic idea behind this approach, it is therefore convenient to examine first the magnetic field distribution of the first three resonant modes of a rectangular waveguide cavity,

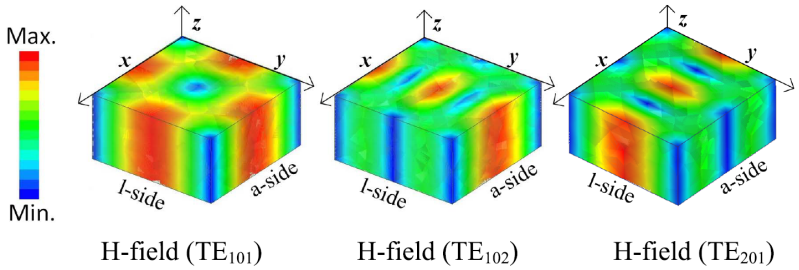

Figure 2.12: Simulated magnetic field distributions of TE_{101}, TE_{102}, and TE_{201} modes.

as shown in Fig. 2.12. As we can see from the field distribution, locating the inductive irises in the center of the side wall of the resonator, as shown in Fig. 2.13 (b), will strongly reduce the TE_{102} resonance coupling. The out-of-band performance will therefore be effectively extended without introducing additional elements in the structure, as shown in Fig. 2.13.

However, all the contributions discussed so far are applicable only to narrow-band filter structures. This is because they all use inductive windows to control the coupling between resonators. As the frequency is increased, the section of waveguide used to implement the inductive window will go above cut-off, thereby allowing energy to propagate freely between input and output.

An effective alternative to improve the out-of-band response of band-pass filters is to use capacitive irises [59] and [60], as shown in Fig. 2.14. Capacitive irises have the opposite frequency behavior of inductive irises. If the frequency is increased, they eventually behave as a short circuit thereby not allowing energy to propagate from input to output. However, the appearance of unwanted resonances below the filter pass-band is a drawback. Furthermore, small values of the height of the capacitive irises may be required, and that may result in high power limitations.

Furthermore, additional examples of the use of capacitive structures are shown in [61] and [62], as shown in Fig. 2.15, where low-pass structures (capacitive discontinuities) are used in a filter as coupling elements in order to provide a wide spurious free out-of-band response and improve the stop-band attenuation.

A small number of contributions can also be found in the technical literature discussing the design and implementation of waveguide structures using hybrid irises (that is inductive and capacitive ones) in rectangular waveguide. In [63], for instance, a band-pass filter in Ku-band is discussed using small-aperture irises for coupling the adjacent cavities. Also, a C-band filter has been designed in [64], where both inductive and capacitive irises are used. The use of two-sided double-slot capacitive irises (that are resonant irises with

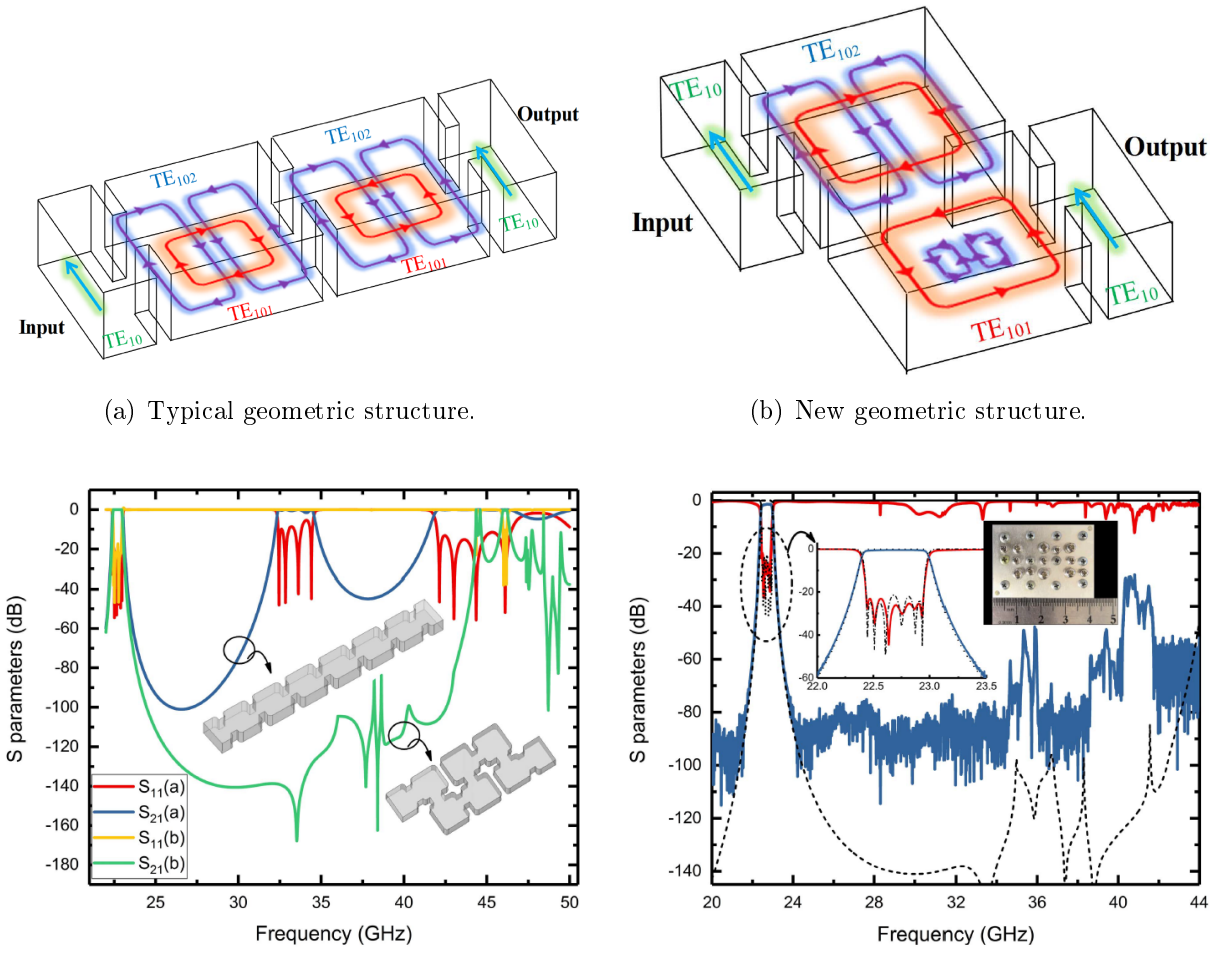

(a) Typical geometric structure.

(b) New geometric structure.

(c) Simulated performance of the filter.

(d) Manufactured of the filter.

Figure 2.13: Waveguide structure of the inductive staircase filter.

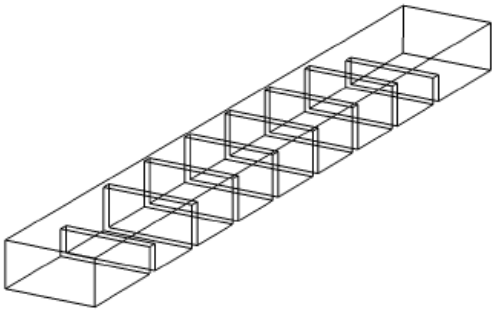

(a) Structure of the CIRWBPF.

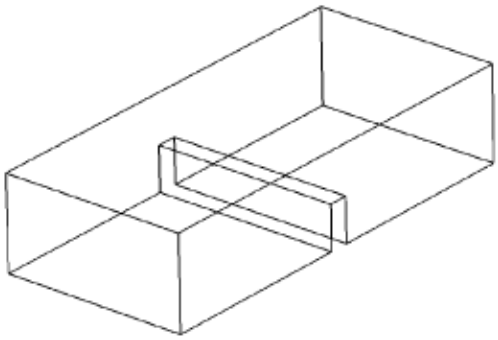

(b) Structure of the capacitive iris.

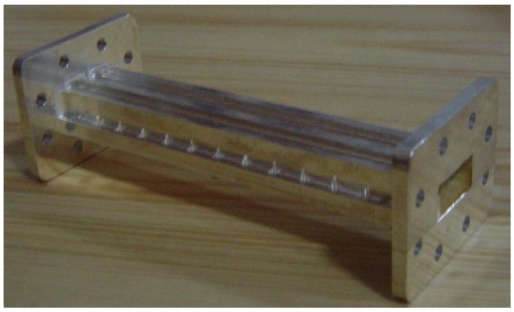

(c) Manufactured filter.

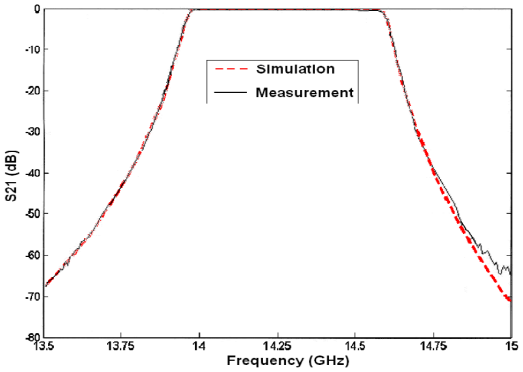

(d) Performance of the filter.

Figure 2.14: Implementation of the high-power rectangular waveguide band pass filter with capacitive coupling iris (CIRWBPF).

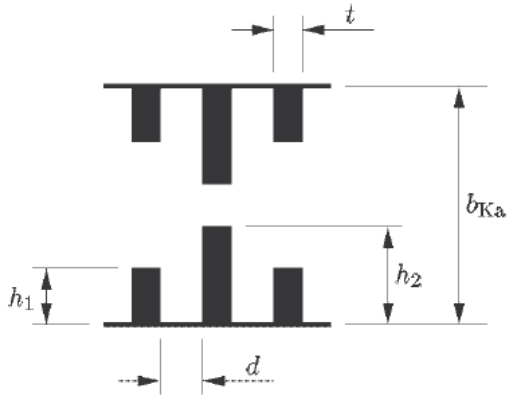

(a) Structure of a simple low-pass structure.

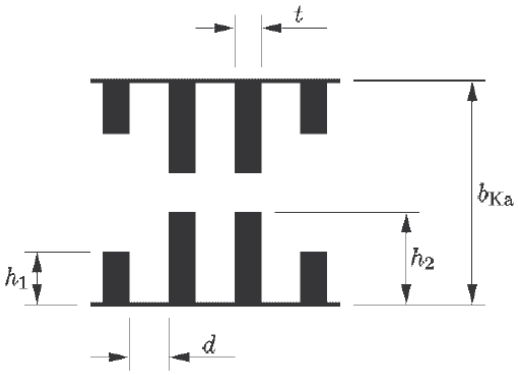

(b) Structure of the low-pass structure with capacitive irises.

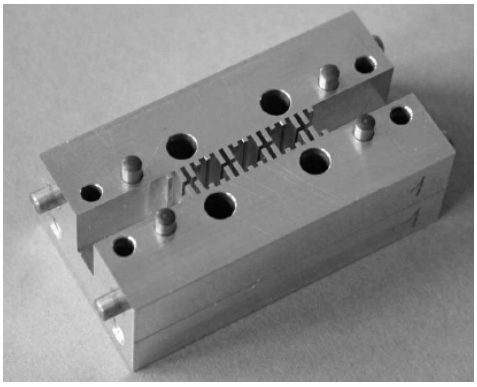

(c) Manufactured filter.

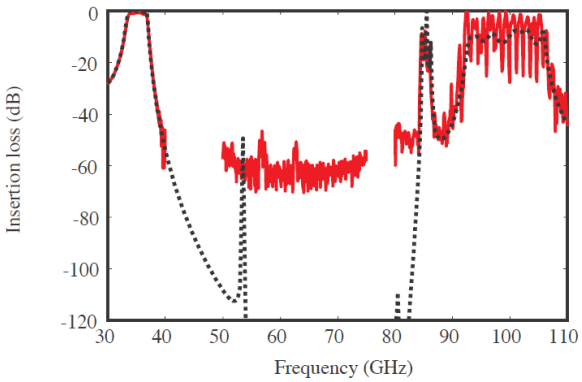

(d) Measured performance of the filter.

Figure 2.15: Side view of a filter inverter realized as a low-pass structure with capacitive irises.

more complex geometry) has been proposed in [65]. However, all of the contributions discussed so far, have considered only narrow-band applications.

In this context, therefore, in the remainder of this thesis, we will discuss how to extend the state-of-the-art of rectangular waveguide filters by introducing a number of techniques to obtain wide-band responses with an important improvement in terms of both selectivity and out-of-band performance, while reducing, at the same time, the footprint of the filter.

2.2.3 Improving Filter Selectivity

An important aspect of the performance of a microwave filter is the selectivity. A well-known technique that can be used to improve both the out-of-band performance and the filter selectivity is the introduction of transmission zeros (TZs) in the filter transfer function. Classic approaches to generate TZs are the use of cross-couplings between non-adjacent resonators, the introduction of additional signal paths, and the use of extracted poles [6]. For instance, in [66] an inductive filter has been designed with different cavity configuration, as shown in Fig. 2.16, where the higher order mode interactions are exploited to generate an additional signal path, thus introducing TZs in the out-of-band response of the filter.

Furthermore, topologies for the waveguide implementation of additional paths have been proposed in [67], as shown in Fig. 2.17, with the objective of generating easily controllable TZs above the pass-band of the filter. Also, in [68] a rectangular waveguide filter is discussed where a capacitive coupling scheme is used together with an E-plane stub in the waveguide resonator, as shown in Fig. 2.18, to implement TZs below the pass-band of the filter.

Additionally, several filter structures using both inductive and capacitive couplings, the so-called hybrid folded rectangular waveguide (HFRW) filters, have been proposed to generate TZs both above and below the pass-band in a very wide frequency range. In [69], for instance, a trisection (or triplet) has been designed using a compact folded E-plane arrangement where adjacent resonators are coupled through capacitive windows, and non-adjacent resonators are coupled through simple inductive windows, as shown in Fig. 2.19, with the objective of introducing TZs above the pass-band. Also, in [70] an HFRW filter has been proposed to provide several TZs below the pass-band with an improved geometry, as shown in Fig. 2.20. Finally, a new approach based on a simple capacitive obstacle has been proposed in [71], as shown in Fig. 2.21. The structure is obtained by combining a capacitive window with thin stubs in order to control the coupling strength, and generate, at the same time, TZs both above and below the pass-band in a very wide frequency range.

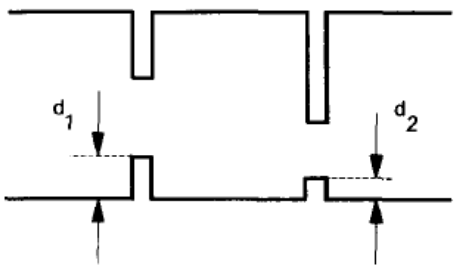

(a) Single cavity with offset coupling windows.

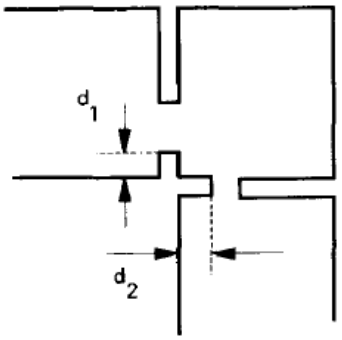

(b) Example of corner cavity configuration.

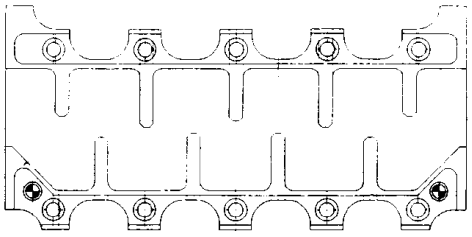

(c) Structure of the filter.

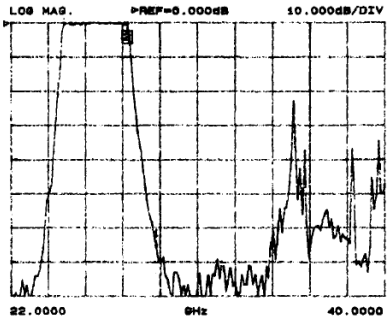

(d) Measured performance of the filter.

Figure 2.16: Configurations of inductive filter cavities for generating TZs.

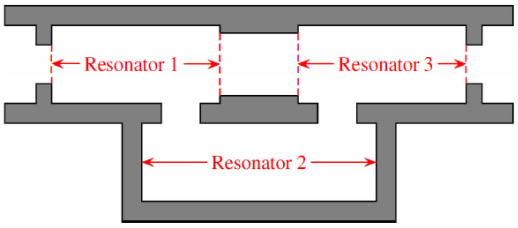

(a) Geometry of a trisection.

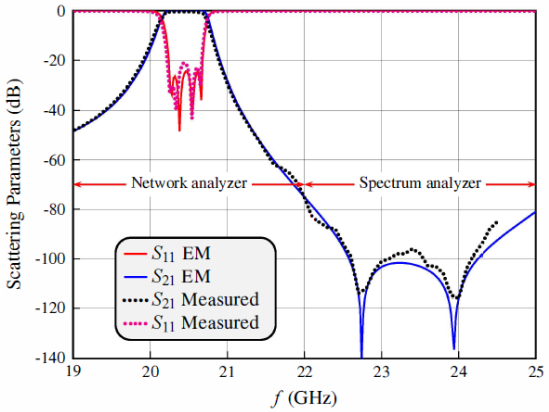

(b) Simulated performance of the filter.

Figure 2.17: An alternative waveguide implementation of a trisection.

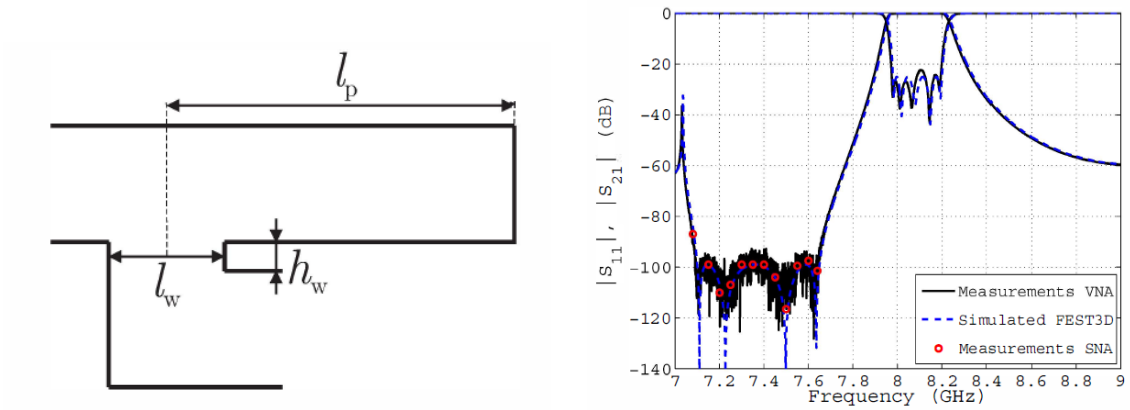

(a) Geometry of the basic block. (b) Performance of the filter.

Figure 2.18: Basic building block with the capacitive coupling scheme and the E-plane stub.

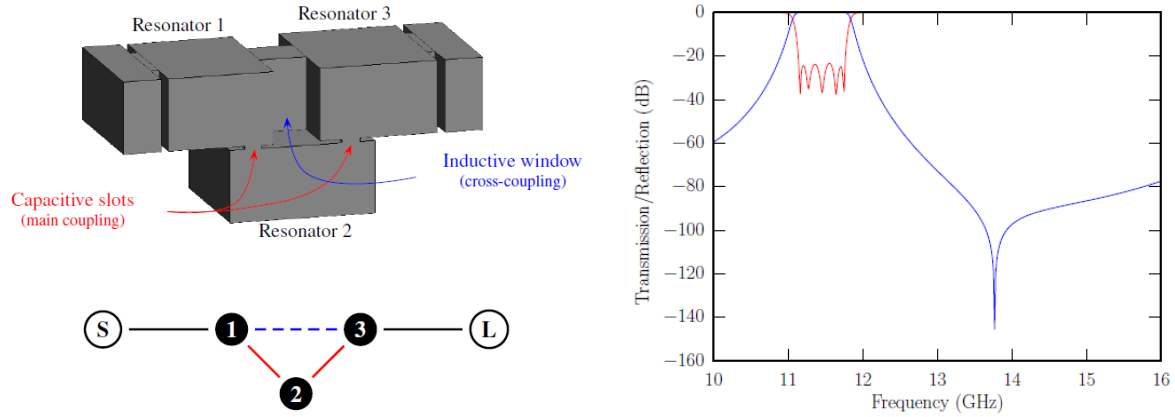

(a) Geometry of the basic block. (b) Simulated performance of the filter.

Figure 2.19: Geometry of the basic triplet block and routing scheme. Solid lines indicate direct couplings whereas dashed lines refer to cross-couplings.

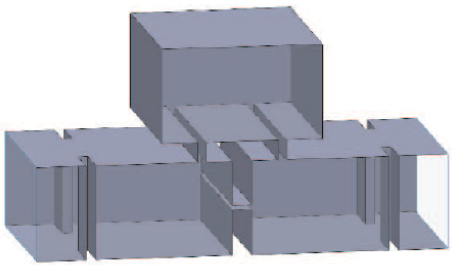

(a) Capacitive iris used as direct coupling.

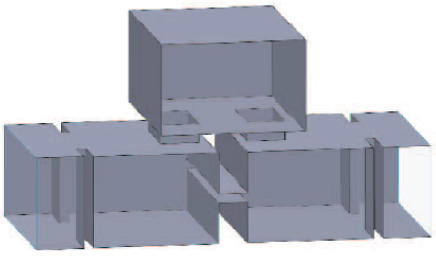

(b) Inductive iris used as direct coupling.

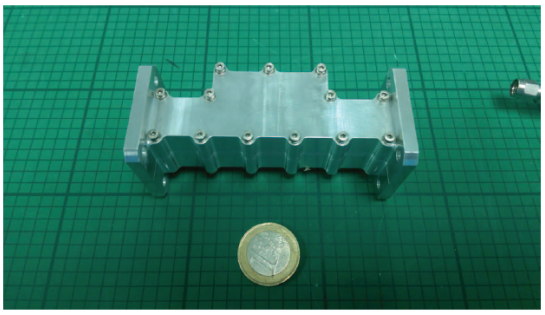

(c) Manufactured of the filter.

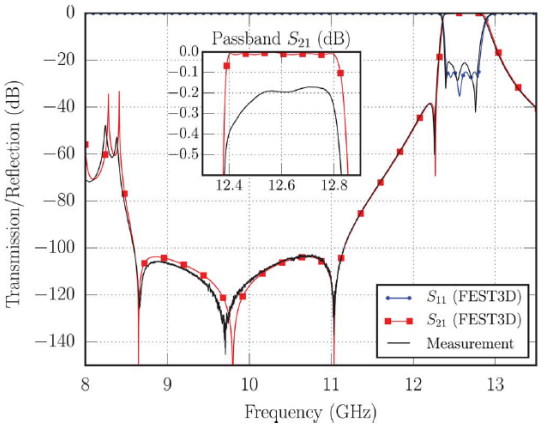

(d) Measured of the filter.

Figure 2.20: Geometries of the trisections that provide TZs below the pass-band using a classical capacitive window as cross-coupling.

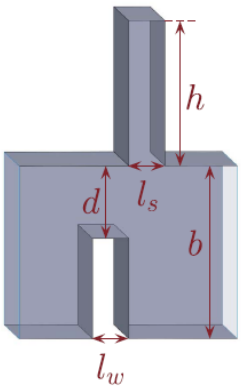

(a) Geometry of the basic block.

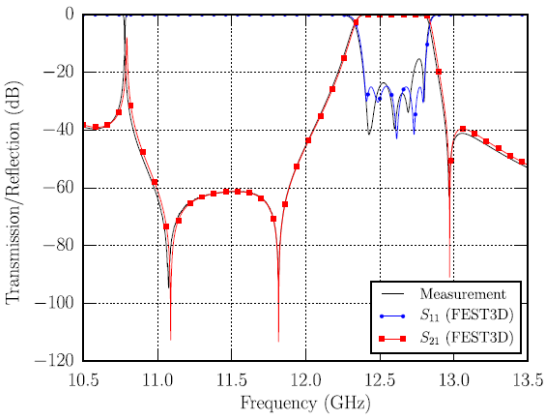

(b) Simulated performance of the filter.

Figure 2.21: Geometry of a capacitive obstacle including one stub.

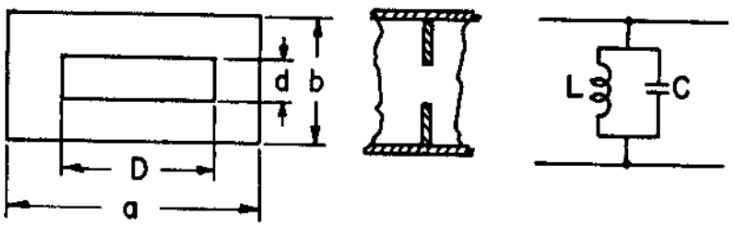

Figure 2.22: Left: Dimensions of a resonant iris. Center: Location of the iris in the waveguide. Right: Lumped-element equivalent circuit of a resonant iris.

2.2.4 Resonant Apertures

An alternative structure to implement a filter in rectangular waveguide is based on the use of resonant apertures (RAs) [7]. The basic geometry of a resonant aperture (or resonant iris) is shown in Fig. 2.22. A wide-band network model of these RAs has also been proposed in [72] and [73].

Many different waveguide filter implementations have indeed been explored using RAs. For instance, an evanescent mode filter with tuning screws has been discussed in [74], where the cutoff guide is modeled as a π-network of lumped inductors, and the resonators are composed of capacitive obstacles along the guide. Furthermore, in [75] and [76] evanescent mode filters have been designed with direct-coupled resonant apertures, with the objective of extending the out-of-band performance and reducing the total length of the filter. More recently, an evanescent mode filter has been discussed in [77], where low insertion loss is demonstrated using capacitive irises and below cut-off rectangular waveguides.

An additional interesting technique to improve the performance of microwave filters in rectangular waveguide, is the use of asymmetric irises to introduce TZs. For instance, in [78] an asymmetric-iris coupled-cavity filter has been designed, where an improvement in the out-of-band response of the filter is achieved using the interference between higher order modes, as shown in Fig. 2.23. Moreover, further implementations have been discussed in [79] and [80], using rectangular waveguide structures which are coupled by rectangular iris loaded E- or H-plane T-junctions.

The use of complex capacitive irises has also been proposed in [81], to obtain resonant irises with a variety of different geometries in order to improve the out-of-band response of the filters.

In another contribution [82], a compact in-line pseudo-elliptic filter is discussed based on the combination of bypass coupling irises with other resonances, such as the TE_{101} and

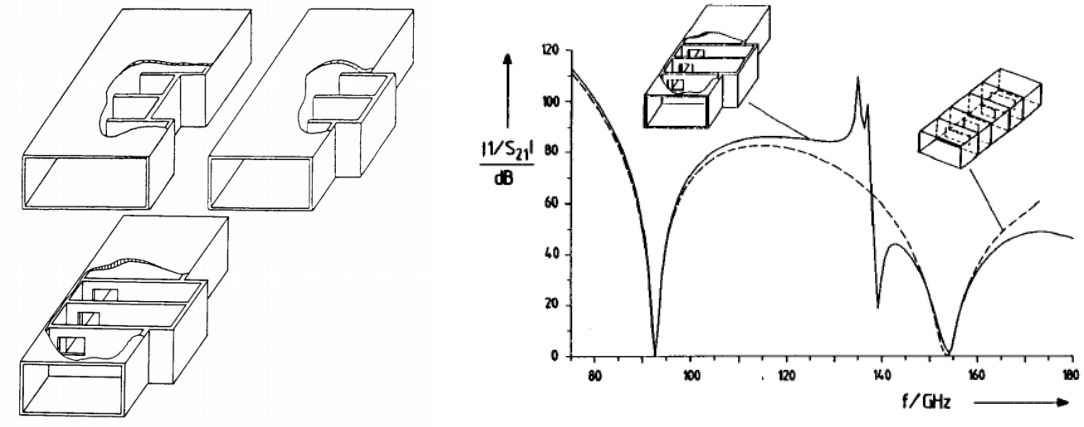

(a) Geometry of the basic block.

(b) Simulated performance of the filter.

Figure 2.23: Geometry of asymmetric-iris coupled-cavity filters.

TM_{110} rectangular waveguide cavity modes. Also, a compact in-line pseudo-elliptic filter has been proposed in [83], as shown in Fig. 2.24, based on the TM_{110} mode resonance, in order to achieve wide stop-bands. Furthermore, a new class of broadband pseudo-highpass waveguide filters has been proposed in [84], based on the TM_{101} resonance together with a resonant iris. Additionally, a number of bandpass filters based on TM dual-mode cavity have been proposed in [85]. More recently, several papers have focused on dual-mode TM resonators in order to improve the pass-band and the out-of-band performance, as discussed for instance in [86] and [87].

In the technical literature we can also find several examples of the use of resonant irises for wide-band filters in rectangular waveguide technology. For instance, wide-band band-pass filters with high selectivity have been proposed in [88] and [89], where the filter structures are based on the use of directly coupled resonant irises. Also, a directly coupled non-centered resonant irises filter has been discussed in [90], as shown in Fig. 2.25, with the objective of obtaining a broadband and highly selective response in Ka-band and provide, at the same time, a good spurious-free range. Another example has been proposed in [91], where a microwave band-pass filter has been designed using coupled resonant irises.

Furthermore, a number of contributions can be found in the technical literature discussing the design of filters based on a multi-aperture irises. In [92], an analysis of the coupling by multi-aperture irises in rectangular waveguide by using TE^x_{mn} modal expansion in conjunction with the moment method has been proposed. In [93], the reflection resonances of a double-aperture resonant iris in rectangular waveguide have been studied. Also, in [94] a wideband equivalent circuit of multi-aperture waveguide irises based on the electromagnetic analysis of the resonances have been discussed, as shown in Fig. 2.26.

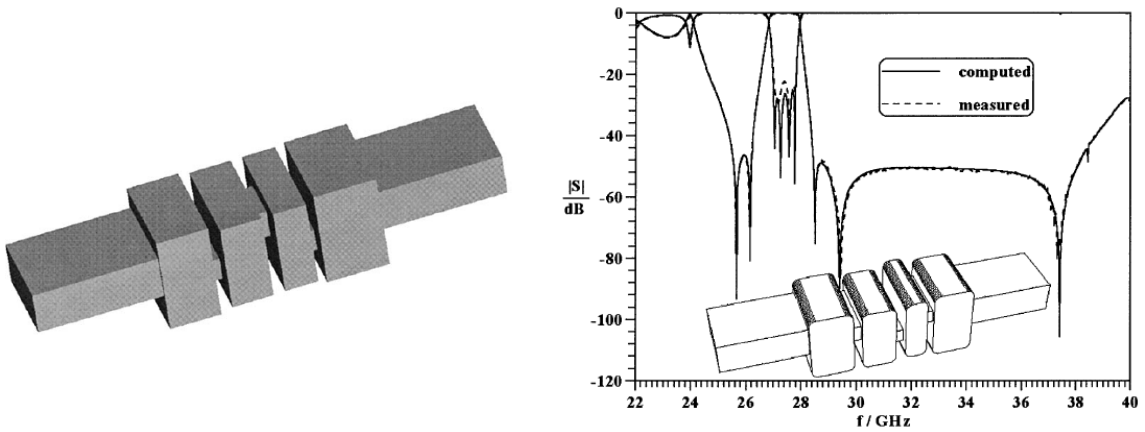

(a) Geometry of the filter. (b) Measured of the filter.

Figure 2.24: Structure of a TM_{110} mode in-line filter that uses bypass couplings of non-resonating $TE_{10/01}$ modes.

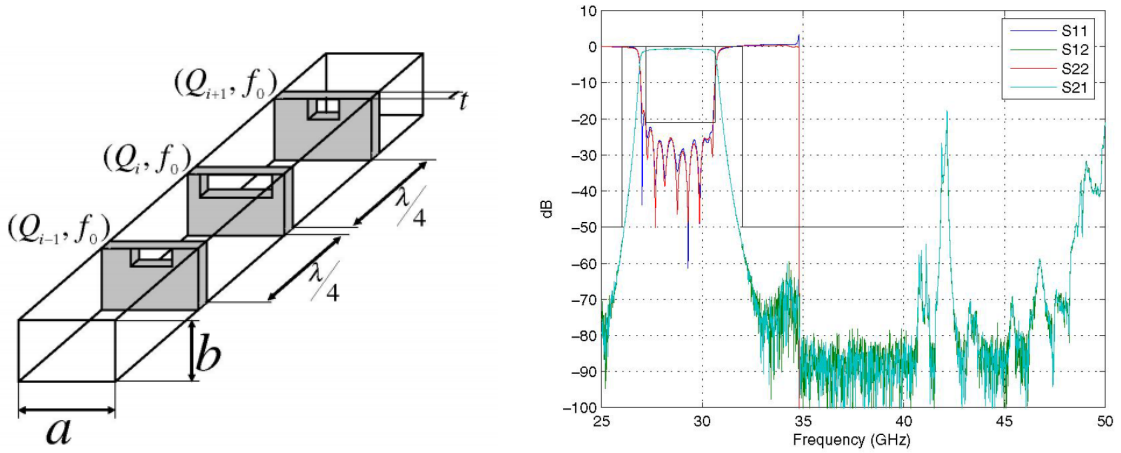

(a) Geometry of the filter. (b) Measured of the filter.

Figure 2.25: Implementation of non-centered resonant irises filter.

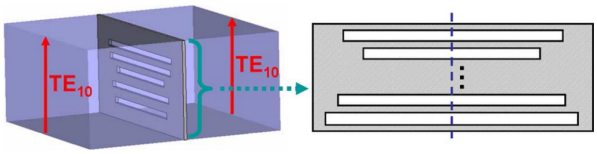

(a) Geometry of the multi-aperture waveguide iris.

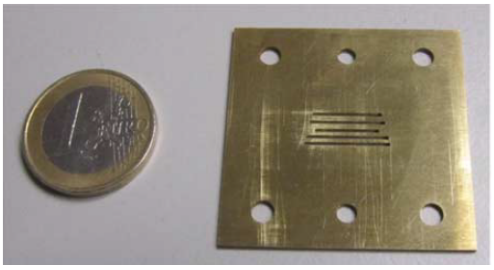

(b) Manufactured waveguide iris with five apertures.

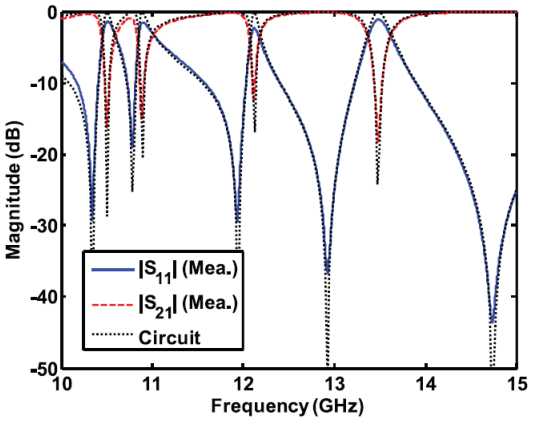

(c) Measured of the waveguide iris with five apertures.

Figure 2.26: Implementation of multi-aperture waveguide iris.

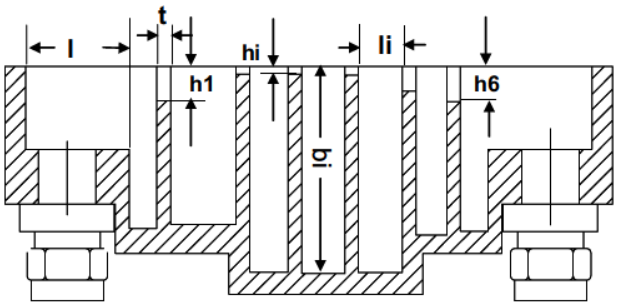

(a) Configuration of the resonating iris filter with coupled shorting stubs.

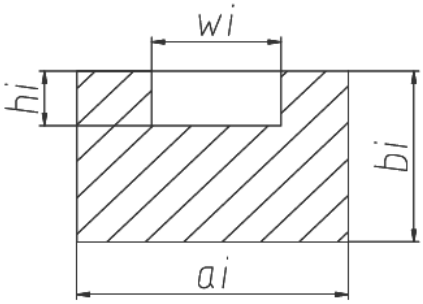

(b) Configuration of the resonating iris.

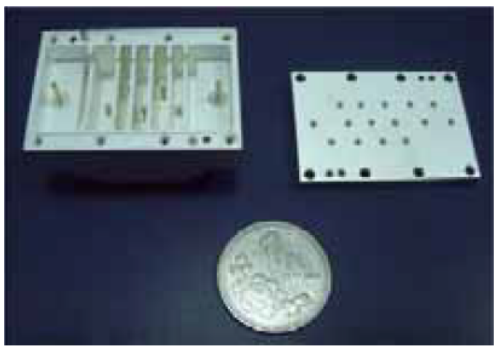

(c) Manufactured filter.

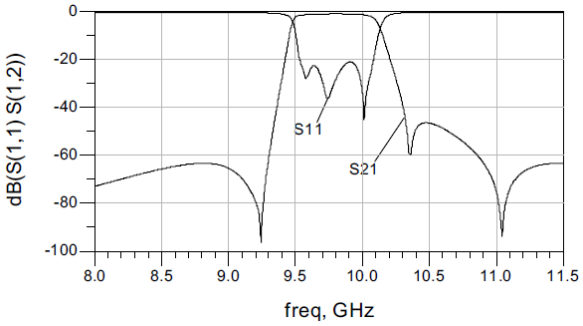

(d) Measured performance of the filter.

Figure 2.27: Structure of filter with resonating irises and shorting stubs.

Furthermore, in [95] a novel formulation based on integral equation methods has been discussed in order to obtain the response of multi resonant iris-like discontinuities in waveguide. An additional example of the use of multi-aperture irises is shown in [96], where the combination of aperture-type and patch-type resonances are used.

Another example on the use of resonant apertures in conjunction with E-plane stubs can be found in [97], where irises and stubs are used as resonating and coupling elements. Recently, a compact filter with resonant-irises and coupled shorting stubs has been proposed in [98], where each shorted stub, not only creates a transmission zero, but is also used as an impedance inverter between adjacent resonating irises to form the band-pass filter, as shown in Fig. 2.27. More recently, a notch waveguide filter has been proposed in [99], where a multi-aperture iris has been designed to generate a TZ at a given frequency.

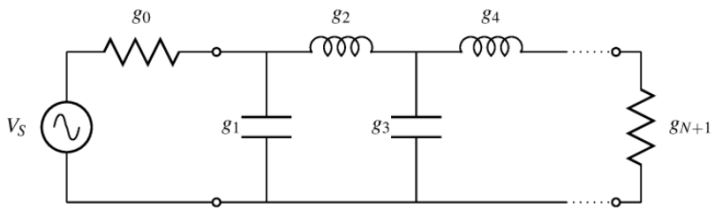

Figure 2.28: Lumped-element ladder network for a lowpass filter prototype with a shunt capacitor as the first element.

2.3 Design of Wide-band Microwave Filters

After having reviewed a large variety of past contributions in the area of microwave filters in rectangular waveguide, it is now appropriate to review the design procedure of a wide-band microwave filter.

The design of a microwave filter always starts with the definition of a set of performance specifications. Traditionally, the next step is the definition of a lumped-element ladder network for a low-pass filter prototype that satisfies the given set of specifications.

This network is defined from the return loss (RL) level and order of the filter (N), and depending on the configuration chosen, it is possible to obtain a prototype with a shunt capacitance or a series inductance as the first element. In the procedure we followed for the filters described in this thesis, we have chosen the network shown in Fig. 2.28 [1] and [100].

The values of g_i elements are obtained computing first a set of auxiliary parameters for a Chebyshev response filter, namely:

$$\varepsilon = \frac{1}{\sqrt{10^{\frac{RL}{10}} - 1}} \tag{2.1a}$$

$$s = \sqrt{1 + \varepsilon^2} \tag{2.1b}$$

$$\beta = \ln \frac{s+1}{s-1} \tag{2.1c}$$

$$\gamma = \sinh \frac{\beta}{2N} \tag{2.1d}$$

$$a_k = \sin \frac{(2k-1)\pi}{2N} \quad k = 1, 2, 3...N \tag{2.1e}$$

$$b_k = \gamma^2 + \sin^2 \frac{(k\pi)}{2N} \quad k = 1, 2, 3...N \tag{2.1f}$$

Once we have the values of the auxiliary parameters, we can then proceed to calculate

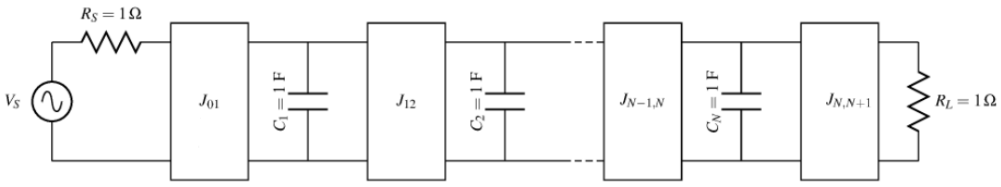

Figure 2.29: Lowpass prototype filter with admittance inverters.

the lumped-elements values g_i of the ladder network as follows:

$$g_0 = 1 \tag{2.2a}$$

$$g_1 = \frac{2a_1}{\gamma} \tag{2.2b}$$

$$g_k = \frac{4a_{k-1}a_k}{b_k g_{k-1}} \quad k = 2, 3, ...N \tag{2.2c}$$

$$g_{N+1} = \begin{cases} 1 & \text{N even} \\ (\varepsilon + s)^2 & \text{N odd} \end{cases} \tag{2.2d}$$

Next, the low-pass prototype is transformed into a network with admittance inverters, as shown in Fig. 2.29 [100]. Fig. 2.29 shows the normalized N-order filter with N shunt capacitors of values $C_i = 1$ F, generator and load resistances of values $R_S = R_L = 1\Omega$, respectively, and $N + 1$ admittance inverters with the following inversion constants:

$$J_{i,i+1} = \frac{1}{\sqrt{g_i g_{i+1}}} \quad i = 0, 1, 2....N \tag{2.3}$$

To obtain the band-pass filter prototype, as shown in Fig. 2.30, a frequency transformation is performed [100]. In this step, the actual center frequency (f_0) and frequency bandwidth (BW) of the filter response are used. The relationship between the capacitance and the shunt resonators is as follows:

$$C = 1F \rightarrow \begin{cases} C_0 = \dfrac{1}{\dfrac{\Delta\omega}{\Delta\omega}} \\ L_0 = \dfrac{\Delta\omega}{\omega_0^2} \end{cases} \tag{2.4}$$

where $\Delta\omega$ corresponds to $2\pi BW$ and ω_0 corresponds to $2\pi f_0$.

From the lumped element model, it is possible to obtain the distributed model of the filter based on transmission lines and inverters, as shown in Fig. 2.31 [100]. In this step, the guided wavelength of the rectangular waveguide (λ_g), center frequency ($f_0 = \sqrt{f_1 f_2}$)

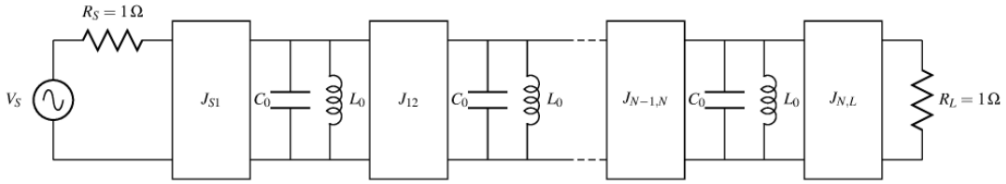

Figure 2.30: Lumped band-pass prototype filter with admittance inverters.

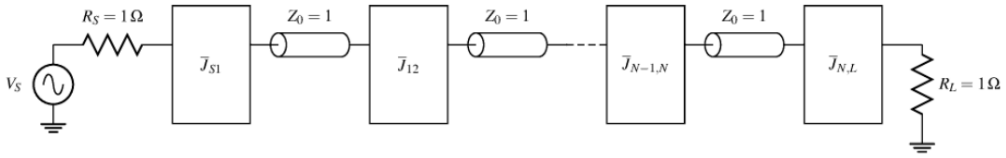

Figure 2.31: Distributed band-pass prototype filter with admittance inverters.

and the characteristic impedance (Z_0) are used.

The normalized distributed band-pass filter network ($Z_0 = 1$) is shown in Fig. 2.31. The final expressions for the normalized inversions constants of the inverters are:

$$\bar{J}_{i,i+1} = \frac{J_{i,i+1}}{Y_0} = \frac{\pi \mathcal{W}_\lambda}{2\sqrt{g_i g_{i+1}}} \tag{2.5a}$$

$$\bar{J}_{S1} = \frac{J_{S1}}{\sqrt{Y_0}} = \frac{1}{\sqrt{g_0 g_1}}\sqrt{\frac{\pi}{2}\mathcal{W}_\lambda} \tag{2.5b}$$

$$\bar{J}_{NL} = \frac{J_{NL}}{\sqrt{Y_0}} = \frac{1}{\sqrt{g_N g_{N+1}}}\sqrt{\frac{\pi}{2}\mathcal{W}_\lambda} \tag{2.5c}$$

where $\mathcal{W}_\lambda$ is the guided-wavelength fractional bandwidth defined as follows:

$$\mathcal{W}_\lambda = \mathcal{W}\left(\frac{\lambda_{g0}}{\lambda_0}\right)^2 \tag{2.6}$$

and $\mathcal{W}$ is the fractional bandwidth in terms of frequencies:

$$\mathcal{W} = \frac{f_2 - f_1}{f_0} \tag{2.7}$$

Finally, another lumped-element equivalent circuit that can be used to design a band-pass filter is the generalized equivalent circuit with admittance inverters shown in Fig. 2.32 [100]. With this model, it is possible to design and implement any band-pass

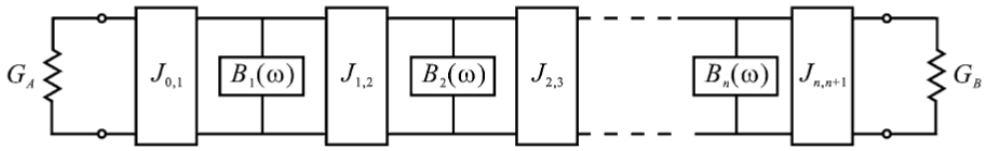

Figure 2.32: Generalized equivalent circuit for a band-pass filter circuit with admittance inverters.

filter using shunt resonators with susceptances $\mathcal{B}_i(\omega)$. This will be possible following the procedure and formulas described in [1] and [3].

The values for the admittance inverters of the generalized equivalent circuit of a band-pass filter can be computed using the following formulas:

$$J_{0,1} = \sqrt{\frac{G_A \mathcal{W}_\lambda \mathcal{B}_1}{g_0 g_1}}, \quad i = 0 \tag{2.8a}$$

$$J_{i,i+1} = \mathcal{W}_\lambda \sqrt{\frac{\mathcal{B}_i \mathcal{B}_{i+1}}{g_i g_{i+1}}}, \quad i = 1, \ldots, N-1 \tag{2.8b}$$

$$J_{N,N+1} = \sqrt{\frac{G_B \mathcal{W}_\lambda \mathcal{B}_N}{g_N g_{N+1}}} \tag{2.8c}$$

where G_A and G_B are the conductances of the generator and the load, $\mathcal{W}_\lambda$ is the guided-wavelength bandwidth, and $\mathcal{B}_i$ is the susceptance slope parameter of each resonator.

It is important to mention that to design the filters described in this investigation, we will use two basic procedures. The first one is the design technique proposed in [101], that leads to a step-by-step approach to define the dimensions of the complete filter structure using the EM simulator FEST3D. The second procedure that we follow is the advanced Aggressive Space Mapping (ASM) procedure described in [102]. This method relies on the use of two types of electromagnetic simulators, namely:

- Low-Accuracy (LA): The full-wave EM simulator used is FEST3D, with a set of computational parameters that can give a fast but low-accuracy (LA) simulation [103].
- High-Accuracy (HA): HFSS or CST Stuido Suite, which can provide very accurate results but with time-consuming simulations.

Further details concerning the steps required for each filter design will be discussed when describing the individual filters. In addition, for all filters that we discuss in this document, we will perform detailed sensitivity and higher power analyses to identify the

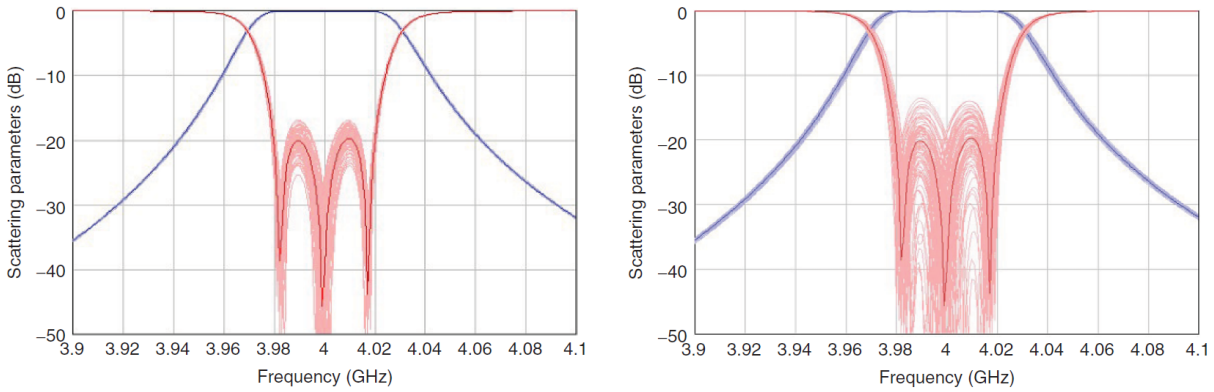

(a) The maximum allowed deviation is ±15 μm.

(b) The maximum allowed deviation is ±38.5 μm.

Figure 2.33: Tolerance analysis of an inductive filter.

most adequate manufacturing process, and the maximum power allowed by the structure without initiating multipaction [6].

It is important to note that the sensitivity analysis that we will use extensively in this investigation is carried out for the following reasons [6]:

- It helps in identifying the most suitable manufacturing technology.
- Improves the performance of the final filter, because it allows to identify the key elements of the structure that are more sensitive to manufacturing errors.
- It helps in adapting the filter structure to the specific features of the manufacturing process that has been selected, thereby ensuring a good manufactured filter response.

Fig. 2.33 shows an example of the sensitivity analysis for an inductive filter with the following specifications: $N = 3$, $RL = 20$ dB, $f_0 = 4$ GHz and $BW = 40$ MHz [6]. It is clearly visible that the effect of the manufacturing tolerances in the response of the filter is an important issue for the manufacture of microwave filters.

The higher power analysis that we will use extensively in this investigation will focus on the multipaction effect. It is well known that the multipaction effect is an RF breakdown phenomenon. Breakdown can, in fact, take place if, under vacuum conditions, the mean free path of the electrons is larger than the gap between the metallic walls guiding the flow of RF power [6]. The multipaction effect depends on the following set of parameters:

- Vacuum condition.
- Surface conditions.
- Applied RF voltage, frequency of operation and geometry of the RF components.

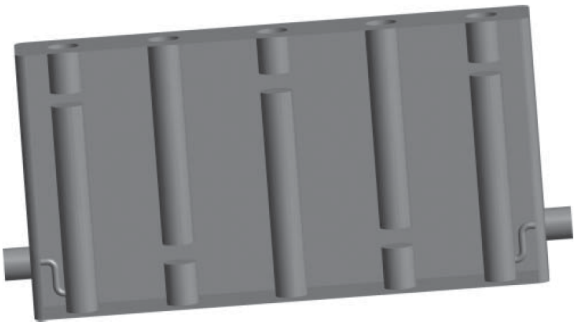

(a) Geometry of a five-pole interdigital filter.

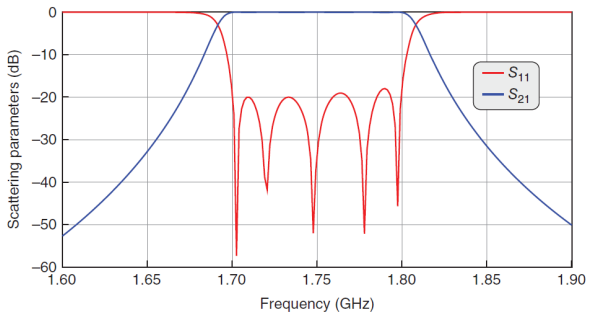

(b) Simulated performance of the interdigital filter.

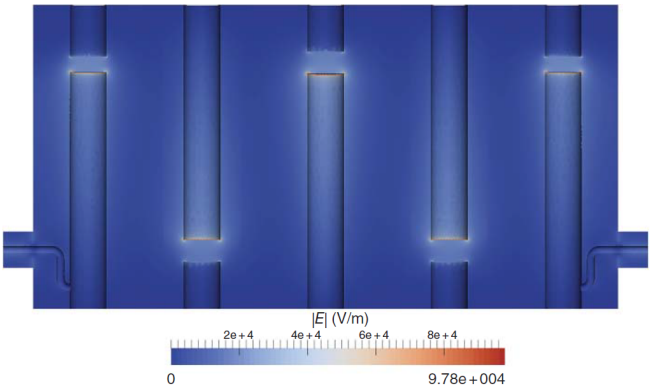

(c) Simulated electric field at 1.75 GHz (1 W input power).

Figure 2.34: Higher power analysis of an in-line interdigital filter.

- Number of carriers and modulation.

Fig. 2.34 shows an example of the high power analysis for an in-line interdigital filter with the following specifications: $N = 5$, $RL = 20$ dB, $f_0 = 1.75$ GHz and $BW = 100$ MHz [6].

Having reviewed in detail the state-of-the-art of rectangular waveguide filters, and outlined the filter design procedure that we will follow, we are now ready to discuss the novel contributions that have been the objective of our research.

Chapter 3

Hybrid Filters and Stepped Impedance Resonators

In this chapter, we show how to obtain a significant improvement in the out-of-band response of wideband waveguide filters based on stepped impedance resonators (SIRs). This result is also achieved using a combination of capacitive and inductive coupling irises. In the remainder of this chapter, we discus in detail the design procedure that we have used. Furthermore, in addition to theory, we also show the measurements of a prototype indicating excellent agreement with simulations, thereby fully validating both the filter structure and the design procedure.

Our investigation on wideband hybrid waveguide filters based on stepped impedance resonators has resulted in the following publications:

- J. Valencia, M. Guglielmi, S. Cogollos, J. Vague and V.E. Boria, "Enhancing the performance of stepped impedance resonator filters in rectangular waveguide", in *2017 47th European Microwave Conference (EuMC)*, Oct. 2017, pp. 989-992.
- J. Valencia, V.E. Boria, M. Guglielmi and S. Cogollos, "Compact wideband hybrid filters in rectangular waveguide with enhanced out-of-band response", in IEEE Transactions on Microwave Theory and Techniques, vol. 68, no. 1, pp. 87-101, Jan. 2020.

The novel SIR filter structure that we discuss in this chapter, is based on the use of both inductive and capacitive coupling irises, and has the following advantages with respect to the state-of-the-art:

- It exhibits a wide bandpass, while, at the same time, providing a very wide spurious-free range above the filter passband.
- It has very sharp selectivity both above and below the pass-band.
- Finally, it exhibits a slightly reduced footprint with respect to classic implementations that use only capacitive irises.

3.1 Wideband Filters Specifications

As it is usually the case, the design of any filter structure starts with the definition of a set of performance requirements or specifications. In the remainder of this chapter we will therefore use the following specifications:

- Order $N = 8$
- Bandwidth $BW = 1410$ MHz
- In-band return loss $RL > 20$ dB
- Center frequency $f_0 = 11$ GHz
- Guided-wavelength fractional bandwidth $\mathcal{W}_\lambda = 20$ %
- Input-output ports in WR-90: $a = 22.86$ mm and $b = 10.16$ mm

3.2 Filter Design Procedure

The filter structure that we want to obtain, must satisfy the specifications given in the previous section, and must exhibit, at the same time, a spurious-free range, both below and above the pass-band, that is as large as possible. To this end, the design procedure that we propose to follow involves the following steps:

- We first derive, from the specifications, the normalized lumped-element low pass network (g_i values) of a Chebyshev filter of order 8, as shown in Fig. 2.28.
- We then transform the low pass network into the model with admittance inverters and shunt capacitors, as shown in Fig. 2.29.
- The shunt capacitors are then transformed into shunt resonators. This is accomplished using the low-pass to bandpass frequency transformation, obtaining the filter prototype shown in Fig. 2.30.
- Once we have obtained the bandpass filter model, we can then choose the specific waveguide for the physical realization of the filter. After that, we can obtain all the elements of the distributed model shown in Fig. 2.31. This prototype is based on cascading inverters and transmission lines that take into account the fundamental TE_{10} mode propagation. The admittance inverters $J_{i,i+1}$, $i = 0, \ldots, N$ are obtained

using well-known expressions (see [1] and [100]):

$$\bar{J}_{i,i+1} = \frac{1}{\sqrt{g_i g_{i+1}}}\sqrt{\frac{\pi}{2}\mathcal{W}_\lambda}, \quad i = 0, N \tag{3.1a}$$

$$\bar{J}_{i,i+1} = \frac{1}{\sqrt{g_i g_{i+1}}}\frac{\pi}{2}\mathcal{W}_\lambda, \quad i = 1, \ldots, N-1 \tag{3.1b}$$

where $\mathcal{W}_\lambda$ is the bandwidth defined in terms of the guided-wavelength, as defined in [1], and the modal characteristic impedance of the TE_{10} mode is used for the normalization.

- Once we have obtained the values of the normalized inverters ($\bar{K}_{i,i+1}$ or $\bar{J}_{i,i+1}$), we can then follow any of the available procedures, in order to obtain the physical dimensions of the irises [1], [6] and [101]. In our case, we have used the procedure described in [101].
- The next step is to use a full-wave simulator to compute the EM performance of the real coupling windows and resonators in rectangular waveguide.
- This design phase is concluded with a final optimization of the complete structure. This is required in order to obtain a fully compliant in-band response. This step is necessary because the formulas that we have used are approximations obtained in the narrow bandwidth limit. In our case, therefore, as our filter is a wideband filter, they can still be used to obtain a starting point, but to reach the desired result, a final optimization is required.

This concludes the first phase of our design. It is important to note at this point that the waveguide filter structure that we have obtained is indeed fully compliant with our specifications but cannot be manufactured as it is. This is because the software package FEST3D has been used, so far, with a set of computational parameters that gives a very rapid simulation, but with low-accuracy (LA). The transition to a high-accuracy (HA) structure will be discussed in the following sections of this chapter.

It is also important to note that the design procedure just outlined, can be used for *any* type of filter in rectangular waveguide, since we have not specified the details of the specific implementation of the coupling between resonators. As a matter of fact, all of the filters discussed in this thesis have been designed using the procedure just described.

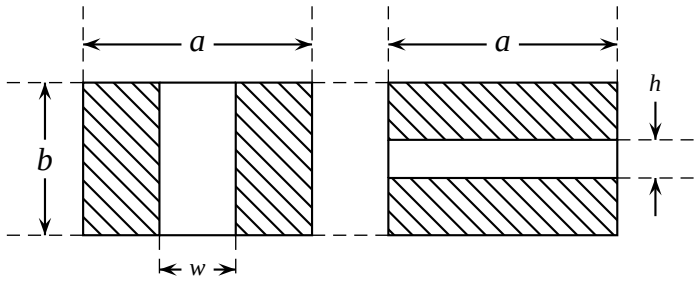

Figure 3.1: Typical irises in a rectangular waveguide (front view). Left: centered inductive iris of width w. Right: centered capacitive iris of height h.

3.3 Hybrid Filters

If the coupling between adjacent resonators is implemented with thick inductive windows, we obtain what is normally called an inductive filter. Microwave filters based on inductive windows are probably the oldest and most common implementation of filters in rectangular waveguide technology [1] and [6]. The basic structure involves half-wavelength lengths of uniform waveguides, the resonators, and a number of inductive windows (see Fig. 3.1, left). The design procedure described in the previous section can very effectively be used to obtain a compliant LA structure.

The main feature of this structure is that it can exhibit an excellent performance for (relatively) narrow-band applications. However, if a wide-band performance is required, it may result into an important degradation of the out-of-band response of the filter. This is because the combined effects of the high-frequency response of the resonators and of the inductive coupling irises result into the appearance of spurious responses at higher frequencies.

On the other hand, using capacitive irises (see Fig. 3.1, right) can result into an attenuation of the the spurious response at higher frequency. However, for narrow-band filter implementations, the capacitive coupling irises required may have a very small height, and this is not practical for manufacturing. For wide-band implementations, the capacitive irises are normally higher, and the manufacture is not a problem. This is why inductive filters are normally preferred for narrow-band implementations, while capacitive filters are a better choice for wide-band implementations.

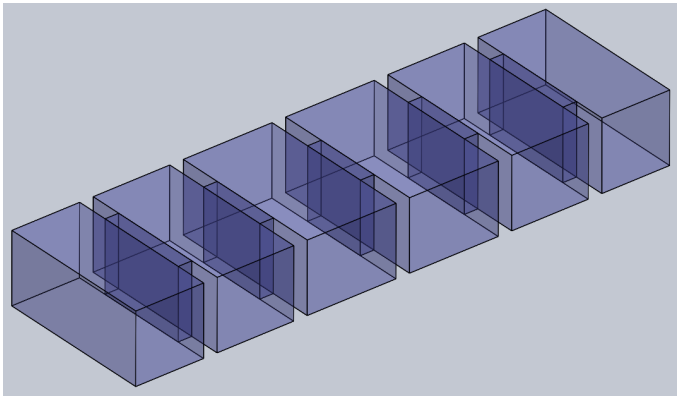

Figure 3.2: Structure of a four-pole inductive filter.

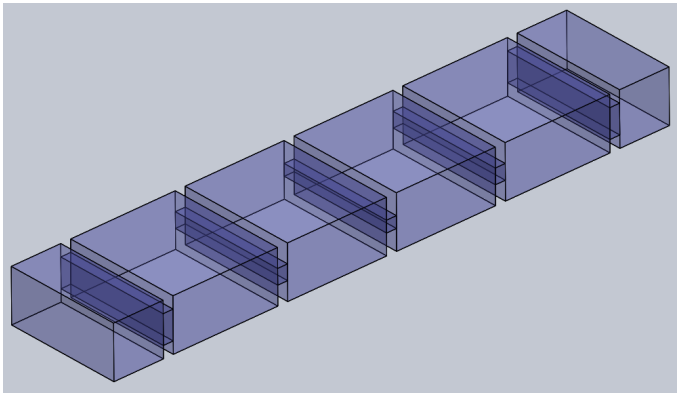

Figure 3.3: Structure of a four-pole capacitive filter.

3.3.1 Classical Filters

In order to identify the filter configuration that is best suitable for our specifications, we now study in detail both inductive and capacitive filters. Fig. 3.2 and Fig. 3.3 show the typical structures of four-pole inductive and capacitive filters, respectively, where the two filters have been designed to satisfy the specifications given in Section 3.1 (with the exception of the filter order).

Fig. 3.4 shows a comparison of the simulated behavior of the structures of Fig. 3.2 (4-P Ind Filter) and Fig. 3.3 (4-P Cap Filter), respectively. The performances shown in Fig. 3.4 have been obtained with the commercial tool FEST3D (v.2021 by AuroraSAT, now with Dassault Systèmes).

As we can see in Fig. 3.4, there are significant differences between filters with inductive and capacitive couplings, namely:

- For lower frequencies, inductive irises provide significant rejection below the passband. Capacitive irises, instead, produce an unwanted resonant behavior below the

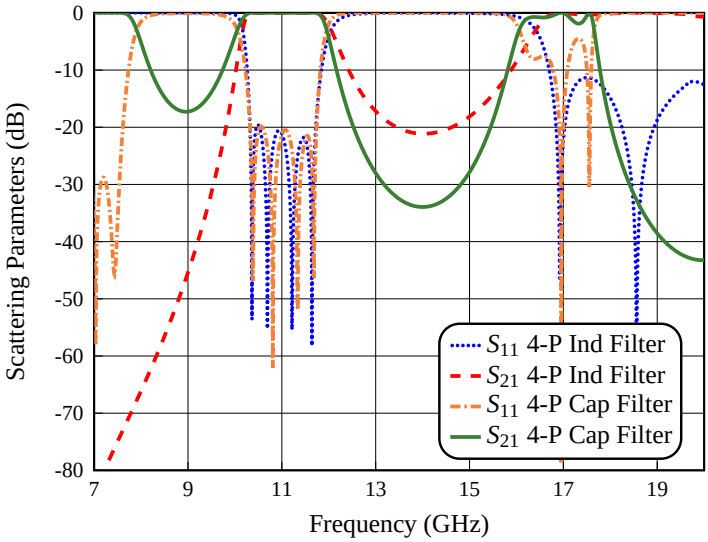

Figure 3.4: Simulated performance of the four-pole inductive filter (4-P Ind Filter) and four-pole capacitive filter (4-P Cap Filter).

filter pass-band.

- For higher frequencies, the capacitive filter provide a better attenuation above the pass-band. By contrast, the inductive filter provides very poor response.

We can therefore conclude that using capacitive irises we can obtain an important attenuation of the spurious response above the filter pass-band. However, the presence of resonances below the pass-band is an issue that may not be acceptable from a system point of view.

3.3.2 Hybrid Filters

The solution that we propose, to take advantage of the best characteristics offered by the two topologies, is to mix inductive and capacitive irises along the structure of the filter, thereby obtaining what we call a *hybrid* filter structure.

For this purpose, we now investigate the relative positions of the inductive and capacitive irises to obtain the best overall filter performance. The first observation that we can make is that the central part of any filter structure generally requires smaller coupling strengths. On the other hand, the couplings that are required in the input and output portions of the filter are generally stronger.

To continue, we have designed two 4-pole hybrid filters. The first has an inductive iris in the center section, and all other are capacitive couplings, as shown in Fig. 3.5. The second has an inductive window in the first and last couplings, and all other are capacitive

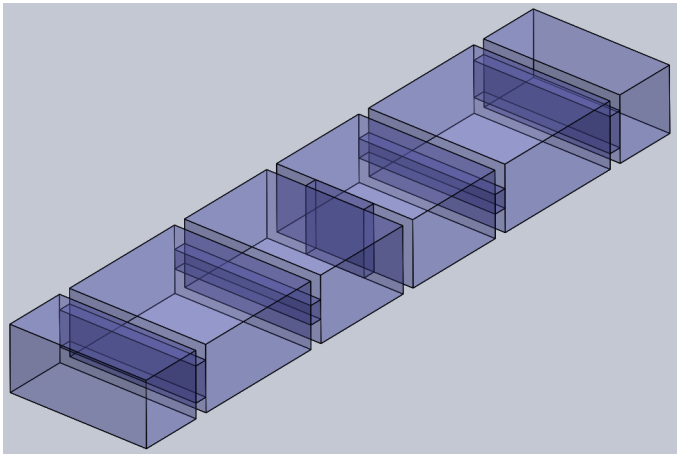

Figure 3.5: Structure of the four-pole hybrid filter with an inductive iris in the center section.

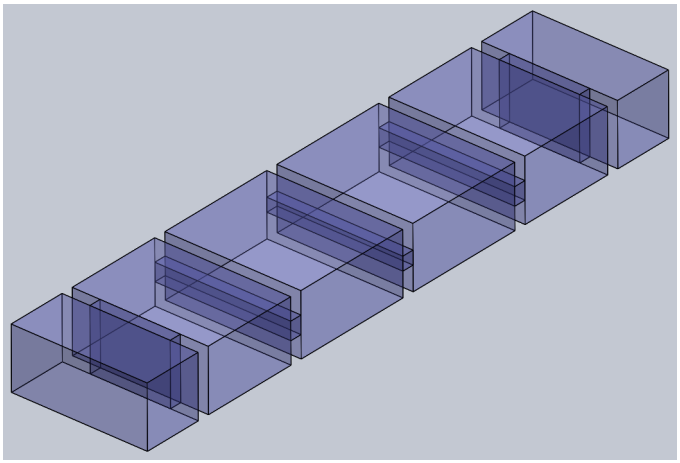

Figure 3.6: Structure of the four-pole hybrid filter with inductive irises in the first and last couplings.

couplings, as shown in Fig. 3.6.

Fig. 3.7 shows a comparison of the simulated behavior of the structures of Fig. 3.5 (4-P Hyb Filter I) and Fig. 3.6 (4-P Hyb Filter II). As we can see, the 4-P Hyb Filter II shows an improvement in the attenuation of the spurious response, however, the unwanted resonances below the pass-band remains present. On the other hand, the 4-P Hyb Filter I shows a slight improvement in the attenuation of the spurious response at higher frequencies and, at the same time, an improvement in the frequency range close to the cutoff frequency of the input waveguide, where the unwanted resonances have been attenuated.

We can therefore conclude that if the central section of the hybrid filter is designed with inductive irises, and the input-output sections use capacitive irises, we can obtain a

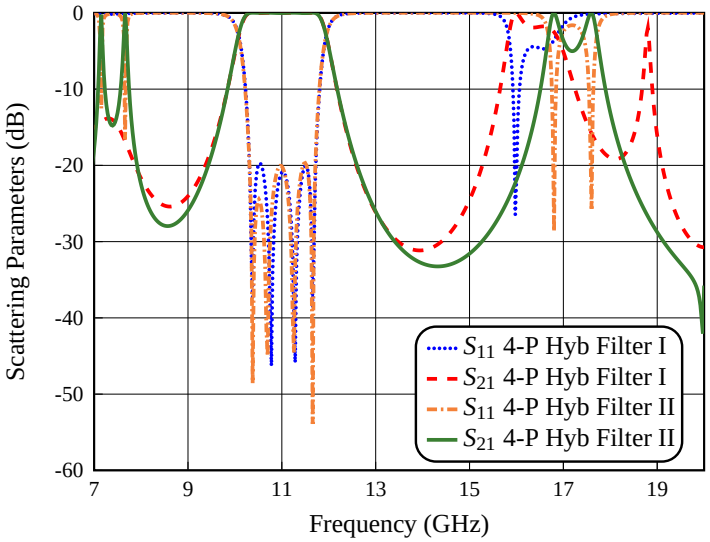

Figure 3.7: Simulated performance of the four-pole hybrid filters with an inductive iris in the center section (4-P Hyb Filter I) and inductive irises in the first and last couplings (4-P Hyb Filter II).

number of advantages, namely:

1. The use of inductive irises with smaller width may improve the out-of-band response.
2. The unwanted resonance due to the capacitive irises can be mitigated.
3. If the capacitive irises are used only in the input and output sections, we avoid the problem of having to manufacture irises with a small height.

3.3.3 Optimal Hybrid Filters

To validate the hybrid solution just discussed, we explore in this section the effect of placing the coupling windows in different positions in filters of higher order. To do that, we next design two eight-pole filters, one inductive and one capacitive, as shown in Fig. 3.8 and Fig. 3.9, respectively.

Fig. 3.10 shows a comparison of the simulated behavior of the structures of Fig. 3.8 (8-P Ind Filter) and Fig. 3.9 (8-P Cap Filter). As we can see, the inductive filter exhibits an excellent performance for lower frequencies in comparison with the capacitive filter. By contrast, for higher frequencies the capacitive filter rejects the high frequency spurious response better than the inductive filter. However, for lower frequencies, the capacitive filter shows significant spurious resonances.

As already mentioned, for a filter of order $N = 4$, the best solution is to place

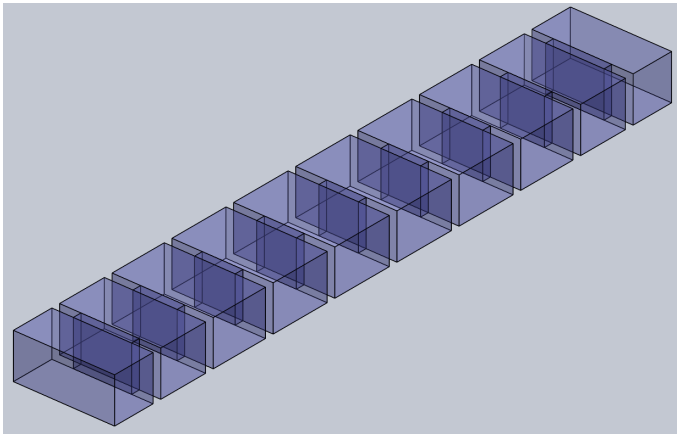

Figure 3.8: Structure of the eight-pole inductive filter.

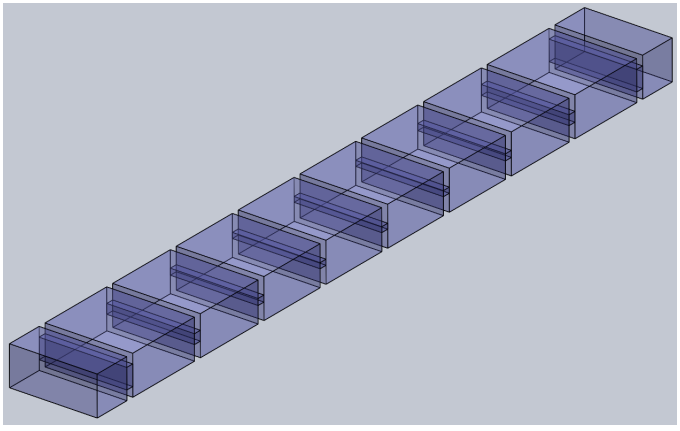

Figure 3.9: Structure of the eight-pole capacitive filter.

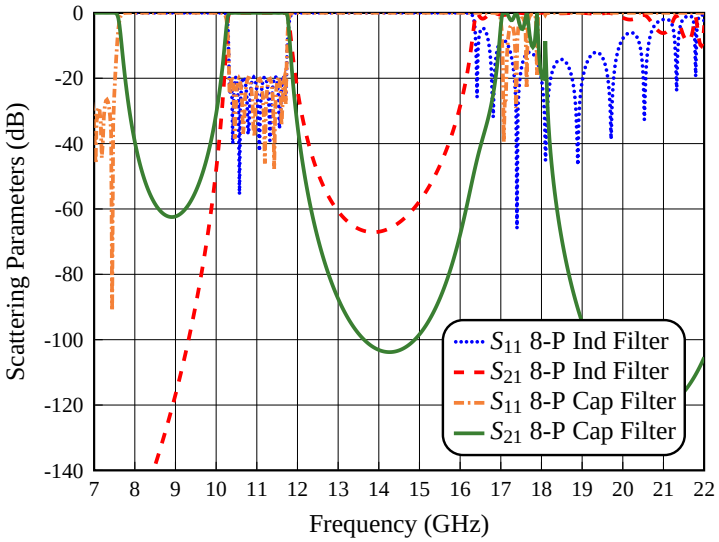

Figure 3.10: Simulated performance of the eight-pole inductive filter (8-P Ind Filter) and eight-pole capacitive filter (8-P Cap Filter).

inductive irises in the center of the filter. In order to validate this solution for higher orders, we now design two hybrid filters of order $N = 8$. Fig. 3.11 and Fig. 3.12 show the structures of the eight-pole hybrid filters with three inductive coupling windows in the central section of the filter, and five capacitive windows in the central section of the filter, respectively.

Fig. 3.13 shows a comparison of the simulated behavior of the structures of Fig. 3.11 (8-P Hyb Filter I) and Fig. 3.12 (8-P Hyb Filter II). As we can clearly see, the 8-P Hyb Filter I shows an important improvement of the out-of-band response with respect to the 8-P Hyb Filter II.

We can therefore conclude that the best solution is to use a number of inductive irises in the center of the filter. In our case, using three inductive irises gives the best result. With this topology, the advantages we obtain are as follows:

- Improved out-of-band performance, both in the lower and upper frequency ranges.
- Simpler manufacturing procedure since we do not use capacitive irises with very small height.
- The footprint of the filter is reduced, with respect to an all capacitive solution, due to the reduction in length of the resonators that are coupled by inductive irises.

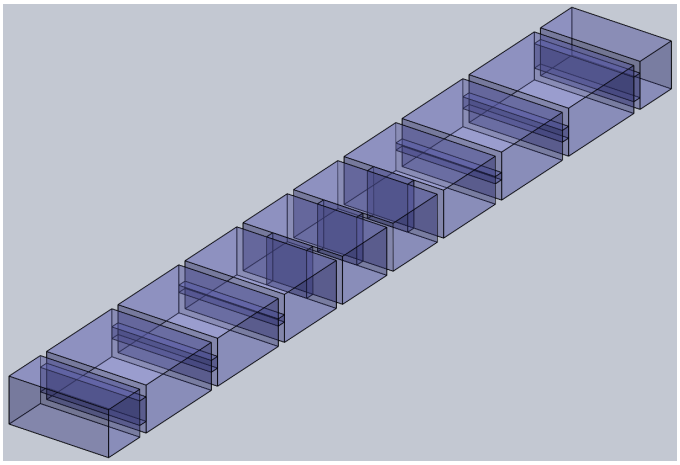

Figure 3.11: Structure of the eight-pole hybrid filter with three inductive coupling windows in the center section.

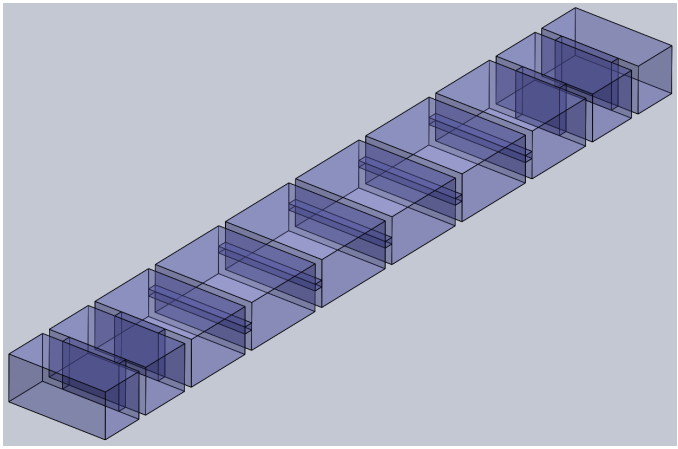

Figure 3.12: Structure of the eight-pole hybrid filter with two inductive irises in the first and last coupling sections.

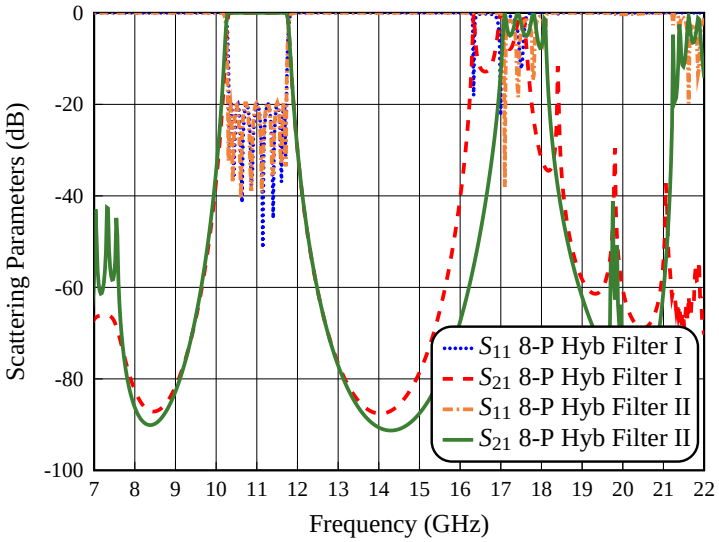

Figure 3.13: Simulated performance of the eight-pole hybrid filters with three inductive irises in the center section (8-P Hyb Filter I), and two inductive irises in the first and last coupling sections (8-P Hyb Filter II).

3.4 Changing Resonator Width

In the previous sections we have designed inductive and capacitive filter structures where all resonators had same width as the input and output waveguide. In this section, we propose an alternative for the improvement of the out-of-band response of the classic inductive and capacitive filters that is based on changing the width of the resonators. This is indeed a well-known technique that we are now going to explore for wide-band applications.

3.4.1 Inductive Filters

To understand the effect on the out-of-band performance for a filter with different resonator widths, we now design two different topologies, namely:

- One with decreasing widths of resonators as we approach the center of the structure.
- The other with increasing width as we approach the center of the structure.

The first filter is shown in Fig. 3.14. Fig. 3.15 shows a comparison of the simulated behavior of the structures of Fig. 3.8 (Ind Ref Filter) and Fig. 3.14 (Ind W Filter I). The thickness of the inductive windows has been kept constant.

The second topology is shown in Fig. 3.16. Fig. 3.17 shows a comparison of the simulated behavior of the structures of Fig. 3.8 (Ind Ref Filter) and Fig. 3.16 (Ind W Filter II).

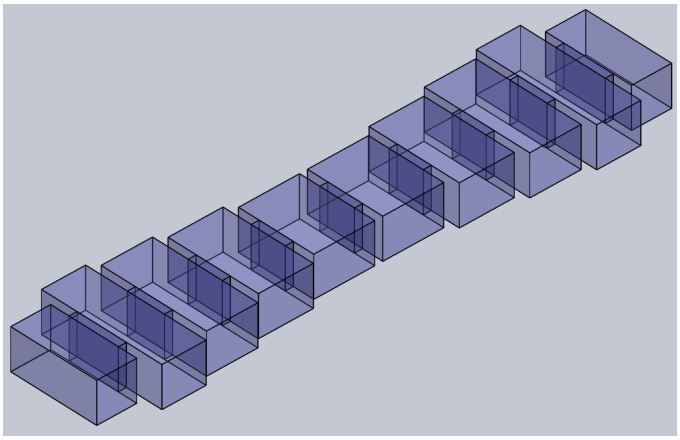

Figure 3.14: Structure of the inductive filter with widths that decrease as we approach the center of the structure.

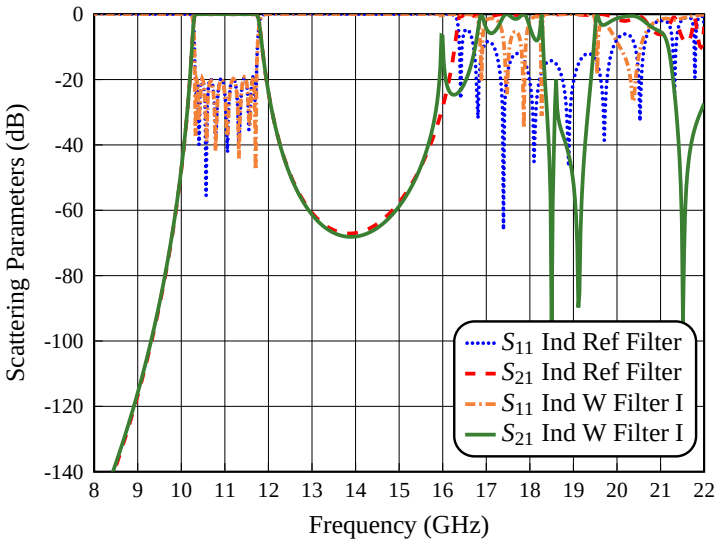

Figure 3.15: Simulated performance of the inductive filter (Ind Ref Filter) and inductive filter with widths that decrease as we approach the center of the structure (Ind W Filter I).

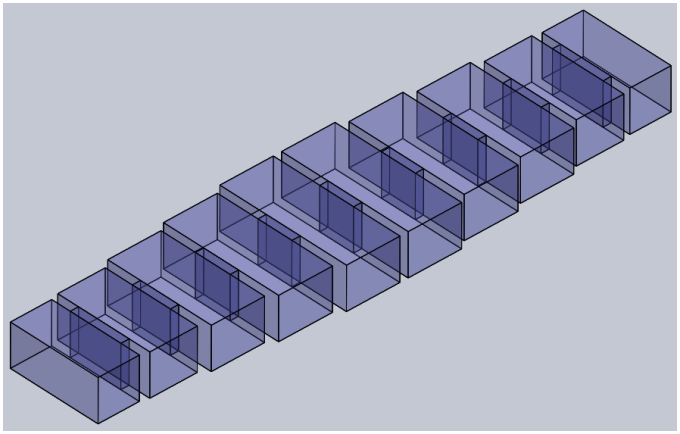

Figure 3.16: Structure of the inductive filter with widths that increase as we approach the center of the structure.

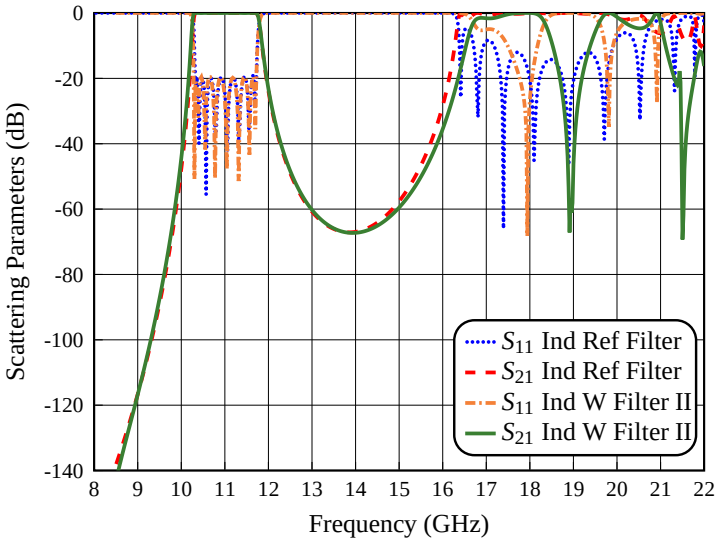

Figure 3.17: Simulated performance of the inductive filter (Ind Ref Filter) and inductive filter with widths that increase as we approach the center of the structure (Ind W Filter II).

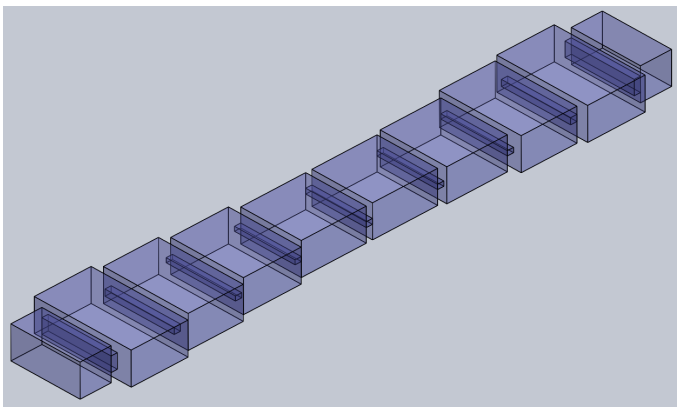

Figure 3.18: Structure of the capacitive filter with widths that decrease as we approach the center of the structure.

As we can clearly see in Fig. 3.15 and Fig. 3.17, both Ind W Filter I and Ind W Filter II shown a slight improvement in the attenuation of the first harmonic resonance, as compared to the classic inductive filter. However, changing the width of the resonators increases the total length of both filters.

3.4.2 Capacitive Filters

To further explore the change in width of the resonators, we now design capacitive filters with changes in width. We design first an eight-pole capacitive filter with widths that decrease as we approach the center of the structure, as shown in Fig. 3.18. Fig. 3.19 shows the comparison of the simulated behavior of the structures in Fig. 3.9 (Cap Ref Filter) and Fig. 3.18 (Cap W Filter I), respectively. The thickness of the capacitive irises has been kept constant.

Next, we design an eight-pole capacitive filter with widths that increase as we approach the center of the structure, as shown in Fig. 3.20. Fig. 3.21 shows the comparison of the simulated behavior of the structures in Fig. 3.9 (Cap Ref Filter) and Fig. 3.20 (Cap W Filter II), respectively.

As we can clearly see of Fig. 3.19 and Fig. 3.21, the Cap W Filter I shows an important reduction of the first harmonic resonance in comparison with the Cap W Filter II. However, this filter shows a slight increase of resonances below the pass-band. By contrast, the Cap W Filter II shows a slightly better rejection of both the first harmonic resonance and the resonances below the pass-band in comparison of the Cap W Filter I.

In view of that, the best topology with changing resonator width, is to decrease the widths towards the center of the filter structure.

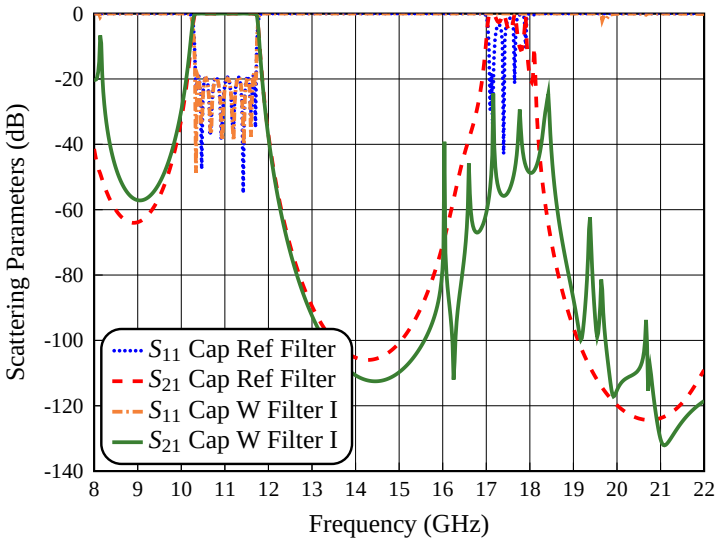

Figure 3.19: Simulated performance of the capacitive filter (Cap Ref Filter) and capacitive filter with widths decreasing as we approach the center of the structure (Cap W Filter I).

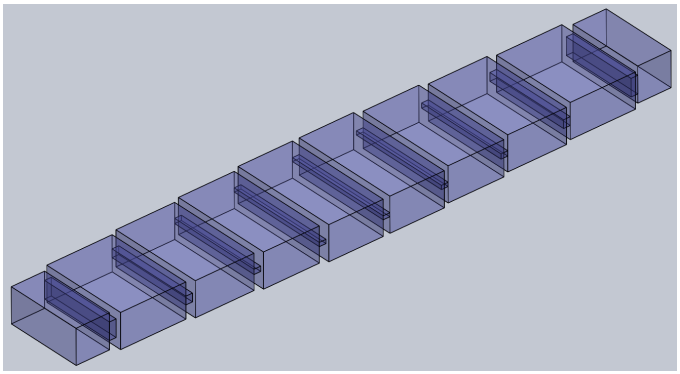

Figure 3.20: Structure of the capacitive filter with widths that increase as we approach the center of the structure.

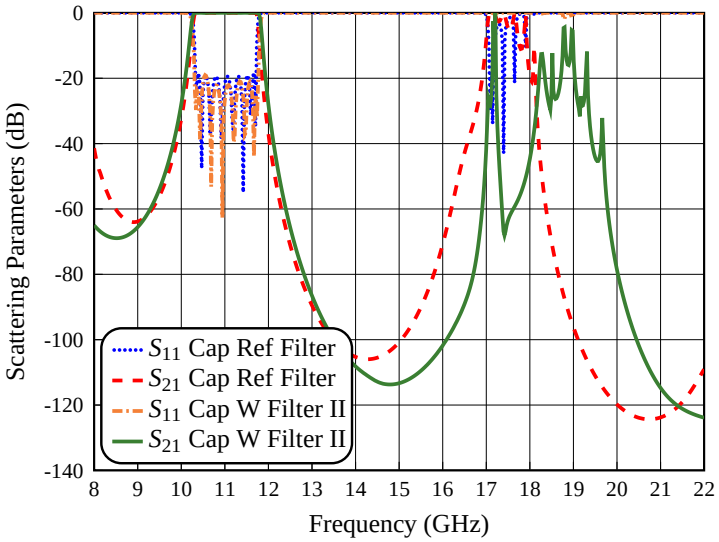

Figure 3.21: Simulated performance of the capacitive filter (Cap Ref Filter) and capacitive filter with widths increasing as we approach the center of the structure (Cap W Filter II).

3.5 Design of Wideband SIR Filters

In the previous sections we have built the inductive and capacitive topologies with resonators having uniform width and height, or impedance, along each of them (i.e. Uniform Impedance Resonators, UIRs). In this section, as an alternative for the improvement of the out-of-band performance, we replace the uniform resonators with stepped impedance resonators (SIRs), as discussed in [4] for narrow-band implementations.

3.5.1 Basic SIR

To illustrate the basic concept behind the SIRs, we show in Fig. 3.22 the geometry (side view) of a SIR with capacitive input and output coupling irises. The main idea behind a SIR is to introduce a shunt capacitor in the center of a resonator, that is a length of waveguide of reduced height. The shunt capacitor divides the resonator into two lengths of uniform waveguide. As a result, the harmonic resonances of the SIR are moved to higher frequencies, and a wider spurious-free region is obtained. The use of this type of resonator introduces the following two main advantages:

1. The out-of-band response of the filter can be significantly improved by properly adjusting the dimensions of the structure, namely, H_1, H_2, L_1 and L_2.
2. The length of each resonator is reduced, due to the effect of the central section (the capacitive loading).

Fig. 3.22 shows the geometrical parameters of the SIR, namely, H_1, H_2, L_1 and L_2.

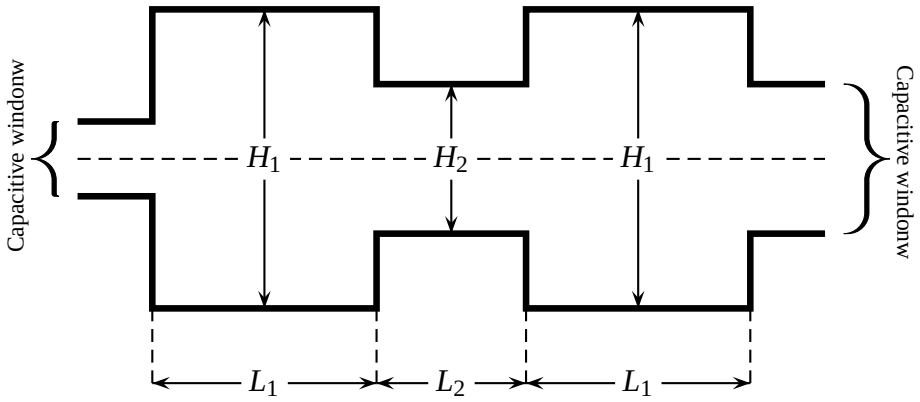

Figure 3.22: Geometry (side view) of a basic SIR with capacitive input and output couplings.

To better understand the behavior of the structure in Fig. 3.22, we now design a four-pole SIR filter, with capacitive irises, which satisfies the specifications of Section 3.1.

The geometrical parameters of the basic SIR have been optimized with a full-wave EM simulation tool (FEST3D), in order to obtain a good rejection level and a spurious-free range that is as large as possible. The dimensions that we have obtained at the end of a preliminary parametric study are: $H_1 = 8.0$ mm, $L_2 = 5.0$ mm, and different values of H_2 from 4 to 7 mm, respectively. It is important to mention that the dimension L_1 has been obtained by optimization in order to center the resonance frequency of our SIR, so that the desired filter performance is obtained.

Fig. 3.23 shows a comparison of the simulated behavior of the four-pole capacitive filter with UIRs (Reference) and SIRs. As we can see, the implementation of the SIRs in the structure results into an important improvement of the rejection level, with a spurious-free range that goes up to 20 GHz.

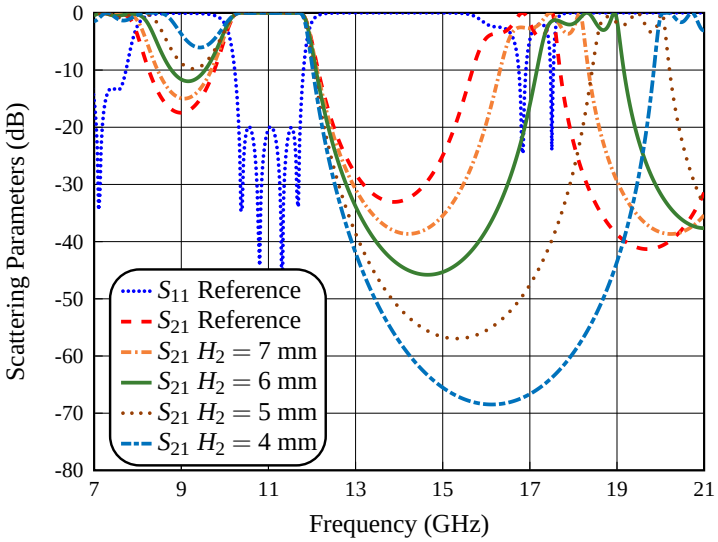

Figure 3.23: Simulated performance of the capacitive four-pole filter with several SIR implementations.

3.5.2 Inductive SIR Filter

To proceed with the study of the advantages offered by SIRs, we now design an eight-pole inductive SIR filter. Fig. 3.24 shows the structure. Fig. 3.25 shows a comparison of the simulated behavior of the structures of Fig. 3.8 (Ind Ref Filter) and Fig. 3.24 (Ind SIR Filter). The dimensions of the SIRs are: $H_1 = 10.16$ mm, $H_2 = 6.0$ mm, and $L_2 = 5.0$ mm, where L_1 is obtained by optimization.

As we can see, the inductive SIR filter does show an important improvement of the out-of-band response (up to 19.25 GHz) in comparison with the inductive reference filter.

3.5.3 Capacitive SIR Filter

To continue, we design next an eight-pole capacitive SIR filter. Fig. 3.26 shows the structure. Fig. 3.27 shows the comparison of the simulated behavior of the structures of Fig. 3.9 (Cap Ref Filter) and Fig. 3.26 (Cap SIR Filter I), respectively. The dimensions of the SIRs are: $H_1 = 10.16$ mm, $H_2 = 6.0$ mm, and $L_2 = 5.0$ mm, where L_1 is again obtained by optimization.

As we can see, the capacitive SIR filter shows a spurious-free range up to 20.25 GHz. This is an improvement with respect to the capacitive reference filter. However, due to the use of capacitive coupling irises, the unwanted resonances below the pass-band have been increased.

A further important improvement of the out-of-band response of the capacitive SIR

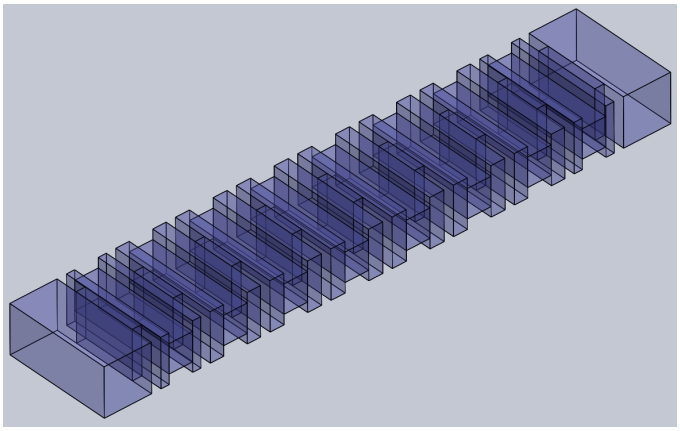

Figure 3.24: Structure of the inductive filter with SIRs of dimensions $H_1 = 10.16$ mm, $H_2 = 6.0$ mm and $L_2 = 5.0$ mm.

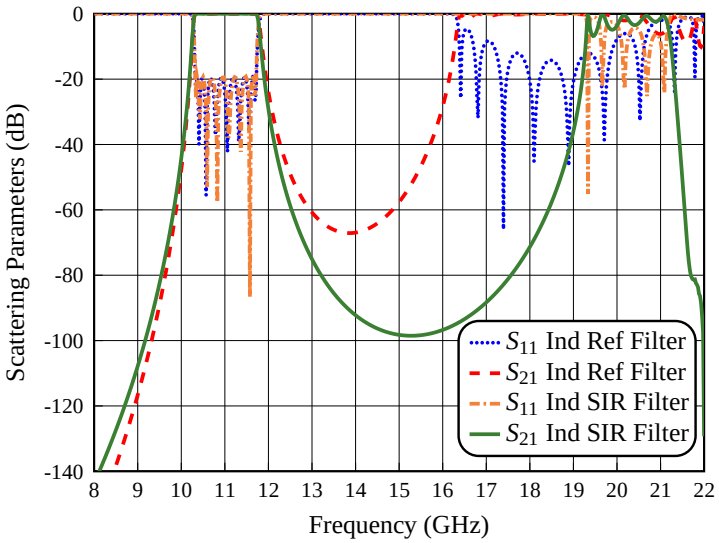

Figure 3.25: Simulated performance of the inductive reference filter (Ind Ref Filter) and inductive filter with SIRs (Ind SIR Filter).

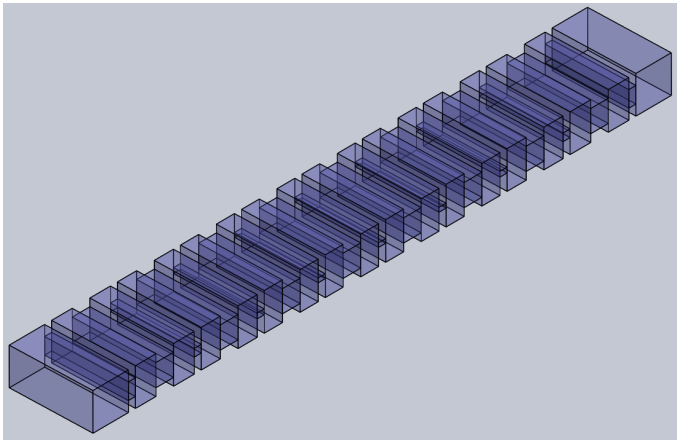

Figure 3.26: Structure of the capacitive filter with SIRs of dimensions $H_1 = 10.16$ mm, $H_2 = 6.0$ mm and $L_2 = 5.0$ mm.

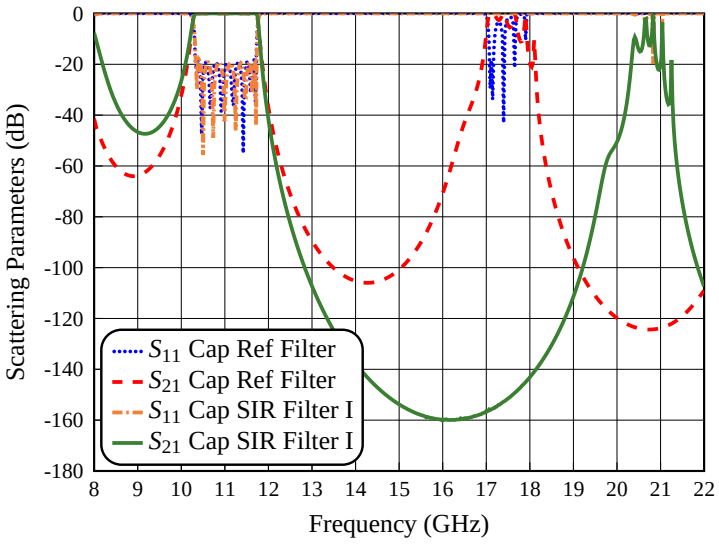

Figure 3.27: Simulated performance of the capacitive reference filter (Cap Ref Filter) and the first capacitive filter with SIRs (Cap SIR Filter I).

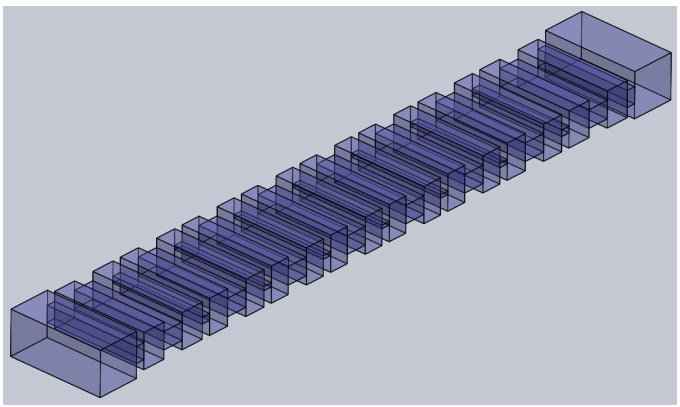

Figure 3.28: Structure of the capacitive filter with SIRs of dimensions $H_1 = 8.0$ mm, $H_2 = 4.0$ mm and $L_2 = 5.0$ mm.

filter can be achieved by changing the height of the SIRs, namely, H_1 and H_2. In fact, our previous study of the behavior of a SIR (see Fig. 3.23) shows that for $H_2 = 4.0$ mm, the response of the capacitive SIR filter (light blue line) is significantly better than the one of the UIR filter (red line). For that reason, we now use $H_1 = 8.0$ mm, $H_2 = 4.0$ mm and $L_2 = 5.0$ mm in the SIRs. The dimension of L_1 for all SIRs is, as in all other cases, obtained during the filter design process.

Fig. 3.28 shows the structure of the new capacitive SIR filter that is obtained by reducing the height of the resonators. Fig. 3.29 shows a comparison of the simulated behavior of the structures in Fig. 3.26 (Cap SIR Filter I) and Fig. 3.28 (Cap SIR Filter II), respectively. As we can see, the change of height of the resonators produces an important improvement in the rejection of the spurious-free response (up to 21.4 GHz), with a slight increase of the unwanted resonances below the pass-band.

To conclude this section, we now show the comparison of the responses of a capacitive reference filter designed with UIRs (Cap Ref Filter), the capacitive filter with widths that decrease as we approach the center of the structure (Cap W Filter), and the second capacitive SIR filter (Cap SIR Filter), as shown in Fig. 3.30.

As we can clearly see in Fig. 3.30, the implementation of the SIRs in the capacitive structures has attenuated the spurious responses and, at the same time, has moved the peaks further away from the pass-band of the filter. However, the S_{21} response of the filter below the pass-band shows a slight increase due to the use of capacitive coupling irises. However, the response of the filter below the pass-band can be improved with the use of inductive irises in the central section of the filter. In any case, the out-of-band performance of the capacitive filter with SIRs is much better as compared to the capacitive filter with changes in the width of the resonators.

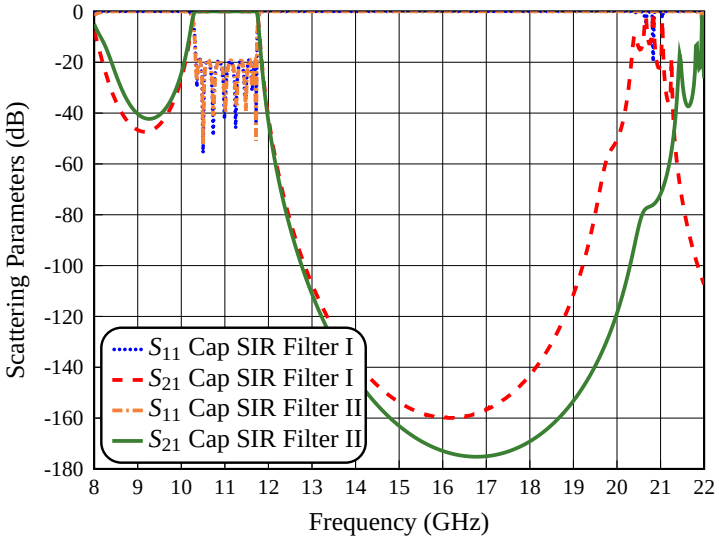

Figure 3.29: Simulated performance of the first capacitive filter with SIRs (Cap SIR Filter I) and the second capacitive filter with SIRs (Cap SIR Filter II).

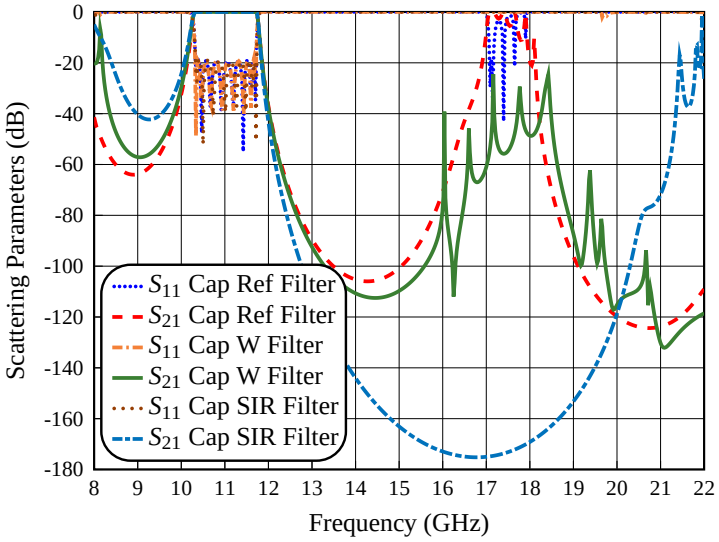

Figure 3.30: Simulated performance of the capacitive reference filter (Cap Ref Filter), capacitive filter with widths that decrease as we approach the center of the structure (Cap W Filter) and capacitive filter with SIRs (Cap SIR Filter).

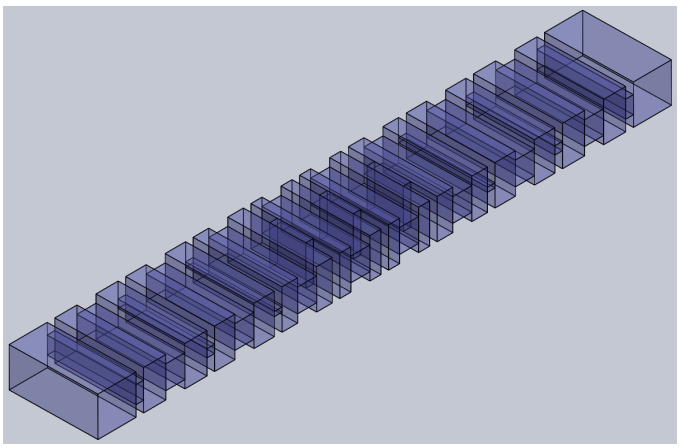

Figure 3.31: Structure of the hybrid filter with SIRs of dimensions $H_1 = 10.16$ mm, $H_2 = 6.0$ mm and $L_2 = 5.0$ mm.

3.5.4 Hybrid SIR Filter

We are now ready to design a hybrid SIR filter, with the objective of improving the out-of-band response both below and above the pass-band. Fig. 3.31 shows the structure of the first hybrid SIR filter. Fig. 3.32 shows a comparison of the simulated behavior of the structures in Fig. 3.11 (Hyb Ref Filter) and Fig. 3.31 (Hyb SIR Filter I), respectively. For this first hybrid SIR filter we have used the following SIRs dimensions: $H_1 = 10.16$ mm, $H_2 = 6.0$ mm, and $L_2 = 5.0$ mm. The value of L_1 is obtained by optimization.

As we can see, the use of hybrid couplings and SIRs results in a very important improvement of the response. The unwanted resonances below the pass-band have, in fact, been reduced to a value below -50 dB. In addition, the level of the spurious responses has been reduced, and a spurious-free range up to 18.85 GHz has been obtained.

A further improvement of the out-of-band response is achieved by changing the height of the resonators. Fig. 3.33 shows the structure of the hybrid SIR filter with changes in the height of the resonators. Fig. 3.34 shows a comparison of the simulated behavior of the structures in Fig. 3.31 (Hyb SIR Filter I) and Fig. 3.33 (Hyb SIR Filter II), respectively. For this last hybrid SIR filter, the dimensions of the SIRs are: $H_1 = 8.0$ mm, $H_2 = 4.0$ mm, and $L_2 = 5.0$ mm, where L_1 is obtained by optimization.

As we can see, changing the height of the SIRs results in a further improvement of the out-of-band response, namely, we now have a spurious response below -40 dB from 12 to 22 GHz, with a spike reaching -30 dB at 21.30 GHz. Also, below the pass-band a rejection level of -50 dB has been achieved. This is indeed an important improvement.

In conclusion, using the techniques discussed so far, namely, the combined use of inductive and capacitive couplings, together with SIRs (based on waveguides of different

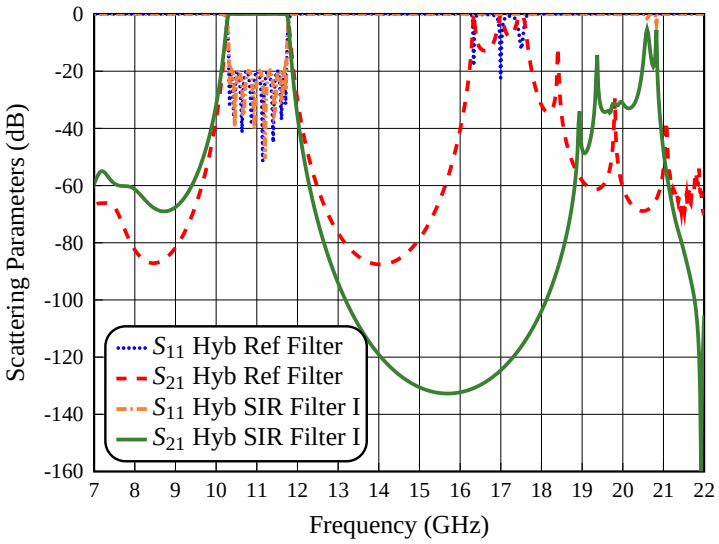

Figure 3.32: Simulated performance of the hybrid reference filter (Hyb Ref Filter) and the first hybrid filter with SIRs (Hyb SIR Filter I).

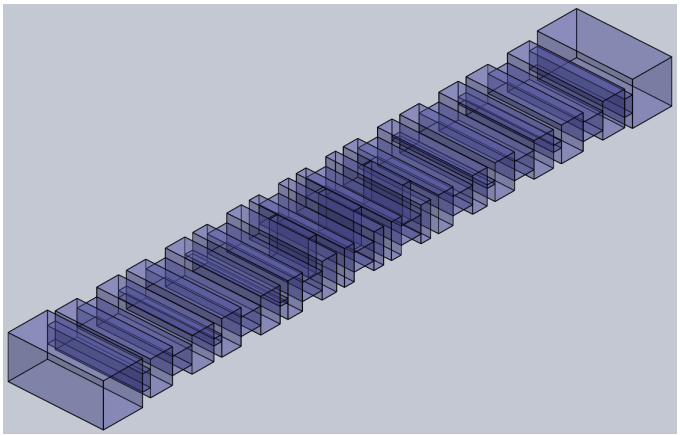

Figure 3.33: Structure of the hybrid filter with SIRs $H_1 = 8.0$ mm, $H_2 = 4.0$ mm and $L_2 = 5.0$ mm.

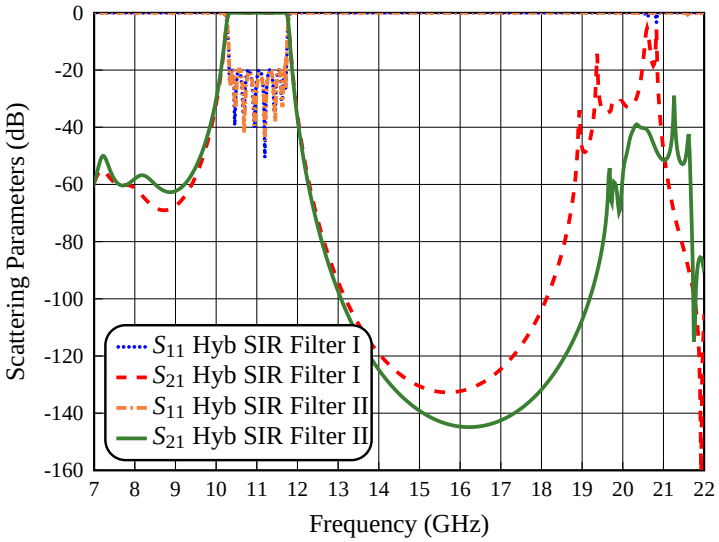

Figure 3.34: Simulated performance of the first hybrid filter with SIRs (Hyb SIR Filter I) and the second hybrid filter with SIRs (Hyb SIR Filter II).

heights), we have obtained the following improvements:

- A wider spurious-free region above the pass-band with an important attenuation of the spurious response.
- A very good rejection level below the pass-band.

The results that we have obtained are indeed excellent. However, the filter that we have obtained cannot be manufactured as it is, because all the simulations have been carried out using FEST3D in a low-accuracy setting (LA). In the next section, we will discuss in detail the procedure to go from the LA prototype to the high-accuracy (HA) prototype that can then be manufactured and measured. This transition will be based on the use of the procedure discussed in [101], and the use of the Aggressive Space Mapping (ASM) technique described in [102].

3.6 High-Accuracy Wideband Hybrid SIR Filter

The objective of this section is to describe the design procedure to obtain the HA version of the optimal wideband hybrid SIR filter that we have finally obtained in Section 3.5 (see Fig. 3.33). Before we do that, however, we find it appropriate to briefly review the complete LA design procedure that we have used so far for all the filter prototypes.

3.6.1 LA The Design Procedure

The complete LA design procedure for all the filters discussed in this chapter is composed of the following steps:

1. We first design the basic waveguide filter with capacitive couplings elements and uniform waveguide lengths as resonators (UIRs). For this purpose, we can follow the procedure outlined in [101].
2. Once we have designed the basic waveguide filter, we introduce the required number of inductive irises in the central portion of the filter. The number of inductive irises depends on the rejection requirements below the filter pass-band. In our research, the filters have been implemented using three inductive irises in filters of order eight. Again, the filter design procedure described in [101] can be used to obtain the hybrid structure.
3. The next step is to replace all resonators with SIRs. The optimal dimensions of the SIRs are chosen following the guidelines given in Section 3.5. The total length of each SIR in Fig. 3.22 is around $\lambda_g/2$, where λ_g is the guided wavelength evaluated at the center frequency. The length of the central section of the SIR is approximately $L_2 = \lambda_g/6$. Finally, the remaining SIR dimensions, namely, H_1, H_2 and L_1 are defined following the guidelines given in Section 3.5.

Having summarized the LA design procedure, we can now describe the HA design procedure for the prototype we are going to manufacture.

3.6.2 The HA Prototype

There are a number of differences between the LA and the HA prototypes, namely:

- In the LA design, all concave angles are sharp 90° angles.
- In the HA design, all concave angles located in the E-plane of the waveguide are rounded with a radius $r = 1.0$ mm. This choice is due to the fact that the hardware will be cut longitudinally in the cited E-plane, and will be manufactured using milling in two identical halves.
- The final fundamental difference is that, even though both the LA and HA prototype give the exact same band-pass response at the end of the design process, the actual physical dimensions of the two filters are not the same.

Fig. 3.35 shows the high-precision structure that we have obtained for the filter discussed in this Chapter. The HA design procedure that we have used is as follows:

1. Use the procedure described in [101] to obtain the initial dimensions of the filter structure in LA, but including all rounded corners.

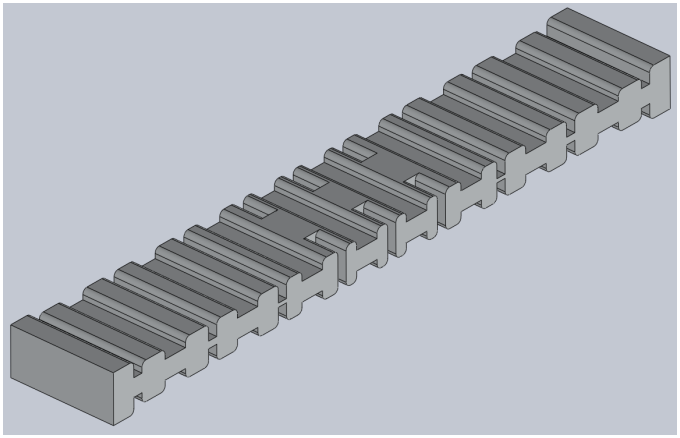

Figure 3.35: Structure of the in-line wideband hybrid SIR filter designed with a radius equal to r =1.0 mm.

2. Use the aggressive spacing mapping (ASM) technique discussed in [102], to obtain the final dimensions of the HA structure. ASM is based on the use of two electromagnetic simulators:
   - The first one is FEST3D, that is very efficient when used in an LA setting.
   - The second simulator we used is CST Design Studio (v.2021, CST GmbH, now with Dassault Systèmes) which is highly accurate, but is computationally less efficient.
3. It is interesting to note that the procedure described in [101] has also been used in the context of the ASM in order to build, step-by-step, the final HA hardware.
4. Once the complete HA model has been assembled, one last ASM iteration using the complete HA and LA models is performed.

Fig. 3.36 shows the comparison of the simulated behavior of the hybrid SIR filter structure obtained with the commercial tools FEST3D (LA) and CST Studio Suite (HA) at the end of the design process. As we can see, the agreement is very good. Furthermore, the simulations show a very good out-of-band response, with spurious below -30 dB from 19.5 to 22 GHz, and spikes reaching -3.25, -21.85 and -17.5 dB at 20.25, 21.25 and 21.45 GHz, respectively.

Table 3.1 shows the final values for all dimensions of the HA hybrid SIR filter. The dimensions are given up to the center of the filter because the structure is symmetrical. The thickness of the inductive and capacitive windows is t, and all SIRs have the same width as the input waveguide. The other variables are indicated in Fig. 3.1 and Fig. 3.22.

Table 3.1: Physical dimensions for the in-line hybrid SIR filter.

Section Type	Dimensions (mm)
Input Waveguide	$a = 22.86$ $b = 10.16$
Capacitive window 1-6	$a = 22.86$ $h_1 = h_6 = 3.772$ $t = 2$
SIR 1-8	$H_1 = 8.000$ $L_1 = 5.632$ $H_2 = 4.000$ $L_2 = 5.000$
Capacitive window 2-5	$a = 22.86$ $h_2 = h_5 = 1.476$ $t = 2$
SIR 2-7	$H_1 = 8.000$ $L_1 = 5.025$ $H_2 = 4.000$ $L_2 = 5.000$
Capacitive window 3-4	$a = 22.86$ $h_3 = h_4 = 0.805$ $t = 2$
SIR 3-6	$H_1 = 8.000$ $L_1 = 3.771$ $H_2 = 4.000$ $L_2 = 5.000$
Inductive window 1-3	$w_1 = w_3 = 9.363$ $b = 8.000$ $t = 2$
SIR 4-5	$H_1 = 8.000$ $L_1 = 2.576$ $H_2 = 4.000$ $L_2 = 5.000$
Inductive window 2	$w_2 = 8.546$ $b = 8.000$ $t = 2$

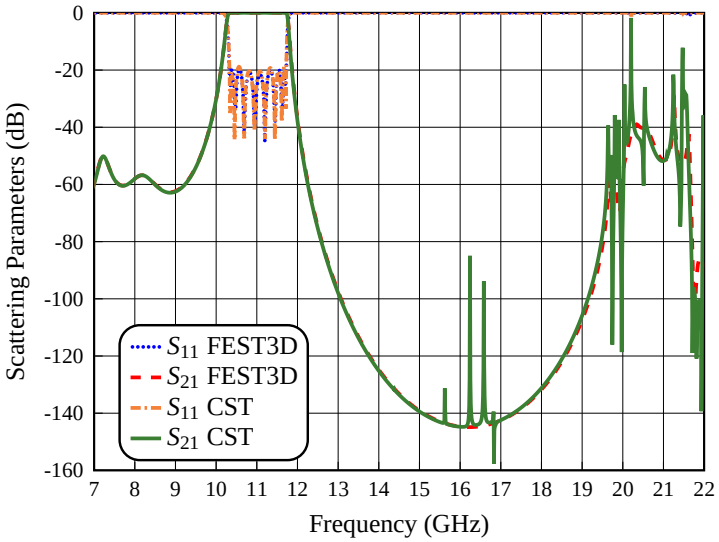

Figure 3.36: Simulated performance of the in-line hybrid SIR filter using FEST3D and CST.

Figure 3.37: Manufactured prototype in aluminum of the in-line hybrid SIR filter (no silver plating).

3.6.3 Measurements

To validate the design procedure described in this chapter, we have manufactured a prototype of the HA hybrid SIR filter in a clam-shell configuration. For this purpose, we have used a combination of milling and spark erosion, as shown in Fig. 3.37. The use of the spark erosion process, however, has been limited to the capacitive window 3.

Next, we have performed the comparison between measured and simulated in-band responses, as shown in Fig. 3.38. As we can see, although the in-band performance is indeed centered at 11 GHz, there is a slight discrepancy between simulation and measurements, namely, the return loss is degraded with respect to the simulations at the edges of the pass-band.

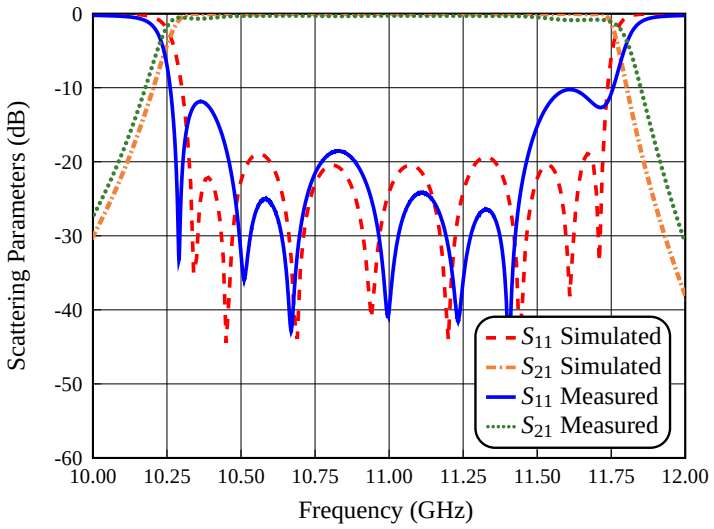

Figure 3.38: Measurement of the in-band performance of the filter compared with the EM simulation (CST).

Fig. 3.39 shows the comparison between the measured and the simulated out-of-band responses. As we can see, the agreement between simulation and measurement in the out-of-band response is very good. However, the appearance of spikes from 19.5 to 22 GHz is probably due to manufacturing errors. To measure the electrical response of the filter in the wide frequency range shown in Fig. 3.39, we have used four standard waveguide calibrations, namely, WR-90, WR-75, WR-62 and WR-51. In all cases we have used the TRL (Through, Reflection and Line) calibration procedure, with a noise floor about -70 dB.

It is important to note that, although the agreement between simulations and measurements is good enough to validate both the filter structure and the design procedure that we have proposed, it is nevertheless important to understand the reason for the disagreement between measurements and simulations.

In the next section we will therefore perform a detailed investigation to better understand what is happening.

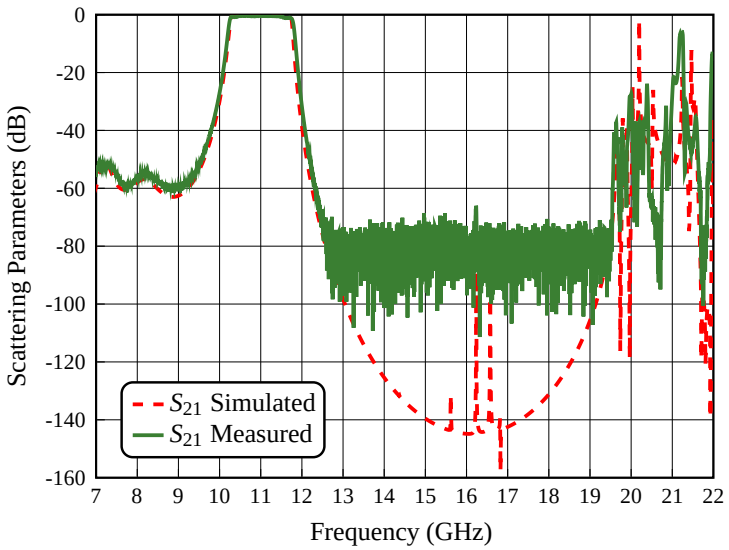

Figure 3.39: Measurement of the out-of-band performance of the filter compared with the EM simulation (CST).

3.6.4 Inverse ASM

The process that we have used to better understand the measured performance of the filter is to use an *inverse* ASM procedure. In other words, we have used the measured response of the filter as a target for the optimization of the structure in the LA space (FEST3D model). The idea is that, once the LA simulations agree with the measured response, we will obtain an estimation of the manufacturing errors by examining the change of dimensions from the initial optimized LA model.

Fig. 3.40 shows the comparison of the in-band results of the inverse ASM simulation with the measured behavior. As we can see, we have been able to recover reasonably well the in-band performance of the measurement.

To validate the inverse ASM procedure, we have measured the mechanical dimensions of the inside of the prototype that we have manufactured. Table 3.2 and Table 3.3 show the summary of the errors measured in the fabricated structure as compared to the errors obtained from the inverse ASM simulations. As we can see, the correlation is indeed strong. It is important to mention that we have only considered in the simulations the heights of the capacitive windows (h_i), the widths of the inductive windows (w_i) and the lengths of the two parts (of higher height) of the SIRs (i.e. L_{1_1} and L_{1_2})

This analysis indicates that there are manufacturing errors in excess of 60 μm in the filter structure. The discrepancy observed between measurements and simulations with errors of this order is indeed reasonable.

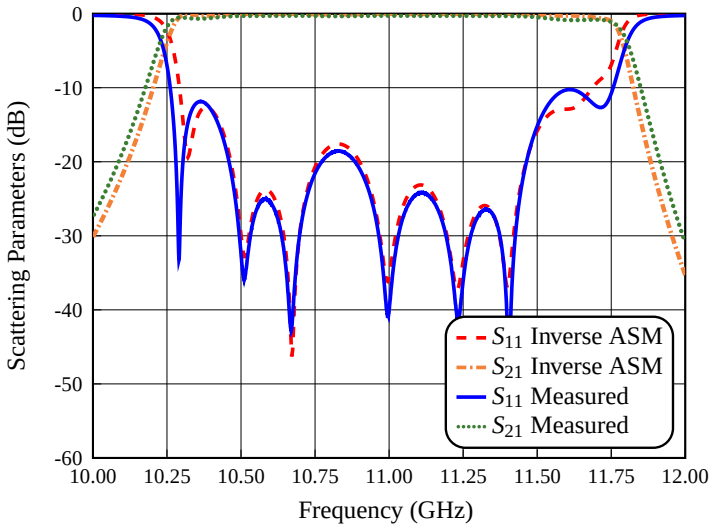

Figure 3.40: Inverse ASM in-band performance compared with the measurement of the in-band performance.

Table 3.2: Errors of the measures of the fabricated structure and inverse ASM.

Filter Type	Measures and inverse ASM	
Windows	Error Measured	Error ASM
h_1	27 μm	15.74 μm
h_2	72 μm	21.30 μm
h_3	70 μm	59.42 μm
w_1	139 μm	130.49 μm
w_2	118 μm	137.10 μm
w_3	142 μm	131.98 μm
h_4	45 μm	47.16 μm
h_5	52 μm	47.46 μm
h_6	28 μm	42.29 μm

To continue with our study, we show in Fig. 3.41 the comparison of the out-of-band measured results with the inverse ASM simulation. As we can see, there is a slight discrepancy between the frequency location of the spurious response.

We can therefore conclude that the discrepancies between measurements and simulations, both in the in-band and the out-of-band responses, are due to excessive manufacturing errors. To overcome this limitations, therefore, it is necessary to use a more

Table 3.3: Errors of the measures of the fabricated structure and inverse ASM.

Filter Type	Measures and inverse ASM			
Resonators	Error Measured		Error ASM	
SIR 1	L_{1_1} =32 μm	L_{1_2} =49 μm	L_{1_1} =17.56 μm	L_{1_2} =33.45 μm
SIR 2	L_{1_1} =62 μm	L_{1_2} =34 μm	L_{1_1} =54.97 μm	L_{1_2} =39.09 μm
SIR 3	L_{1_1} =50 μm	L_{1_2} =62 μm	L_{1_1} =43.50 μm	L_{1_2} =145.45 μm
SIR 4	L_{1_1} =28 μm	L_{1_2} =47 μm	L_{1_1} =10.58 μm	L_{1_2} =28.36 μm
SIR 5	L_{1_1} =22 μm	L_{1_2} =33 μm	L_{1_1} =10.83 μm	L_{1_2} =19.41 μm
SIR 6	L_{1_1} =25 μm	L_{1_2} =43 μm	L_{1_1} =76.23 μm	L_{1_2} =40.67 μm
SIR 7	L_{1_1} =53 μm	L_{1_2} =60 μm	L_{1_1} =101.11 μm	L_{1_2} =121.15 μm
SIR 8	L_{1_1} =59 μm	L_{1_2} =39 μm	L_{1_1} =76.39μm	L_{1_2} =39.95 μm

Table 3.4: Tolerance analysis of the fabricated structure.

Filter Type	Yield of the Structures				
Tolerance	5 μm	10 μm	15 μm	25 μm	40 μm
In-line Hybrid SIR Filter	72 %	12 %	7 %	2 %	1 %

accurate hardware manufacturing process.

3.7 Tolerance Analysis

To complete our discussion on the performance of the prototype we have just measured, we now discuss the results of a detailed tolerance (or yield) analysis. In this context, it is important to recall at this point that the filters designed in this chapter all have a wide pass-band. Wideband filters are normally considered to be *less sensitive* to manufacturing errors.

The tolerance analysis has been done using the commercial tool FEST3D introducing a random error (with a Gaussian distribution) in the filter dimensions. Different values of the standard deviation have also been used, namely, $\pm$ 5, $\pm$ 10, $\pm$ 15, $\pm$ 25 and $\pm$ 40 μm. Furthermore, we have considered a threshold value for the yield estimation of 18 dB, since the filter has been designed with a return loss of 20 dB. Table 3.4 shows the summary of the results obtained.

Fig. 3.42 shows a number of simulations, including random errors in the dimensions. It is interesting to note that, from both the simulations and the results in Table 3.4, we

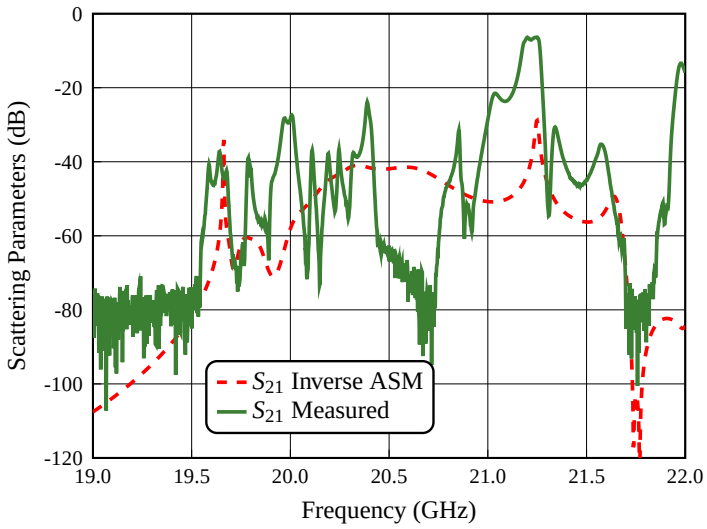

Figure 3.41: Inverse ASM out-of-band performance compared with the measurement of the out-of-band performance.

can clearly conclude that it is not possible to obtain an acceptable in-band response for this filter with manufacturing errors above $\pm$ 10 μm. This is indeed in perfect agreement with the inverse ASM analysis we performed before.

3.8 High Power Analysis

It is well-known that the multipactor behavior of microwave filters, is one of the most important features for space applications when high power is required [104]. In this section, we will therefore explore multipactor effect in the structure that we have designed. For this purpose, a number of simulations have been carried out in order to identify the power level (in Watts) at which a multipactor discharge can be initiated.

It is important to mention that in our simulations we have concentrated our attention on the central section of the in-line hybrid SIR filter, due to the small dimensions of the involved irises, namely, h_3, w_1 and w_2, and of the SIRs central sections (i.e. H_2 of SIR3 and SIR4). Furthermore, we have selected a number of frequencies that will be used to identify the multipactor behavior of the structure. We selected first the frequencies where the group delay shows a maximum in the response, namely, f_1 and f_3, together with the center frequency of the filter, namely, f_2. The simulations have been carried out using FEST3D for the EM fields. SPARK3D has been used for the multipaction prediction. The parameters used with SPARK3D are as follows:

1. Initial power: 50 W

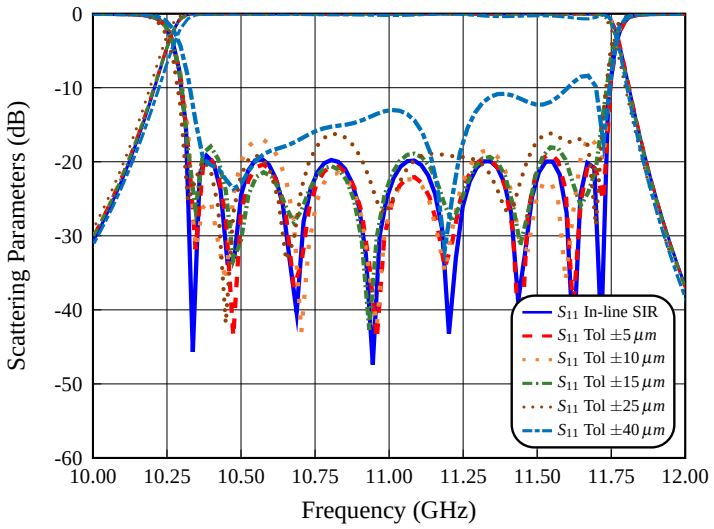

Figure 3.42: Tolerance analysis of the in-line hybrid SIR filter.

Table 3.5: High power analysis of the in-line hybrid SIR filter.

Structure	Power of the Structure		
Frequency	$f_1 = 10.30$ GHz	$f_2 = 11.00$ GHz	$f_3 = 11.75$ GHz
h_3	1070 W	868 W	145 W
$w_1 = w_3$	> 1 MW	> 1 MW	> 1 MW
w_2	> 1 MW	> 1 MW	> 1 MW
SIR 3	1437 W	5949 W	1412 W
SIR 4	1006 W	4024 W	1212 W

2. Maximum power: 1 MW
3. Growth factor of the power: 10^2
4. Frequencies of simulation : f_1, f_2 and f_3
5. Initial number of electrons: 10000

Table 3.5 shows the power thresholds that we have obtained for our filter. As expected, the capacitive window (h_3) shows the lowest power threshold at 11.75 GHz with 145 W, while the inductive irises are not affected at all by the high power levels. Finally, in Fig. 3.43 we show the values obtained in the capacitive window for each simulation.

We can conclude that the filter structures studied in this chapter does perform well in terms of bandpass and out-of-band rejection, but is not appropriate for high power applications. It is possible, however, that using an additional pair of inductive irises, the

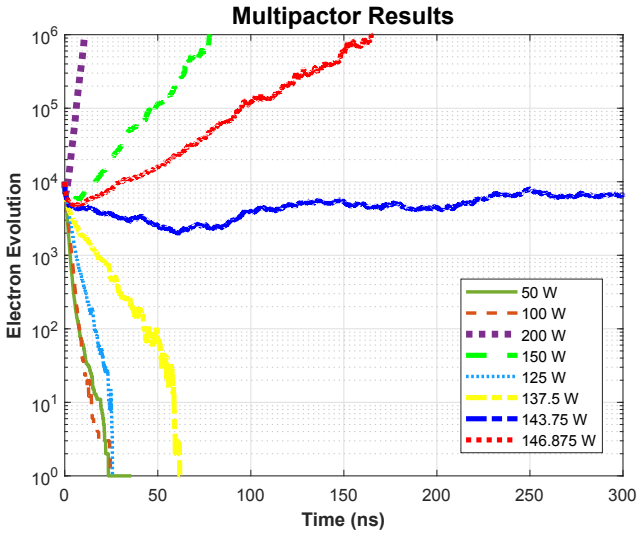

Figure 3.43: Multipactor results (electron evolution) for the capacitive window of height h_3 at 11.75 GHz of the in-line hybrid SIR filter.

power behavior of the filter could be greatly enhanced.

3.9 Higher Order Modes Analysis

In the previous sections we have measured the in-band and out-of-band responses of the filter considering only the fundamental mode excitation, namely, TE_{10}. In this section we extend the analysis to include the presence of higher order modes in the excitation. This is important because any mechanical imperfection in the filter, or in the waveguide system to which the filter is connected, could indeed excite higher order modes. To start, we have computed the cut-off frequencies of the higher order modes that could be excited in the stop-band response of our filter, as shown in Table 3.6.

Fig. 3.44, Fig. 3.45, Fig. 3.46, Fig. 3.47, and Fig. 3.48 show the comparison of the simulated performances of the filter excited with the higher order TE_{20}, TE_{01}, TE_{11}, TM_{11}, TE_{30}, TE_{21} and TM_{21} modes obtained with FEST3D and CST, respectively.

As we can see, the higher order TE_{01}, TE_{11}, TM_{11}, TE_{21} and TM_{21} modes show an important attenuation of the filter output (up to -90 dB). On the other hand, the higher order TE_{20} and TE_{30} modes need to be studied in more detail. Fig. 3.44 shows that the TE_{20} mode output power is below -40 dB from 13 to 22 GHz, with a spike reaching -30 dB at 16.45 GHz. We conclude, therefore, if the higher order TE_{20} mode is excited, no significant spurious signal would be observed in the response of the filter.

Fig. 3.47, on the other hand, shows a spurious response beginning at about 19.7

Table 3.6: Cut-off frequencies of higher order modes exciting the in-line inline hybrid SIR filter.

Mode	Cut-off frequency
Waveguide WR-90	a =22.86 mm b =10.16 mm
TE_{10}	f_c =6.557 GHz
TE_{20}	f_c =13.114 GHz
TE_{01}	f_c =14.753 GHz
TE_{11}	f_c =16.145 GHz
TM_{11}	f_c =16.145 GHz
TE_{30}	f_c =19.671 GHz
TE_{21}	f_c =19.739 GHz
TM_{21}	f_c =19.739 GHz

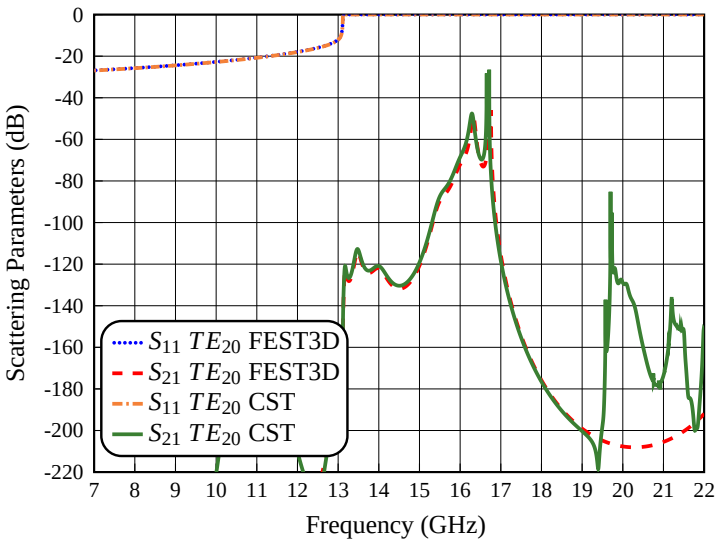

Figure 3.44: Simulated performance of the in-line hybrid SIR filter for the higher order mode TE_{20} using FEST3D and CST.

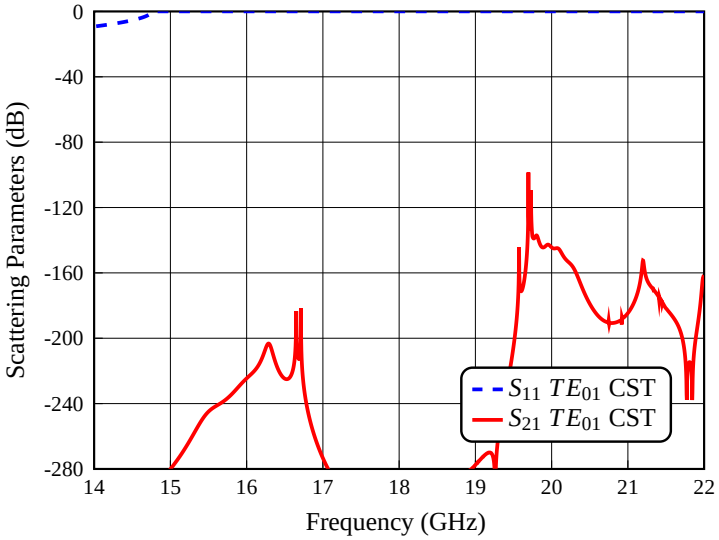

Figure 3.45: Simulated performance of the in-line hybrid SIR filter for the higher order mode TE_{01} using CST.

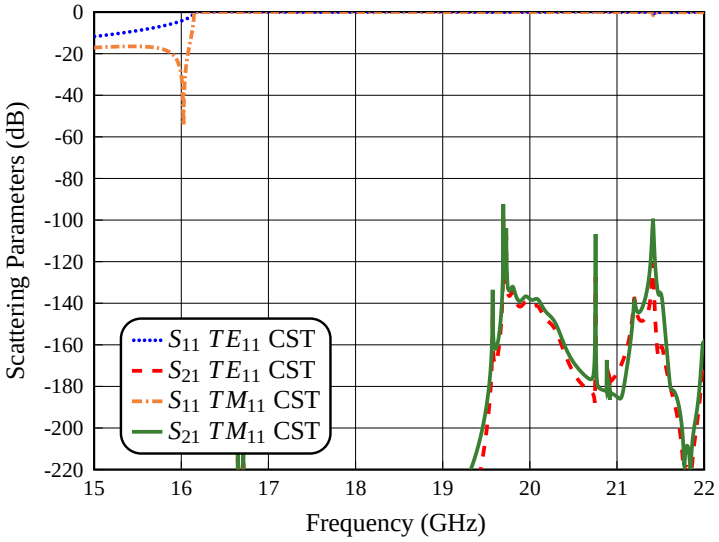

Figure 3.46: Simulated performance of the in-line hybrid SIR filter for the higher order modes TE_{11} and TM_{11} using CST.

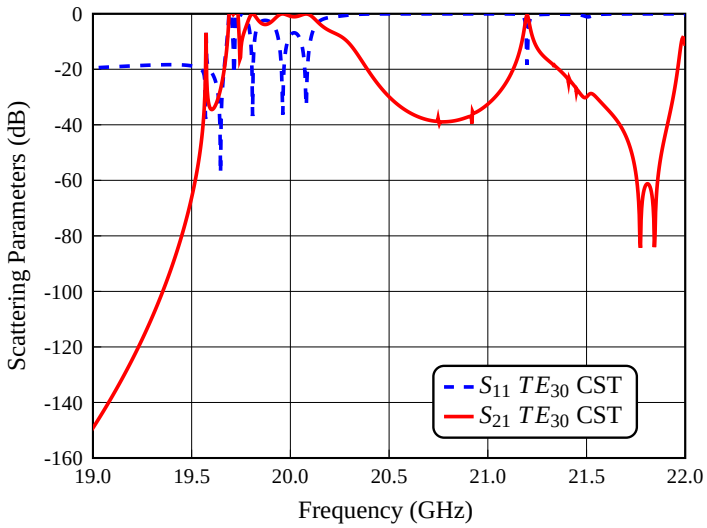

Figure 3.47: Simulated performance of the in-line hybrid SIR filter for the higher order mode TE_{30} using CST.

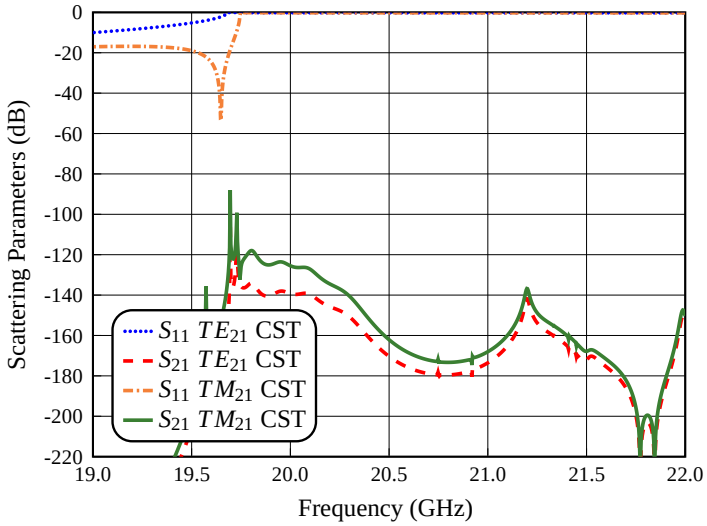

Figure 3.48: Simulated performance of the in-line hybrid SIR filter for the higher order modes TE_{21} and TM_{21} using CST.

GHz, that is due to the TE_{30} mode. We can therefore conclude that if the TE_{30} is indeed present in the excitation of the filter, spurious responses above 19.7 GHz may be observed. This frequency, however, is at the end of the spurious-free range of our filter.

We can therefore conclude that the presence of higher order modes in the excitation will not produce significant degradation in the filter response.

3.10 Conclusions

In this chapter we have discussed the complete design procedure of a wideband waveguide filter structure based on the combined use of capacitive and inductive irises, together with SIRs.

Furthermore, we have also carried out detailed tolerance and high power analyses in order to identify the manufacturing accuracy that is required to ensure high yield, and the maximum power at which multipactor discharge can occur.

The filter performance has also been studied with higher order modes in the excitation. The results obtained indicate that the presence of higher order modes in the input of the filter does not produce any significant degradation of the filter performance.

Finally, in addition to theory, we have also discussed the measured results of a prototype showing reasonable agreement with simulations, thereby fully validating both the filter structure and the design procedure.

Chapter 4

Advanced Topologies for Wideband Hybrid SIR Filters in Rectangular Waveguide

In this chapter, we discuss several wideband hybrid SIR filter topologies that can either provide advantages in the fabrication process, or provide simultaneously a reduced footprint and lower insertion losses. In the reminder of this chapter we will first discuss in detail the structures and their design procedure. The chapter is concluded discussing the measured results of a number of prototypes. In all cases, the agreement between simulations and measurements is shown to be excellent, thereby fully validating all of the filter topologies that we have investigated.

The results of the investigations discussed in this chapter have resulted in the following publication:

- J. Valencia, V.E. Boria, M. Guglielmi and S. Cogollos, "Compact wideband hybrid filters in rectangular waveguide with enhanced out-of-band response", in IEEE Transactions on Microwave Theory and Techniques, vol. 68, no. 1, pp. 87-101, Jan. 2020.

Before describing the advanced filter topologies that are the object of this chapter, it is appropriate to review the two main limitations of the structure described in Chapter 3, namely:

- The in-line hybrid SIR filter provided a wide spurious-free range above the pass-

band, however, the resulting structure was rather long.
- Furthermore, the use of capacitive irises resulted into high power limitations.

In this context, therefore, in this chapter we propose three alternative structures with the following advantages:

- We will first discuss a filter structure based on a body and a top cover, in order to simplify the manufacturing and provide, at the same time, an improvement of the out-of-band response of the filter.
- We will then introduce tuning screws in the SIR, with the objective of reducing the high manufacturing accuracy requirements.
- Finally, we will discuss a folded configuration, in order to reduce the footprint of the filter, and obtain, at the same time, further out-of-band improvements.

4.1 Wideband Hybrid SIR Filters Specifications

To evaluate the performance of the filter structures discussed in this chapter, we will use again the specifications given in the Section 3.1 of Chapter 3. In addition, we will use the performance of the first in-line hybrid SIR filter (see Fig. 3.33) as a reference for further improvements.

4.2 Changing the Offset of the Irises

The first modification of the filter structure discussed in Chapter 3 that we study is a change in the offset of the coupling irises. Our objective is to obtain structures that are simpler to manufacture. The performance of both offset inductive and capacitive irises will be first evaluated in detail.

4.2.1 Inductive Irises

We first study the effect of changing the offset of inductive irises. Fig. 4.1 shows the structure of a filter with an offset in the position of the inductive irises.

Fig. 4.2 shows a comparison of the simulated behavior of the structures of Fig. 3.8 (Ind Ref Filter) and Fig. 4.1 (Ind Offset Filter), respectively. As we can see, the introduction of an offset in the inductive irises does show a slight improvement of the spurious response.

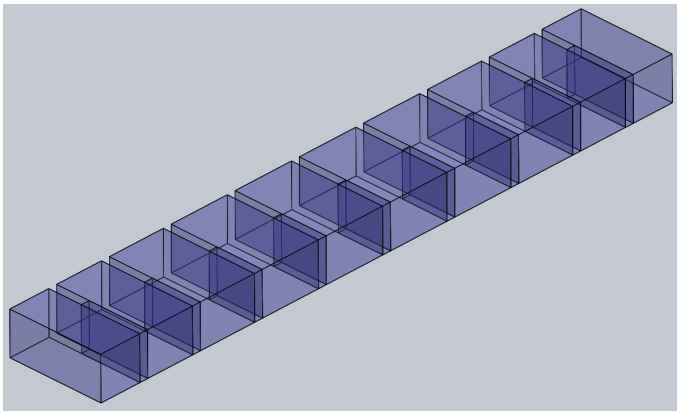

Figure 4.1: Structure of a filter with an offset in the position of the inductive irises.

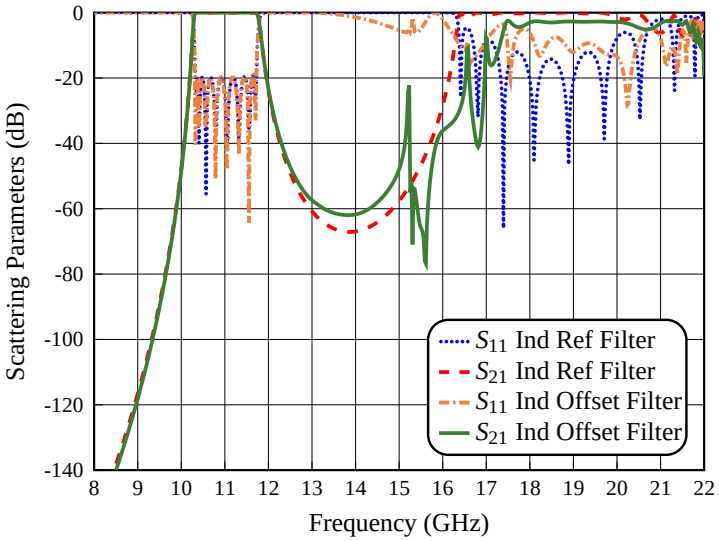

Figure 4.2: Simulated performance of the inductive filter (Ind Ref Filter) and the inductive filter with an offset in the position of the inductive irises (Ind Offset Filter).

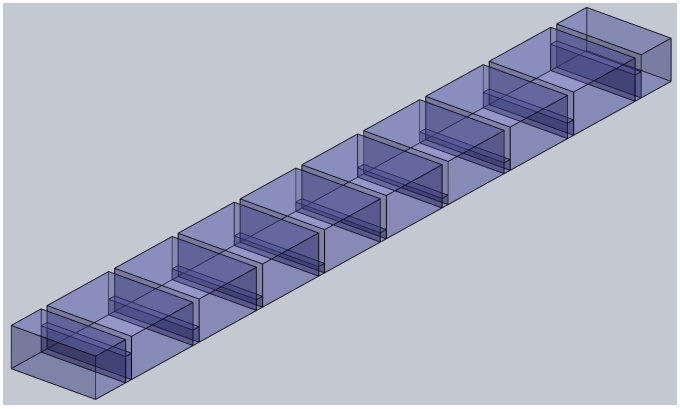

Figure 4.3: Structure of a filter with an offset in the position of the capacitive irises.

4.2.2 Capacitive Irises

Next, the same procedure is applied to a capacitive filter. Fig. 4.3 shows the structure of a filter with an offset in the position of the capacitive irises.

Fig. 4.4 shows a comparison of the simulated behavior of the structures in Fig. 3.9 (Cap Ref Filter) and Fig. 4.3 (Cap Offset Filter), respectively. As we can see, the change in the position of the capacitive irises has a negative effect, namely, a reduction of the frequency location of the first spurious response. However, an advantage of this implementation is that the height of capacitive irises is higher, thus easing the manufacturing procedure and enhancing the high power (multipactor) response.

4.2.3 Hybrid SIR Filters

Once we have discussed the effects of changing the offset of the irises, we can now design a new hybrid SIR filter with offset coupling irises, as shown in Fig. 4.5.

Fig. 4.6 show a comparison of the simulated behavior of the structures of Fig. 3.33 (Hyb SIR Ref Filter) and Fig. 4.5 (Hyb SIR O Filter I). As we can see, the change in the position of both the inductive and capacitive irises does not show a substantial improvement in comparison with the in-line hybrid SIR filter.

Given the results obtained so far, we have decided to redesign the filter in Fig. 4.5, leaving all inductive irises with zero offset, and using an offset only on the capacitive irises, as shown in Fig. 4.7. The comparison between the responses of structures in Fig. 4.5 (Hyb SIR O Filter I) and Fig. 4.7 (Hyb SIR O Filter II) is shown in Fig. 4.8. As we can see, the implementation of this change does result in an improvement in the out-of-band response, reducing the first spurious response.

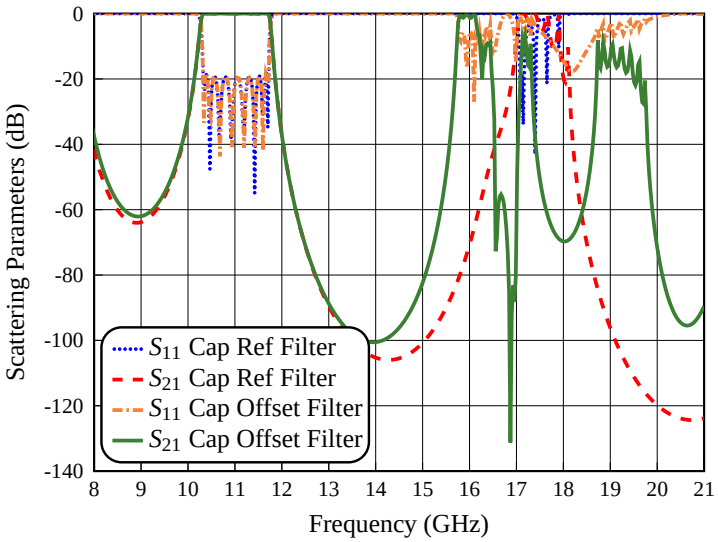

Figure 4.4: Simulated performance of the capacitive filter (Cap Ref Filter) and the capacitive filter with an offset in the position of the capacitive irises (Cap Offset Filter).

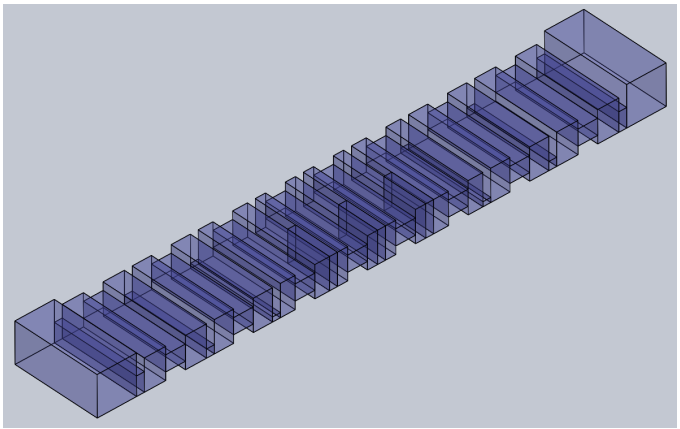

Figure 4.5: Structure of the first hybrid SIR filter with an offset in the position of the irises.

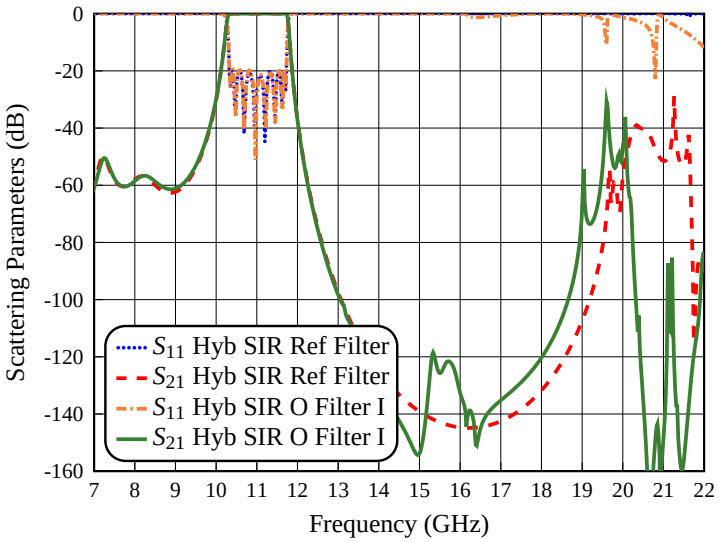

Figure 4.6: Simulated performance of the hybrid SIR filter (Hyb SIR Ref Filter) and the first hybrid SIR filter with an offset in the position of the irises (Hyb SIR O Filter I).

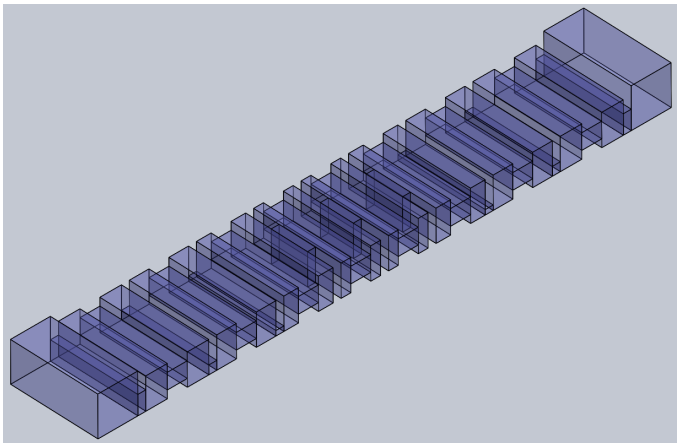

Figure 4.7: Structure of the second hybrid SIR filter with an offset only in the position of the capacitive irises.

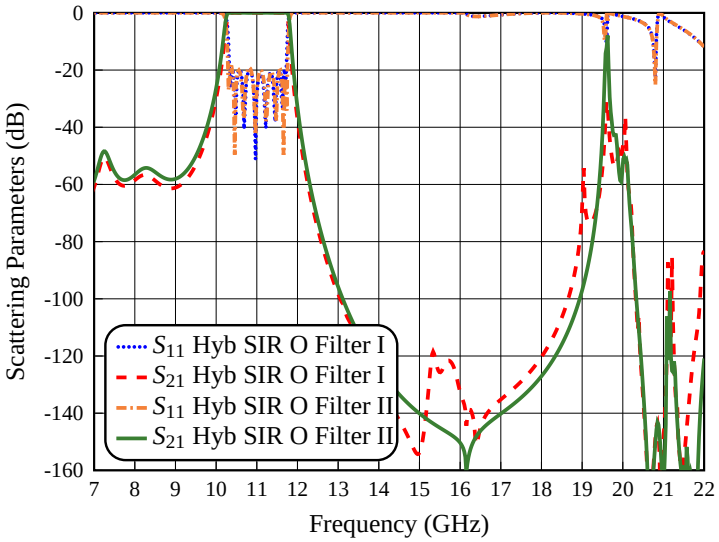

Figure 4.8: Simulated performance of the first hybrid SIR filter (Hyb SIR O Filter I) and the second hybrid SIR filter (Hyb SIR O Filter II) with an offset only in the position of the capacitive irises.

4.3 Changing the Position of the SIRs

The next step in the design of our filter is to change the offset of the capacitive loading in the SIR sections. Fig. 4.9 shows the structure of the filter with an offset in the position of both the capacitive irises and the SIR sections. Fig. 4.10 shows a comparison of the simulated behavior of the structures in Fig. 4.7 (Hyb SIR O Filter II) and Fig. 4.9 (Hyb SIR O-S Filter I), respectively.

As we can see, the resulting structure shows an important improvement reaching -60 dB in the out-of-band response from 12 to 17.5 GHz. However, spurious responses have appeared at 17.75 GHz, with spikes reaching about -10 dB from 17.75 to 22 GHz. Also, the response below the pass-band shows a slight deterioration.

In an attempt to improve the overall filter response, we now change the height of the SIRs. The dimensions of the SIRs used so far are $H_1 = 8.0$ mm and $H_2 = 4.0$ mm. In the new filter we have reduced the height of the SIRs to $H_1 = 7.0$ mm and $H_2 = 4.0$ mm, respectively. Fig. 4.11 shows the structure of the filter of the Fig. 4.9 with these modifications. Fig. 4.12 shows a comparison of the simulated behavior of the structures in Fig. 4.9 (Hyb SIR O-S Filter I) and Fig. 4.11 (Hyb SIR O-S Filter II), respectively.

As we can see, the change in the position of both capacitive irises and SIR sections with reduced height produces a further improvement in the attenuation of the spurious response of the filter, namely, we now have a wider spurious response below -60 dB and a

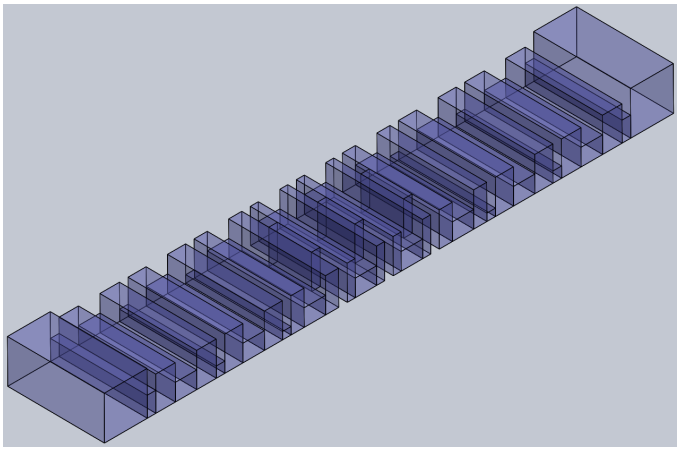

Figure 4.9: Structure of the first hybrid SIR filter with an offset in both capacitive irises and SIRs.

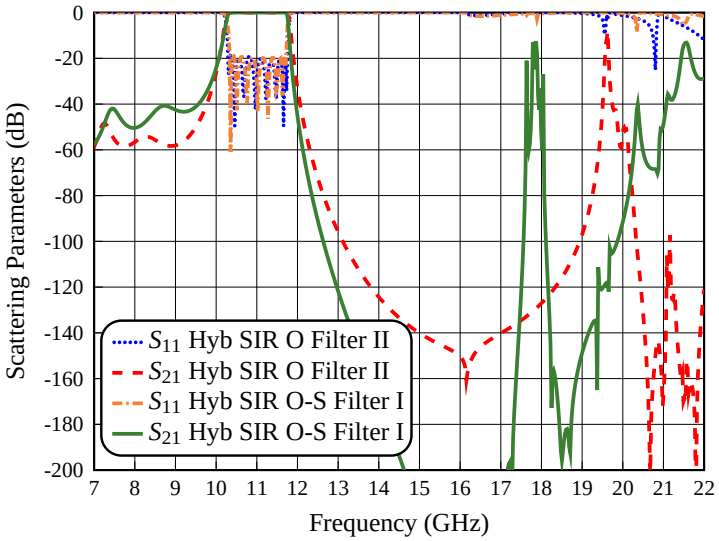

Figure 4.10: Simulated performance of the second hybrid SIR filter with an offset in the position of the capacitive irises (Hyb SIR O Filter II) and the first hybrid SIR filter with an offset in both capacitive irises and SIRs (Hyb SIR O-S Filter I).

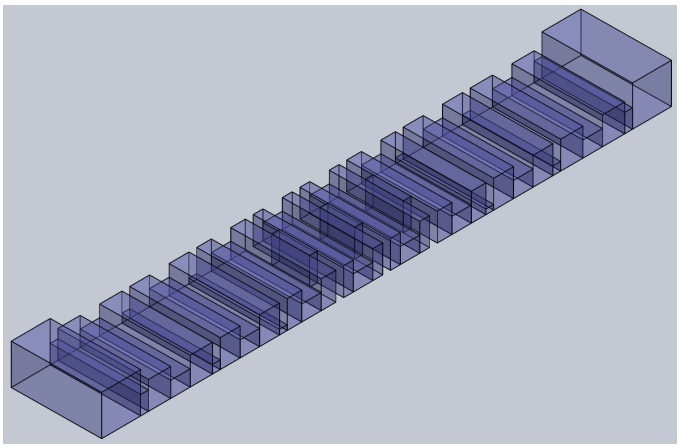

Figure 4.11: Structure of the second hybrid SIR filter with an offset in both capacitive irises and SIRs.

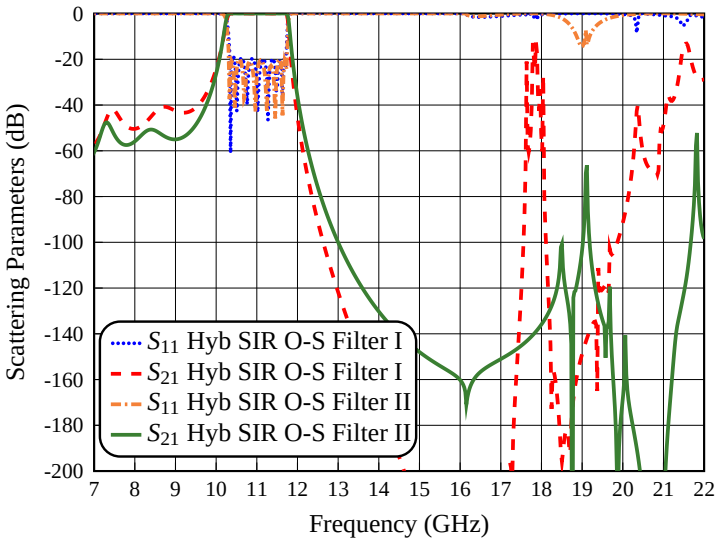

Figure 4.12: Simulated performance of the first hybrid SIR filter with an offset in both capacitive irises and SIRs (Hyb SIR O-S Filter I) and the second hybrid SIR filter with the modifications in the SIRs (Hyb SIR O-S Filter II).

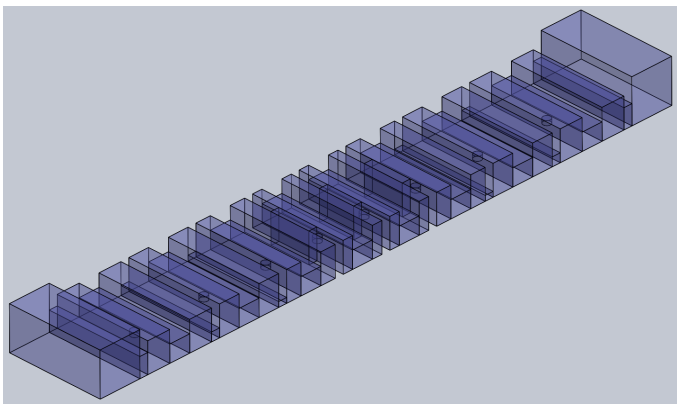

Figure 4.13: Structure of the hybrid SIR filter with an offset in both capacitive irises and SIRs and, at the same time, with tuning screws.

spike reaching -50 dB at 21.70 GHz. Also, this filter exhibits an excellent performance for lower frequencies. Finally, an additional advantage of this structure is that the height of the capacitive irises is higher, and that the complete structure can now be manufactured by conventional milling, without needing the more expensive spark erosion technique.

4.4 Hybrid SIR Filter With Tuning Screws

Another important advantage introduced by the filter structure discussed in the previous section, is that we can now easily introduce tuning screws in the SIRs in an attempt to compensate for manufacturing errors. In Fig. 4.13 we show the final geometry of the hybrid SIR filter with tuning elements of radius $r = 0.9$ mm in the central section of the SIRs. For manufacturing, the structure will be divided into two parts, namely, a body and a cover, with the following features:

- The body of the filter will contain all the irises and SIR sections.
- The cover of the filter will contain only the tuning elements of the SIRs. It is important to mention that, due to the limited height of the coupling irises, it is not possible to use tuning elements in the couplings as well.

Fig. 4.14 shows a comparison of the simulated behavior of the structures in Fig. 4.11 (Hyb SIR O-S Filter II) and Fig. 4.13 (Hyb SIR O-S TS Filter), respectively. As we can see, the introduction of the tuning elements results in a slight increase in the spurious response without deteriorating the overall response of the filter.

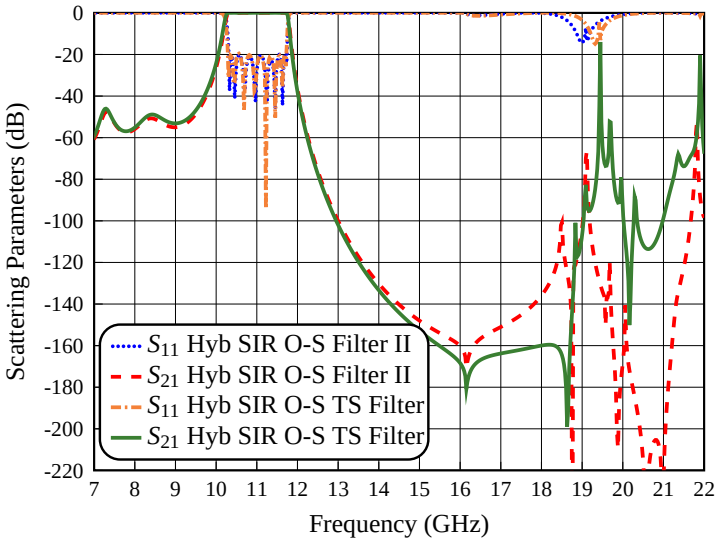

Figure 4.14: Simulated performance of the second hybrid SIR filter with an offset in both capacitive irises and SIRs (Hyb SIR O-S Filter II) and the same filter with screws (Hyb SIR O-S TS Filter).

4.5 HA Design With Body and Cover

The hybrid SIR filter structure with body and cover discussed in Section 4.4, has been designed in FEST3D with a low-accuracy (LA) setting. The next step is therefore to go from the LA structure to the HA structure. To do that, we have followed the same exact procedure described in Section 3.6, namely, the combined use of the procedure described in [101] and the Aggressive Space Mapping (ASM) discussed in [102]. Similarly to what we have done before, the last step has been to include rounded corners with a radius $r = 1.0$ mm in the final HA design.

4.5.1 The Prototype

The final structure that we have obtained is shown in Fig. 4.15. Fig. 4.16 shows a comparison of the simulated behavior of the hybrid SIR filter structure with tuning screws obtained with the commercial tools FEST3D and CST Studio Suite. As we can see, the agreement is very good. Furthermore, the simulations show a very good out-of-band response, with spurious response below -50 dB from 12 to 22 GHz, and with spikes reaching -7.5 and -20 dB at 19.7 and 20 GHz, respectively.

The physical dimensions for the in-line hybrid SIR filter with body and cover are shown in Table 4.1. The dimensions are given up to the center of the filter because the structure is symmetrical. The thickness of the coupling windows is t, and the SIRs have the same width as the input waveguide.

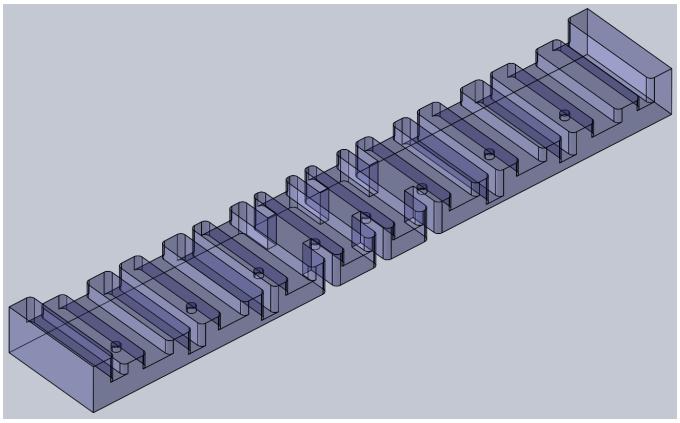

Figure 4.15: Structure of the in-line hybrid SIR filter designed with rounded corners (r =1.0 mm), and tuning screws of radius r =0.9 mm.

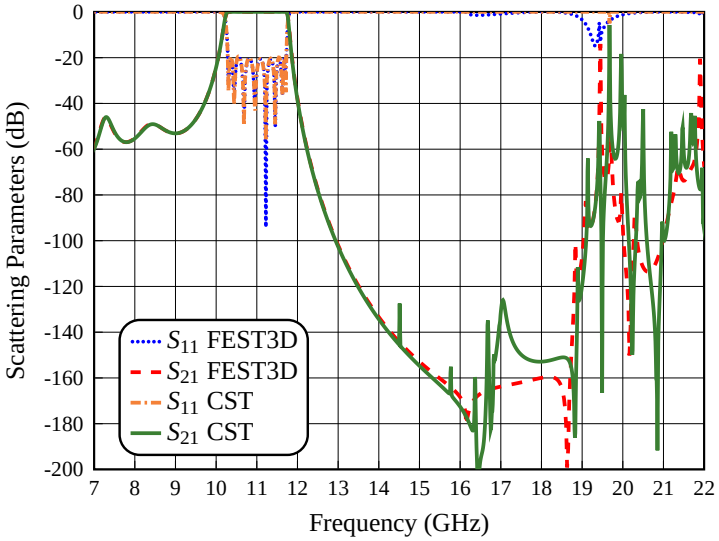

Figure 4.16: Simulated performance of the in-line hybrid SIR filter with tuning screws using both FEST3D and CST software tools.

Table 4.1: Physical dimensions for the hybrid SIR filter with body and cover.

Section Type	Dimensions (mm)
Input Waveguide	$a = 22.86$ $b = 10.16$
Capacitive window 1-6	$a = 22.86$ $h_1 = h_6 = 4.734$ $t = 2$
SIR 1-8	$H_1 = 7.000$ $L_1 = 5.485$ $H_2 = 4.000$ $L_2 = 5.000$
Capacitive window 2-5	$a = 22.86$ $h_2 = h_5 = 2.028$ $t = 2$
SIR 2-7	$H_1 = 7.000$ $L_1 = 4.943$ $H_2 = 4.000$ $L_2 = 5.000$
Capacitive window 3-4	$a = 22.86$ $h_3 = h_4 = 1.199$ $t = 2$
SIR 3-6	$H_1 = 7.000$ $L_1 = 3.624$ $H_2 = 4.000$ $L_2 = 5.000$
Inductive window 1-3	$w_1 = w_3 = 9.541$ $b = 7.000$ $t = 2$
SIR 4-5	$H_1 = 7.000$ $L_1 = 2.382$ $H_2 = 4.000$ $L_2 = 5.000$
Inductive window 2	$w_2 = 8.616$ $b = 7.000$ $t = 2$

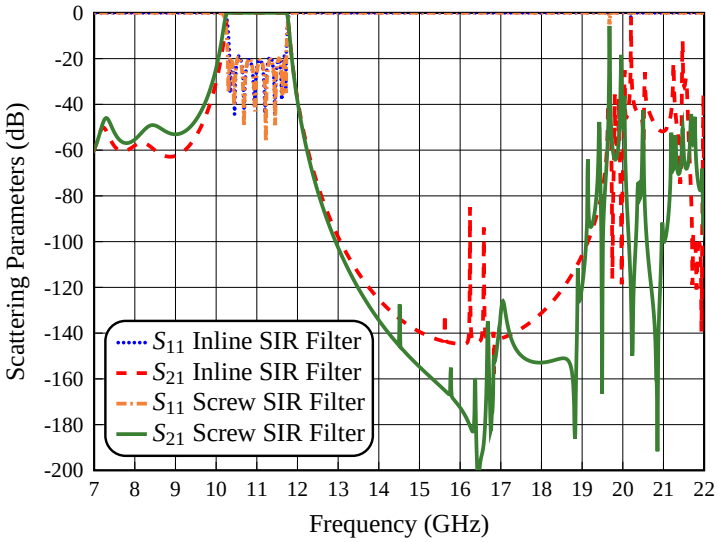

Figure 4.17: Simulated performance of the in-line hybrid SIR filter (Inline SIR Filter), and inline hybrid filter with body and cover (Screw SIR Filter) using CST.

To validate the design of the hybrid SIR filter with tuning elements, we have next compared the performance of the in-line hybrid SIR filter (Inline SIR Filter) discussed in the Chapter 3, with the in-line hybrid SIR filter with body and cover (Screw SIR Filter) discussed in this chapter. Fig. 4.17 shows the comparison of the simulated performances obtained with CST of the two filter structures. As we can see, the out-of-band response of the SIR filter with screws has been significantly improved in comparison with the in-line SIR Filter.

4.5.2 Measurements

The next step has been to manufacture a prototype of the in-line hybrid SIR filter with body and cover. Manufacturing has been done using standard milling, as shown in Fig. 4.18. Fig. 4.19 and Fig. 4.20 show the comparison between measured and simulated in-band and out-of-band responses, respectively.

As we can see in Fig. 4.19, although the measured in-band response is indeed centered at 11 GHz, we can still observe a degradation of the return loss at the edges of the filter. There is also a small shift in the center frequency of the pass-band, even though the filter now has eight tuning elements.

To measure the electrical response in the stopband in a wide frequency range, as shown in Fig. 4.20, we have used the same calibration procedure as for the in-line hybrid SIR filter of the Chapter 3. As we can see in Fig. 4.20, the measured out-of-band response shows a slight disagreement with the simulated results. There are also spikes reaching

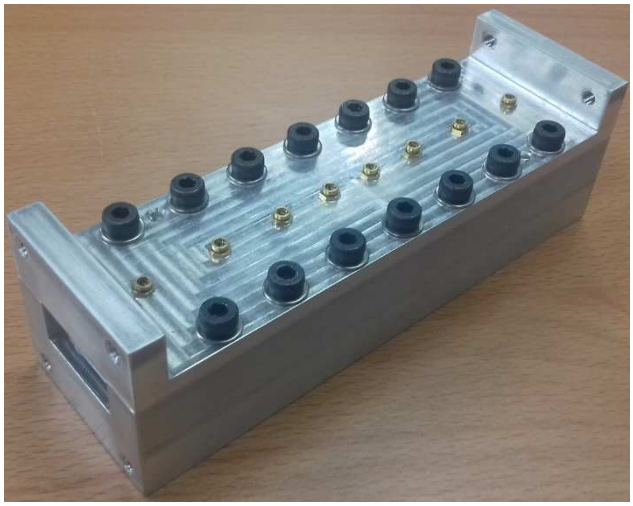

Figure 4.18: Manufactured prototype in aluminum of the in-line hybrid SIR filter with body and cover (no silver plating).

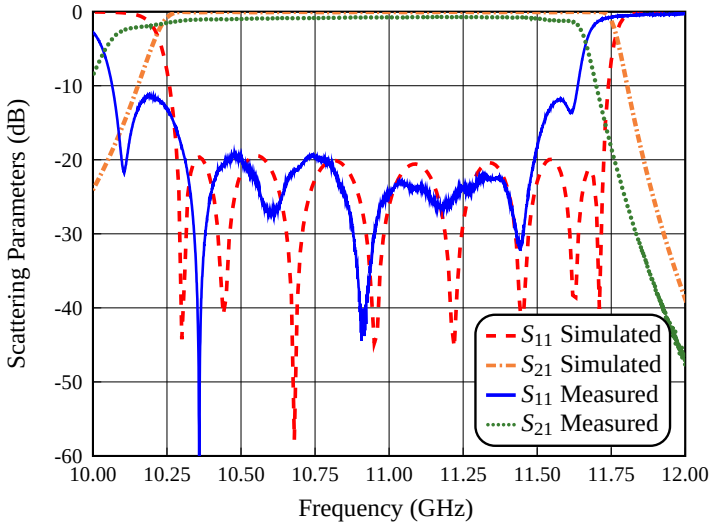

Figure 4.19: Measurement of the in-band performance of the filter with body and cover compared with the EM simulation (CST).

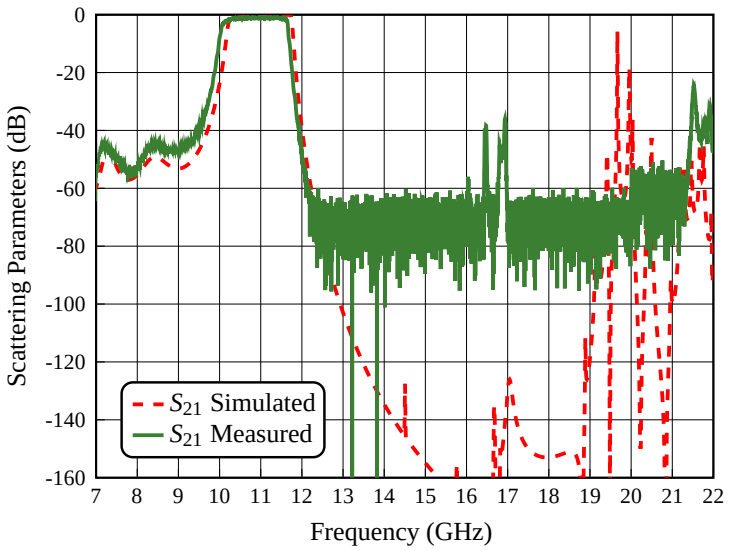

Figure 4.20: Measurement of the out-of-band performance of the filter with body and cover compared with the EM simulation (CST).

-38.5 and -35.7 dB at about 16.5 and 16.75 GHz, and a spurious response below -23.5 dB beginning at about 21.5 GHz. These discrepancies are probably due again to the low manufacturing accuracy.

In conclusion, we can say that we have clearly demonstrated that using tuning elements allows to produce a viable lower cost implementation of the in-line hybrid SIR filters. However, it is important to note that the problems caused by the low manufacturing accuracy cannot be completely eliminated using tuners only in the SIR sections.

4.6 Compact Hybrid SIR Filter Design

In this section, we explore a more compact alternative: a folded structure of the in-line hybrid SIR filter shown in Fig. 3.33. The structure has been folded twice. First, we have folded the central section of the filter, at the location of the second inductive irises (w_2). We have then folded the input and output ports of the filter. The resulting structure is shown in Fig. 4.21.

Fig. 4.22 shows a comparison of the simulated behavior of the structures in Fig. 3.33 (Hyb SIR Ref Filter) and Fig. 4.21 (Fol Hyb SIR Filter I), respectively. As we can see, folding the in-line hybrid SIR structure results in a further improvement of the out-of-band response of the filter, namely, we now have a spurious response below -50 dB from 12 to 22 GHz. This is indeed an important improvement.

Next, we have redesigned the filter in Fig. 4.21 applying an offset in the first and last

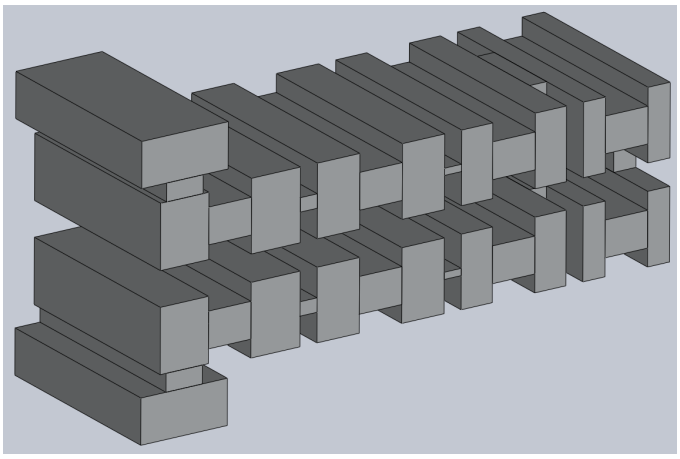

Figure 4.21: Structure of the first E-plane folded hybrid SIR filter.

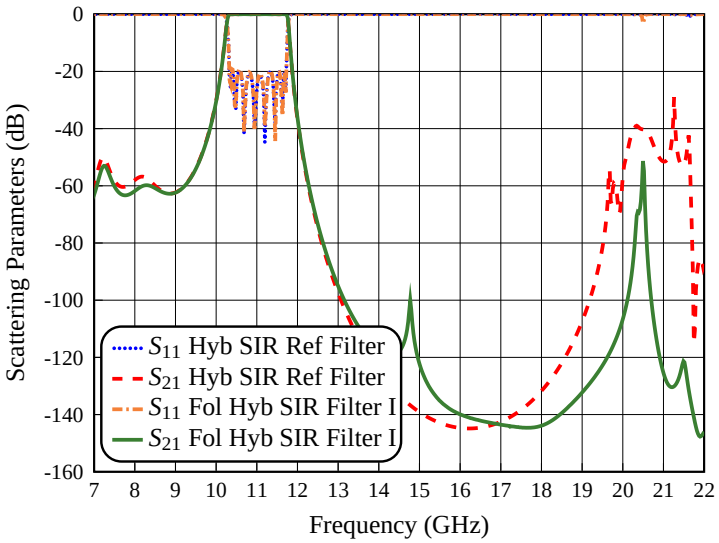

Figure 4.22: Simulated performance of the in-line hybrid SIR filter (Hyb SIR Ref Filter) and the first E-plane folded hybrid SIR filter (Fol Hyb SIR Filter I).

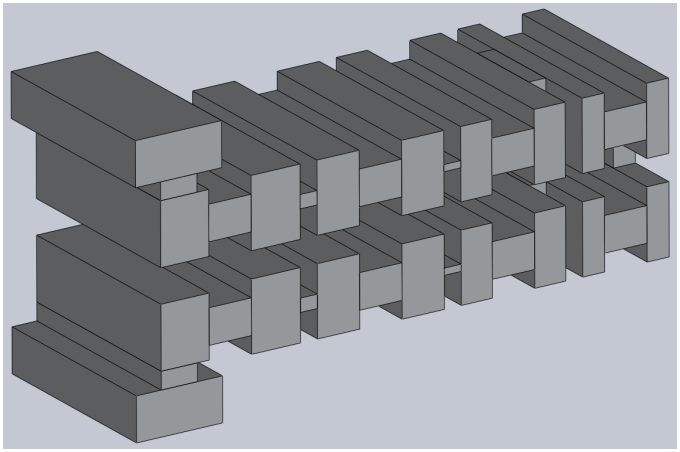

Figure 4.23: Structure of the second E-plane folded hybrid SIR filter.

capacitive irises, in order to facilitate the manufacturing process. The structure obtained is shown in Fig. 4.23. Fig. 4.24 shows a comparison of the simulated behavior of the structures in Fig. 4.21 (Fol Hyb SIR Filter I) and Fig. 4.23 (Fol Hyb SIR Filter II), respectively.

As we can see, applying this change in the structure the level of spurious response is slightly higher. However, we still have a spurious response below -50 dB from 12 to 22 GHz, with a spike reaching -40 dB at 20.25 GHz.

4.6.1 The HA Design

After having completed the LA design, we now need to obtain the HA structure that can be manufactured. As already mentioned, we have used the same procedure described in Section 3.6 (see Chapter 3). The final structure that we have obtained has the following features:

- The central inductive iris (w_2) has a thickness of 3.0 mm in order to avoid mechanical problems.
- We have introduced two more 90° bends in the routing of the structure, with the objective to simplify the connection of the input and output waveguides.
- Finally, we have included in the final structure the effects of rounded corners ($r = 1.0$ mm) in order to reduce the manufacturing cost, as shown in Fig. 4.25.

Fig. 4.26 shows the comparison of the simulated behavior of the E-plane folded hybrid SIR filter obtained with the commercial tools FEST3D and CST Studio Suite, respectively. As we can see, the agreement is very good. The simulations also show a very good out-of-band response, with a rejection of the spurious response up to 20 GHz.

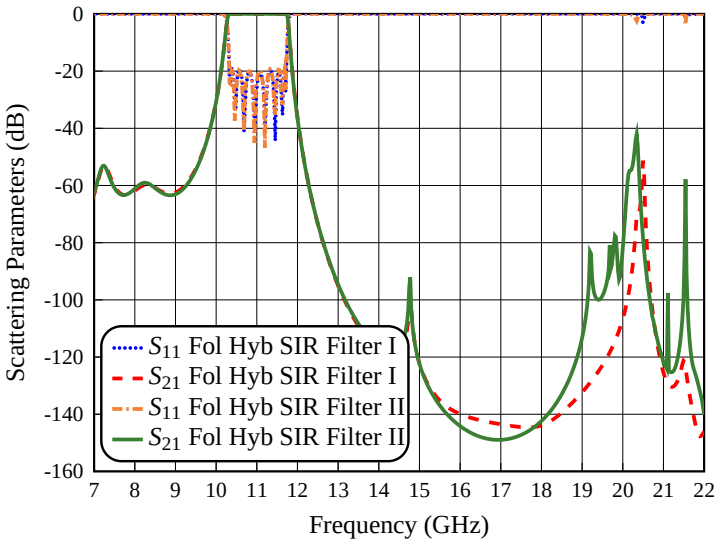

Figure 4.24: Simulated performance of the first E-plane folded hybrid SIR filter (Fol Hyb SIR Filter I) and the second E-plane folded hybrid SIR filter (Fol Hyb SIR Filter II).

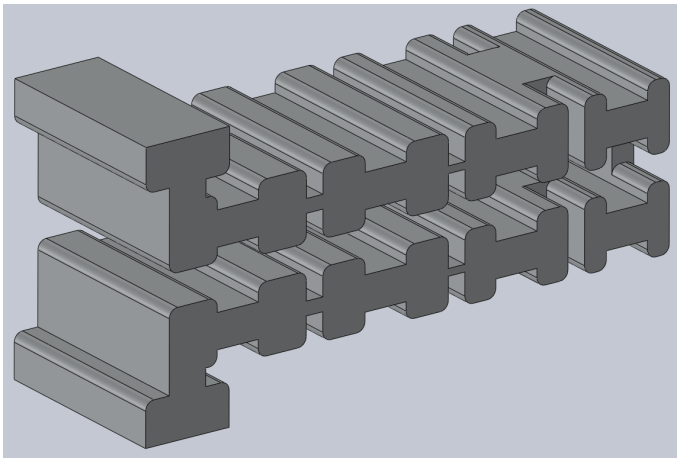

Figure 4.25: Structure of the E-plane folded hybrid SIR filter designed with a radius equal to r =1.0 mm.

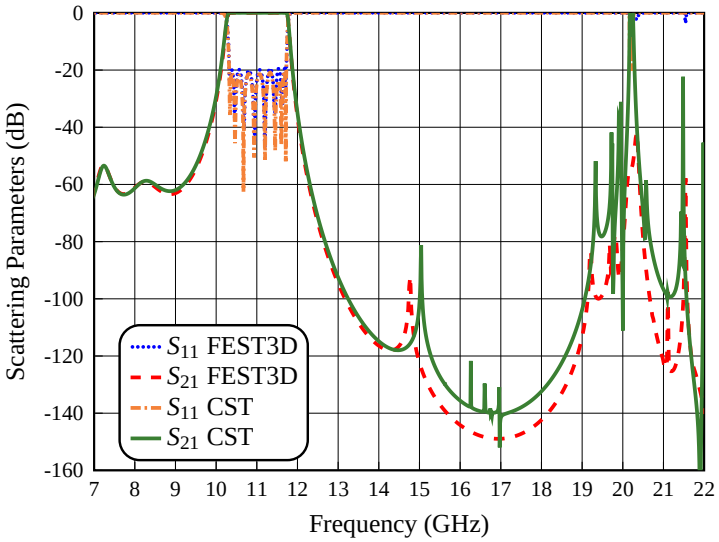

Figure 4.26: Simulated performance of the E-plane folded hybrid SIR filter using FEST3D and CST.

The detailed physical dimensions for the E-plane folded hybrid SIR filter are shown in Table 4.2. The dimensions are given up to the center of the filter because the structure is symmetrical. The thickness of the coupling windows is t, and the SIRs have the same width as the input waveguide.

To conclude this section, we have compared the performance of the in-line hybrid SIR filter (Inline SIR Filter) discussed in Chapter 3, and the E-plane folded hybrid SIR filter (Folded SIR Filter) discussed in this chapter. Fig. 4.27 shows a comparison of the simulated behavior with (CST) of the two structures.

As we can see, the out-of-band response of the Folded SIR Filter shows an important reduction of the spurious response in comparison with the Inline SIR Filter. Furthermore, the footprint of the last structure is substantially smaller.

4.6.2 Measurements

The prototype of the E-plane folded hybrid SIR filter has been manufactured in a clam-shell configuration using a combination of milling and spark erosion, as shown in Fig. 4.28. It is important to mention, at this point, that for this prototype we have used a more accurate manufacturing process, in order to produce a tuning-less device. The manufacturing error has, in fact, been kept below 10 μm for all the curved corners, and below 5 μm for all other filter elements.

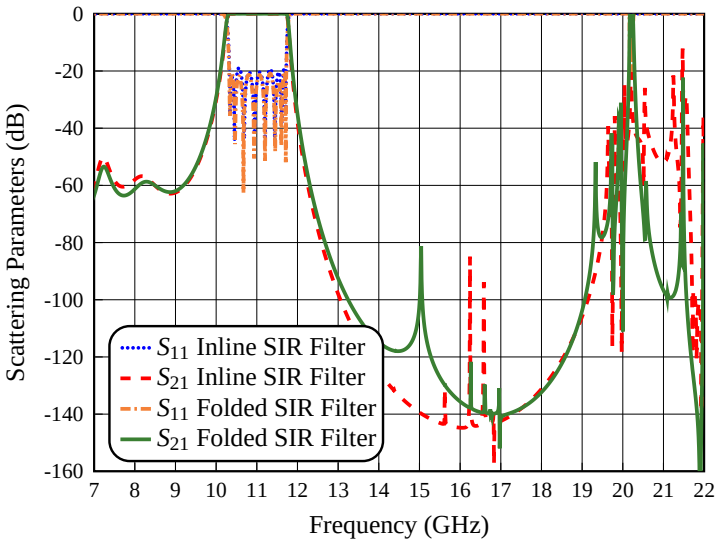

Figure 4.27: Simulated performance of the in-line hybrid SIR filter (Inline SIR Filter), and the E-plane folded hybrid SIR filter (Folded SIR Filter) using CST.

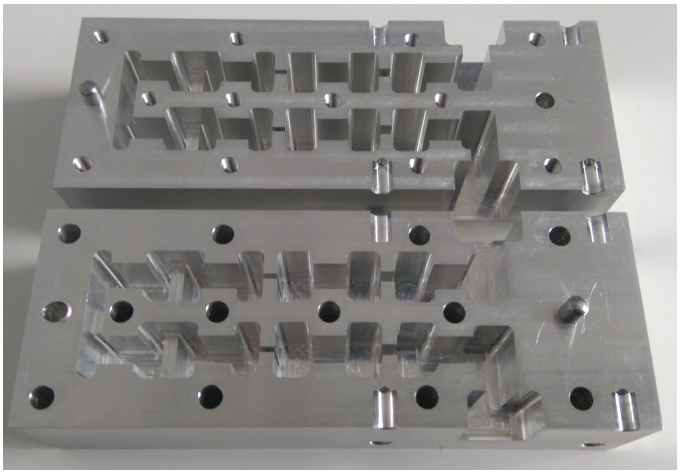

Figure 4.28: Manufactured prototype in aluminum of the E-plane folded hybrid SIR filter (no silver plating).

Table 4.2: Physical dimensions for the E-plane folded hybrid SIR filter.

Section Type	Dimensions (mm)
Input Waveguide	$a = 22.86$ $b = 10.16$
Capacitive window 1-6	$a = 22.86$ $h_1 = h_6 = 4.445$ $t = 2$
SIR 1-8	$H_1 = 7.271$ $L_1 = 5.828$ $H_2 = 4.000$ $L_2 = 5.000$ $H_1 = 8.000$ $L_1 = 5.834$
Capacitive window 2-5	$a = 22.86$ $h_2 = h_5 = 1.591$ $t = 2$
SIR 2-7	$H_1 = 8.000$ $L_1 = 5.138$ $H_2 = 4.000$ $L_2 = 5.000$
Capacitive window 3-4	$a = 22.86$ $h_3 = h_4 = 0.830$ $t = 2$
SIR 3-6	$H_1 = 8.000$ $L_1 = 3.771$ $H_2 = 4.000$ $L_2 = 5.000$
Inductive window 1-3	$w_1 = w_3 = 9.617$ $b = 8.000$ $t = 2$
SIR 4-5	$H_1 = 8.000$ $L_1 = 2.657$ $H_2 = 4.000$ $L_2 = 5.000$
Inductive window 2	$w_2 = 10.442$ $b = 2.657$ $t = 3$

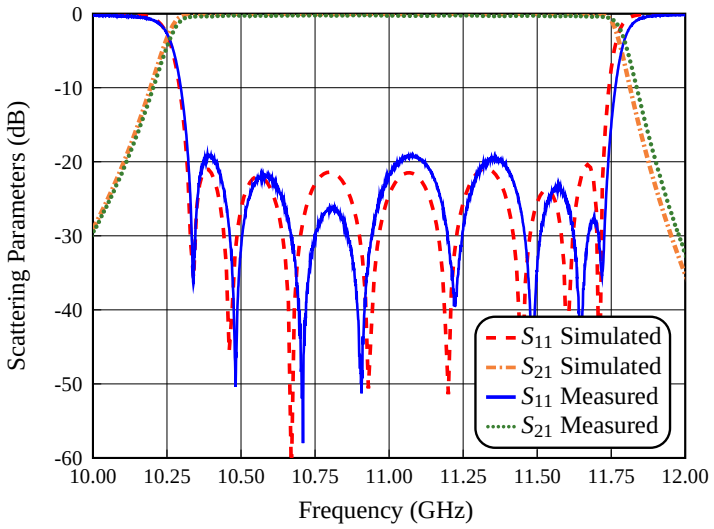

Figure 4.29: Measurement and simulated results (with CST) of the in-band performance of the E-plane folded hybrid SIR filter.

Fig. 4.29 and Fig. 4.30 show the comparison between measured and simulated in-band and out-of-band responses, respectively. As we can see in Fig. 4.29, the measured in-band response is indeed centered at 11 GHz. In addition, the agreement with the simulation is now excellent. We can clearly see the 8 reflection zeros of the filter, and the return loss (RL) level is also very close to the simulations.

The next measurement is the electrical response in the stopband, as shown in Fig. 4.30. This measurement has been obtained using the same calibration procedure of the in-line hybrid SIR filter discussed in Chapter 3. As we can see in Fig. 4.30, the out-of-band response shows a good agreement between simulation and measurements. However, we can see a spike reaching -45 dB at about 16.76 GHz.

In conclusion, we have clearly demonstrated that folding the structure results in an excellent filter performance and, at the same time, a greatly reduced footprint. Furthermore, the effects of the increased quality of the manufacturing process are clearly evident, even though the effects of errors can not be completely eliminated.

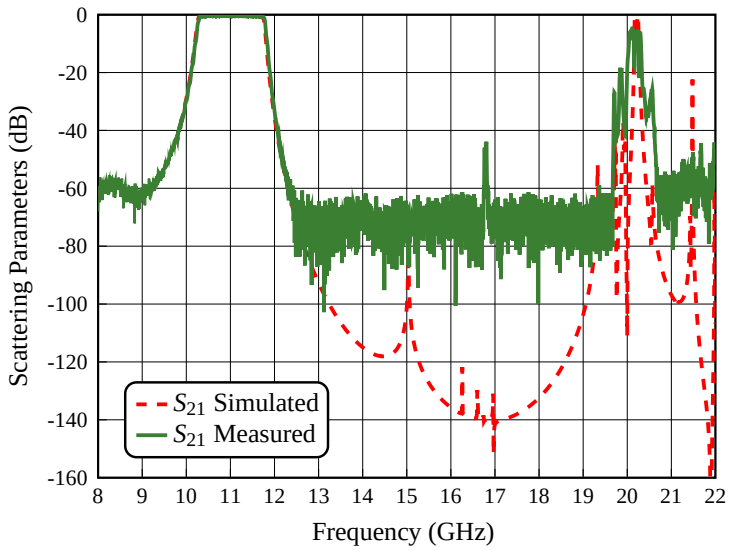

Figure 4.30: Measurement and simulated results (with CST) of the out-of-band performance of the E-plane folded hybrid SIR filter with the EM simulation (CST).

Table 4.3: Tolerance analysis of the structures that we have fabricated.

Filter Type	Yield of the Structures				
Tolerance	5 μm	10 μm	15 μm	25 μm	40 μm
In-line Screw Hybrid SIR Filter	84 %	43 %	10 %	2 %	1 %
E-plane Folded Hybrid SIR Filter	52 %	11 %	4 %	1 %	1 %

4.7 Tolerance Analysis

To complete the design of this last filter, we will discuss in this section the yield analysis for all the filters designed and manufactured in this chapter. For this purpose, we have repeated the same yield analysis discussed in Chapter 3, using the relevant specifications. Table 4.3 shows the summary of the results obtained.

The tolerance analysis results for the hybrid SIR filter with body and cover with tuning elements (Inline Screw Hybrid SIR filter) is shown in Fig. 4.31. As we can see in Table 4.3, it is possible to obtain an acceptable response of the structure with manufacturing errors below $\pm$ 25 μm, once the tuning elements are properly adjusted.

The degradation of the in-band performance that we have measured (see Fig. 4.19) is, therefore, due to the sensitivity in the dimensions of the capacitive irises that could not be tuned. This is indeed why the in-band response can not be recovered using tuning elements in the resonators only.

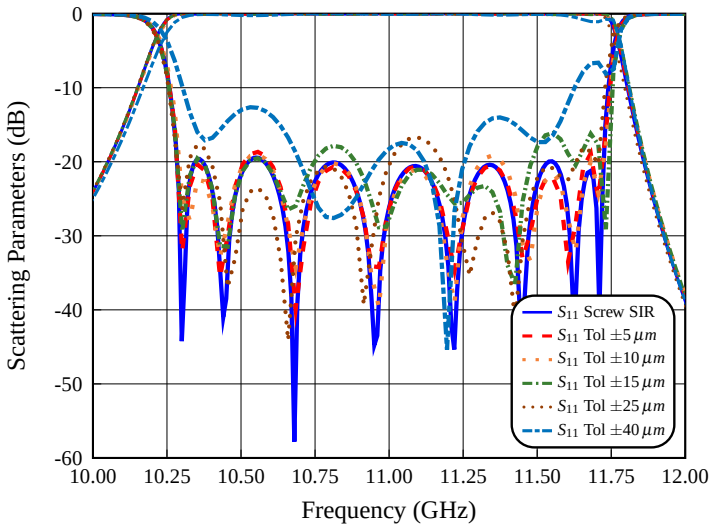

Figure 4.31: Tolerance analysis of the in-line hybrid SIR filter with body and cover.

The tolerance analysis of the E-plane folded hybrid SIR filter is shown in Fig. 4.32. As we can see from Table 4.3, with manufacturing errors less than 10 μm, the in-band response of the filter should show good agreement with respect to the simulations. This is, in fact, confirmed by our measured results.

4.8 High Power Analysis

Similarly to what we have done for the in-line hybrid SIR filter in Chapter 3, we now show the results of the high power analysis for all the filters structures designed in this chapter. To do that, we have repeated the same procedure used in Chapter 3. Again, we have focused the high power analysis on the central section of the in-line hybrid SIR filter (due to the small dimensions of the irises, namely h_3, w_1 and w_2, and of the SIR3 and SIR4 central sections, i.e. H_2). We have also used FEST3D for computing the EM fields, and SPARK3D for the multipactor analysis (with the same values of all involved parameters given in Section 3.8). Tables 4.4 and 4.5 show the power thresholds that we have obtained for the in-line hybrid SIR filter with tuning screws and the E-plane folded hybrid SIR filter, respectively.

As expected, the capacitive window (h_3) for both the in-line hybrid SIR filter with tuning screws, and the E-plane folded hybrid SIR filter shows the lowest power threshold at 11.75 GHz with 403 and 145 W, respectively. Finally, in Figs. 4.33 and 4.34 we show the values obtained for each simulation in the capacitive window for the in-line hybrid SIR filter with tuning screws, and the E-plane folded hybrid SIR filter, respectively.

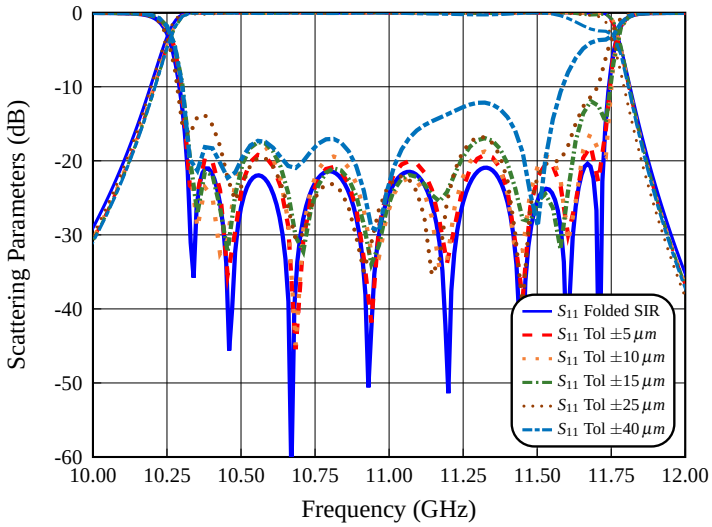

Figure 4.32: Tolerance analysis of the E-plane folded hybrid SIR filter.

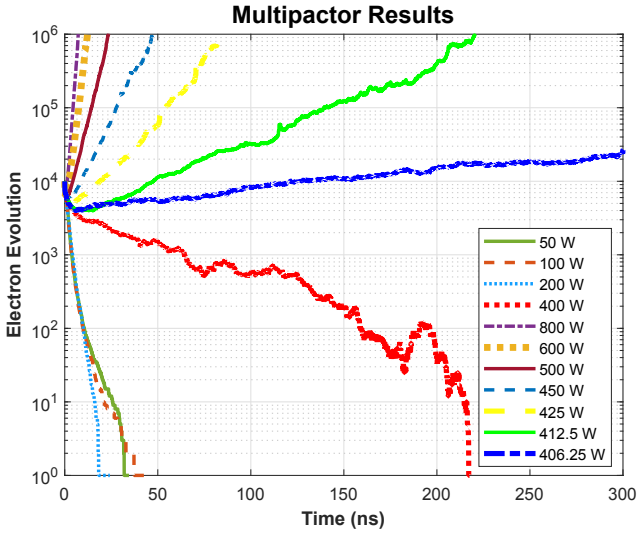

Figure 4.33: Multipactor results (electron evolution) for the capacitive window of height h_3 at 11.75 GHz of the in-line hybrid SIR filter with tuning screws.

Table 4.4: High power analysis of the in-line hybrid SIR filter with tuning screws.

Structure	Power of the structure		
Frequency	$f_1 = 10.27$ GHz	$f_2 = 11.00$ GHz	$f_3 = 11.75$ GHz
h_3	2524 W	2296 W	403 W
$w_1 = w_3$	192 kW	> 1 MW	393.6 kW
w_2	80 kW	480 kW	637.8 kW
SIR 3	2774 W	10099 W	2224 W
SIR 4	1737 W	6849 W	2037 W

Table 4.5: High power analysis of the E-plane folded hybrid SIR filter.

Structure	Power of the structure		
Frequency	$f_1 = 10.30$ GHz	$f_2 = 11.00$ GHz	$f_3 = 11.75$ GHz
h_3	993 W	893 W	145 W
$w_1 = w_3$	> 1 MW	> 1 MW	> 1 MW
w_2	1112 W	7049 W	43598 W
SIR 3	1487 W	6149 W	1412 W
SIR 4	918 W	3624 W	1162 W

We can conclude this chapter confirming that the structures that we have discussed do need further development in order to increase the multipaction power threshold. As in the in-line hybrid SIR filter of Chapter 3, a possible solution could be to add one more pair of inductive irises to replace the smallest capacitive irises.

4.9 Higher Order Modes Analysis

In this section, we will discuss the results of the study of the effects of the higher order modes. Based on the results obtained for the in-line hybrid SIR filter in Section 3.9, we have considered only the TE_{20} and TE_{30} higher order modes.

Fig. 4.35 and Fig. 4.36 show the comparison of the simulated performances of the in-line hybrid SIR filter with body and cover excited with the TE_{20} and TE_{30} modes, obtained with FEST3D and CST. As we can see in Fig. 4.35 and Fig. 4.36, the higher order TE_{20} mode shows a spurious response below -30 dB from 13 to 22 GHz, with a spike reaching -17.5 dB at 16.75 GHz. In addition, the TE_{30} mode shows a spurious response beginning at about 19.70 GHz.

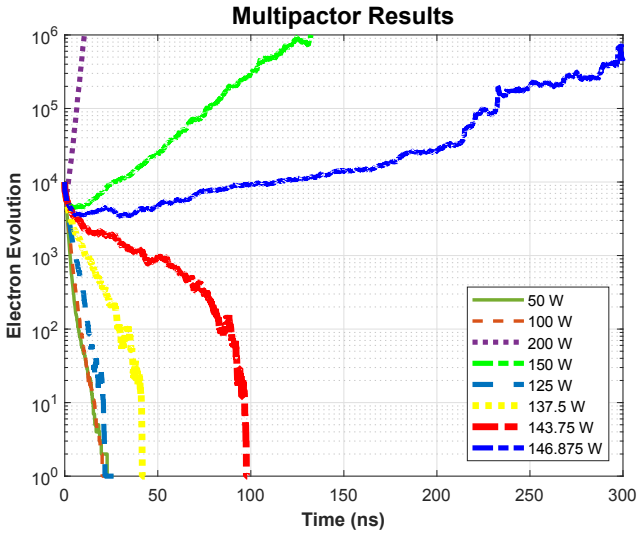

Figure 4.34: Multipactor results (electron evolution) for the capacitive window of height h_3 at 11.75 GHz of the E-plane folded hybrid SIR filter.

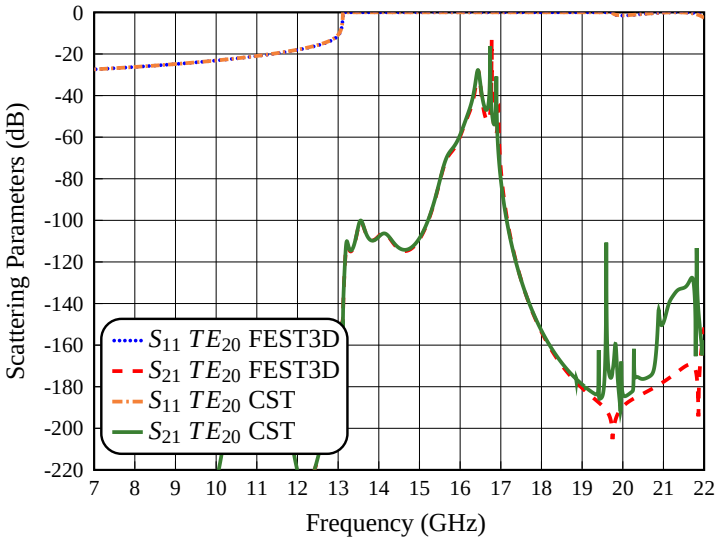

Figure 4.35: Simulated performance of the in-line hybrid SIR filter with body and cover for the higher order mode TE_{20} using FEST3D and CST.

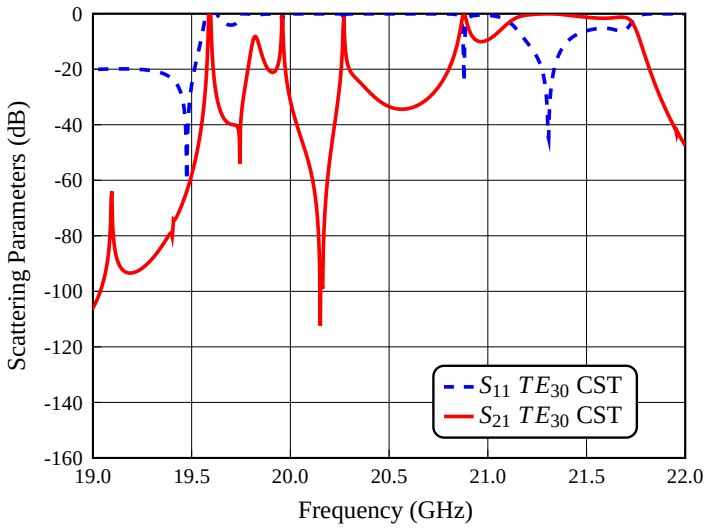

Figure 4.36: Simulated performance of the in-line hybrid SIR filter with body and cover for the higher order mode TE_{30} using CST.

It is important to mention that the in-line hybrid SIR filter with body and cover has been manufactured with errors above 40 μm. Although the higher order modes may indeed be excited by the errors in the manufacturing process, the out-of-band performance of the filter is in general very good, as we can see in the results of Fig. 4.20.

Next, Fig. 4.37 and Fig. 4.38 show the comparison of the simulated performances of the E-plane folded hybrid SIR filter excited with the higher order TE_{20} and TE_{30} modes obtained with FEST3D and CST, respectively. As we can see in Fig. 4.37 and Fig. 4.38, the TE_{20} mode shows a spurious response below -50 dB from 13 to 22 GHz, with a spike reaching -17.5 dB at 16.70 GHz. In addition, the TE_{30} mode shows an acceptable response up to 19.7 GHz.

Since the E-plane folded hybrid SIR filter has been manufactured with errors below 10 μm, the excitation of higher order modes will be weak. Even if the higher order modes were indeed excited, their presence does not result in a degradation of the out-of-band performance of the filter, as we can see in the results of Fig. 4.30.

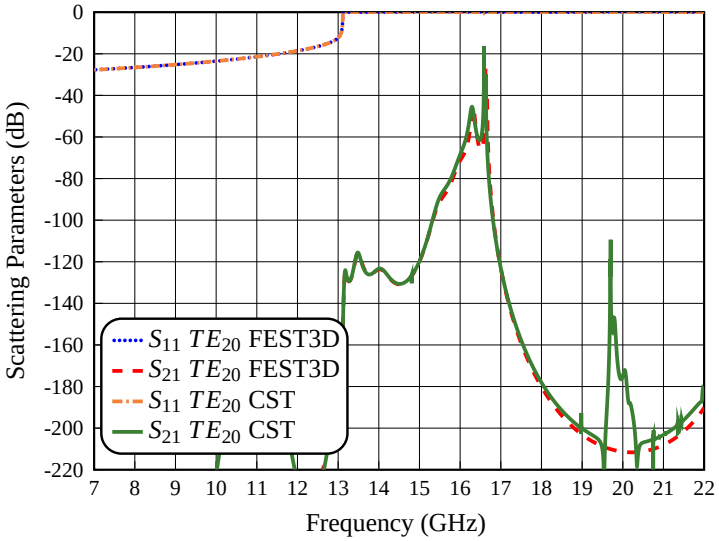

Figure 4.37: Simulated performance of the E-plane folded hybrid SIR filter for the higher order mode TE_{20} using FEST3D and CST.

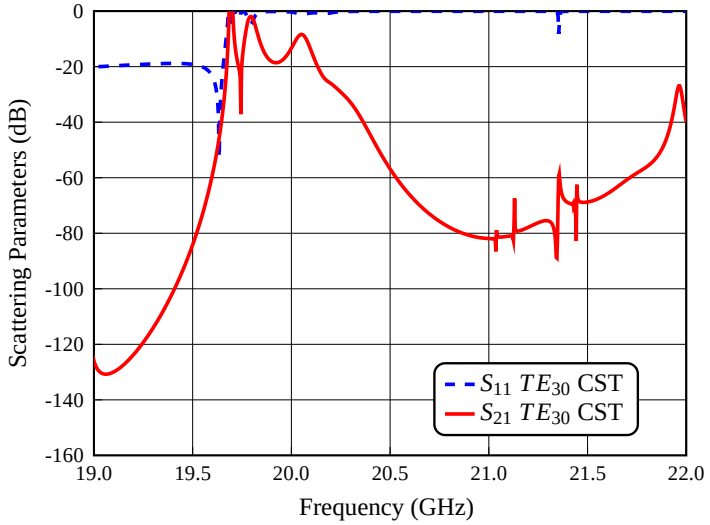

Figure 4.38: Simulated performance of the E-plane folded hybrid SIR filter for the higher order mode TE_{30} using CST.

4.10 Conclusions

In this chapter we have discussed the design of two novel wideband hybrid SIR filters in rectangular waveguide based on H-plane (body and cover design) and E-plane (clam-shell design) configurations. Furthermore, we have shown that using these alternative structures, it is indeed possible to significantly simplify the manufacturing process and obtain, at the same time, more compact structures with a very wide spurious-free out-of-band response.

In addition to the theory, we have also shown experimental results for the two prototypes proposed. The difference between the simulation and measurement of the first prototype has been shown to be due to the manufacturing errors. This is further confirmed by the excellent agreement between simulations and measurements of the second prototype, where the manufacturing technique used is more accurate.

Furthermore, we have also carried out the tolerance and high power analysis for the two new filter prototypes proposed.

Finally, we have also performed a study aimed at identifying the effects of the presence of higher order modes in the excitation of these filters. The results obtained clearly show that there is no degradation in the out-of-band response of the filters due to higher order modes excitation.

Chapter 5

Hybrid Wideband Staircase Filters in Rectangular Waveguide

In this chapter, we describe the design of a new family of hybrid wide-band filters in rectangular waveguide based on a staircase configuration. In addition, we also discuss the use of a number of techniques to enhance the out-of-band response and the selectivity, and attenuate or reduce the effects of higher order modes in the performance of the filter. In the following sections, we first describe the design procedure, then we discuss the results obtained from the measurement of several prototypes.

The results of our investigation in wideband hybrid waveguide filters based on a staircase configuration have produced the following publications:

- J. Valencia, M. Guglielmi, S. Cogollos and V.E. Boria, "Enhancing the out-of-band response of hybrid wide-band filters in rectangular waveguide", in *2020 50th European Microwave Conference (EuMC)*, Jan. 2021, pp. 747-750.
- J.F Valencia Sullca, M. Guglielmi, S. Cogollos and V.E. Boria, "Hybrid wideband staircase filters in rectangular waveguide with enhanced out-of-band response", in IEEE Transactions on Microwave Theory and Techniques, vol. 69, no. 8, pp. 3783-3796, Aug. 2021.

The objective of the work described in this chapter is to propose novel structures for wide-band filters in rectangular waveguide, that can overcome the limitations of the filters described in the previous chapters, namely:

- The use of SIRs requires a rather complex design procedure.

- The filters exhibit a relatively poor selectivity near the pass-band.
- All filters have significant high power limitations.
- The use of spark erosion in some of the structures results into a more expensive manufacturing process.

In this context, therefore, the new staircase configuration that we propose has the following advantages:

- The filter structures are simpler and more compact.
- They use simple E-plane T-junctions and manifold connections to enhance the filter selectivity.
- In addition, several solutions are also proposed to substantially reduce the effects of the presence of higher order modes in the structure.

5.1 Hybrid Wideband Filter Specifications

All microwave filter designs normally start with a set of requirements that must be satisfied. In the context of this chapter we will use the same specifications that we have already used in Chapters 3 and 4. This is done to compare the performance of the new filter structure of this chapter with the ones described in the previous chapters.

As in all previous filter designs, our objective is to satisfy the pass-band requirements, to extend as much as possible the spurious-free frequency range above the pass-band, and, at the same time, to improve the selectivity near the pass-band.

5.2 Hybrid Staircase Filters

In this section, we describe a new class of rectangular waveguide filters with an inherent harmonic rejection capability. This feature is obtained connecting resonators to each other in a way that prevents coupling of the higher order resonances.

A similar approach has been recently demonstrated for narrow-band filters coupled with inductive apertures [5]. In this chapter, we will use instead capacitive couplings in order to obtain wideband filter structures. This change has two important consequences, namely:

1. The first is that capacitive irises can provide substantially higher values of coupling, even for relatively small values of aperture height b.
2. The second advantage is that using capacitive inter-resonator couplings, a substantially stronger decoupling of the higher order resonances can be easily obtained as compared to inductive couplings.

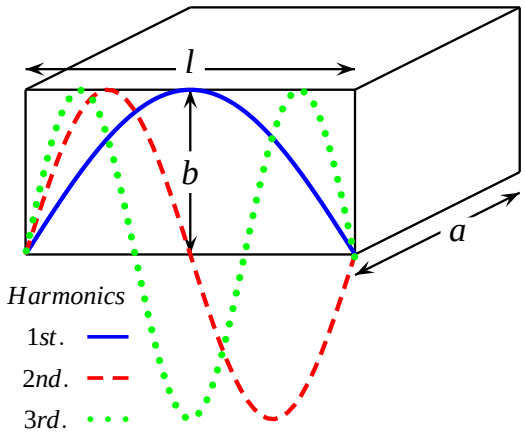

Figure 5.1: The resonant modes of a rectangular waveguide cavity.

5.2.1 Basic Staircase

We begin our study of the basic staircase configuration by examining the electric field distribution of the first three resonant modes along the length l of a rectangular waveguide cavity of width a, height b, as shown in Fig. 5.1.

The higher order resonances shown in Fig. 5.1, have alternating maximum and zero intensity values (of electric and magnetic fields) along the length l of the resonator. It is important to recall in this context, that a capacitive coupling needs to have a difference of potential across the aperture in order to transfer energy to the next resonator. As a consequence, if we locate the capacitive apertures on the bottom (or top) wall of the resonators in a location where the higher order mode that we want to suppress has a maximum (of electric filed), we will strongly reduce the transfer of energy of that mode to the next resonator, because the aperture in question is in a location where the difference of potential is close to zero.

5.2.2 Inductive Staircase Filters

To better illustrate this concept, we look first at a resonator with inductive couplings in the front and end walls, as shown in Fig. 5.2. Next, we show the geometry of a resonator with inductive couplings that takes advantage of the staircase configuration, as shown in Fig. 5.3. In this case, the inductive input and output coupling irises are opened in the center of two resonator walls that are at an angle of ninety degrees with respect to each other. With this arrangement, the second resonance of the rectangular waveguide resonator has a zero (of magnetic field) in the center of the longitudinal direction (see

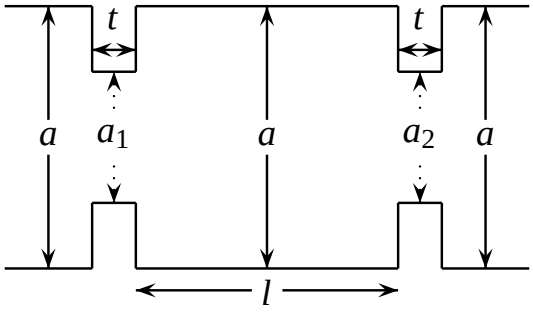

Figure 5.2: Geometry of a resonator coupled with inductive couplings in the front and end walls (top view).

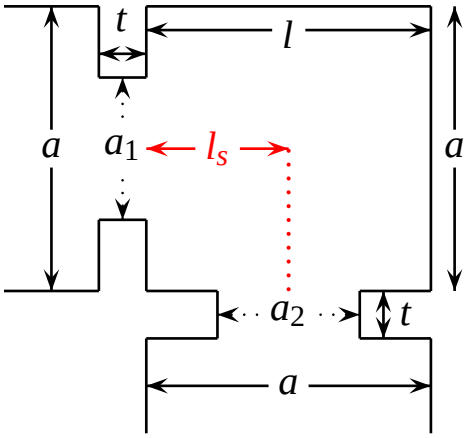

Figure 5.3: Geometry of a staircase resonator with inductive couplings (top view).

Fig. 5.1). As a consequence, if we couple the second resonator with a window centered in the lateral wall of the first resonator ($l_s = l/2$), we will eliminate (or strongly reduce) the coupling to this second resonance.

To continue, we design next a four-pole inductive filter (our reference). The center frequency is 11 GHz, and the bandwidth 300 MHz (narrow-band). The filter has been implemented in a WR-90 (a =22.86 mm and b =10.86 mm) rectangular waveguide.

Fig. 5.4 shows the structure of this filter (4-P Ind Ref Filter). Next, we have designed the same filter using the staircase concept (4-P Ind Stair Filter I). All inductive irises are now located in the center of walls that are at ninety degrees from each other, as we can see in Fig. 5.5.

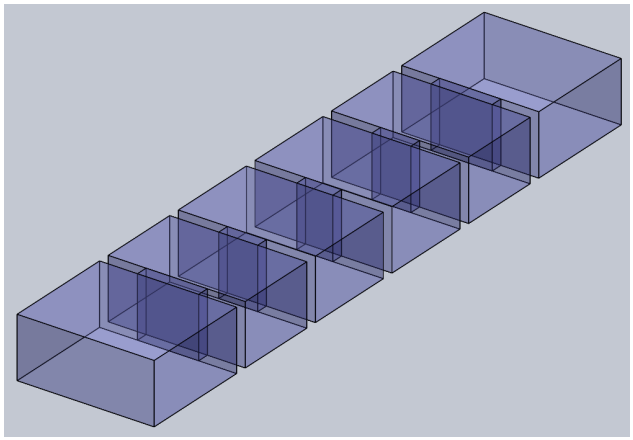

Figure 5.4: Structure of the four-pole inductive filter with $BW = 300$ MHz.

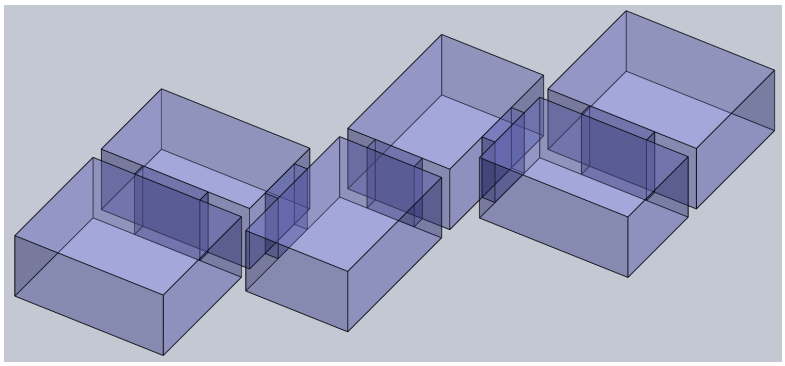

Figure 5.5: Structure of the four-pole inductive staircase filter with $BW = 300$ MHz.

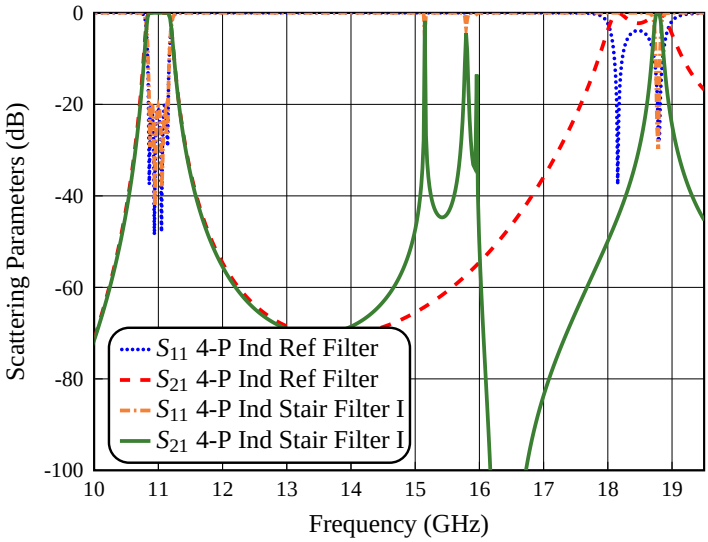

Figure 5.6: Simulated performance of the four-pole inductive reference filter (4-P Ind Ref Filter) and four-pole inductive staircase filter (4-P Ind Stair Filter I) with $BW = 300$ MHz.

Fig. 5.6 shows a comparison of the simulated behavior of the structures in Fig. 5.4 (4-P Ind Ref Filter) and Fig. 5.5 (4-P Ind Stair Filter I), respectively. The performances shown in Fig. 5.6 have been obtained with the commercial tool FEST3D (v.2021 by AuroraSAT, now with Dassault Systèmes).

As we can see, the 4-P Ind Ref Filter has a spurious (harmonic) response at about 18.5 GHz, which is due to the second resonance (TE_{102}). By contrast, the 4-P Ind Stair Filter I shows a substantial reduction of the second harmonic.

To improve the response of the inductive staircase filter, we will implement some changes in the structure of the filter. We change first the width of the resonator, as shown in Fig. 5.7. Fig. 5.8 shows the comparison of the simulated behavior of the structures in Fig. 5.5 (4-P Ind Stair Filter I) and Fig. 5.7 (4-P Ind Stair Filter II), respectively.

As we can see, the 4-P Ind Stair Filter II shows an important attenuation and reduction of the second harmonic, namely, below -40 dB from 15.0 to 19.5 GHz, with a spike reaching about -30 dB at 15.5 GHz.

A further improvement of the out-of-band response of the staircase filter is achieved by applying an offset in the central inductive coupling of the filter, as shown in Fig. 5.9. Fig. 5.10 shows the comparison of the simulated behavior of the structures in Fig. 5.4 (4-P Ind Ref Filter) and Fig. 5.9 (4-P Ind Stair Filter III), respectively.

As we can see, the 4-P Ind Stair Filter III shows an important attenuation and reduction of the second harmonic, namely, below -40 dB from 15.0 to 19.5 GHz. We can

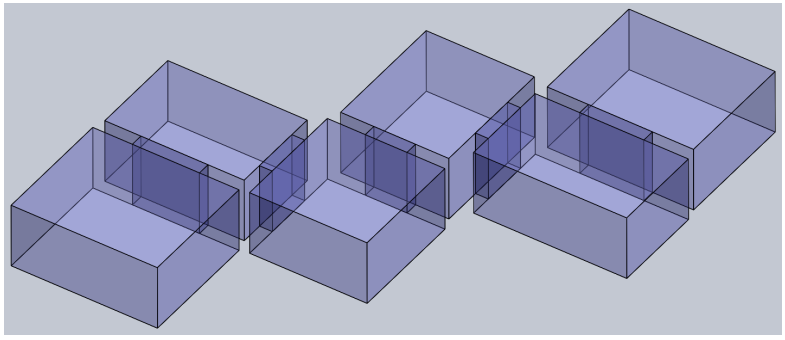

Figure 5.7: Structure of the four-pole inductive staircase filter, changing the width of the resonators, with $BW = 300$ MHz.

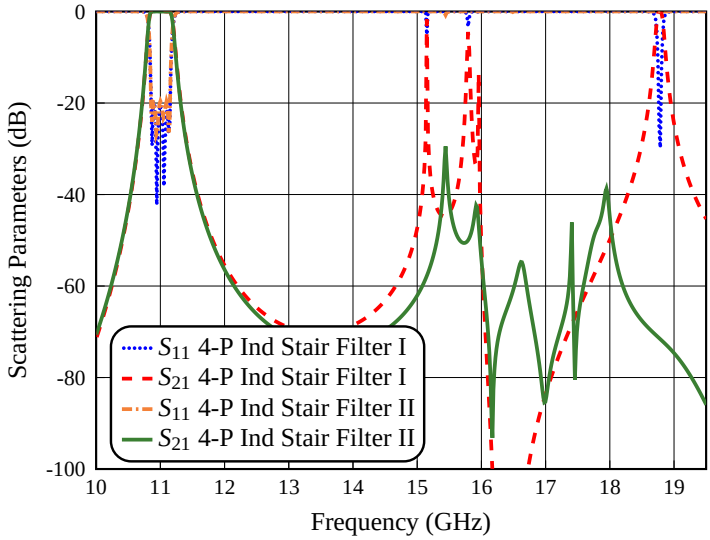

Figure 5.8: Simulated performance of the four-pole inductive staircase filter (4-P Ind Stair Filter I) and four-pole inductive staircase filter, changing the width of the resonators (4-P Ind Stair Filter II), with $BW = 300$ MHz.

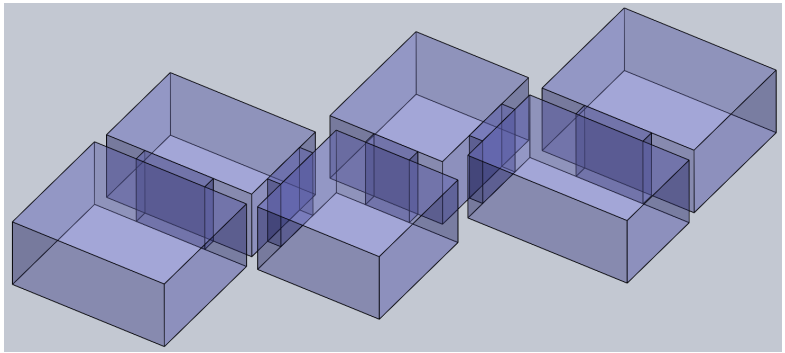

Figure 5.9: Structure of the four-pole inductive staircase filter, changing the width of the resonators and applying an offset in the central inductive coupling, with $BW = 300$ MHz.

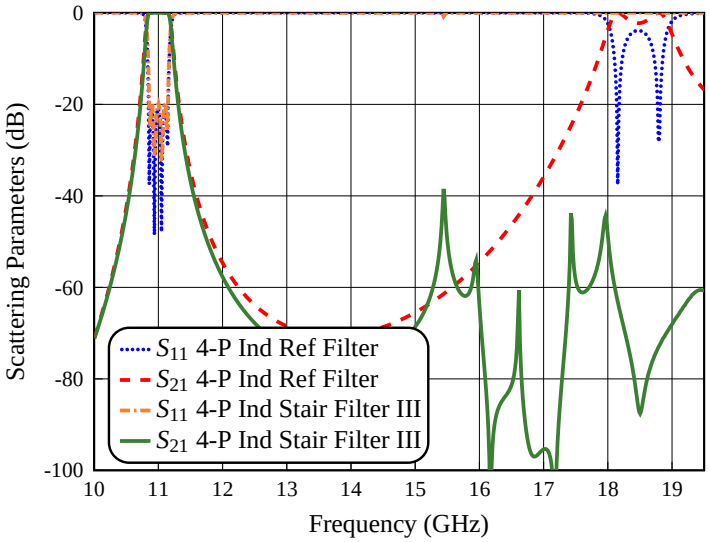

Figure 5.10: Simulated performance of the four-pole inductive reference filter (4-P Ind Ref Filter) and the four-pole inductive staircase filter changing the width of the resonators and applying an offset in the central inductive coupling (4-P Ind Stair Filter III), with $BW = 300$ MHz.

therefore conclude that the staircase configuration in inductive filters, originally proposed in [5], does provide an important attenuation of the spurious response in narrow-band filters.

To verify the validity of the same concept for inductive filters of higher bandwidth and order, we now increase the bandwidth and order of the inductive filter to $BW = 720$ MHz ($\mathcal{W}_\lambda = 10$ %), and order eight, respectively.

Fig. 5.11 shows the structure of a standard eight-pole inductive filter (8-P Ind Ref Filter). To continue, we show in Fig. 5.12 the staircase version of the same filter (8-P Ind Stair Filter I). Fig. 5.13 shows the comparison of the simulated behavior of the structures in Fig. 5.11 (8-P Ind Ref Filter) and Fig. 5.12 (8-P Ind Stair Filter), respectively.

As we can see, the 8-P Ind Ref Filter has a spurious (harmonic) response at about 18.25 GHz, which is due to the second resonance (TE_{102}). By contrast, the 8-P Ind Stair Filter shows a substantial reduction of the second harmonic. However, additional spurious responses appear near the pass-band, seriously deteriorating the out-of-band response.

Next, we explore the effect of the staircase configuration for wider bandwidths, namely, $BW = 1410$ MHz ($\mathcal{W}_\lambda = 20$ %). Fig. 5.14 and Fig. 5.15 show the structures of an in-line eight-pole inductive filter (8-P Ind Ref BW Filter) and of an eight-pole inductive staircase filter (8-P Ind Stair BW Filter), respectively.

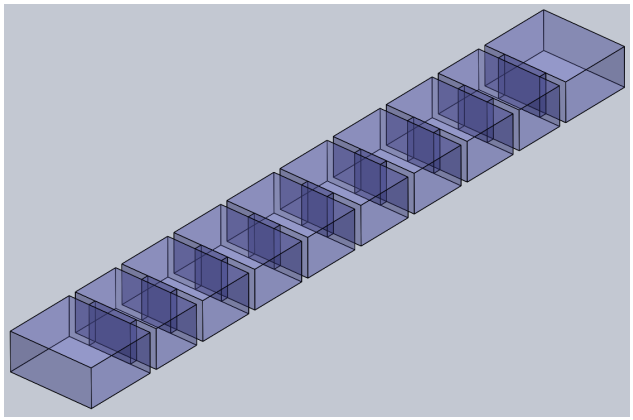

Figure 5.11: Structure of the eight-pole inductive filter with $BW = 720$ MHz.

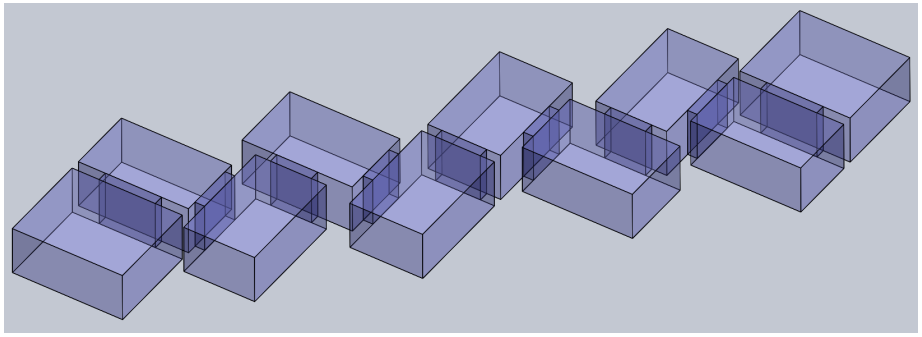

Figure 5.12: Structure of the eight-pole inductive staircase filter with $BW = 720$ MHz.

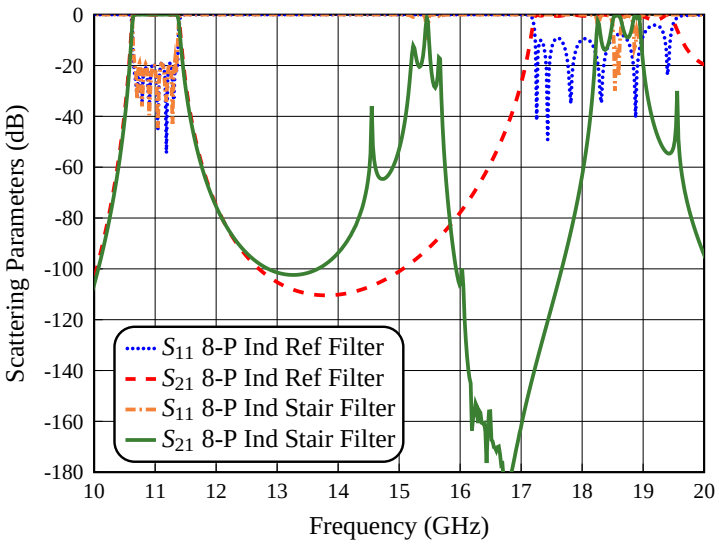

Figure 5.13: Simulated performance of the eight-pole inductive reference filter (8-P Ind Ref Filter) and eight-pole inductive staircase filter (8-P Ind Stair Filter) with $BW = 720$ MHz.

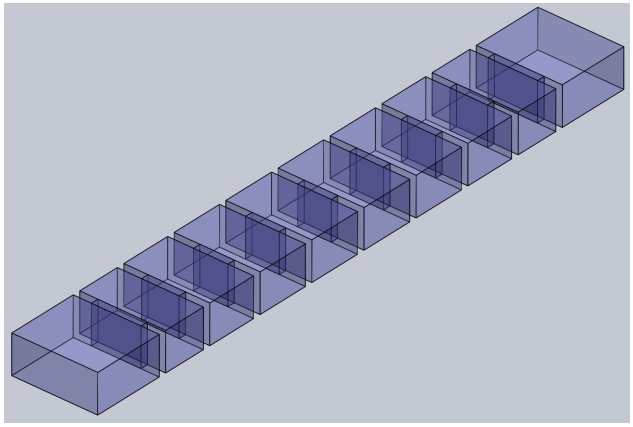

Figure 5.14: Structure of the eight-pole inductive filter with $BW = 1410$ MHz.

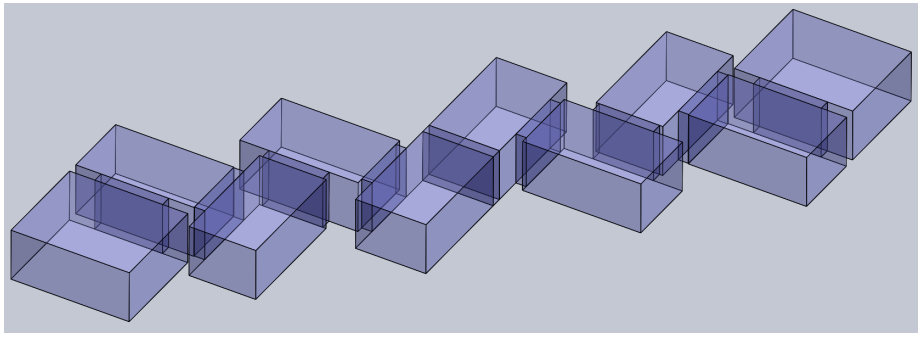

Figure 5.15: Structure of the eight-pole inductive staircase filter with $BW = 1410$ MHz.

Fig. 5.16 shows the comparison of the simulated behavior of the two structures. As we can see, the second resonance has been slightly reduced. However, spurious responses have appeared near the pass-band at 15 GHz, strongly degrading the filter performance. This degradation might be attenuated partially by introducing offsets in some inductive couplings, but suppressing all spurious peaks of Fig. 5.16 seems a rather complex task.

We can therefore conclude that using the staircase configurations in inductive narrow-band filters does produce an important attenuation and reduction of the harmonics. However, when we increase the bandwidth and order of the filter, the response is strongly degraded. To address this issue, we explore in the next section the use of capacitive staircase structures.

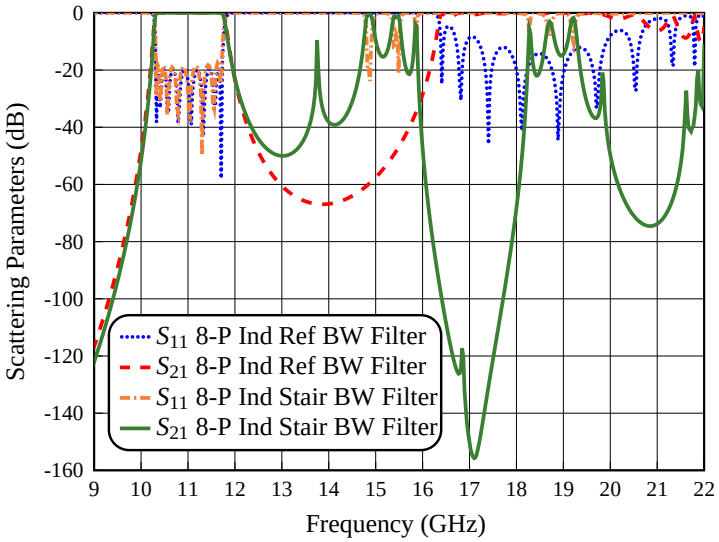

Figure 5.16: Simulated performance of the eight-pole inductive reference filter (8-P Ind Ref BW Filter) and eight-pole inductive staircase filter (8-P Ind Stair BW Filter) with $BW =$ 1410 MHz.

5.2.3 Capacitive Staircase Filters

To overcome the limitations of the wideband inductive staircase filters, we propose to implement the staircase configuration in capacitive filters. For this purpose, we first look at a resonator with capacitive couplings in the front and end walls, as shown in Fig. 5.17. Next, we show in Fig. 5.18 the geometry of a resonator with capacitive couplings with the staircase configuration.

For this staircase configuration, the capacitive coupling irises are opened on the top wall of the resonators. It is important to mention that if the coupling irises were located in the center of the resonators, there would have been no coupling between adjacent resonators. This is because, as already discussed, the first resonance of a rectangular waveguide resonator has a maximum of electric field in the middle of the resonator (see Fig. 5.1). Therefore, in the configuration that we propose the coupling irises are located at $l_s = 3l/4$, where the second resonance has a maximum, with the objective of coupling the first resonance, while *decoupling* the second resonance.

With this choice, we next design a four-pole capacitive filter with bandwidth $BW =$ 720 MHz ($\mathcal{W}_\lambda = 10$ %). Fig. 5.19 shows the structure of this filter (4-P Cap Ref Filter). Next, we have implemented the staircase configuration obtaining the filter shown in Fig. 5.20.

Fig. 5.21 shows a comparison of the simulated behavior of the structures in Fig. 5.19 (4-P Cap Ref Filter) and Fig. 5.20 (4-P Cap Stair Filter), respectively. As we can see, the

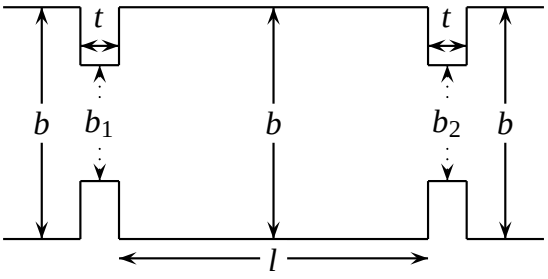

Figure 5.17: Geometry of a resonator coupled with capacitive couplings in the front and end walls (side view).

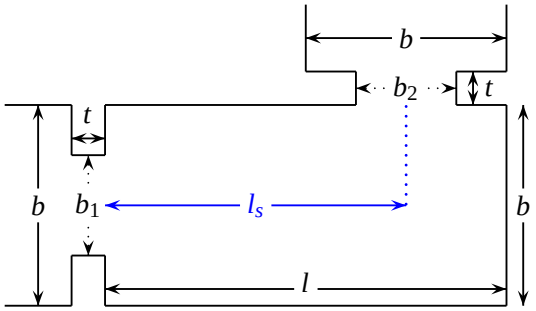

Figure 5.18: Geometry of a staircase resonator with capacitive couplings (side view).

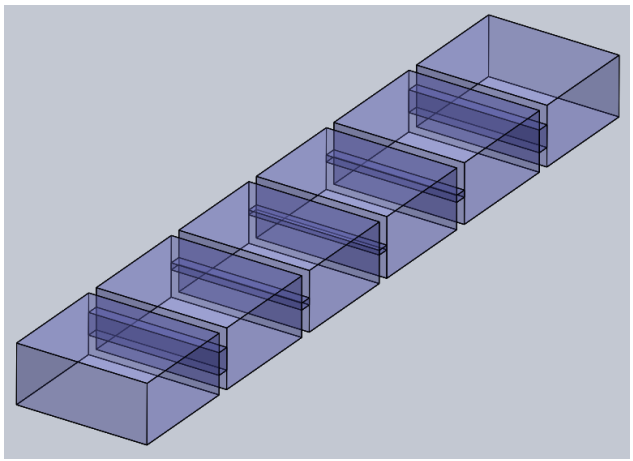

Figure 5.19: Structure of the four-pole capacitive filter with $BW = 720$ MHz.

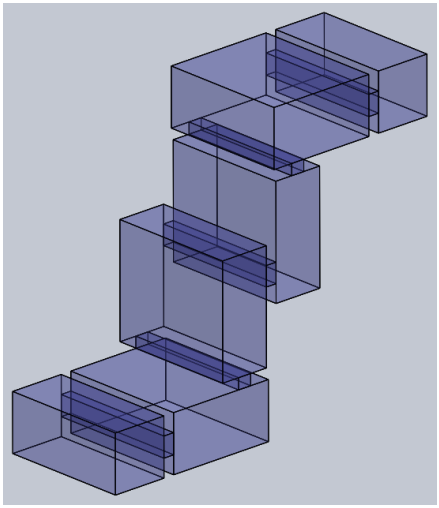

Figure 5.20: Structure of the four-pole capacitive staircase filter with $BW = 720$ MHz.

4-P Cap Ref Filter has a spurious (harmonic) response at about 17 GHz, which is due to the second resonance (TE_{102}). By contrast, the 4-P Cap Stair Filter shows a substantial reduction and attenuation of the second harmonic, with spikes reaching about -15 dB at 17.4 and 18.5 GHz, respectively. However, we now have unwanted resonances below the pass-band, which is due to the use of capacitive irises.

The next structure that we design is a filter with wider bandwidth, namely $BW = 1410$ MHz ($\mathcal{W}_\lambda = 20$ %). Fig. 5.22 and Fig. 5.23 show the structures of an in-line eight-pole capacitive filter (8-P Cap Ref Filter) and of the eight-pole capacitive staircase filter (8-P Cap Stair Filter), respectively.

Fig. 5.24 shows the comparison of the simulated behavior of the structures in Fig. 5.22 (8-P Cap Ref Filter) and Fig. 5.23 (8-P Cap Stair Filter), respectively. As we can see, the application of the staircase configuration results into a reduction of the second resonance of about -15 dB. However, we now have an important degradation of the response below the pass-band due to use of the capacitive irises.

It must be note that, in order to design the two previous capacitive staircase filters, the positions of the capacitive irises (i.e. l_s in Fig. 5.18) have been properly optimized.

We can therefore conclude that the implementation of the staircase configuration in capacitive structures does result into an important reduction of the harmonic resonances for both narrow-band and wideband implementations. However, significant unwanted resonances appear below the pass-band. In the next section, we explore the use of hybrid coupling structures (i.e. inductive and capacitive irises) in order to address this issue.

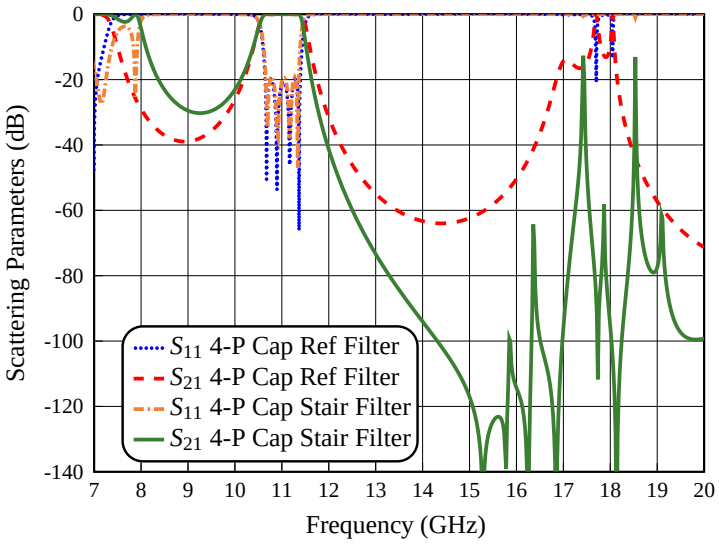

Figure 5.21: Simulated performance of the four-pole capacitive reference filter (4-P Cap Ref Filter) and capacitive staircase filter (4-P Cap Stair Filter) with $BW = 720$ MHz.

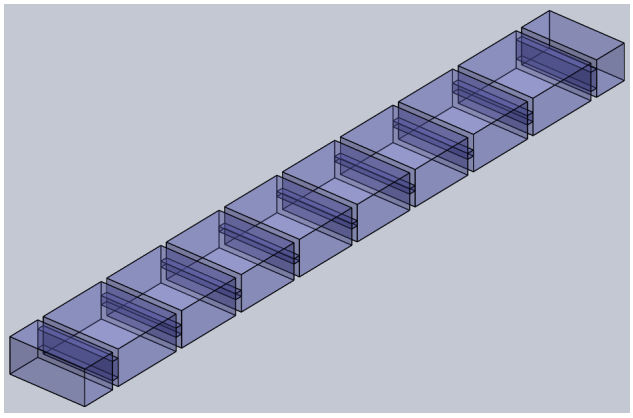

Figure 5.22: Structure of the eight-pole capacitive filter with $BW = 1410$ MHz.

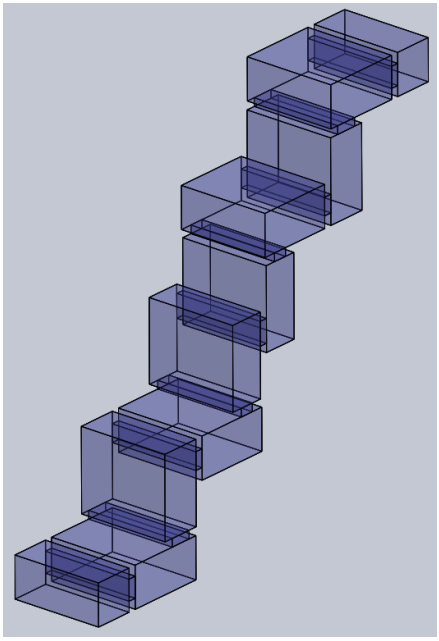

Figure 5.23: Structure of the eight-pole capacitive staircase filter with $BW = 1410$ MHz.

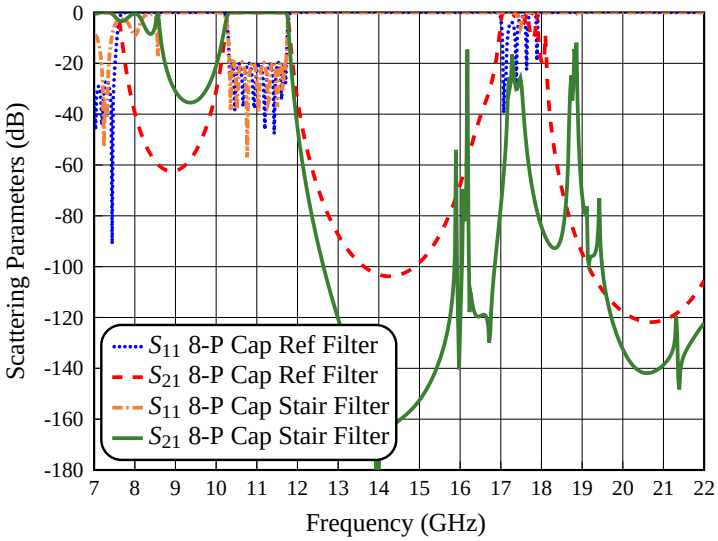

Figure 5.24: Simulated performance of the eight-pole capacitive reference filter (8-P Cap Ref Filter) and capacitive staircase filter (8-P Cap Stair Filter) with $BW = 1410$ MHz.

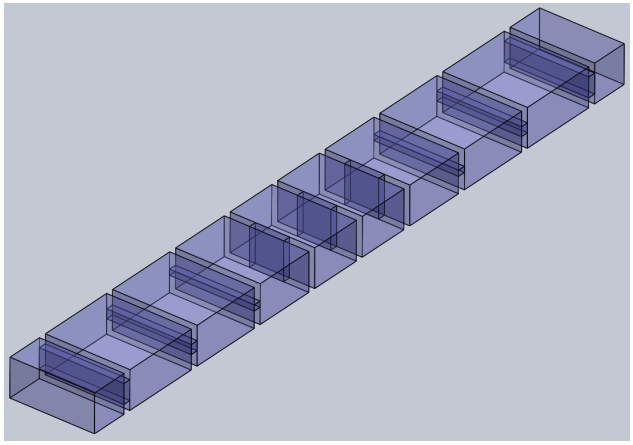

Figure 5.25: Structure of the hybrid (reference) eight-pole filter with $BW = 1410$ MHz.

5.2.4 Hybrid Staircase Filters

In Chapters 3 and 4 we have already shown how the use of inductive and capacitive couplings (hybrid filters) can effectively improve the out-of-band performance of wideband filters. With this in mind, we have designed a hybrid (reference) eight-pole in-line filter. This structure has three inductive apertures to couple the two central cavities. All other irises are capacitive, as shown in Fig. 5.25.

We next explore two possibilities to improve the out-of-band performance, namely:

1. First, we implement the staircase configuration in the first (and last) three resonators of the hybrid filter.
2. Then, we identify the best configuration for the central part of the filter (inductive couplings) to improve the performance both below and above of the pass-band of the filter.

To continue, we now observe that there are indeed several possible variations of the basic staircase configuration, that could be effectively used to further improve the out-of-band performance. Table 5.1 shows four possible staircase configurations. These configurations have been obtained by changing the relative orientation of the first (and last) three resonators.

In addition to cavity orientation, we can create additional topologies by changing the location of the capacitive irises. Table 5.2 shows the four topologies that we have obtained changing iris location.

As we can see from Tables 5.1 and 5.2, there are a number of possible staircase configurations. We are now going to study all of them in detail.

Table 5.1: Position of the first three resonators for each staircase configuration.

Type	Resonator 1	Resonator 2	Resonator 3
Staircase 1	Horizontal	Vertical	Horizontal
Staircase 2	Horizontal	Vertical	Vertical
Staircase 3	Horizontal	Horizontal	Horizontal
Staircase 4	Horizontal	Horizontal	Vertical

Table 5.2: Location of the capacitive irises for each topology.

Type	Topology 1	Topology 2	Topology 3	Topology 4
Staircase 1	$l_{s_1} = l_1/4$ $l_{s_2} = l_2/4$	$l_{s_1} = 3l_1/4$ $l_{s_2} = l_2/4$	$l_{s_1} = 3l_1/4$ $l_{s_2} = 3l_2/4$	$l_{s_1} = l_1/4$ $l_{s_2} = 3l_2/4$
Staircase 2	$l_{s_1} = l_1/4$ $l_{s_2} = l_2/4$ $l_{s_3} = l_3/4$	$l_{s_1} = 3l_1/4$ $l_{s_2} = l_2/4$ $l_{s_3} = l_3/4$	$l_{s_1} = 3l_1/4$ $l_{s_2} = 3l_2/4$ $l_{s_3} = l_3/4$	$l_{s_1} = l_1/4$ $l_{s_2} = 3l_2/4$ $l_{s_3} = l_3/4$
Staircase 3	$l_{s_1} = l_1/4$ $l_{s_{2a}} = l_2/4$ $l_{s_{2b}} = l_2/4$ $l_{s_3} = l_3/4$	$l_{s_1} = 3l_1/4$ $l_{s_{2a}} = l_2/4$ $l_{s_{2b}} = l_2/4$ $l_{s_3} = l_3/4$	$l_{s_1} = 3l_1/4$ $l_{s_{2a}} = l_2/4$ $l_{s_{2b}} = 3l_2/4$ $l_{s_3} = l_3/4$	$l_{s_1} = l_1/4$ $l_{s_{2a}} = l_2/4$ $l_{s_{2b}} = 3l_2/4$ $l_{s_3} = l_3/4$
Staircase 4	$l_{s_1} = l_1/4$ $l_{s_{2a}} = l_2/4$ $l_{s_{2b}} = l_2/4$	$l_{s_1} = 3l_1/4$ $l_{s_{2a}} = l_2/4$ $l_{s_{2b}} = l_2/4$	$l_{s_1} = 3l_1/4$ $l_{s_{2a}} = l_2/4$ $l_{s_{2b}} = 3l_2/4$	$l_{s_1} = l_1/4$ $l_{s_{2a}} = l_2/4$ $l_{s_{2b}} = 3l_2/4$

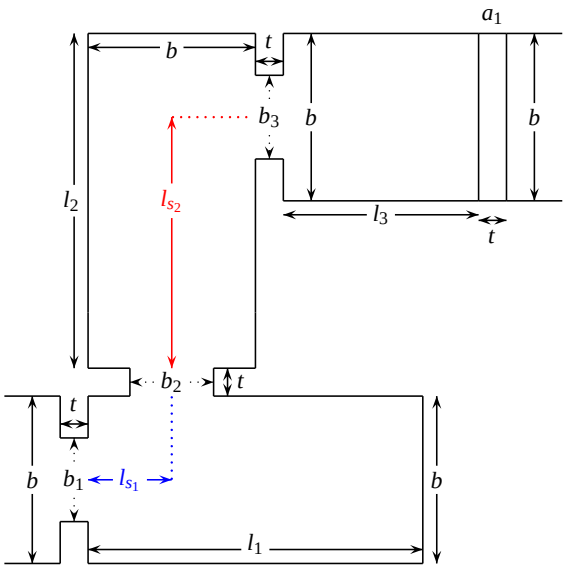

Figure 5.26: Geometry of the first three-resonator arrangement of the first staircase configuration with the capacitive coupling apertures located at $l_{s_1} = l_1/4$ and $l_{s_2} = 3l_2/4$, respectively, from the resonator input.

5.2.4.1 Staircase 1

We now study the first of the four topologies shown in Table 5.2 for Staircase 1. Fig. 5.26 shows the structure. The central section of the filter remains as shown in Fig. 5.25.

Fig. 5.27 and Fig. 5.28 show the simulated behavior of the reference in-line hybrid filter (Hybrid) together with the four hybrid staircase filters, namely, from the topology 1 to 4, respectively. As we can see, the hybrid staircase filter of the topology 4 shows an attenuation and reductions of the spurious response in comparison with the other topologies. Also, a transmission zero at 8 GHz has been obtained near the pass-band. However, a spike has appeared reaching -30 dB at 7.5 GHz. Finally, Fig. 5.29 shows the structure of the complete hybrid staircase filter with topology 4 (Topo 4).

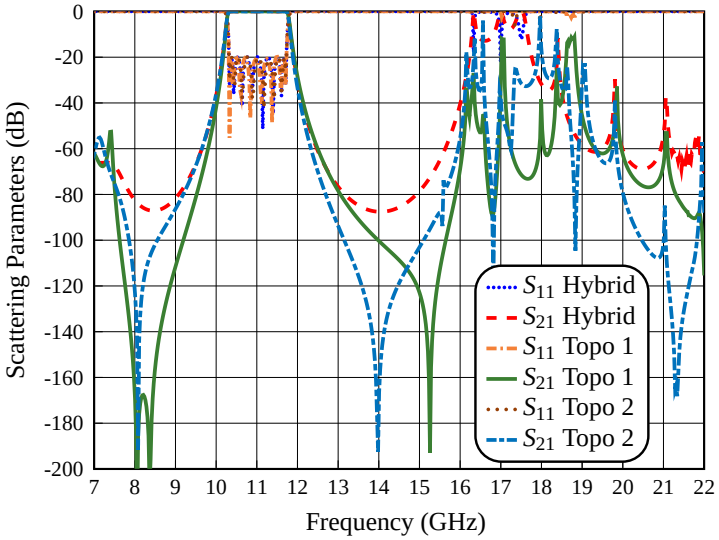

Figure 5.27: Simulated performance of the hybrid reference filter (Hybrid) and hybrid staircase filter with the topologies 1 (Topo 1) and 2 (Topo 2) for the first staircase configuration.

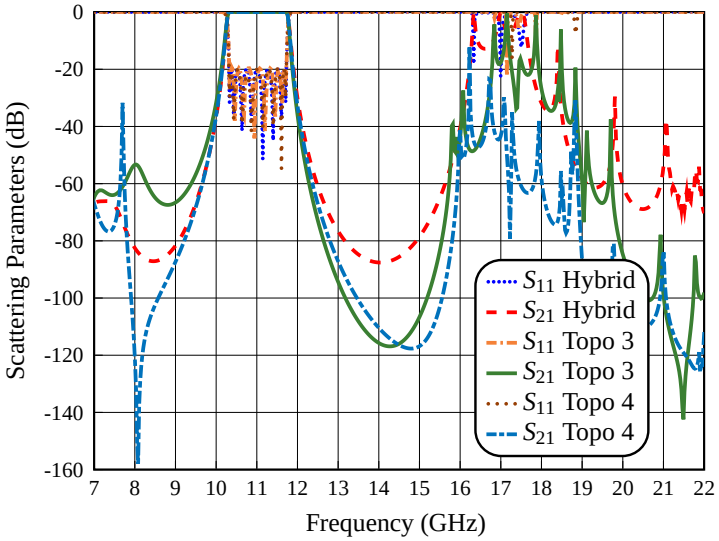

Figure 5.28: Simulated performance of the hybrid reference filter (Hybrid) and hybrid staircase filter with the topologies 3 (Topo 3) and 4 (Topo 4) for the first staircase configuration.

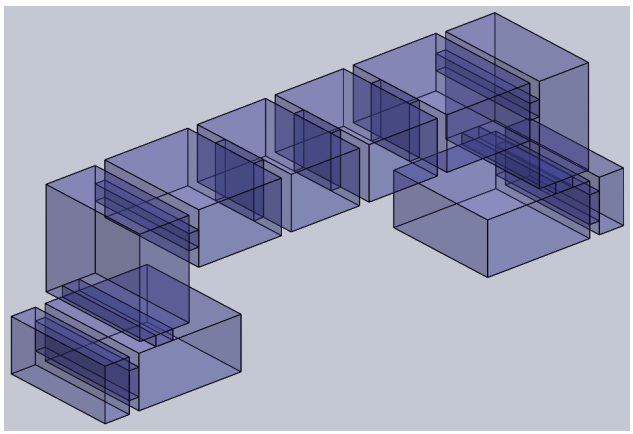

Figure 5.29: Structure of the hybrid staircase filter of the first staircase configuration with the topology 4.

5.2.4.2 Staircase 2

Next, we study the second staircase configuration, as shown in Fig. 5.30. The comparison of the simulated behavior of the reference in-line hybrid filter (Hybrid) with the four hybrid staircase filters with topologies 1 to 4, are shown in the Fig. 5.31 and Fig. 5.32, respectively.

As we can see, the filter with topology 4 shows a significant reduction and attenuation of the second harmonic in comparison with the other topologies. In addition, the structure of topology 4 (Topo 4) also generates two TZs near the pass-band (at 8 and 14 GHz). However, a spike has appeared reaching -50 dB just before 8.0 GHz. The structure of the complete filter using the second staircase configuration with topology 4 is shown in Fig. 5.33.

5.2.4.3 Staircase 3

The geometry of the third staircase configuration is shown in Fig. 5.34. Fig. 5.35 and Fig. 5.36 show the comparison of the simulated behavior of the reference in-line hybrid filter (Hybrid) with the four hybrid staircase filters, from topologies 1 to 4.

As we can see, the hybrid staircase filter with topology 4 shows a reduction and attenuation of the second harmonic, and better filter selectivity in comparison with the other topologies. Fig. 5.37 shows the structure of the complete filter using the third staircase configuration with topology 4. This filter has also generated two TZs near the pass-band (at 8 and 12.5 GHz). However, a spike has appeared reaching -35 dB at 8.2 GHz.

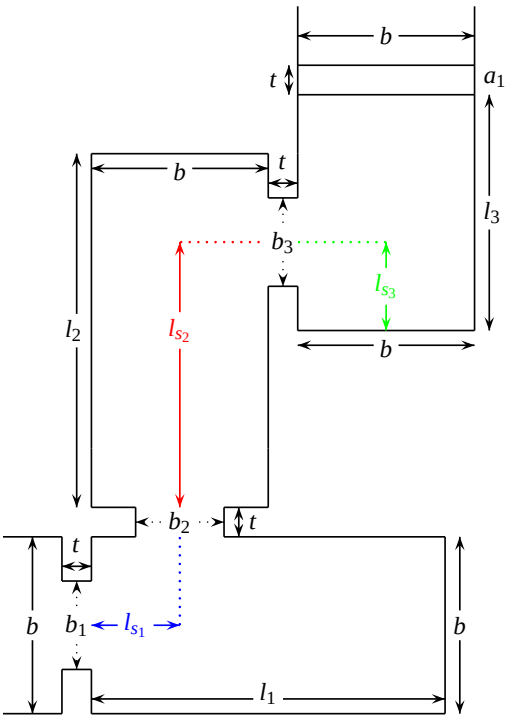

Figure 5.30: Geometry of the three-resonator arrangement of the second staircase configuration with the capacitive coupling apertures located at $l_{s_1} = l_1/4$, $l_{s_2} = 3l_2/4$ and $l_{s_3} = l_3/4$, respectively, from the resonator input.

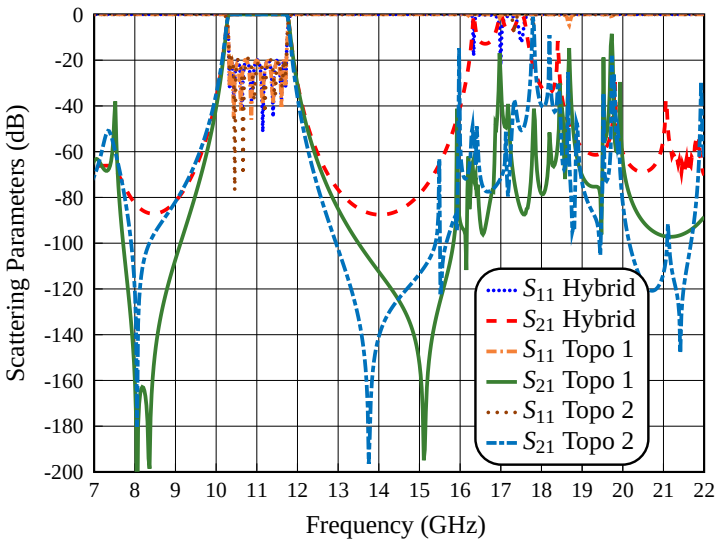

Figure 5.31: Simulated performance of the hybrid reference filter (Hybrid) and hybrid staircase filter with the topologies 1 (Topo 1) and 2 (Topo 2) for the second staircase configuration.

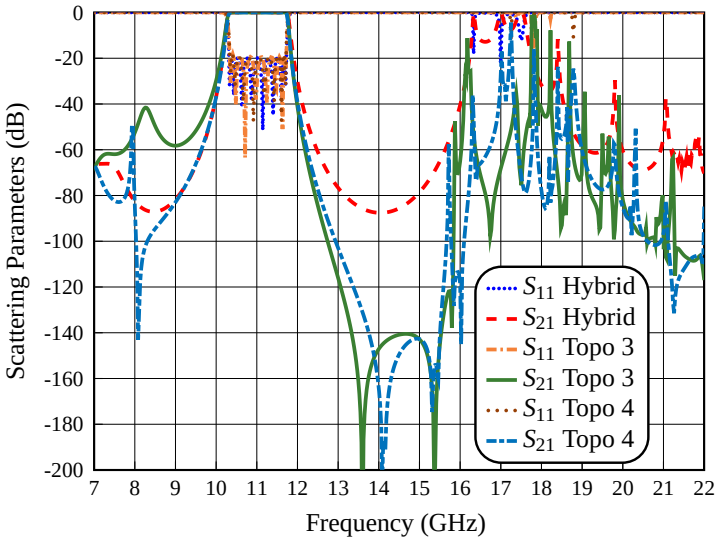

Figure 5.32: Simulated performance of the hybrid reference filter (Hybrid) and hybrid staircase filter with the topologies 3 (Topo 3) and 4 (Topo 4) for the second staircase configuration.

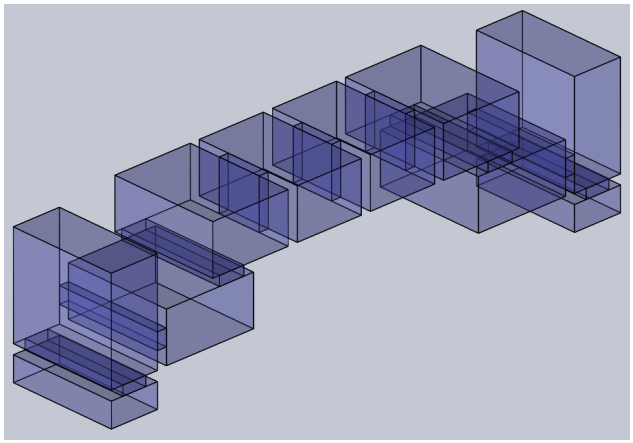

Figure 5.33: Structure of the hybrid staircase filter of the second staircase configuration with the topology 4.

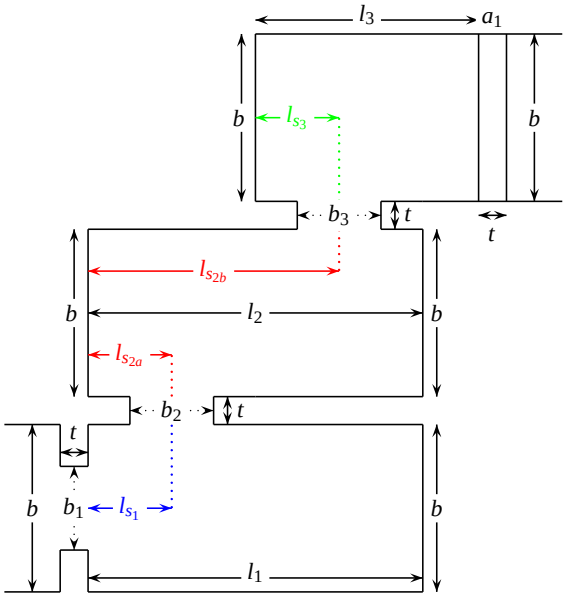

Figure 5.34: Geometry of the three-resonator arrangement of the third staircase configuration with the capacitive coupling apertures located at $l_{s_1} = l_1/4$, $l_{s_{2a}} = l_2/4$, $l_{s_{2b}} = 3l_2/4$ and $l_{s_3} = l_3/4$, respectively, from the resonator input.

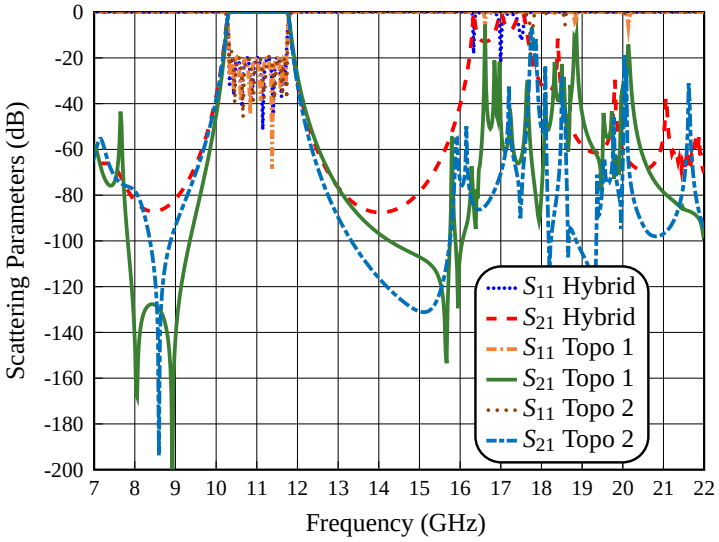

Figure 5.35: Simulated performance of the hybrid reference filter (Hybrid) and hybrid staircase filter with the topologies 1 (Topo 1) and 2 (Topo 2) for the third staircase configuration.

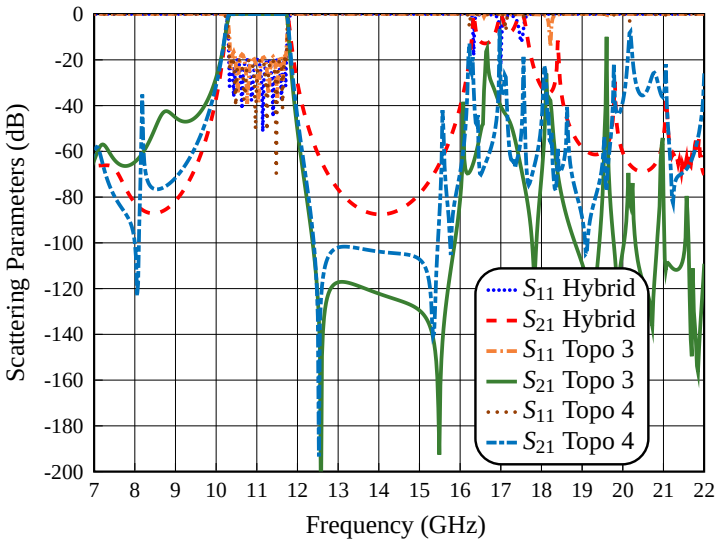

Figure 5.36: Simulated performance of the hybrid reference filter (Hybrid) and hybrid staircase filter with the topologies 3 (Topo 3) and 4 (Topo 4) for the third staircase configuration.

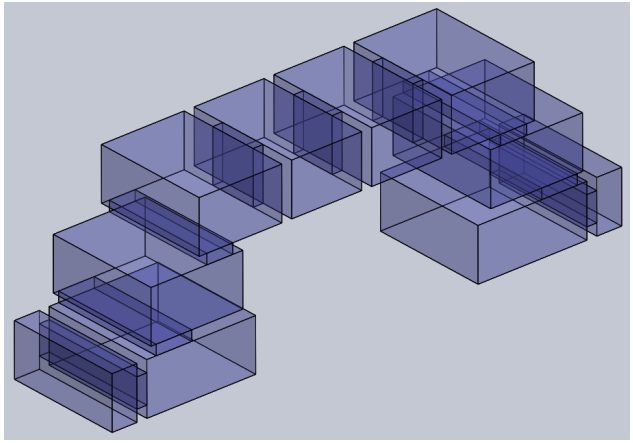

Figure 5.37: Structure of the hybrid staircase filter of the third staircase configuration with the topology 4.

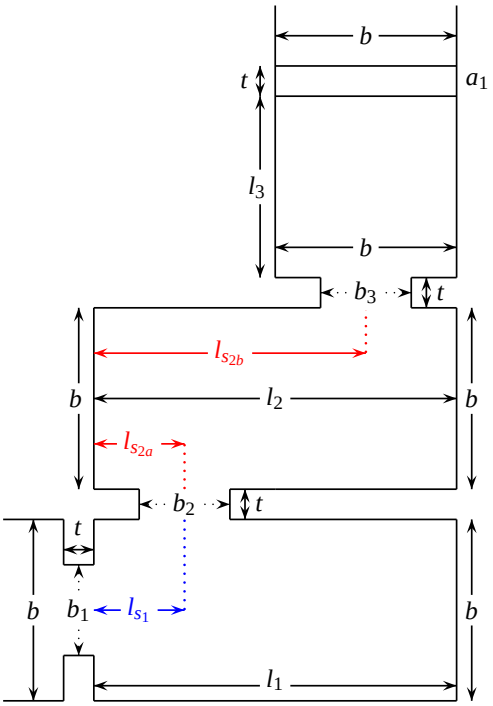

Figure 5.38: Geometry of the three-resonator arrangement of the fourth staircase configuration with the capacitive coupling apertures located at $l_{s_1} = l_1/4$, $l_{s_{2a}} = l_2/4$ and $l_{s_{2b}} = 3l_2/4$, respectively, from the resonator input.

5.2.4.4 Staircase 4

The last geometry that we study is the fourth staircase configuration, as shown in Fig. 5.38. Fig. 5.39 and Fig. 5.40 show the comparison of the simulated behavior of the reference in-line hybrid filter (Hybrid) with the hybrid staircase filters with topologies 1 to 4.

As we can see, the hybrid staircase filter of the topology 4 shows an important improvement of the filter selectivity, with a slightly reduction and attenuation of the second harmonic in comparison with the other topologies. Fig. 5.41 shows the structure of the complete filter with the third staircase configuration and topology 4. This filter has also generated TZs near the pass-band (at 8 and 12.7 GHz). However, a spike has appeared reaching -30 dB at 8.0 GHz.

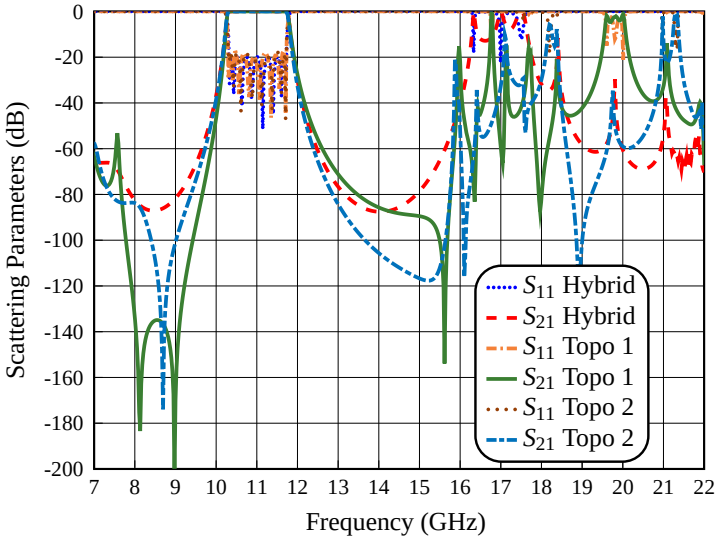

Figure 5.39: Simulated performance of the hybrid reference filter (Hybrid) and hybrid staircase filter with the topologies 1 (Topo 1) and 2 (Topo 2) for the fourth staircase configuration.

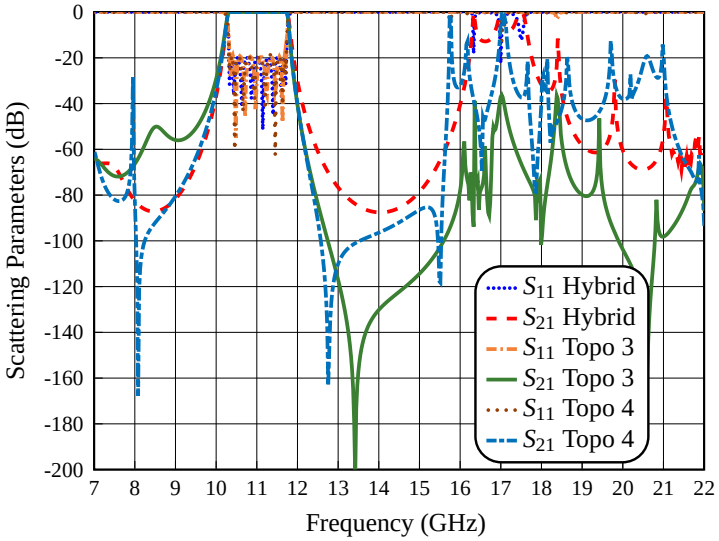

Figure 5.40: Simulated performance of the hybrid reference filter (Hybrid) and hybrid staircase filter with the topologies 3 (Topo 3) and 4 (Topo 4) for the fourth staircase configuration.

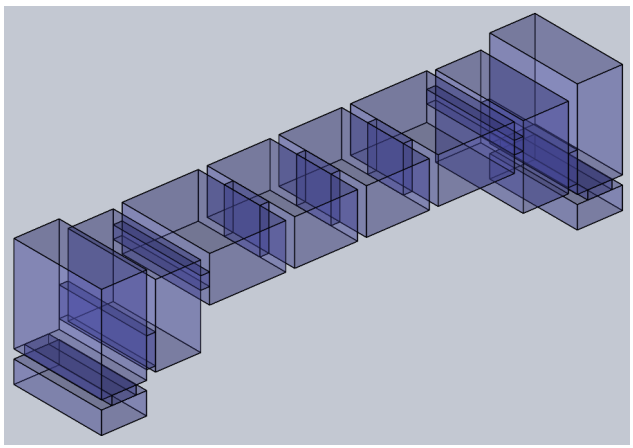

Figure 5.41: Structure of the hybrid staircase filter of the fourth staircase configuration with the topology 4.

5.2.4.5 Comparative Discussion

Fig. 5.42 and Fig. 5.43 show the comparison of the simulated behavior of the hybrid staircase filter with topology 4 and with the first, second, third and fourth configuration, respectively.

As we can see, the first and second staircase configurations are indeed the best ones (Stair 1 Topo 4 and Stair 2 Topo 4), since they show better attenuation of the harmonic resonances as compared to the other ones. We will therefore use these filters for further improvements.

In conclusion, we can therefore say that the implementation of the staircase configuration in hybrid filter does show an important improvement in the out-of-band response. In addition, we note also an increased filter selectivity.

5.3 E-Plane T-Junction Manifold Connection

In the previous sections we have designed hybrid staircase filters with standard capacitive input and output couplings, and we have achieved an important reduction of the harmonic resonances. In this section we study the use of manifold connections, based on E-plane T-junctions, to generate additional TZs to try to improve both the selectivity and the out-of-band response of the filter.

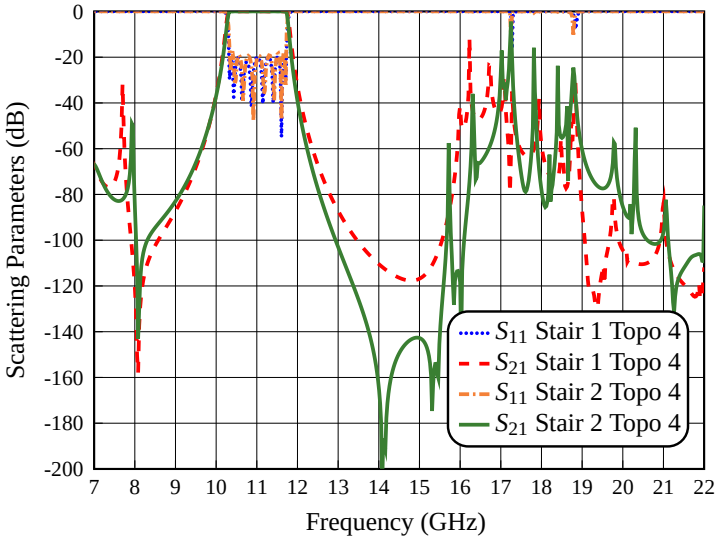

Figure 5.42: Simulated performance of the hybrid staircase filter with the topology 4 of the first configuration (Stair 1 Topo 4) and second configuration (Stair 2 Topo 4).

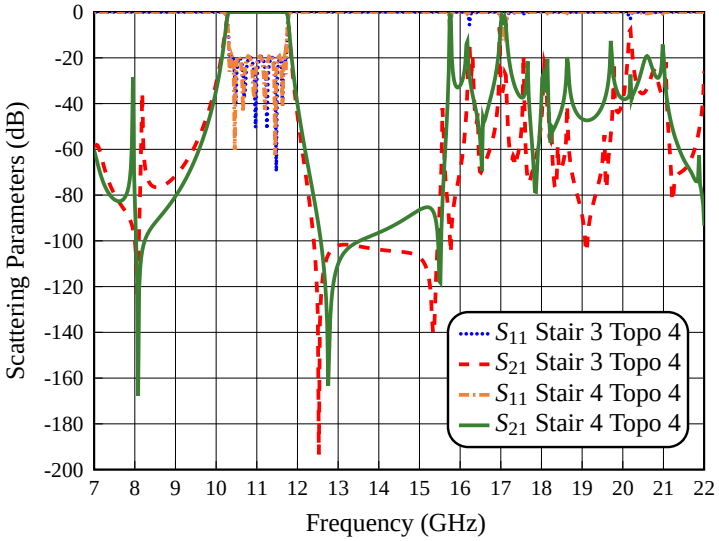

Figure 5.43: Simulated performance of the hybrid staircase filter with the topology 4 of the third configuration (Stair 3 Topo 4) and fourth configuration (Stair 4 Topo 4).

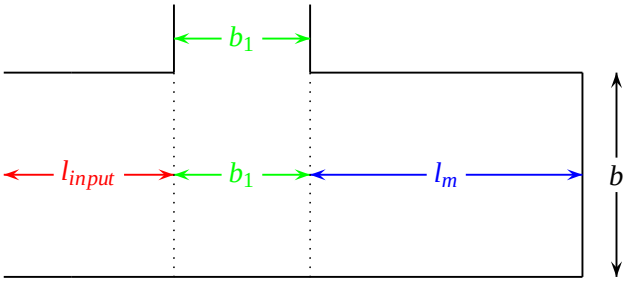

Figure 5.44: Geometry of a simple E-plane manifold connection.

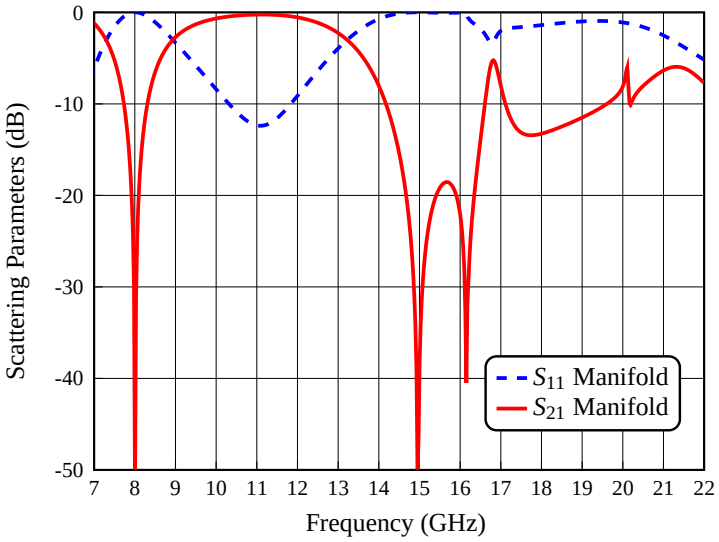

Figure 5.45: Simulated performance of the E-plane manifold connection with a stub of length $l_m = \lambda/2 - b/2$.

5.3.1 Basic Manifold Structure

To better understand this concept, we show in Fig. 5.44 and Fig. 5.45 the geometry and the simulated performance of a simple E-plane manifold connection.

As we can see in Fig. 5.45, using a manifold connection it is possible to generate TZs both below and above the pass-band of the filter. It is important to mention that the location of the specific TZs depends on the length of the stub l_m and the height of the input capacitive coupling b_1. Therefore, if we change both the length of the stub and the height of capacitive input coupling, we can move the location of the TZs to the desired frequency.

We propose to take advantage of this feature by using manifold connections both

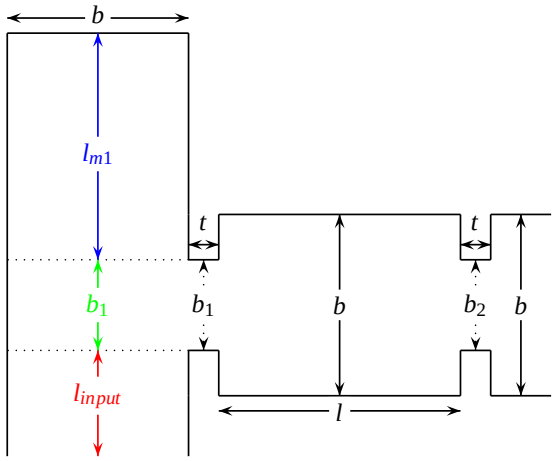

Figure 5.46: Geometry of the E-plane T-junction in the input (or output) port of a rectangular waveguide filter with capacitive couplings.

in the input and in the output ports of our filter, with the objective of improving the out-of-band performance of the filter response. Fig. 5.46 shows the new geometry at the input and output ports of the filter.

Having studied the behavior of the manifold connections, we can deduce a simple procedure to position the TZs in the wanted frequency location. The steps of this procedure are as follow:

1. We first design the waveguide filter with a capacitive coupling in the input and output ports.
2. Next, we add the manifold connection to both the input and the output ports of the filter.
3. To locate the TZ to the left of the pass-band, we then use a stub of length approximately equal to $l_{m1} \approx \lambda/2 - b/2 - b_1/4$, where λ is the guide wavelength evaluated at the center frequency, b is the height of the rectangular waveguide and b_1 is the height of the capacitive window in the input port of the filter.
4. To locate the TZ to the right of the pass-band, we then use a stub of length approximately equal to $l_{m1} \approx \lambda/2 - b/2 + b_1/2$, where b_1 is the height related to the capacitive coupling in the output port of the filter.
5. The next step is to adjust by optimization the capacitive input and output irises to recover the desired filter performance.
6. Finally, in the last step it is necessary to fine tune by optimization the dimensions l_{m1} and b_1 in both the input and output ports, in order to have the two TZs at the desired frequency locations.

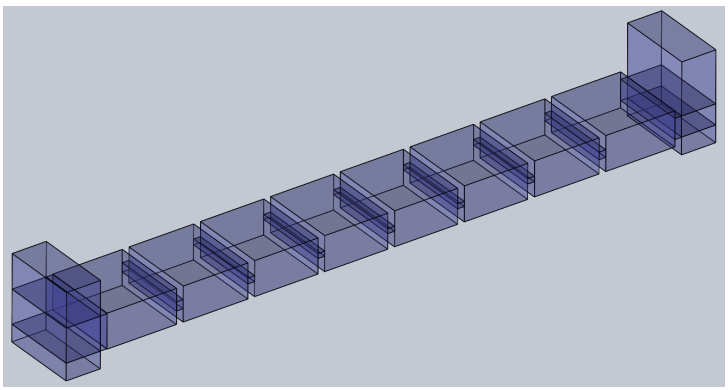

Figure 5.47: Structure of the capacitive filter with manifold input-output connections.

It is important to mention that there is a limitation with respect to the proximity of the TZs to the pass-band edges. As the TZ moves closer to the edge of the pass-band, the capacitive input coupling iris will need to be larger in order to recover the desired filter performance. As a consequence, the limit is reached when the coupling iris has the same height of the resonator to which it is connected. On the other hand, an alternative to move the TZ closer to the edge of the filter passband, is to reduce the bandwidth of the filter. With this in mind, we can now proceed to implement the manifold connection in our filter structures.

5.3.2 Capacitive Manifold Filter

To validate the concept just proposed, we first implement the manifold connections in the capacitive filter shown in Fig. 5.22. Fig. 5.47 shows the resulting structure. Fig. 5.48 shows a comparison of the simulated behavior of the structures in Fig. 5.22 (Cap Ref Filter) and Fig. 5.47 (Cap Man Filter), respectively.

As we can see, the addition of manifold configurations with E-plane T-junctions produces a further improvement both in the selectivity and in the attenuation of the harmonics, with spurious response below -30 dB. However, below the pass-band the unwanted resonances due to the capacitive irises are still present.

5.3.3 Hybrid Manifold Filter

To continue, we now implement the manifold connections in the hybrid reference filter shown in Fig. 5.25. Fig. 5.49 shows the resulting structure. Fig. 5.50 shows a comparison of the simulated behavior of the structures in Fig. 5.25 (Hyb Ref Filter) and Fig. 5.49 (Hyb Man Filter), respectively.

As we can see, the addition of manifold configurations and E-plane T-junctions

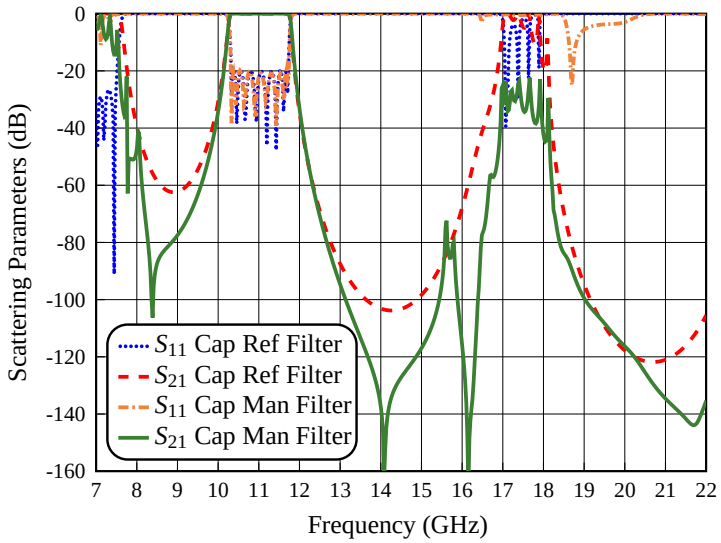

Figure 5.48: Simulated performance of the capacitive filter (Cap Ref Filter) and capacitive filter with manifold connections (Cap Man Filter).

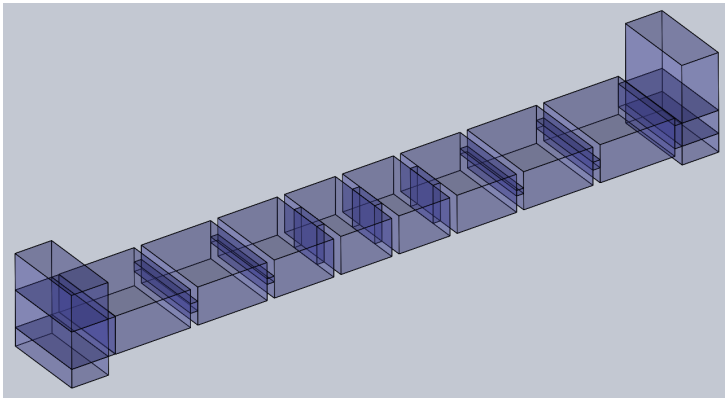

Figure 5.49: Structure of the hybrid filter with manifold input-output connections.

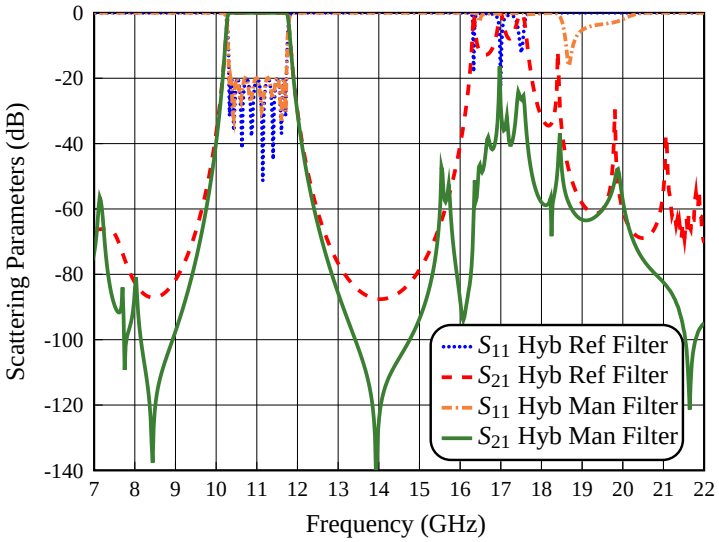

Figure 5.50: Simulated performance of the hybrid filter (Hyb Ref Filter) and hybrid filter with manifold connections (Hyb Man Filter).

produces a further improvement both in the selectivity and in the attenuation of the harmonics, with spurious response below -25 dB from 15 to 22 GHz, and a spike reaching -18 dB at 17.0 GHz. Also, below the pass-band the spurious response has been reduced below -55 dB.

5.3.4 Hybrid Staircase Manifold Filter

Following the design procedure proposed in the previous section, we now use the manifold configuration in the hybrid staircase filters of Section 5.2. Additionally, we have also changed the height of the central section of the filter (the inductive irises and resonators) in order to further improve the filter performance.

To continue, we first implement the manifold connections in the hybrid staircase filter with the first staircase configuration and topology 4, as shown in Fig. 5.51. Fig. 5.52 shows a comparison of the simulated behavior of the structures in Fig. 5.29 (Stair 1 Topo 4) and Fig. 5.51 (Filter 1), respectively.

As we can see, Filter 1 shows a further improvement both in the selectivity and in the attenuation of the harmonics, with spurious response below -40 dB and a spike reaching -35 dB at 16.70 GHz.

Next, we show in Fig. 5.53 the structure of the hybrid staircase filter of the second staircase configuration with topology 4 and manifold connections. The comparison of the simulated behavior of the structures in Fig. 5.33 (Stair 2 Topo 4) and Fig. 5.53 (Filter 2),

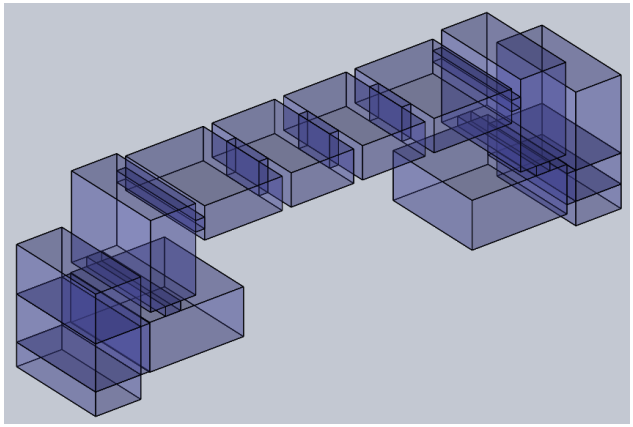

Figure 5.51: Structure of the hybrid staircase filter of the first staircase configuration with the topology 4 and manifold input-output connections.

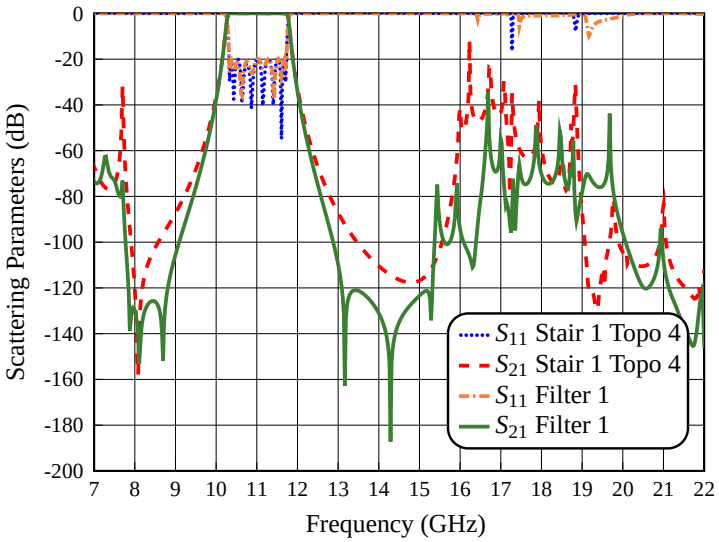

Figure 5.52: Simulated performance of the hybrid staircase filter (Stair 1 Topo 4) and hybrid staircase filter with manifold connections (Filter 1).

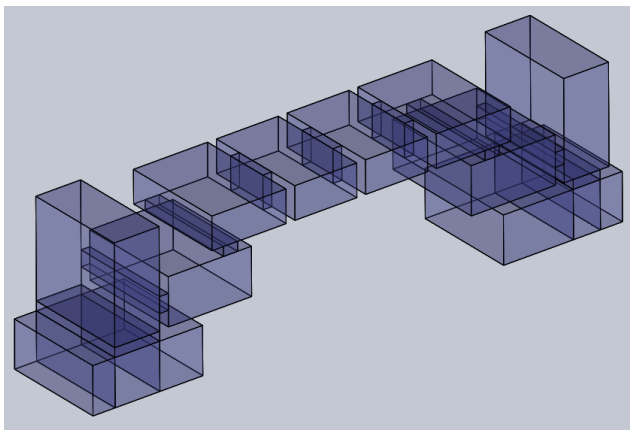

Figure 5.53: Structure of the hybrid staircase filter of the second staircase configuration with the topology 4 and manifold input-output connections.

respectively, is shown in Fig. 5.54.

As we can see, the Filter 2 shows a spurious response below -50 dB with a spike reaching -20 dB at 16.55 GHz. An important improvement of the selectivity and attenuation of the harmonics have clearly been obtained.

To continue with our design, Fig. 5.55 shows the structure of the hybrid staircase filter of the third staircase configuration with topology 4 and manifold connections. Fig. 5.56 shows the comparison of the simulated behavior of the structures in Fig. 5.37 (Stair 3 Topo 4) and Fig. 5.55 (Filter 3), respectively.

As we can see, Filter 3 shows an improvement of the selectivity, however, this structure shows a slight reduction of the rejection of the harmonic resonances.

The last structure that we implement is the hybrid staircase filter of the fourth staircase configuration with topology 4 and manifold connections, as shown in Fig. 5.57. Fig. 5.58 shows a comparison of the simulated behavior of the structures in Fig. 5.41 (Stair 4 Topo 4) and Fig. 5.57 (Filter 4), respectively.

As we can see, the addition of the manifold configuration produces a further improvement in the selectivity with a better rejection outside the pass-band from 7 to 15 GHz. However, Filter 4 shows a slight degradation of the attenuation of the harmonic resonances.

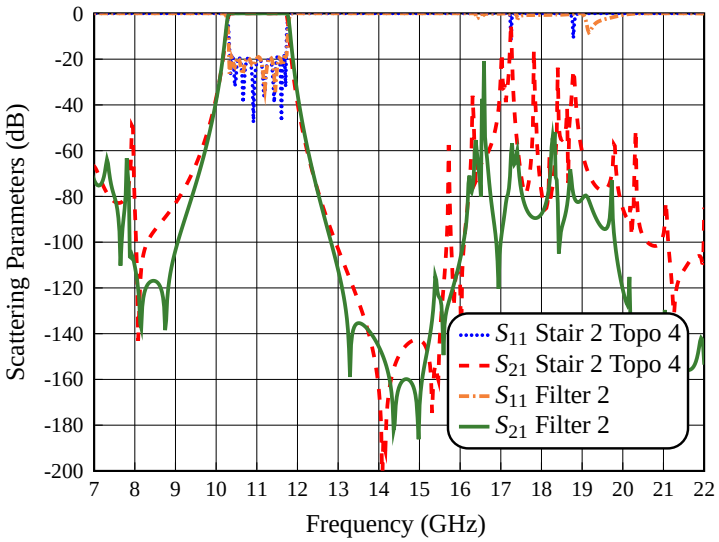

Figure 5.54: Simulated performance of the hybrid staircase filter (Stair 2 Topo 4) and hybrid staircase filter with manifold connections (Filter 2).

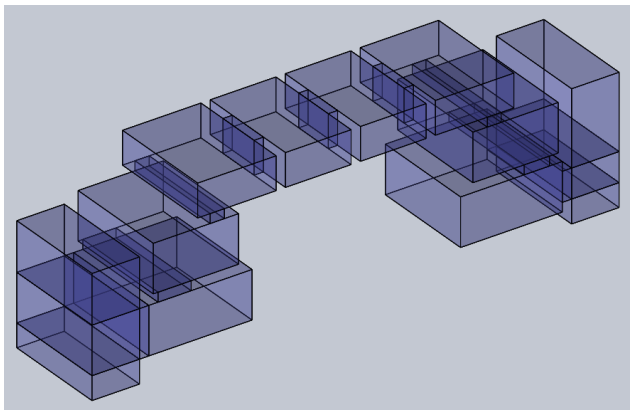

Figure 5.55: Structure of the hybrid staircase filter of the third staircase configuration with the topology 4 and manifold input-output connections.

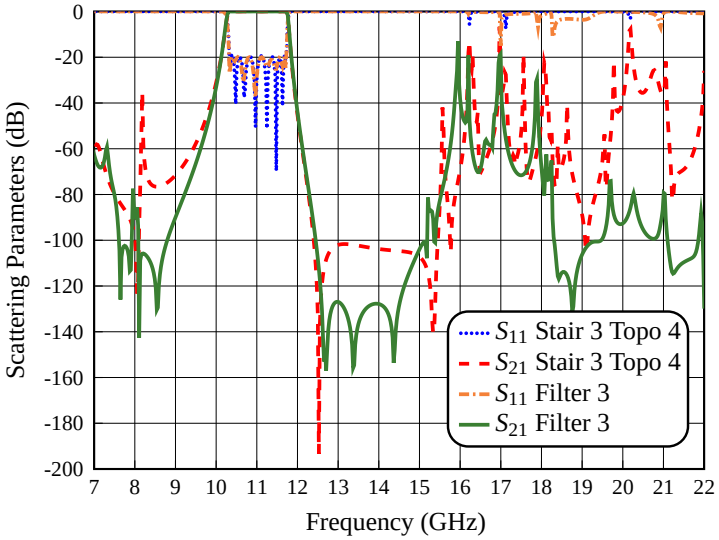

Figure 5.56: Simulated performance of the hybrid staircase filter (Stair 3 Topo 4) and hybrid staircase filter with manifold connections (Filter 3).

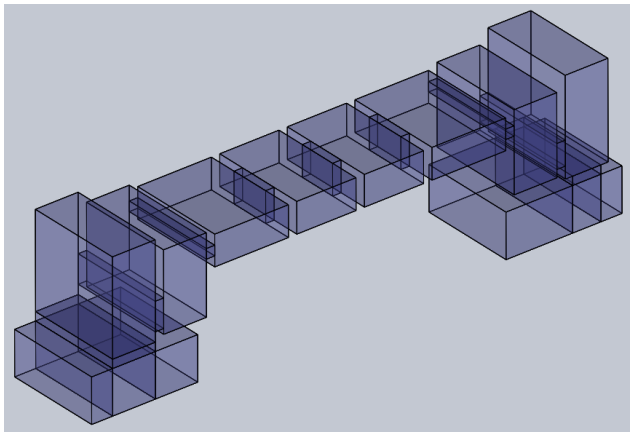

Figure 5.57: Structure of the hybrid staircase filter of the fourth staircase configuration with the topology 4 and manifold input-output connections.

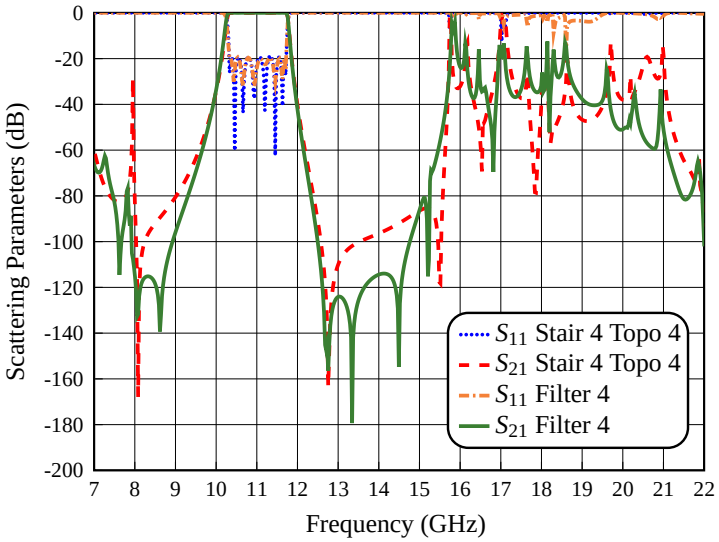

Figure 5.58: Simulated performance of the hybrid staircase filter (Stair 4 Topo 4) and hybrid staircase filter with manifold connections (Filter 4).

We can therefore conclude that the combination of the staircase configuration with the manifold connection, and a reduction of height of the resonators in the central section, result in an important improvement of both the selectivity and the out-of-band response of the hybrid staircase filters. Based on the results obtained, we have decided that the best structure is the one shown in Fig. 5.53 (Filter 2) whose response is compared in Fig. 5.54.

5.4 E-Plane Folded Hybrid Filter

In Section 5.3 we have discussed the use of a manifold connection to provide an improvement of both the out-of-band response and the filter selectivity. A further attenuation of the harmonics in our filter is possible if we can improve the performance of the central inductive section of the filter. To do that, we now fold the inductive part of the filter to attempt to improve the filter performance and to obtain, at the same time, more compact structures.

There are again several possible folding configurations depending on the orientation of the fourth and fifth resonators, and the three inductive irises (a_1, a_2 and a_3), as shown in Table 5.3.

Table 5.3: Position of the fourth resonator, and of the first and second inductive irises, in the central section for each folding configuration.

Config.	Iris 1 (a_1)	Resonator 4	Iris 2 (a_2)
In-line	Horizontal	Horizontal	Horizontal
Folded 1	Horizontal	Horizontal	Vertical
Folded 2	Horizontal	Vertical	Horizontal
Folded 3	Horizontal	Vertical	Vertical
Folded 4	Vertical	Horizontal	Horizontal
Folded 5	Vertical	Horizontal	Vertical
Folded 6	Vertical	Vertical	Horizontal
Folded 7	Vertical	Vertical	Vertical

5.4.1 Basic E-Plane Folded Structure

To continue, we note that the length of the fourth and fifth resonator, and the width of the first and third inductive irises (a_1 and a_3) are equal because the central section of the filter is symmetrical.

Next, the seven possible folded structures have been studied in detail, in order to obtain the best configuration for the Filter 2 just selected in Section 5.3.4. Fig. 5.59 and Fig. 5.60 show the geometries of the in-line reference structure with the seven configurations that we propose to implement in the central inductive part of the filter.

5.4.2 E-Plane Folded Hybrid Staircase Manifold Filter

To continue with our study of this last configuration, we now show in Fig. 5.61, Fig. 5.63, Fig. 5.65, Fig. 5.67, Fig. 5.69, Fig. 5.71 and Fig. 5.73 the hybrid staircase manifold filters with E-plane folded structures using the folding options from 1 to 7, respectively. We then show in Fig. 5.62, Fig. 5.64, Fig. 5.66, Fig. 5.68, Fig. 5.70, Fig. 5.72 and Fig. 5.74 the comparison of the simulated behavior of the structures of Fig. 5.54 (Filter 2) with the folding options 1 to 7.

As we can see, folding the structure in its central section generally results in a further improvement of the out-of-band response in comparison with the one of Filter 2. However, the best results are obtained with the fifth folded configuration (Folded 5), as can be seen in Fig. 5.70.

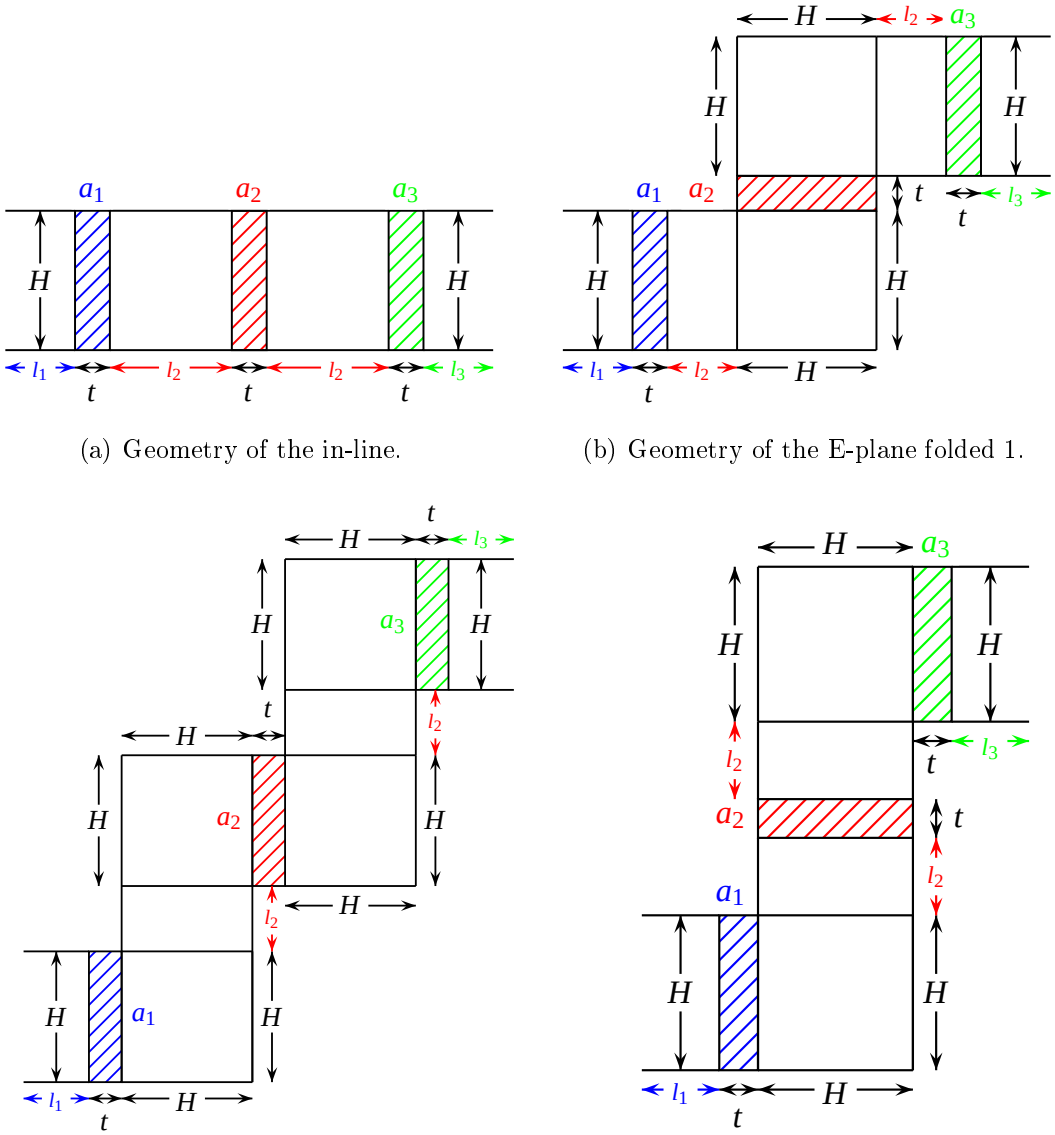

(a) Geometry of the in-line.

(b) Geometry of the E-plane folded 1.

(c) Geometry of the E-plane folded 2.

(d) Geometry of the E-plane folded 3.

Figure 5.59: Geometry of the central section of the in-line filter with inductive couplings and of the E-plane folded configurations 1 to 3 (side view).

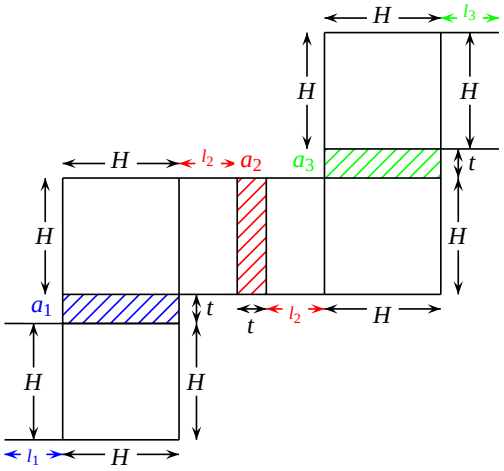

(a) Geometry of the E-plane folded 4.

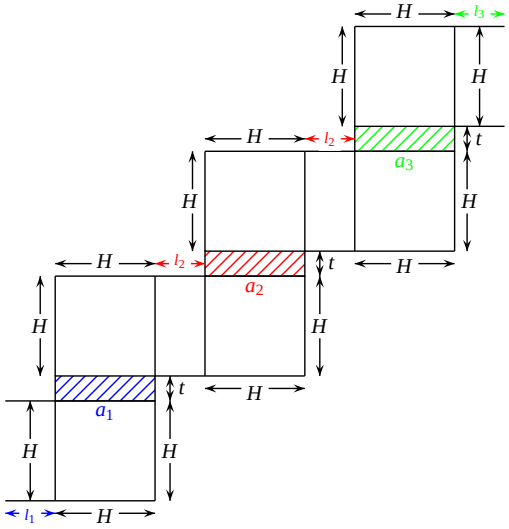

(b) Geometry of the E-plane folded 5.

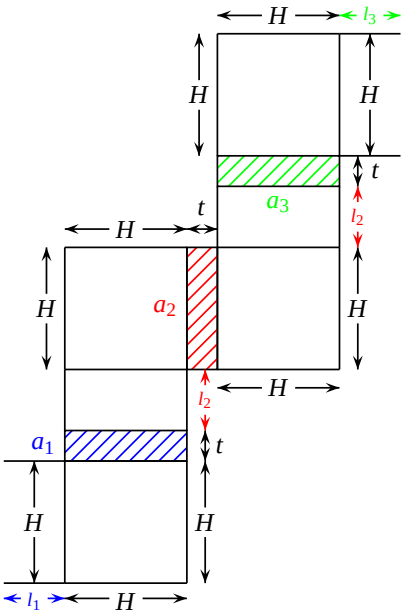

(c) Geometry of the E-plane folded 6.

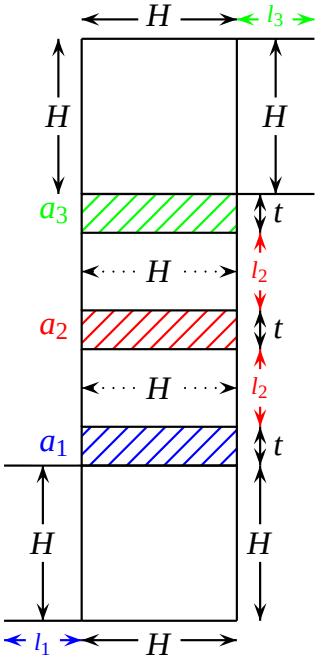

(d) Geometry of the E-plane folded 7.

Figure 5.60: Geometry of the central section of the E-plane folded configurations 4 to 7 (side view).

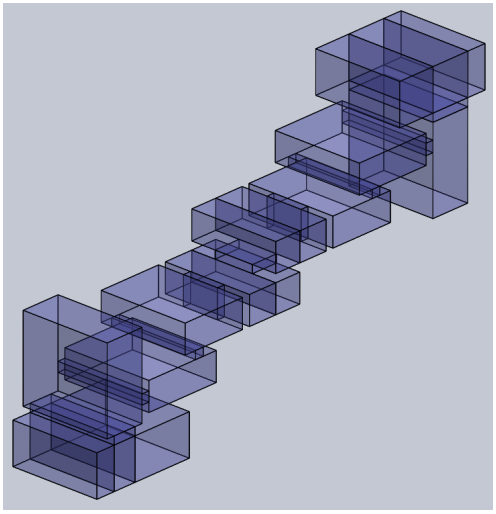

Figure 5.61: Structure of the hybrid staircase filter with manifold inputs, and folded central section (Folded 1 configuration).

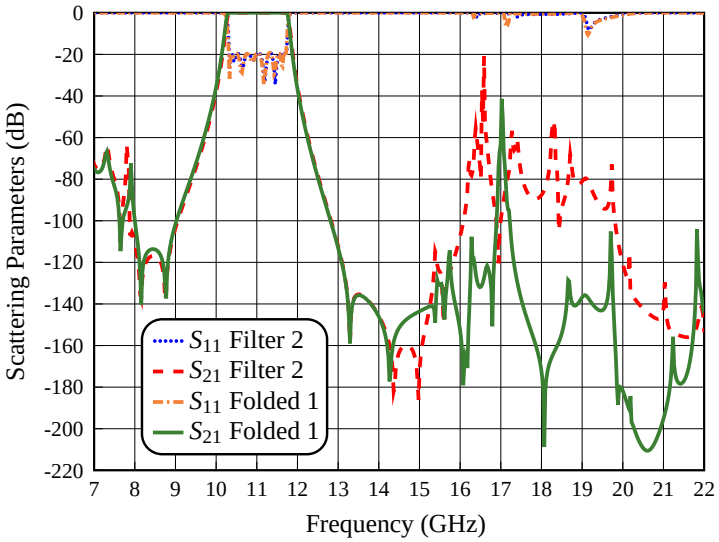

Figure 5.62: Simulated performance of the hybrid staircase filter with manifold connections (Filter 2) compared to the performance of the Filter 2 with folding option 1 (Folded 1).

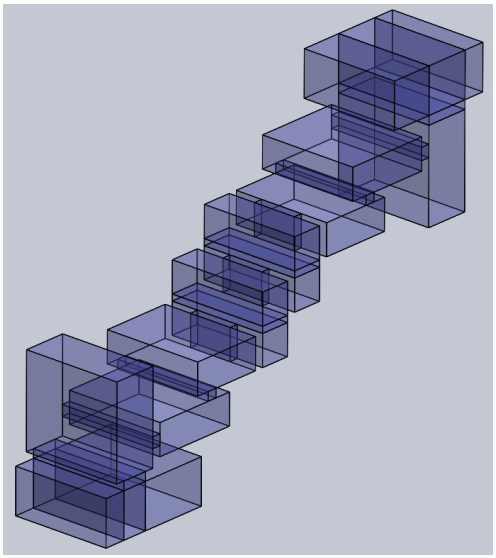

Figure 5.63: Structure of the hybrid staircase filter with manifold inputs, and folded central section (Folded 2 configuration).

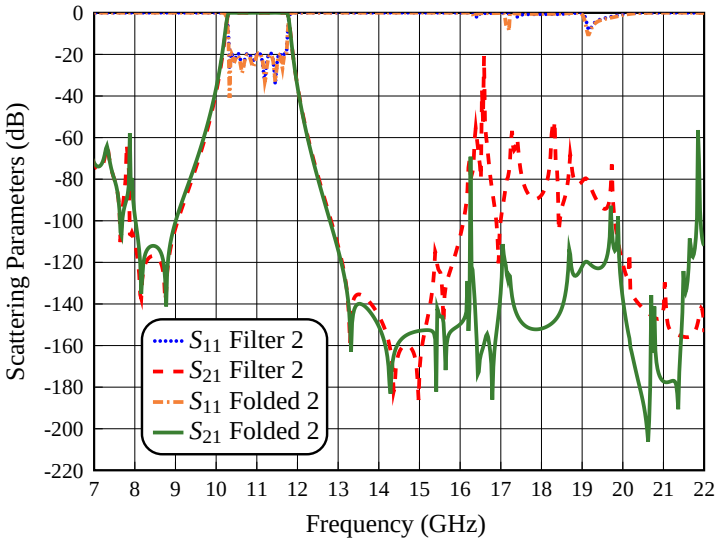

Figure 5.64: Simulated performance of the hybrid staircase filter with manifold connections (Filter 2) compared to the performance of the Filter 2 with folding option 2 (Folded 2).

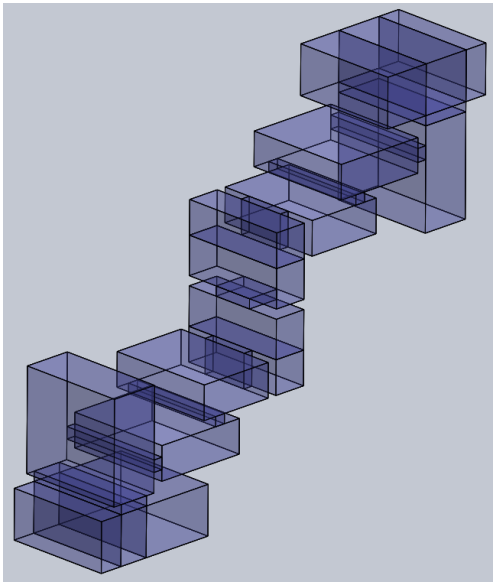

Figure 5.65: Structure of the hybrid staircase filter with manifold inputs, and folded central section (Folded 3 configuration).

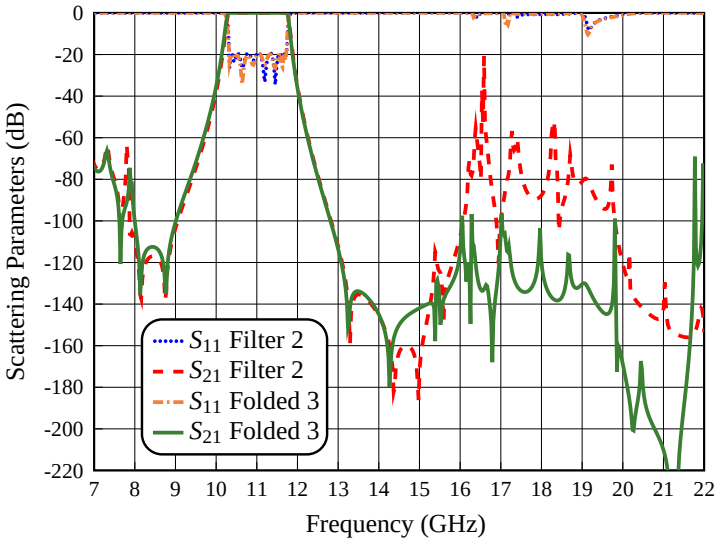

Figure 5.66: Simulated performance of the hybrid staircase filter with manifold connections (Filter 2) compared to the performance of the Filter 2 with folding option 3 (Folded 3).

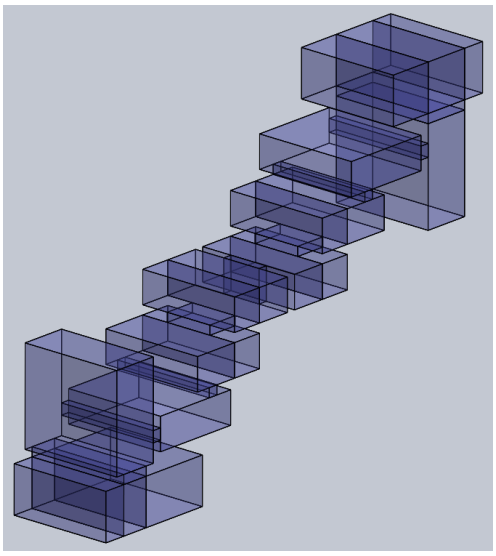

Figure 5.67: Structure of the hybrid staircase filter with manifold inputs, and folded central section (Folded 4 configuration).

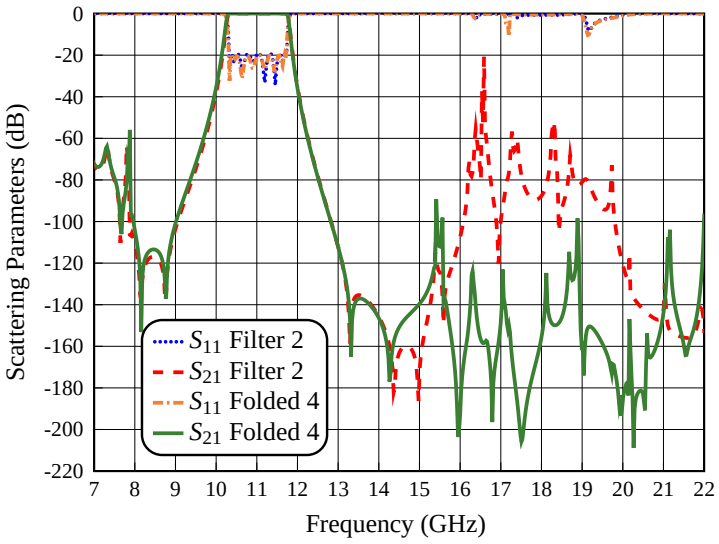

Figure 5.68: Simulated performance of the hybrid staircase filter with manifold connections (Filter 2) compared to the performance of the Filter 2 with folding option 4 (Folded 4).

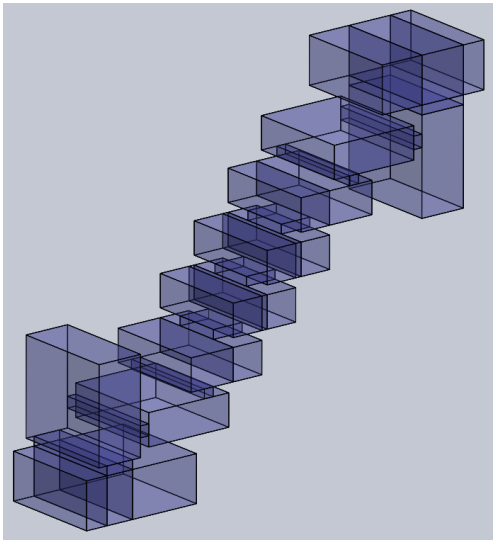

Figure 5.69: Structure of the hybrid staircase filter with manifold inputs, and folded central section (Folded 5 configuration).

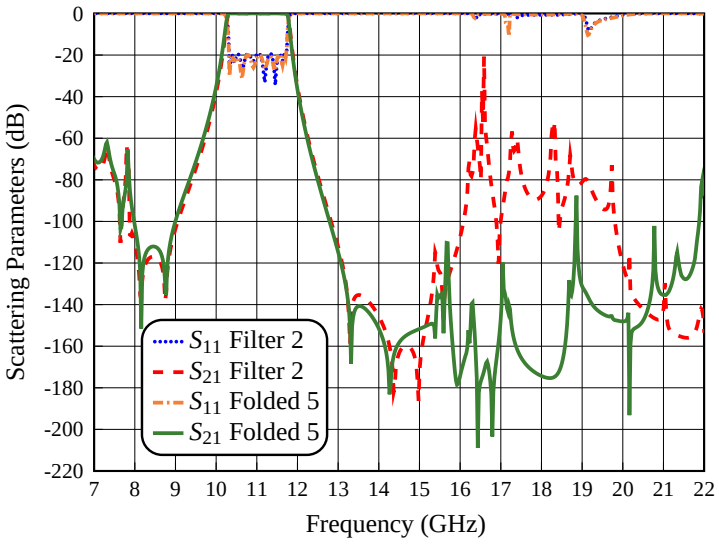

Figure 5.70: Simulated performance of the hybrid staircase filter with manifold connections (Filter 2) compared to the performance of the Filter 2 with folding option 5 (Folded 5).

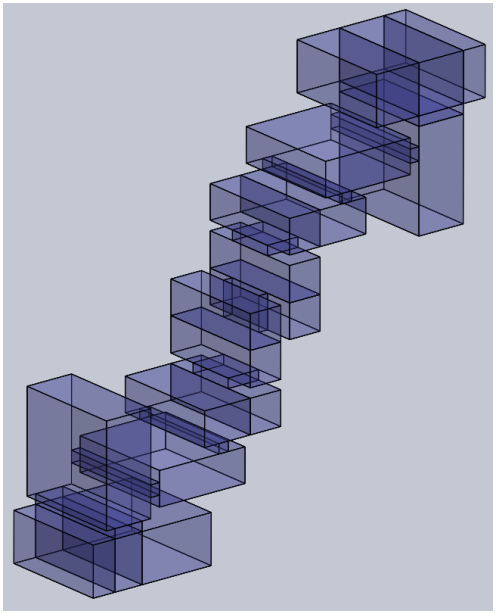

Figure 5.71: Structure of the hybrid staircase filter with manifold inputs, and folded central section (Folded 6 configuration).

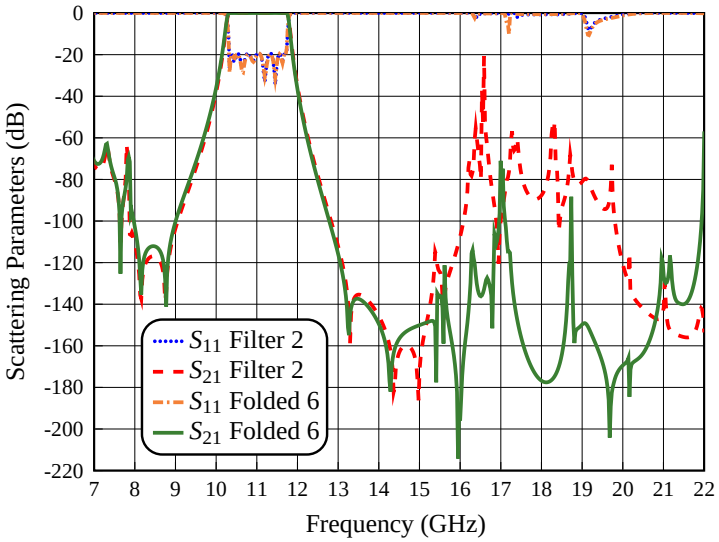

Figure 5.72: Simulated performance of the hybrid staircase filter with manifold connections (Filter 2) compared to the performance of the Filter 2 with folding option 6 (Folded 6).

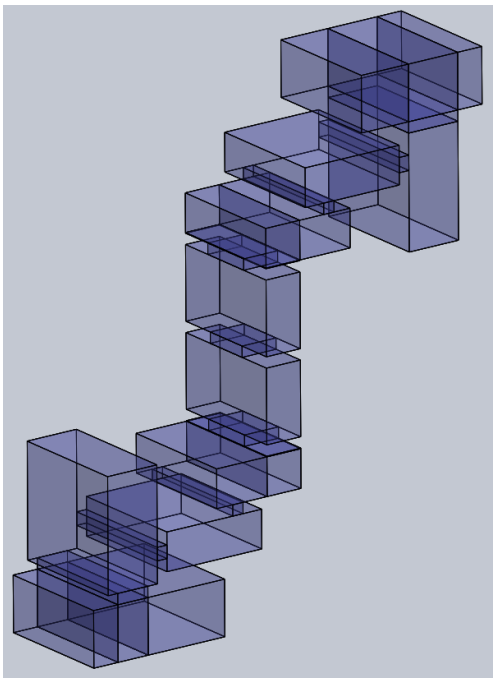

Figure 5.73: Structure of the hybrid staircase filter with manifold inputs, and folded central section (Folded 7 configuration).

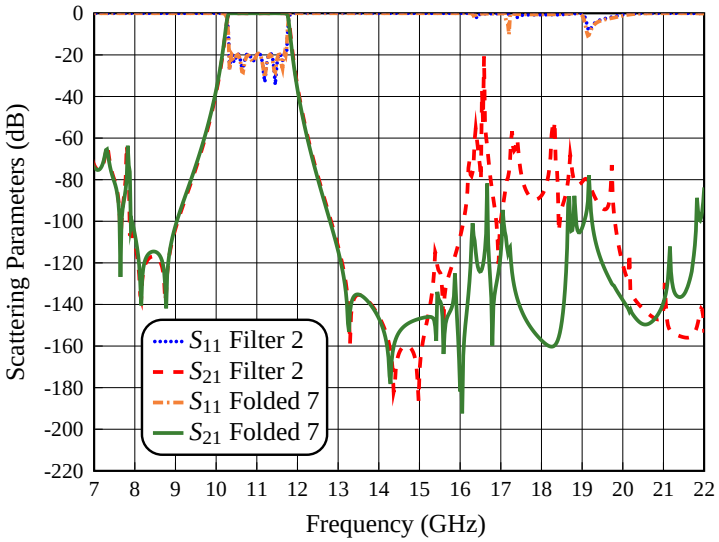

Figure 5.74: Simulated performance of the hybrid staircase filter with manifold connections (Filter 2) compared to the performance of the Filter 2 with folding option 7 (Folded 7).

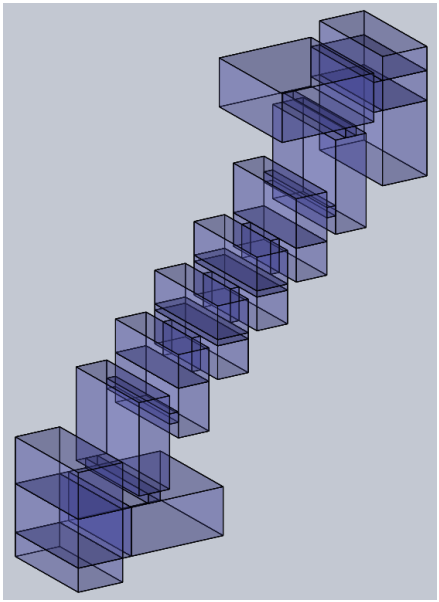

Figure 5.75: Structure of the hybrid staircase filter with manifold inputs and folded central section (Folded 5 configuration), designed with sharp concave corners.

We can therefore conclude that using the Folded 5 configuration results into a further improvement in the reduction and attenuation of the harmonic resonances, and, at the same time, in a more compact structure.

5.5 The Prototype

We now have a filter structure with a very good out-of-band performance. However, all simulations up to now have been performed with FEST3D with a Low-Accuracy (LA) setting. The next step is, therefore, to obtain the High-Accuracy (HA) structure that can then be manufactured. To continue, we now use the same procedure explained in Chapters 3 and 4. As usual, the sharp concave corners (see Fig. 5.75) have been changed into rounded corners of radius equal to $r = 1.1$ mm, in order to facilitate manufacturing.

Fig. 5.76 shows the final structure obtained once rounded corners are included. In Fig. 5.77 we show the comparison of the LA performance (FEST3D), and the HA performance (CST Studio Suite) of the structures in Fig. 5.75 and Fig. 5.76.

As we can see, the agreement in the filter performance is generally very good from 7 to 15.5 GHz. However, in the high frequency end, namely from 15.5 to 22 GHz, we can see a significant difference in the peak levels of the spurious responses. This is due to the fact that in the LA simulations (FEST3D) we have not included enough higher order modes. In this context, the parameters used in each simulator are as follows:

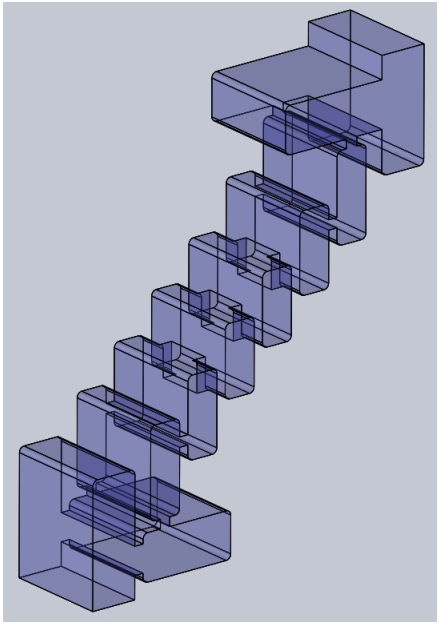

Figure 5.76: Structure of the hybrid staircase filter with manifold inputs and folded central section (Folded 5 configuration), designed with a radius equal to $r = 1.1$ mm.

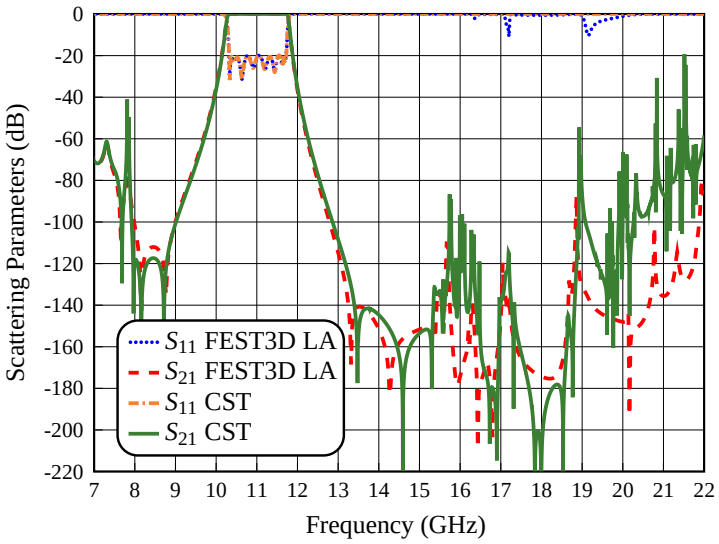

Figure 5.77: Simulated performance of the hybrid staircase filter with manifold inputs and folded central section (Folded 5 configuration), using FEST3D LA and CST.

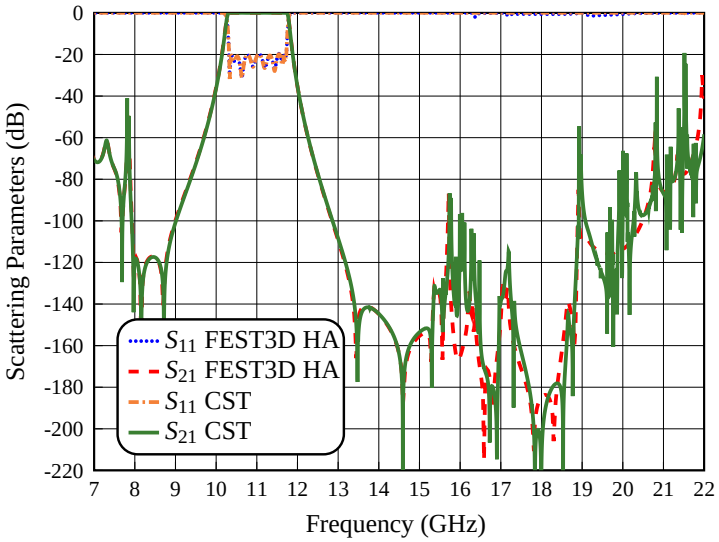

Figure 5.78: Simulated performance of the hybrid staircase filter with manifold inputs and folded central section (Folded 5 configuration), using FEST3D HA and CST.

- Simulator FEST3D LA
- Accessible modes: 16
- Number of basis functions: 48
- Green's function terms: 480

- Simulator CST
- Solver: Frequency Domain Solver
- Frequency Sweep: General Purpose
- Mesh refinement: 11 GHz
- Error Threshold: 0.01
- Maximum number of iterations: 50

To attempt to eliminate the differences in the simulations for the high frequency end, we then performed additional simulations in FEST3D with high accuracy. The parameters used for FEST3D in HA mode are as follow.

- Simulator FEST3D HA
- Accessible modes: 100
- Number of basis functions: 300
- Green's function terms: 3000

Fig. 5.78 shows the comparison of the simulated performances obtained with FEST3D HA and CST for the structures of Fig. 5.75 and Fig. 5.76, respectively.

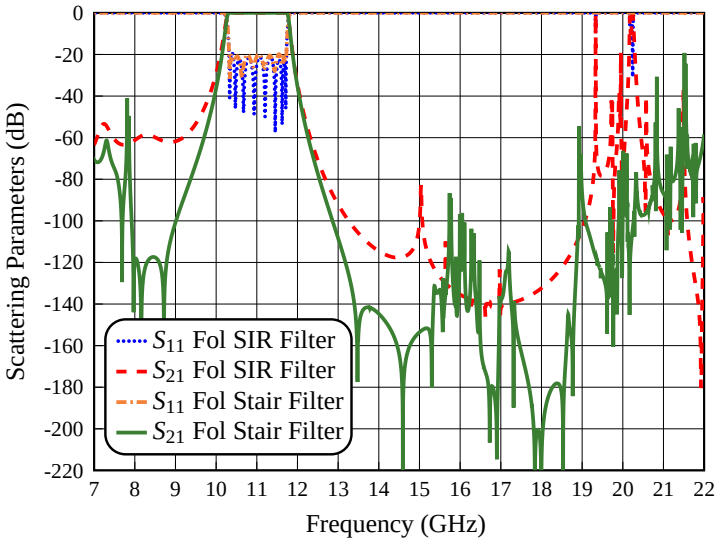

Figure 5.79: Simulated performance of the E-plane folded hybrid SIR filter (Fol SIR Filter), and the E-plane folded hybrid staircase filter with manifold connections (Fol Stair Filter) using CST.

As we can see, the agreement in the simulations of both FEST3D HA and CST in the high frequency end is now generally very good. Tables 5.4 and 5.5 show the final values for all dimensions of the E-plane folded hybrid staircase filter with manifold connections. The dimensions are given up to the center of the filter. This is because the central inductive part of the filter is symmetrical. The thickness of the windows is t, and all resonators have the same width as the input waveguide.

To conclude our design, we have compared the performance of the E-plane folded hybrid SIR filter (Fol SIR Filter) discussed in Chapter 4, with the E-plane folded hybrid staircase filter (Fol Stair Filter) discussed in this chapter. Fig. 5.79 shows the comparison of the simulated performances obtained with CST for the two structures. As we can clearly see, the out-of-band response and the selectivity of the Fol Stair Filter are significantly improved with respect to the Fol SIR Filter. Furthermore, the filter structure discussed in this chapter is significantly simpler than the one discussed in the Chapter 4.

Table 5.4: Physical dimensions (manifold T-junctions and coupling windows) for the E-plane folded hybrid staircase filter with manifold connections.

Section Type	Dimensions (mm)
Input Waveguide	$a = 22.86$ $b = 10.16$ $L_{input} = L_{output} = 25$
Manifold T-junction 1-2	$a = 22.86$ $b = 10.16$ $l_{m1} = 9.660$ $l_{m2} = 15.750$
Capacitive window 1-6	$a = 22.86$ $b_1 = 10.16$ $b_6 = 6.026$ $t = 2$
Capacitive window 2-5	$a = 22.86$ $b_2 = 2.557$ $b_5 = 2.277$ $t = 2$
Capacitive window 3-4	$a = 22.86$ $b_3 = 2.110$ $b_4 = 2.110$ $t = 2$
Inductive window 1-3	$a_1 = a_3 = 10.461$ $b = 7.000$ $t = 2$
Inductive window 2	$a_2 = 9.858$ $b = 7.000$ $t = 2$

Table 5.5: Physical dimensions (resonators) for the E-plane folded hybrid staircase filter with manifold connections.

Section Type	Dimensions (mm)
Input Waveguide	$a = 22.86$ $b = 10.16$ $L_{input} = L_{output} = 25$
Resonator 1-8	$H_1 = 10.16$ $L_1 = 21.294$ $H_8 = 10.16$ $L_8 = 21.213$
Resonator 2-7	$H_2 = 7.000$ $L_2 = 19.420$ $H_7 = 7.000$ $L_7 = 19.659$
Resonator 3-6	$H_3 = 7.000$ $L_3 = 17.379$ $H_6 = 7.000$ $L_6 = 17.379$
Resonator 4-5	$H_4 = 7.000$ $L_4 = 15.505$ $H_5 = 7.000$ $L_5 = 15.505$

Table 5.6: Results of the tolerance analysis.

Filter Type	Yield of the Structures					
Tolerance	5 μm	10 μm	15 μm	20 μm	25 μm	40 μm
Folded 5 Filter	94 %	72 %	38 %	18 %	12 %	2 %

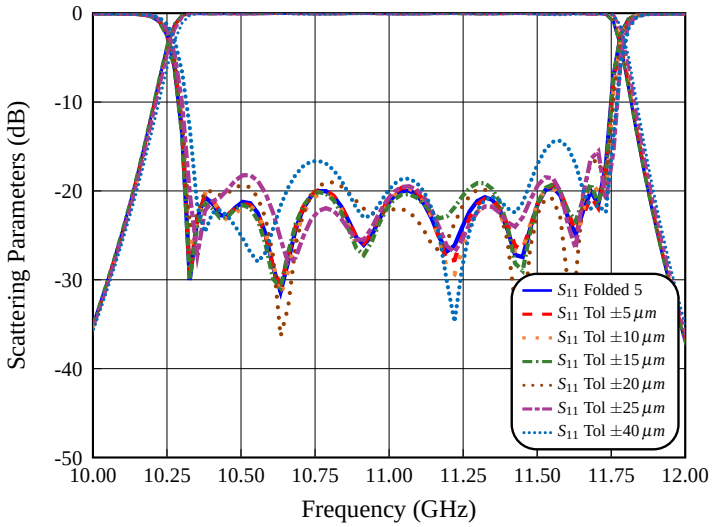

Figure 5.80: Tolerance analysis of the considered E-plane folded hybrid staircase filter with manifold connections (Folded 5).

5.5.1 Yield Analysis

It is important to note at this point that the filter structure we have designed does not include tuning elements. Therefore, before we manufacture the filter, we need to perform a yield analysis to select the most appropriate manufacturing process. For this purpose, we have used the simulator FEST3D to carry out a sensitivity analysis.

We have next selected a number of different values for the standard deviation of the considered nominal dimensions, namely ± 5, ± 10, ± 15, ± 20, ± 25 and ± 40 μm. Furthermore, the threshold value for the yield estimation has been set to 18 dB, since our filter has been designed with a return loss of 20 dB. The results obtained are shown in Table 5.6.

Fig. 5.80 shows the simulated behavior of the structure of Fig. 5.75 (Folded 5 Filter) using standard deviations from ± 5 to ± 40 μm. As we can see, with manufacturing errors between 5 and 10 μm, it should be possible to obtain an acceptable response. With manufacturing errors above 25 μm, the response of the filter is completely deteriorated.

Table 5.7: High power analysis of the the considered E-plane folded hybrid staircase filter with manifold connections (Folded 5).

Structure	Power of the structure		
Frequency	$f_1 = 10.30$ GHz	$f_2 = 11.00$ GHz	$f_3 = 11.73$ GHz
b_3	5093 W	3531 W	1179 W
$a_1 = a_3$	3718 W	21374 W	21124 W
a_2	4281 W	24748 W	17374 W
RES 3	7350 W	38250 W	31125 W
RES 4	908.5 kW	942.5 kW	270.5 kW

5.5.2 High Power Analysis

As we have done for all the other filter structures discussed so far, we are now going to discuss the high power behavior to identify the power (in W) where the multipactor effect is initiated. For this purpose, we have used FEST3D to compute the EM fields, and SPARK3D for the multipaction prediction. The simulations have been carried out where the group delay shows a maximum in the filter response (f_1 and f_3), and at the center frequency of the filter (f_2). It is important to mention that we have concentrated our attention on the central section of the filter due to the small dimensions of the irises, namely b_3, a_1 and a_2, and of the resonators 3 and 4, i.e. H_3 and H_4. The set of parameters for the high power analysis are as follow:

1. Initial power: 500 W
2. Maximum power: 1 MW
3. Growth factor of the power: 10^2
4. Frequencies of simulation: f_1, f_2 and f_3
5. Initial number of electrons: 10000

The power thresholds obtained are shown in Table 5.7. As we can see, the capacitive window (b_3) shows the lowest power threshold at 11.73 GHz with 1179 W. The values obtained for each simulation in the capacitive window (b_3) are shown in Fig. 5.81.

Our analysis clearly indicates that this last filter structure is able to withstand significantly higher power levels as compared to the ones we discussed before (see Chapters 3 and 4). Furthermore, the power level obtained is now fully consistent with the levels currently used in the majority of space applications.

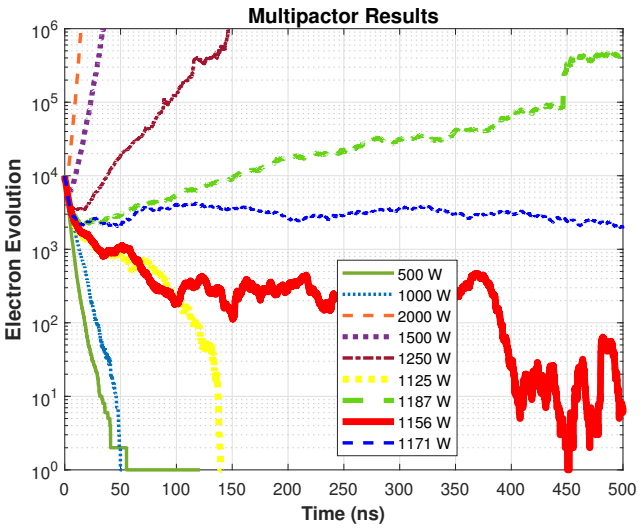

Figure 5.81: Multipactor simulation with discharges for the capacitive window (b_3) of Folded 5 filter at 11.73 GHz.

5.5.3 Measurements

A prototype of the E-plane folded hybrid staircase filter with manifold connections (Folded 5) has been manufactured in a clam-shell configuration, using a combination of standard milling and spark erosion techniques as shown in Fig. 5.82.

It is important to note that most of the filter has been manufactured with standard milling. However, for the small capacitive irises, namely b_3 and b_4, it is mandatory to use spark erosion.

We show, next, the comparison between the measured and the simulated in-band responses of the prototype manufactured, as shown in Fig. 5.83. As we can see, the agreement between simulations and measurements is excellent. The in-band performance is centered at 11 GHz, and the reflection zeros of the filter are clearly visible.

Fig. 5.84 shows the comparison between the measured and the simulated out-of-band responses. To measure the electrical response in such a wide frequency range, we have used four standard waveguide calibrations, namely, WR-90, WR-75, WR-62 and WR-51. All calibrations have been performed using the TRL (Through, Reflection and Line) method. The noise floor achieved in each calibration is about -70 dB.

As we can see, the agreement between simulations and measurements in the out-of-band response is also good. However, a spike reaching -50 dB at about 16.15 GHz has appeared. It is important to mention that the manufacturing error in the prototype has been kept below 10 μm for all the curved corners, and below 5 μm for all other filter

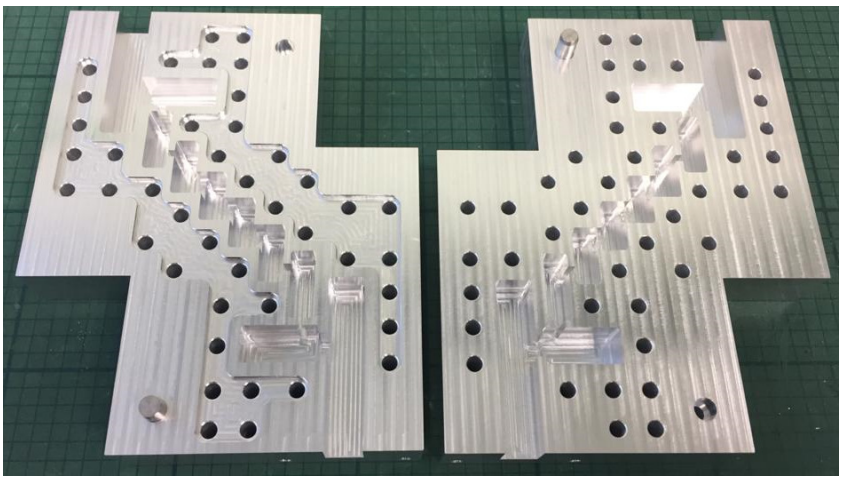

Figure 5.82: Manufactured prototype in aluminum of the E-plane folded hybrid staircase filter with manifold connections (Folded 5), without silver plating.

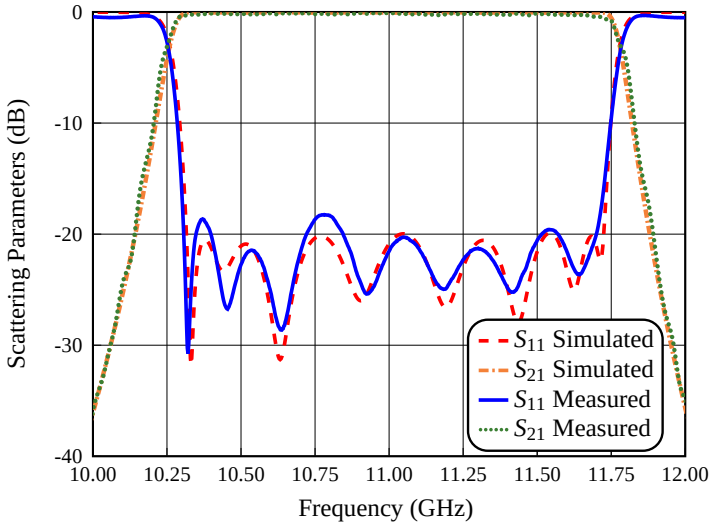

Figure 5.83: Measurement of the in-band performance of Folded 5 filter compared with the EM simulation (CST).

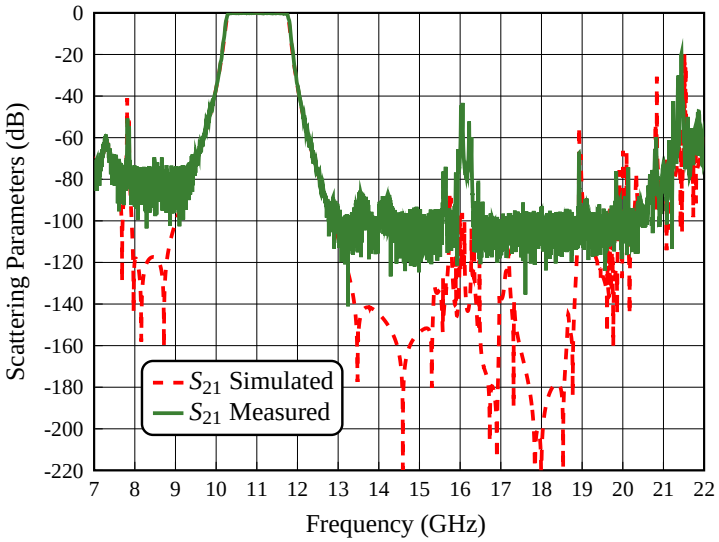

Figure 5.84: Measurement of the out-of-band performance of Folded 5 filter compared with the EM simulation (CST).

elements. The results obtained are therefore fully consistent with the yield analysis that we have performed before.

5.6 High Order Modes Effects

All of the measured results discussed so far, have been obtained using only the fundamental TE_{10} mode excitation. As we have already done for all other filter structures that we discussed in Chapters 3 and 4, we are now going to study the behavior of this last filter under higher order modes excitation. The cut-off frequencies of the higher order modes that we use for this study are shown in Table 5.8.

Fig. 5.85, Fig. 5.86, Fig. 5.87, Fig. 5.88, and Fig. 5.89 show the comparison of the simulated performances of Folded 5 filter excited with the higher order TE_{20}, TE_{01}, TE_{11}, TM_{11}, TE_{30}, TE_{21} and TM_{21} modes obtained with FEST3D and CST.

As we can see, the presence of the TE_{01}, TE_{11}, TM_{11}, TE_{21} and TM_{21} modes in the excitation does not deteriorate the out-of-band response of the filter. However, the higher order mode TE_{20} shows a spurious response at about 16 GHz, as shown in Fig. 5.85. Furthermore, the higher order mode TE_{30} shows a spurious response beginning at about 21.4 GHz with spikes reaching about -10 dB from 19.7 GHz, as shown in Fig. 5.88.

Table 5.8: The higher order modes cut-off frequencies of the Folded 5 filter.

Mode	Cut-off frequency
Waveguide WR-90	a =22.86 mm b =10.16 mm
TE_{10}	f_c =6.557 GHz
TE_{20}	f_c =13.114 GHz
TE_{01}	f_c =14.753 GHz
TE_{11}	f_c =16.145 GHz
TM_{11}	f_c =16.145 GHz
TE_{30}	f_c =19.671 GHz
TE_{21}	f_c =19.739 GHz
TM_{21}	f_c =19.739 GHz

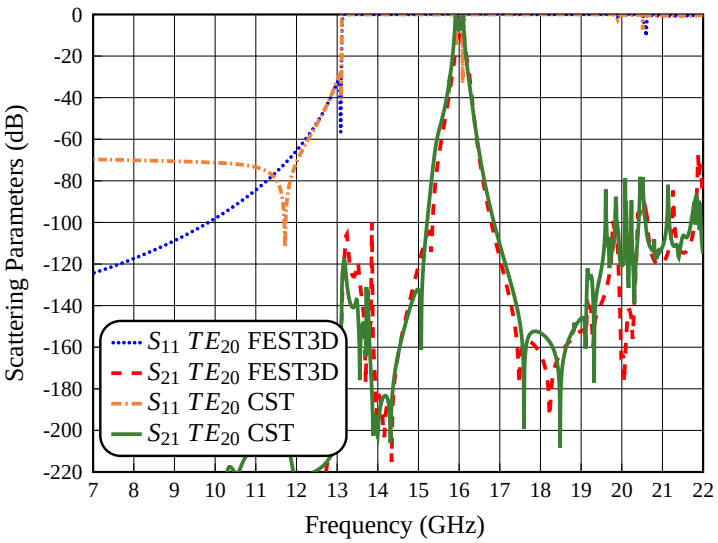

Figure 5.85: Simulated performance of the hybrid staircase filter with manifold inputs and folded central section (Folded 5), for the higher order mode TE_{20} using FEST3D and CST.

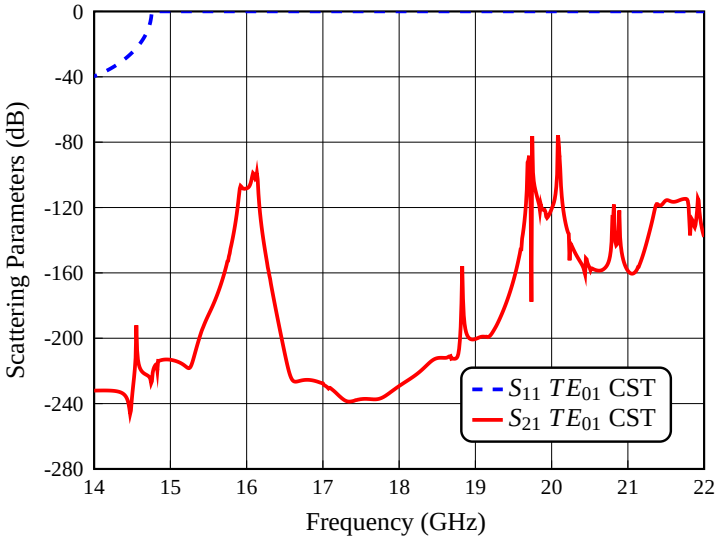

Figure 5.86: Simulated performance of the hybrid staircase filter with manifold inputs and folded central section (Folded 5), for the higher order mode TE_{01} using CST.

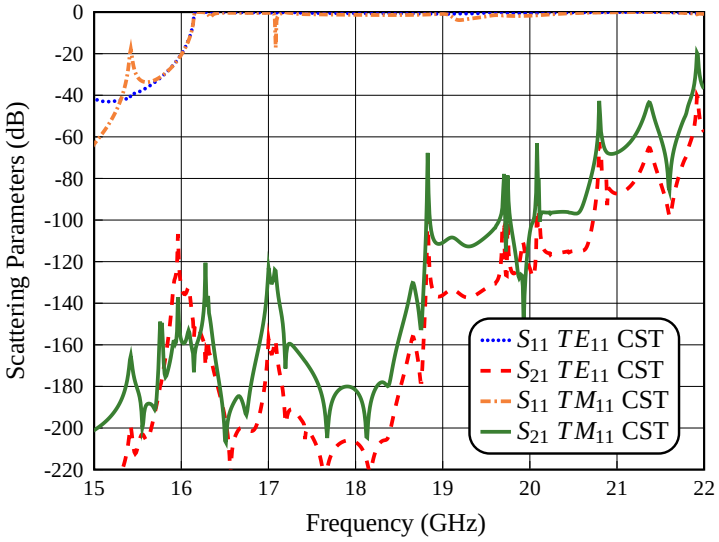

Figure 5.87: Simulated performance of the hybrid staircase filter with manifold inputs and folded central section (Folded 5), for the higher order modes TE_{11} and TM_{11} using CST.

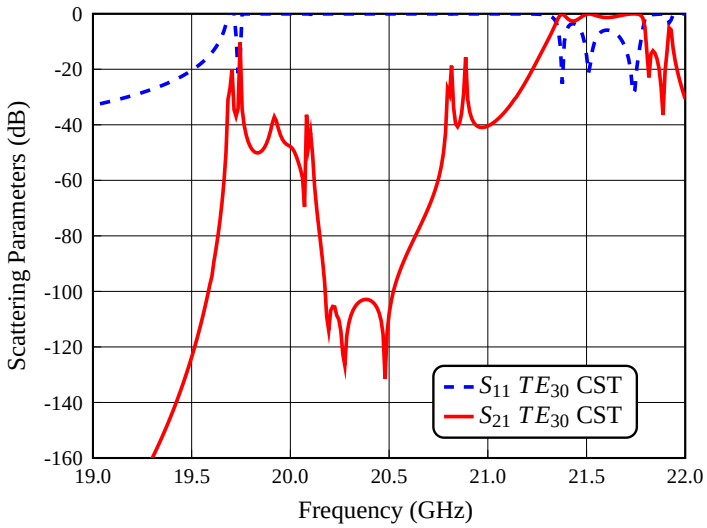

Figure 5.88: Simulated performance of the hybrid staircase filter with manifold inputs and folded central section (Folded 5), for the higher order mode TE_{30} using CST.

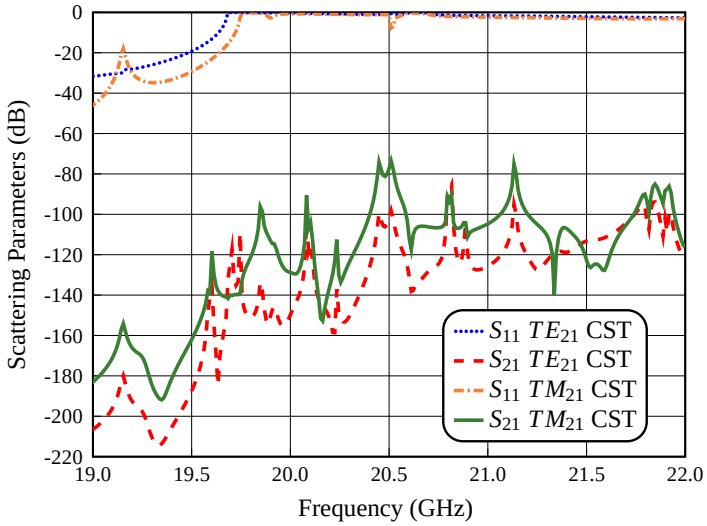

Figure 5.89: Simulated performance of the hybrid staircase filter with manifold inputs and folded central section (Folded 5), for the higher order modes TE_{21} and TM_{21} using CST.

It is important to mention that the slight differences between simulated and measured out-of-band performances of our prototype, could indeed be due to the higher order modes that are excited by manufacturing errors in the structure. However, it is clear from the results obtained that the presence of higher order modes in the excitation produces spurious responses that should be suppressed because they degrade the response of the filter.

To continue, we recall that the procedure we used to measure our filter requires the connection of the filter to a vector network analyzer (VNA) with two coaxial-to-waveguide transitions. The use of the coaxial transitions does ensure that only the fundamental TE_{10} mode is excited in the waveguide. As result, no spurious signal in the input of the filter is indeed observed. Furthermore, in many actual applications, it is very common to use coaxial cables and waveguide transitions to connect waveguide devices to each other. In that case, therefore, no particular action is necessary since the unwanted inputs are not present.

In some applications, however, rectangular waveguide filters may be connected to other components using lengths of rectangular waveguide. In that case, therefore, it is possible that higher order modes are excited in the payload before the filter. The higher order modes would then appear as spurious responses after the filter, and this is clearly not acceptable.

To address this issue, we now propose two simple approaches to suppress the effects of the presence of higher order modes in the input of the filter.

5.6.1 H-Plane Transformer

The first approach is to connect at the output of the filter the device shown in Fig. 5.90. This device is a simple high-pass filter consisting of an H-plane transformer that uses rectangular waveguide sections of smaller width. The length of the narrower waveguide can be chosen to obtain the needed level of spurious rejection.

This simple device is effective because the narrowest waveguide is above cutoff for the bandpass frequencies, but is below cutoff for the unwanted higher order modes. This technique is well known and it is indeed of general value.

The dimensions of the simple high-pass filter proposed in this section are shown in Table 5.9. The dimensions are given up to the center of the device, since the high-pass filter is symmetrical.

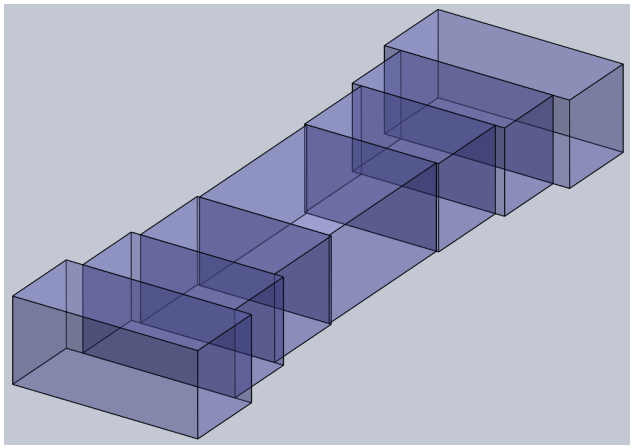

Figure 5.90: Structure of the H-plane transformer composed of rectangular waveguide sections of smaller width.

Table 5.9: Physical dimensions for the high-pass filter.

Section Type	Dimensions (mm)
Input Waveguide	$a = 22.86$ $b = 10.16$ $L_{input} = 10$
Section 1	$w_1 = 18.788$ $h_1 = 10.16$ $L_1 = 9.057$
Section 2	$w_2 = 16.556$ $h_2 = 10.16$ $L_2 = 10.604$
Section 3	$w_3 = 16.000$ $h_3 = 10.16$ $L_3 = 20.000$

In order to demonstrate the improvement introduced by the device that we have proposed, we now show in Fig. 5.91 and Fig. 5.92 the effect of adding the high-pass device to our filter when the TE_{20} and TE_{30} higher order modes are present in the input. As we can see, the TE_{20} mode now shows spurious responses below -70 dB from 15 to 21 GHz, and -60 dB from 21 to 22 GHz. The TE_{30} mode now shows spurious responses below -50 dB from 19.50 to 21.25 GHz and -30 dB from 21.25 to 22 GHz. This is indeed an important improvement.

We have therefore clearly demonstrated that, using the simple device shown in Fig. 5.90 results in an important attenuation and reduction of the spurious responses generated by the higher order modes.

5.6.2 Changing Central Resonator Width

The second approach that we discuss is to change the width of the waveguide that is used to implement the central resonators in our filter. This technique is also very well-known, and is very frequently used to improve the out-of-band response of rectangular waveguide filters. In our case, we can use this approach because all the resonators of the folded hybrid staircase filter designed in the previous sections have the same width as the input waveguide. Fig. 5.93 shows the structure of the folded hybrid staircase filter where the width of the central resonators has been reduced. Fig. 5.94 shows the structure with rounded corners.

Fig. 5.95 shows the comparison of the simulated performances obtained with FEST3D (HA) and CST for the structures in Fig. 5.93 and Fig. 5.94, respectively. As we can see, the agreement in the out-of-band response of the filter is very good. The use of this simple technique results in a very good out-of-band response, with spurious below -50 dB from 13 to 22 GHz and a spike reaching -12.5 dB at 21.50 GHz.

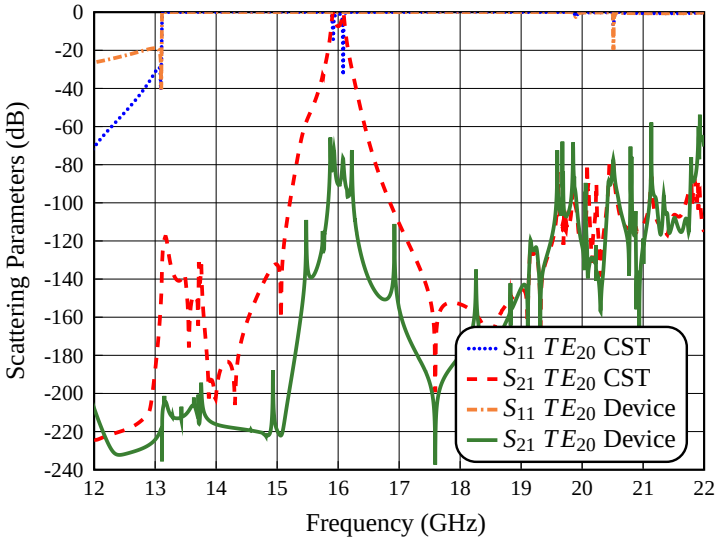

Figure 5.91: Simulated performance (using CST) of our filter with TE_{20} excitation (TE_{20} CST) compared to the performance of the filter plus the high-pass device (TE_{20} Device).

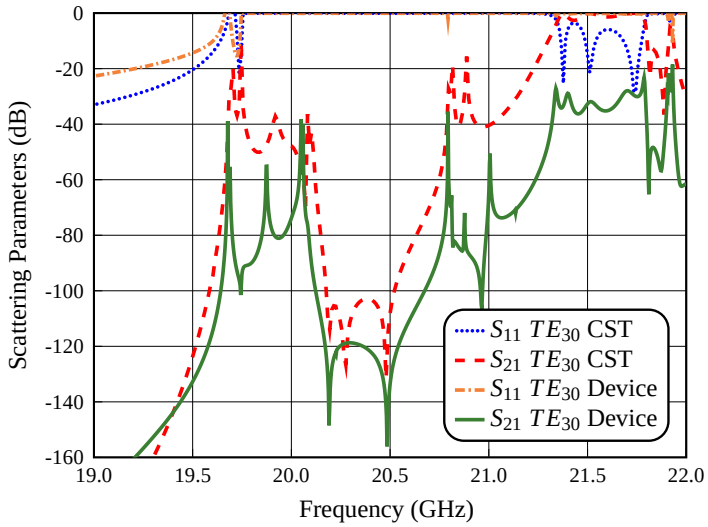

Figure 5.92: Simulated performance (using CST) of our filter with TE_{30} excitation (TE_{30} CST) compared to the performance of the filter plus the high-pass device (TE_{30} Device).

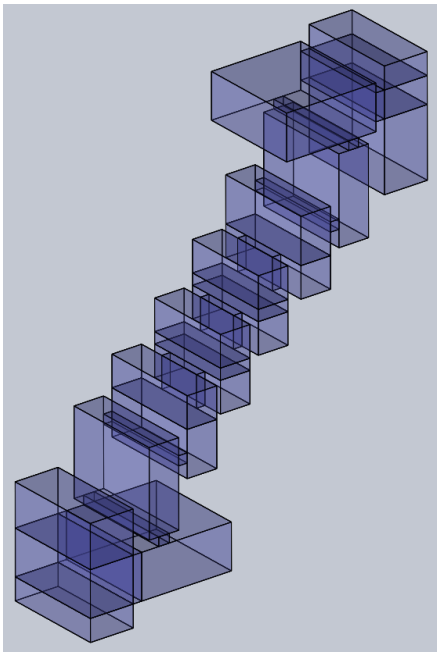

Figure 5.93: Structure of the hybrid staircase filter with manifold inputs and folded central section (Folded 5), designed with sharp concave corners and reducing the width of the central resonators.

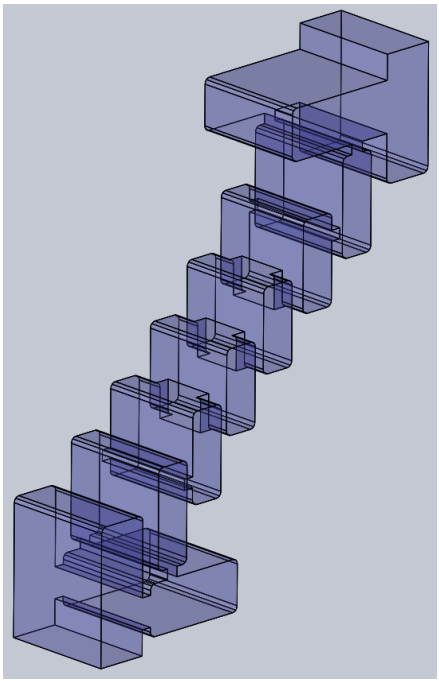

Figure 5.94: Structure of the hybrid staircase filter with manifold inputs and folded central section (Folded 5), designed with a radius equal to $r = 1.1$ mm and reducing the width of the central resonators.

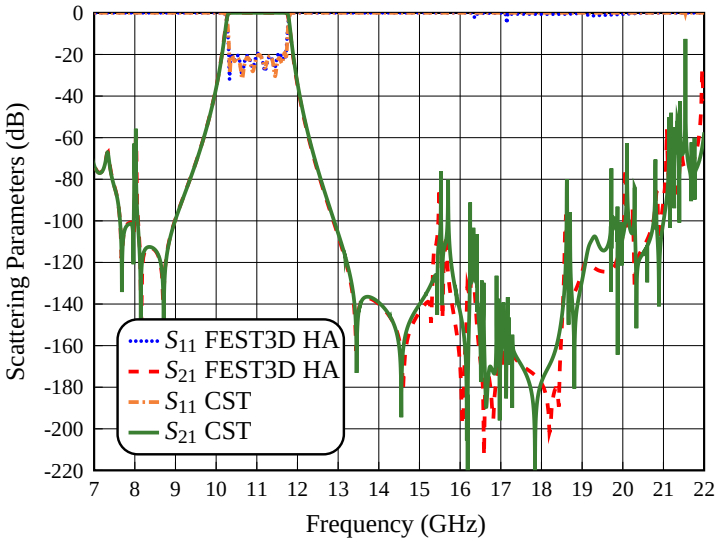

Figure 5.95: Simulated performance of the structures in Fig. 5.93 and Fig. 5.94 (reducing the widths of the central resonators) using FEST3D HA and CST.

Furthermore, Fig. 5.96 and Fig. 5.97 show the comparison of the simulated responses of the modified filter when the higher order modes TE_{20} and TE_{30} are used as excitation. As we can see, the TE_{20} mode now shows spurious responses below -50 dB from 15 to 19.50 GHz. Furthermore, the TE_{30} mode now shows spurious responses below -70 dB from 19.50 to 20.75 GHz, and an important reduction of the spurious from 20.75 to 22 GHz, respectively. This is indeed an important improvement.

Finally, the final values for all dimensions of the modified filter in Fig. 5.94 are shown in Tables 5.10 and 5.11. The dimensions are given up to the center of the filter. This is because the inductive central part of the filter is symmetrical, however the dimensions of the asymmetric parts of the whole structure are also included. The thickness of the windows is t.

We have therefore clearly demonstrated that, by reducing the width of the central resonators we can effectively improve the out-of-band response of our filter and, at the same time, attenuate and reduce the spurious responses generated by the presence of higher order modes in the structure.

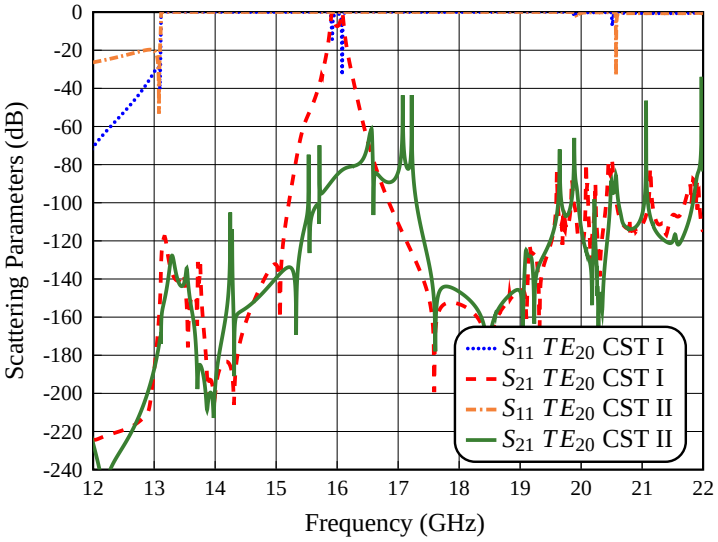

Figure 5.96: Simulated performance (using CST) of the filter in Fig. 5.76 with TE_{20} excitation (TE_{20} CST I), compared to the performance of the filter in Fig. 5.94 reducing the widths of the central resonators (TE_{20} CST II).

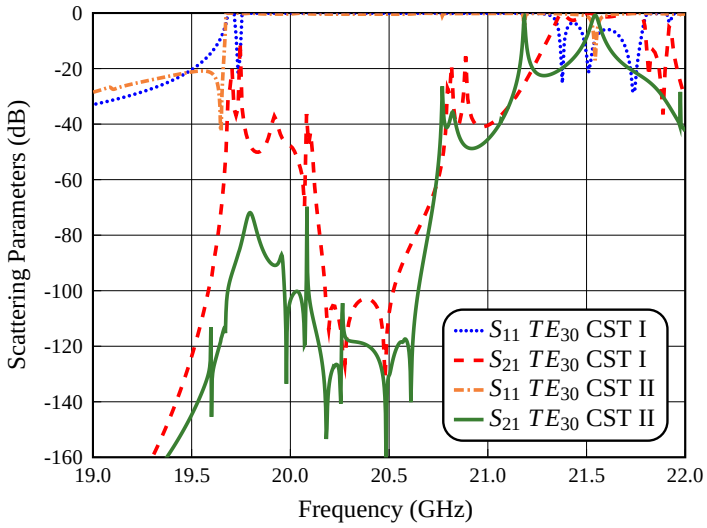

Figure 5.97: Simulated performance (using CST) of the filter in Fig. 5.76 with TE_{30} excitation (TE_{30} CST I), compared to the performance of the filter in Fig. 5.94 reducing the widths of the central resonators (TE_{30} CST II).

Table 5.10: Physical dimensions (manifold T-junctions and coupling windows) for the new E-plane folded hybrid staircase filter with manifold connections, and reducing the width of the central resonators.

Section Type	Dimensions (mm)
Input Waveguide	$a = 22.86$ $b = 10.16$ $L_{input} = L_{output} = 5$
Manifold T-junction 1-2	$a = 22.86$ $b = 10.16$ $l_{m1} = 9.671$ $l_{m2} = 15.750$
Capacitive window 1-6	$a = 22.86$ $b_1 = 10.16$ $b_6 = 6.065$ $t = 2$
Capacitive window 2-5	$a = 22.86$ $b_2 = 2.629$ $b_5 = 2.323$ $t = 2$
Capacitive window 3-4	$a = 21.50$ $b_3 = 2.098$ $b_4 = 2.098$ $t = 2$
Inductive window 1-3	$a_1 = a_3 = 10.604$ $b = 7.000$ $t = 2$
Inductive window 2	$a_2 = 10.081$ $b = 7.000$ $t = 2$

Table 5.11: Physical dimensions (resonators) for the new E-plane folded hybrid staircase filter with manifold connections, and reducing the width of the central resonators.

Section Type	Dimensions (mm)
Input Waveguide	$a = 22.86$ $b = 10.16$ $L_{input} = L_{output} = 5$
Resonator 1-8	$W_1 = 22.86$ $W_8 = 22.86$ $H_1 = 10.16$ $L_1 = 21.334$ $H_8 = 10.16$ $L_8 = 21.322$
Resonator 2-7	$W_2 = 22.86$ $W_7 = 22.86$ $H_2 = 7.000$ $L_2 = 19.467$ $H_7 = 7.000$ $L_7 = 19.726$
Resonator 3-6	$W_3 = 21.50$ $W_6 = 21.50$ $H_3 = 7.000$ $L_3 = 17.943$ $H_6 = 7.000$ $L_6 = 17.943$
Resonator 4-5	$W_4 = 20.00$ $W_5 = 20.00$ $H_4 = 7.000$ $L_4 = 16.265$ $H_5 = 7.000$ $L_5 = 16.625$

5.7 Conclusions

In this chapter, we have discussed the design of a novel hybrid wide-band filter in rectangular waveguide based on the use of a staircase configuration. Furthermore, we have shown that using the staircase configuration, together with E-plane manifold connections and a folded central section, it is possible to develop a simple filter with a very wide spurious-free out-of-band response, and with a significantly improved selectivity.

Furthermore, we have also carried out the tolerance and high power analysis. The results obtained confirm that the structure we have developed can be manufactured with the currently available industrial processes, and can withstand the power levels currently used for both ground and space applications.

In addition to the theory, we have also shown the measured performance of a prototype showing excellent agreement between simulations and measurements, thereby fully validating both the filter structure and the design process.

Finally, we have also carried out a detail study of the negative effects due to the possible presence of higher order modes in the input of the filter. Two different approaches have been proposed to overcome these effects, namely, a simple high-pass filter connected to the output of the filter, and the well-know technique of changing the width of the resonators in the central part of the structure. Both approaches have proved to be very effective, further confirming the practical value of the filter structure that we have developed.

Chapter 6

Dual-Band Filters in Rectangular Waveguide Using Resonant Apertures

In this chapter, we describe a new family of microwave bandpass filters in rectangular waveguide based on resonant apertures, that can be used to implement dual-band filters. The use of several techniques like capacitive stubs, staircase configuration and changes in width of the resonators are also discussed in detail, with the objective of improving both the in-band and the out-of-band response of the filters. In the following sections, we describe in detail the dual-band filter design procedure. We then conclude with the discussion of the performance of several manufactured filter prototypes.

Our investigation in dual-band waveguide filters based on resonant apertures have resulted into two publications. The first has already been accepted. The second is currently being reviewed. They are the following ones:

- J.F Valencia Sullca, S. Cogollos, M. Guglielmi and V.E. Boria, "Dual-band filters in rectangular waveguide based on resonant apertures," in *2021 IEEE MTT-S International Microwave Symposium Digest*, Atlanta, GA, USA, 2021, pp. 1-4.
- J.F Valencia Sullca, S. Cogollos, M. Guglielmi and V.E. Boria, "Compact dual-band and wideband filters with resonant apertures in rectangular waveguide," Under review in IEEE Transactions on Microwave Theory and Techniques.

The research work described in this chapter is motivated by one of the features of the filter structures described in the previous sections. Namely, the fact that the use of capacitive irises to couple the resonators of our filters, results inevitably in the introduction

of spurious responses below the filter pass-band. The procedures that we have used, so far, to reduce the effect of these spurious responses, have been the use of inductive irises in the center of the filter, and the introduction of transmission zeros below the pass-band.

A more in depth analysis of the behavior of a capacitive coupling iris, however, reveals that the spurious response generated is actually due to the resonant behavior of the iris itself, which corresponds to the cutoff frequency of a waveguide with the same dimensions of the iris.

One interesting possibility to avoid the negative effect of this resonance could be to make the resonance itself an integral part of the response of the filter.

In this context, therefore, we propose in this chapter a novel procedure to design dual-band filters based on resonant apertures. The resulting filter structures have one very significant advantage, namely, they are particularly compact. This is because the order of the filter (the total number of poles) is given by the sum of the (resonant) coupling irises plus the number of distributed resonators that are needed. In all the filters discussed so far, the order was given only by the number of distributed resonators. The filters designed using resonant irises are therefore significantly more compact.

6.1 Capacitive Reference Filter

To evaluate the performance of the dual-band filter structures discussed in this chapter, we design first a standard in-line four-pole filter with capacitive couplings. The electrical specification that we used for this *reference* filter are as follows:

- Order $N = 4$
- Bandwidth $BW = 500$ MHz
- In-band return loss $RL > 20$ dB
- Center frequency $f_0 = 10$ GHz
- Guided-wavelength fractional bandwidth $\mathcal{W}_\lambda = 8.787$ %
- Input and output waveguides: WR-90 ($a = 22.86$ mm and $b = 10.16$ mm)

Fig. 6.1 shows the structure of the standard bandpass filter with capacitive inter-resonator couplings. It is important to mention that the thickness of all capacitive irises is equal to $t = 2$ mm in all irises.

Fig. 6.2 shows the simulated behavior of the structure in Fig. 6.1 (Capacitive Filter). The performance shown in Fig. 6.2 has been obtained using the commercial tool FEST3D (v.2021 by AuroraSAT, now with Dassault Systèmes). The performance of this filter will be used in the remainder of this chapter as a reference for further improvements.

As we can see in Fig. 6.2, in addition to the desired pass-band, we can clearly see

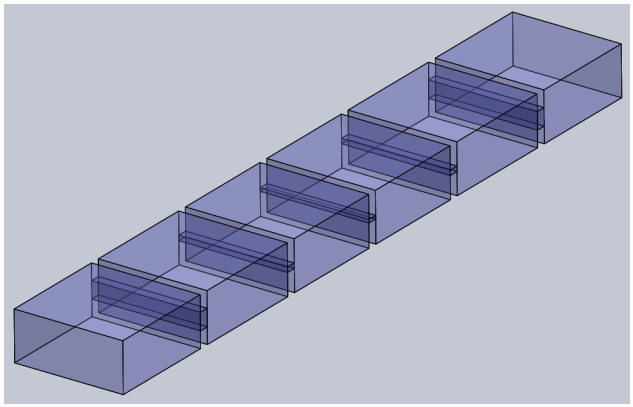

Figure 6.1: Structure of the reference capacitive filter.

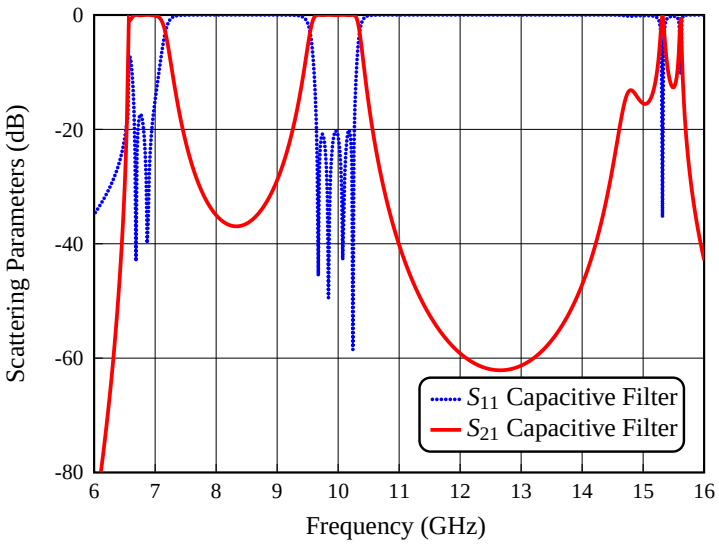

Figure 6.2: Simulated performance of the reference capacitive filter.

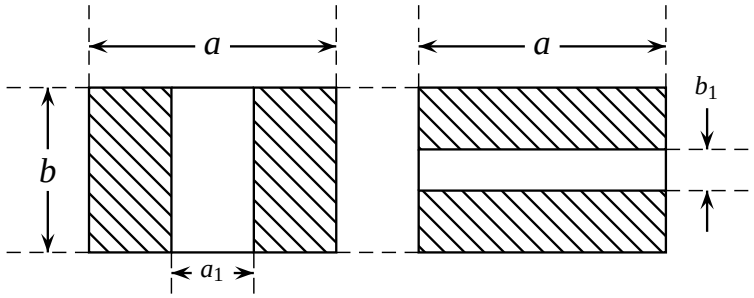

Figure 6.3: Typical irises in a rectangular waveguide (front view). Left: centered inductive iris of width a_1. Right: centered capacitive iris of height b_1.

that near the cutoff frequency of the input waveguide there is also a significant spurious response. As already discussed, this is due to the capacitive irises that, at their cutoff frequency, behave as resonators.

We now describe how to exploit this additional resonance near the cutoff frequency to create an additional pass-band, thereby obtaining a dual-band filter in rectangular waveguide.

6.2 Basic Resonant Aperture

Before discussing the design of dual-band structures, however, it is appropriate to first recall the characteristics of a basic coupling aperture. In this context, therefore, it is well known that the classic inductive and/or capacitive microwave filters in rectangular waveguide, are traditionally designed using half wavelength resonators that are coupled to each other by thick inductive and/or capacitive irises, like the ones shown in Fig. 6.3. It is also well known that the equivalent circuits of the inductive and capacitive irises are a shunt inductor or capacitor, respectively [2].

As we have already observed, capacitive irises produce a resonance at their cutoff frequency. The frequency at which the resonance occurs can also be increased, with respect to the basic waveguide cutoff frequency, if we decrease the width of the capacitive iris, as shown in Fig. 6.4. The width-reduced capacitive iris is now equivalent to a resonator, or a resonant aperture (RA). Furthermore, this type of structure can essentially be considered as a parallel combination of an inductor and a capacitor, placed in shunt with regard to the main waveguide.

We next perform a parametric study with a capacitive aperture in a WR-90 waveguide, to better understand the behavior of a resonant aperture. Fig. 6.5 shows the geometry of the RA, which has the following dimensions:

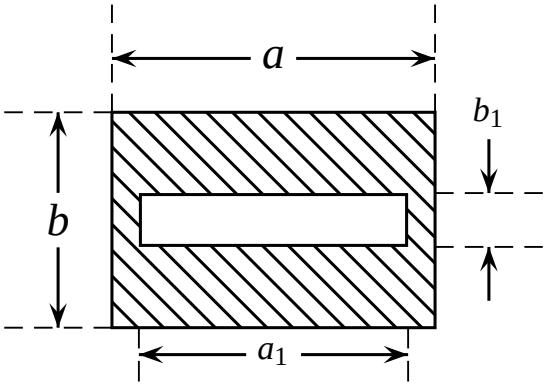

Figure 6.4: Resonant aperture in a rectangular waveguide (front view). The aperture is centered and has width a_1 and height b_1.

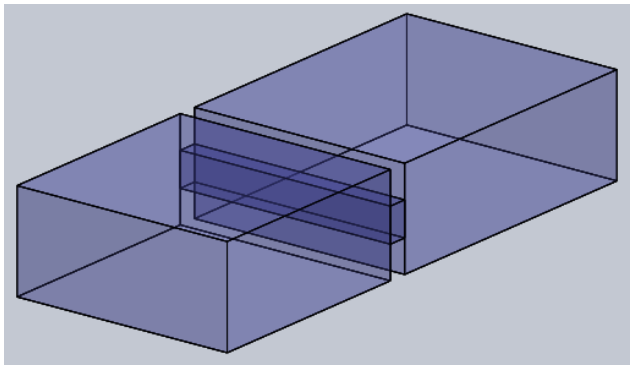

Figure 6.5: Geometry of a resonant aperture in a WR-90 waveguide.

- Width of the RA $a_1 = 22.86$ mm.
- Hight of the RA $b_1 = 3.5$ mm.
- Thickness of the RA $t = 2.0$ mm.

The first parameter that we will change in our study, is the width a_1 of the resonant aperture. Fig. 6.6 shows the effect of changing the width a_1 from 22.86 mm to 19.25 mm. As we can see, the resonance of the resonant aperture for $a_1 = 22.86$ mm is essentially the cutoff of the WR-90 waveguide. Reducing the dimension of the width a_1, the resonance can be moved up to 8.0 GHz.

The second parameter that we change is the height h of the rectangular waveguides used to implement the resonant aperture (i.e. b in Fig. 6.4). The width of the aperture is kept constant at $a_1 = 21.50$ mm. Fig. 6.7 shows the effect of changing the height h from 10.16 mm to 7.50 mm. As we can see, decreasing the height of the waveguide, increases the resonant bandwidth.

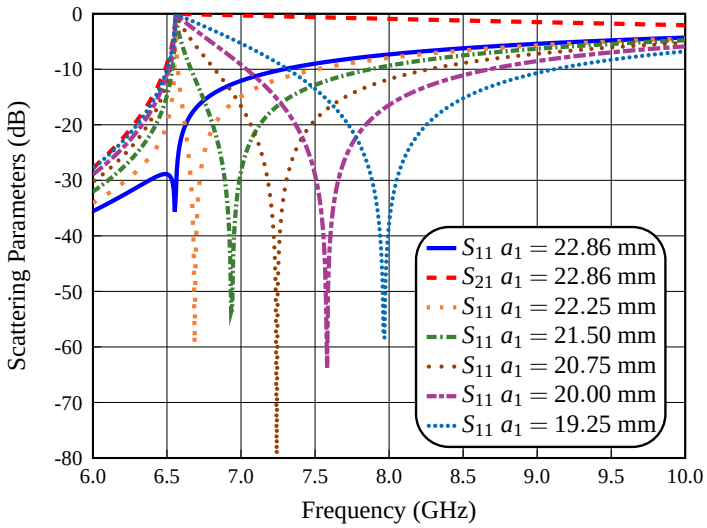

Figure 6.6: Simulated performance of the resonant aperture, changing a_1 from 22.86 mm to 19.25 mm.

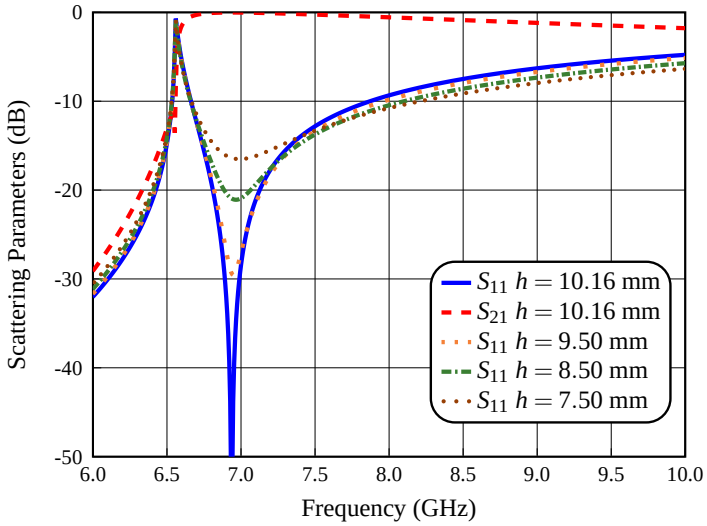

Figure 6.7: Simulated performance of the resonant aperture ($a_1 = 21.50$ mm), changing h from 10.16 mm to 7.50 mm.

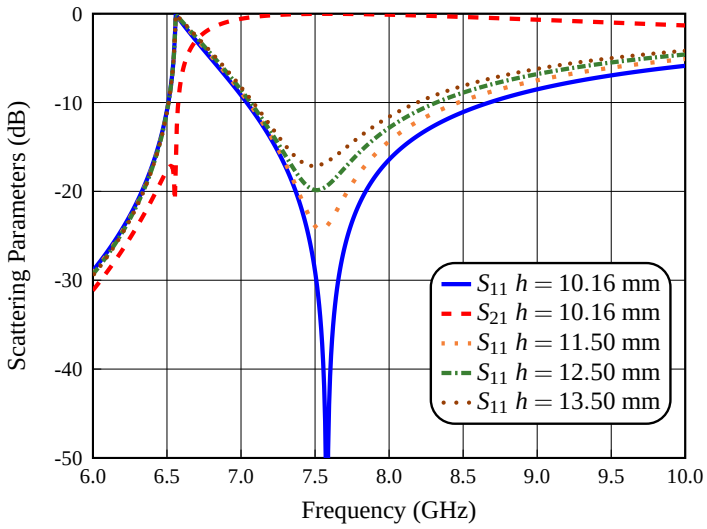

Figure 6.8: Simulated performance of the resonant aperture ($a_1 = 20.00$ mm), changing h from 10.16 mm to 13.50 mm.

Fig. 6.8 shows the effect of changing the height h from 10.16 mm to 13.50 mm, with $a_1 = 20.00$ mm. As we expected, increasing the height of the waveguide, decreases the resonant bandwidth.

The third parameter that we change is the height b_1 of the resonant aperture. The aperture width a_1 and height h are kept constant at $a_1 = 20.00$ mm and $h = 12.50$ mm, respectively. Fig. 6.9 shows the effect of changing the height b_1 from 3.5 mm to 2.0 mm, in steps of 0.5 mm. As we can see, decreasing the aperture height reduces the resonator bandwidth, and lowers the resonant frequency.

Finally, the last parameter that we change is the thickness t of the resonant aperture. All other parameters are kept constant, namely, $a_1 = 20.00$ mm, $h = 12.50$ mm and $b_1 = 2.0$ mm. Fig. 6.10 shows the effect of decreasing the thickness from 2.0 to 0.5 mm, in steps of 0.5 mm. As we can see, decreasing the thickness t has an effect that is similar to increasing the height b_1. However, the effect is not as strong.

Having explored the behavior of the basic resonant aperture, we are ready to start the design of a dual-band filter.

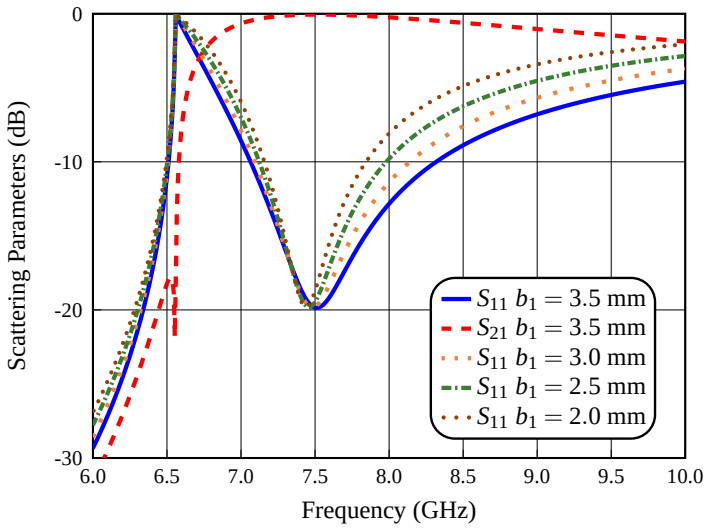

Figure 6.9: Simulated performance of the resonant aperture ($a_1 = 20.00$ mm, $h = 12.50$ mm), changing b_1 from 3.5 mm to 2.0 mm.

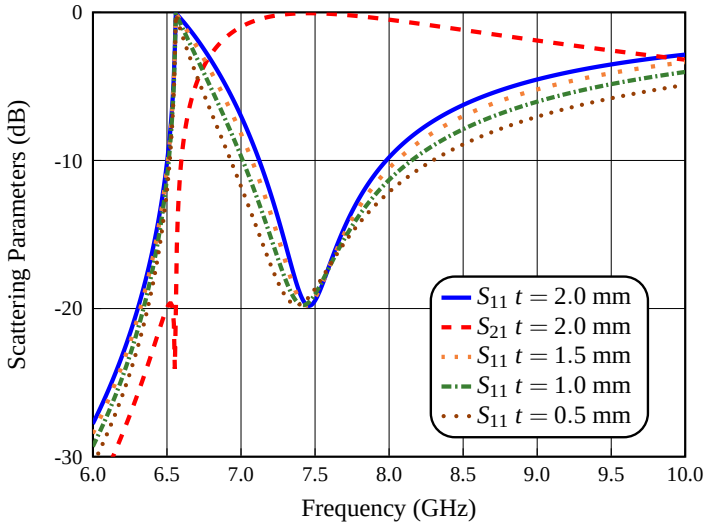

Figure 6.10: Simulated performance of the resonant aperture ($a_1 = 20.00$ mm, $h = 12.50$ mm), changing t from 2.0 mm to 0.5 mm.

6.3 Design Procedure for Dual-Band RA Filters

As already discussed, the presence of a pass-band near the cutoff frequency of the rectangular waveguide in a capacitive filter is due to the capacitive irises that basically behave as lumped element resonators (at the cutoff frequency). We could therefore think to use the lengths of waveguides between coupling irises as *distributed* inverters so that the structure can behave, near cutoff, as *another* filter.

Increasing further the frequency, the capacitive irises will go above cutoff and they will therefore resume their function of coupling elements, while the lengths of uniform waveguides will resume the role of distributed resonator, thereby producing the original filter pass-band.

The design procedure that we propose to implement dual-band filters based on resonant apertures is as follows:

1. For the lower band of the dual-band filter, we first design the normalized lumped-element low-pass network (g_i values) of a Chebyshev filter using the return loss (RL) specifications, and order of the filter $N+1$, as shown in Fig. 2.28.
2. We then design the bandpass network composed of series and shunt resonators. Then, as shown in Fig. 2.32, the series resonators are transformed into shunt resonators using admittance inverters $J_{i.i+1}, i = 0, \ldots, N+1$, with the following values

$$J_{0,1} = \sqrt{\frac{G_A \mathcal{W}_\lambda \mathcal{B}_1}{g_0 g_1}} \tag{6.1a}$$

$$J_{i,i+1} = \mathcal{W}_\lambda \sqrt{\frac{\mathcal{B}_i \mathcal{B}_{i+1}}{g_i g_{i+1}}}, \quad i = 1, \ldots, N \tag{6.1b}$$

$$J_{N+1,N+2} = \sqrt{\frac{G_B \mathcal{W}_\lambda \mathcal{B}_{N+1}}{g_{N+1} g_{N+2}}} \tag{6.1c}$$

   where G_A and G_B are the conductance in the input and output of the filter, $\mathcal{W}_\lambda$ is the guided-wavelength bandwidth and $\mathcal{B}_i$ is the susceptance slope parameter of each resonator.
3. The next step is to transform the admittance inverters into quarter-wavelength waveguides, where the length of each resonator is $l_i(f_1) \approx \lambda_{g_1}/4$, and f_1 is the center frequency of the lower band. With this last step, we finally obtain the first band (lower band).
4. For the upper band of the dual-band filter, we first design a capacitive filter of order N with half-wavelength (distributed) resonators and $N+1$ capacitive irises,

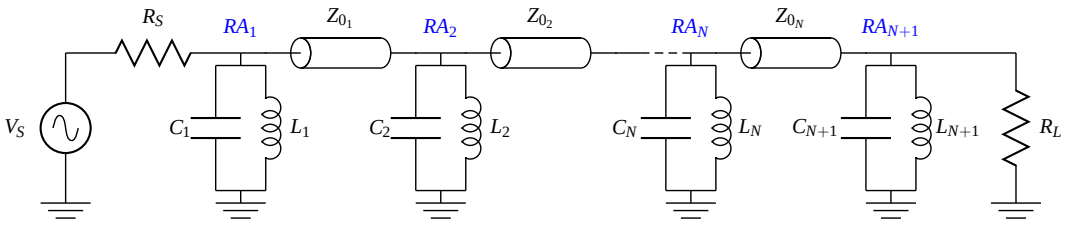

Figure 6.11: Circuital model of the dual-band RA filter.

where the length of each resonator is $l_i(f_2) \approx \lambda_{g_2}/2$, and f_2 is the center frequency of the upper band.

5. Once we have obtained the basic dual-band structure using the guidelines given in the previous paragraphs, we can optimize the performance of both bands simultaneously. This is indeed possible because we do have the needed number of variables, namely, a_1, b_1 and the thickness of each RA, plus the a, b and l dimensions of each distributed resonator to change Z_{0_i}, that is the characteristic impedance of the waveguide implementing each half-wavelength resonator.
6. There is, however, a limitation in the separation of the two bands: the lower band is centered at f_1 so that the lines between RAs are near 90°, while the upper band is centered at f_2 so that the lines between RAs are near 180°, as shown in Fig. 6.11.

With the procedure just described, we have been able to easily design a dual-band filter, with a filter of order $N+1$ at the lower center frequency, due to the $N+1$ resonant apertures (RAs), and the second filter of order N, due to the N half-wavelength resonators, at the upper center frequency.

6.4 Dual-Band RA Filter Design Example

We are now going to apply the design procedure described in the previous section to a specific design example with the following electrical specifications:

- For the lower band:
  - Order $N+1=5$
  - Bandwidth $BW_1 = 850$ MHz
  - In-band return loss $RL_1 > 20$ dB
  - Center frequency $f_1 = 7.42$ GHz
  - Input and output waveguide: WR-90 ($a = 22.86$ mm and $b = 10.16$mm)
- For the upper band:
  - Order $N=4$

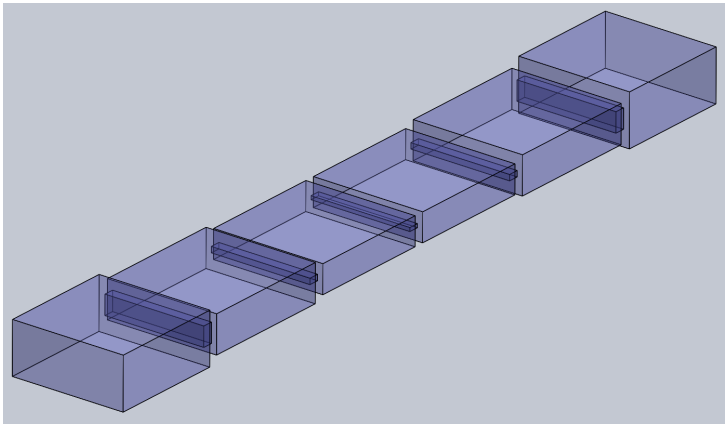

Figure 6.12: Structure of the dual-band RA filter.

- Bandwidth $BW_2 = 1000$ MHz
- In-band return loss $RL_2 > 20$ dB
- Center frequency $f_2 = 10$ GHz
- Input and output waveguide: WR-90 ($a = 22.86$ mm and $b = 10.16$mm)

Fig. 6.12 shows the structure of the dual-band RA filter that we have obtained. Fig. 6.13 shows the simulated behavior of the structure in Fig. 6.12 (DB RA Filter).

As we can see, we have been able to generate two pass-bands. The first one due to the resonant apertures (five-pole filter), and the second pass-band is due to the distributed resonators (four-pole filter). This dual-band filter has a number of interesting features:

- The filter is a very compact nine-pole filter, with only four distributed resonators.
- The spurious response of the filter at 14.5 GHz is only due to the four distributed resonators, even though we have a structure of order nine.

We can conclude that it is indeed possible to use the procedure we have described to obtain dual-band filters using resonant apertures. In the next sections, we propose a number of techniques to improve both the inter-band and out-of-band response of the dual-band filter.

6.4.1 Capacitibe Stubs

One feature of the dual-band filter that we have just designed that needs improvement is the shallow rejection level between the two pass-bands. In this section, we propose to do that using capacitive stubs to introduce transmissions zeros (TZs). Fig. 6.14 shows the basic geometry of the capacitive stubs, where l_{s1} and l_{s2} are the lengths of the stubs, and t_s is the height of the stub, respectively.

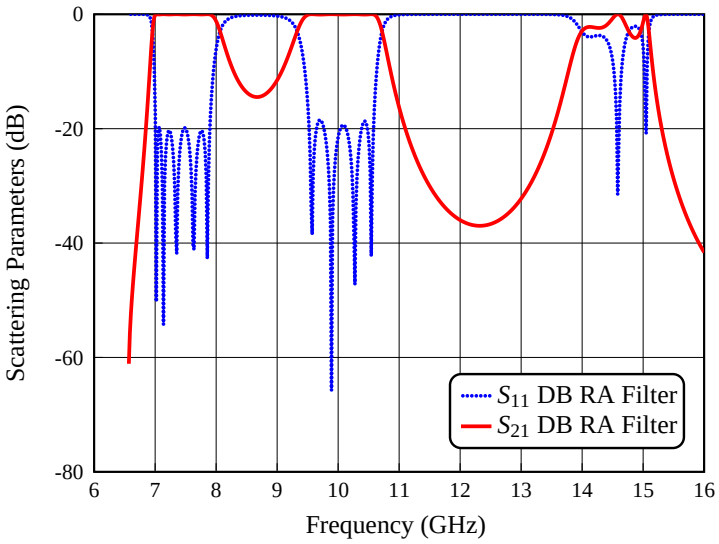

Figure 6.13: Simulated performance of the dual-band RA filter (DB RA Filter).

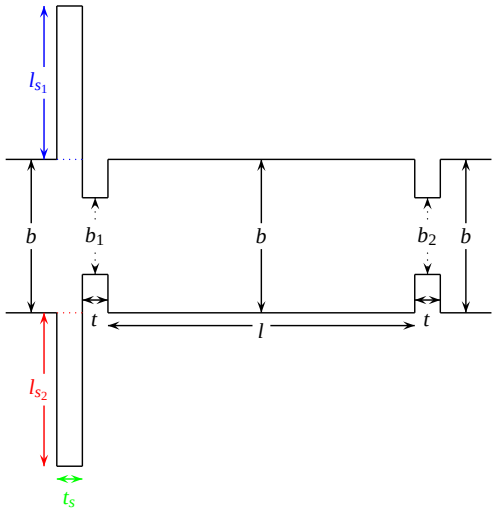

Figure 6.14: Geometry of a resonator coupled with capacitive couplings in the front and end walls, and capacitive stubs (l_{s_1} and l_{s_2}) in the input of the resonator (side view).

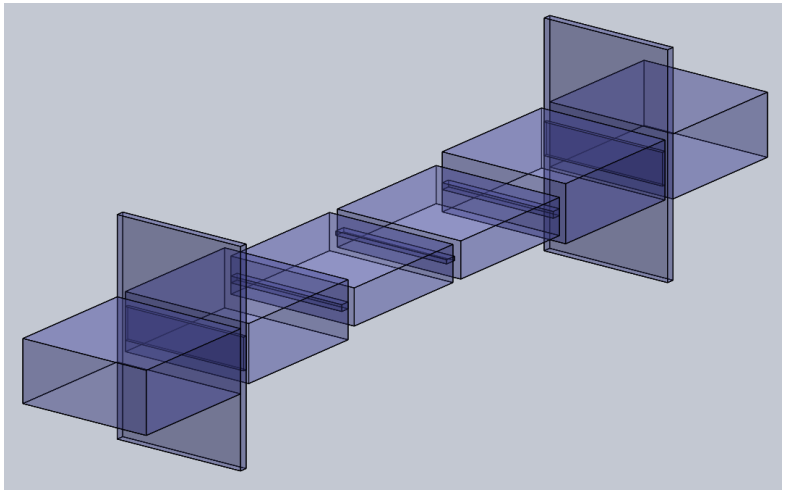

Figure 6.15: Structure of the dual-band RA filter with capacitive stubs before the input and output RAs.

Fig. 6.15 shows the structure of the dual-band RA filter with two capacitive stubs before both the input and output RAs. The four stubs have different dimensions, namely, l_{s_1} and l_{s_2} at the input, and l_{s_3} and l_{s_4} at the output RAs. The height t_s is equal for all capacitive stubs. Next, we show the simulated behavior of the filter (DB RA TZ Filter) in Fig. 6.16.

As we can see, the use of capacitive stubs in the dual-band filter results in a significant improvement of the rejection between the two pass-bands, which is now approximately -40 dB. It is interesting to note that the capacitive stubs have introduced four TZs, at 8.32, 8.52, 8.62 and 8.72 GHz, respectively. This is because the length of the capacitive stubs are all different. Even with the additional stubs, the resulting filter is rather compact for a nine-pole structure.

Above the two pass-bands, however, we can see a spurious response (at 14.5 GHz) due to the distributed resonators. In the next section we discuss a technique to improve the out-of-band response of the filter.

6.4.2 Staircase Filter

The same staircase configuration that we have successfully used in the structures described in the previous chapters, can also be used in the dual-band filter just described.

In Chapter 5, we have already discussed in detail the implementation of the staircase configuration. Therefore, we do not repeat the details here. To continue, if we locate the capacitive irises at $l_s = 3l/4$ along the resonators, we will obtain a very significant reduction of the coupling between higher order resonances and, as a consequence, an

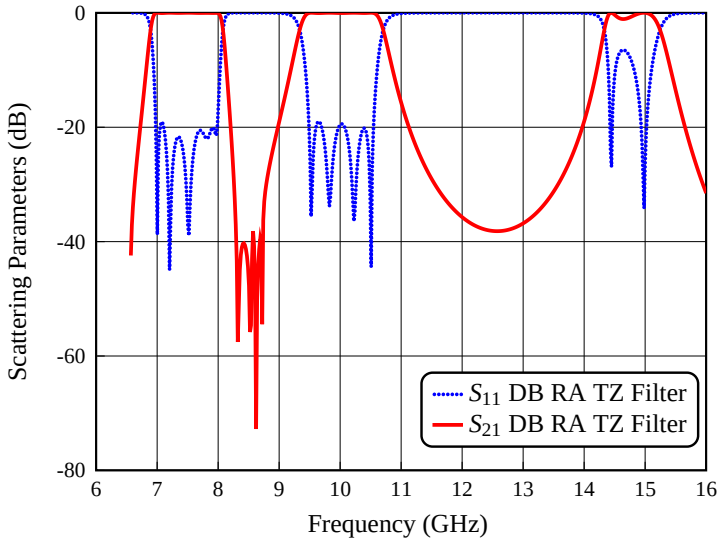

Figure 6.16: Simulated performance of the dual-band RA filter with capacitive stubs before the input and output RAs (DB RA TZ Filter).

improvement of the out-of-band response of the filter. Fig. 6.17 shows the basic staircase structure.

In order to validate the concept just proposed, we have first implemented the staircase configuration in the capacitive reference filter shown in Fig. 6.1, which we designed with the electrical specifications given in Section 6.1.

Fig. 6.18 shows the structure of the complete staircase filter. Fig. 6.19 shows the comparison between the simulated behavior of the structures in Fig. 6.1 (Cap Ref Filter) and Fig. 6.18 (Cap Stair Filter), respectively.

As we can see, the use of this simple staircase structure in the capacitive filter results in a significant reduction and attenuation of the harmonics, with spurious response below -40 dB. However, the rejection below of the filter pass-band is slightly degraded.

As already mentioned, the dual-band RA filter designed in the previous section, has a total of nine poles, with spurious response at approximately 14.5 GHz, as shown in Fig. 6.13. This spurious response is only due to the four distributed resonators, since the RAs behave basically as lumped-elements resonators. We show next in Fig. 6.20, the structure of the dual-band RA filter with the staircase configuration. Fig. 6.21 shows the simulated behavior of the structure in Fig. 6.20 (DB RA Stair Filter).

As we can see, the use of this simple staircase structure in the dual-band RA filter results into a significant reduction and attenuation of the harmonics, with spurious response below -40 dB, and spikes reaching -35 and -30 dB at 14.71 and 15.16 GHz, res-

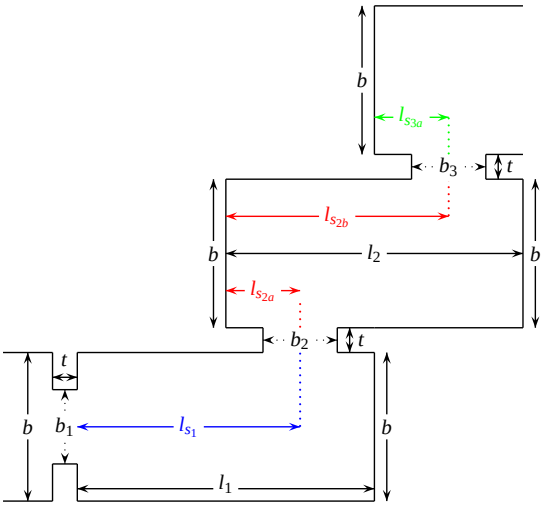

Figure 6.17: Geometry of the basic (three-resonator) staircase configuration with the capacitive coupling apertures located at $l_{s_1} = 3l_1/4$, $l_{s_{2a}} = l_2/4$, $l_{s_{2b}} = 3l_2/4$ and $l_{s_{3a}} = l_3/4$ respectively, from the resonator input.

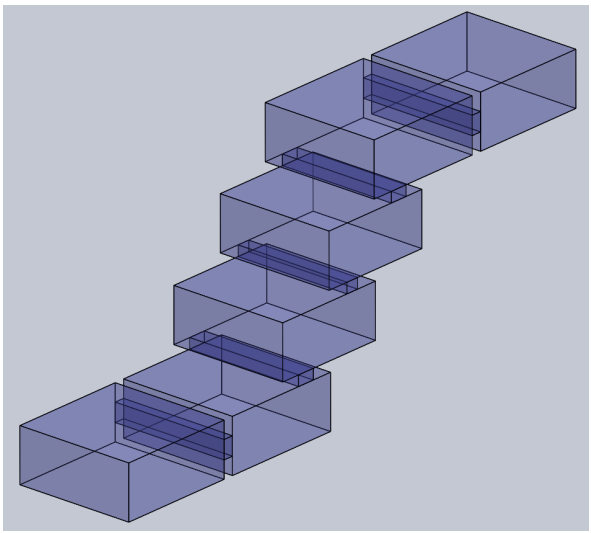

Figure 6.18: Structure of the capacitive staircase filter.

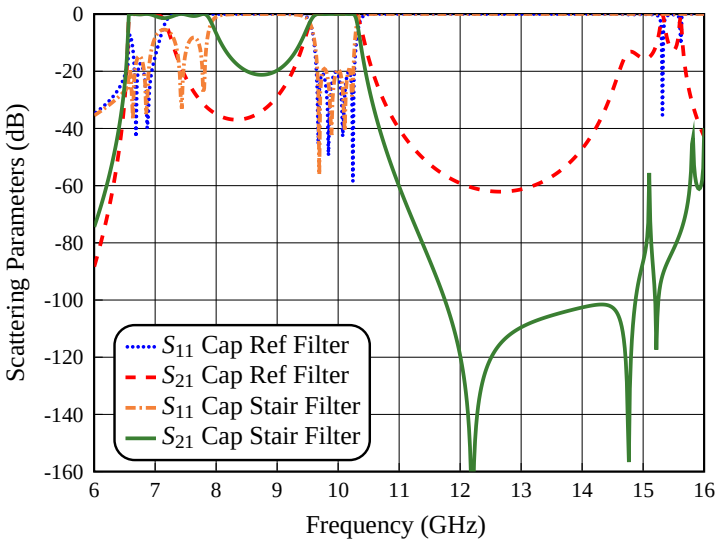

Figure 6.19: Simulated performance of the reference capacitive filter (Cap Ref Filter) and the capacitive staircase filter (Cap Stair Filter).

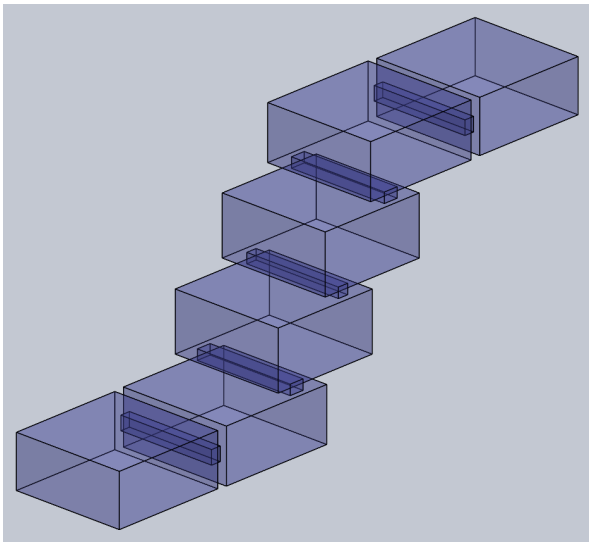

Figure 6.20: Structure of the dual-band RA staircase filter.

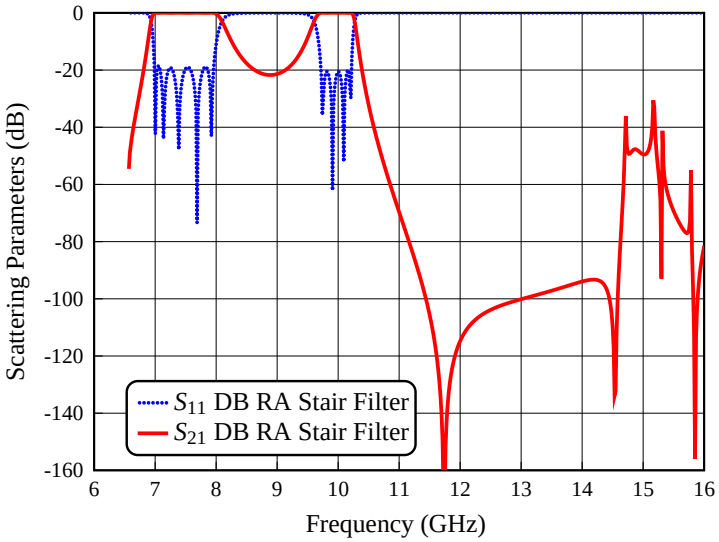

Figure 6.21: Simulated performance of the dual-band RA staircase filter (DB RA Stair Filter).

pectively. However, the rejection level between the two pass-bands is approximately of -22.25 dB.

6.4.3 Staircase Filter With TZs

A further improvement of the out-of-band response of the dual-band RA filter can be obtained if we use the capacitive stubs before the input and output RAs, in conjunction with the staircase configuration. The resulting structure is shown in Fig. 6.22. It is important to mention that we have first designed all stubs with the same length. This gives only one TZ between the two bands.

Next, we show in Fig. 6.23 the simulated behavior of the structure in Fig. 6.22 (DB RA Stair TZ Filter). As we can see, the implementation of both techniques in the dual-band RA filter results into a significant reduction and attenuation of the harmonics, with spurious response below -60 dB, and spikes reaching -52 and -58 dB at 14.71 and 15.45 GHz, respectively. We have also improved the rejection level between the two pass-bands due to the introduction of the TZ.

An additional improvement of the out-of-band response is achieved if we optimize the width a_i, height b_i and thickness t_i of the RAs and the width w_i, height h_i and length l_i of the distributed resonators, as shown in Fig. 6.24.

As we can see, the implementation of capacitive stubs and the optimization of width, height and thickness in the structure result into a significant reduction and attenuation of the harmonics, with spurious response below -110 dB.

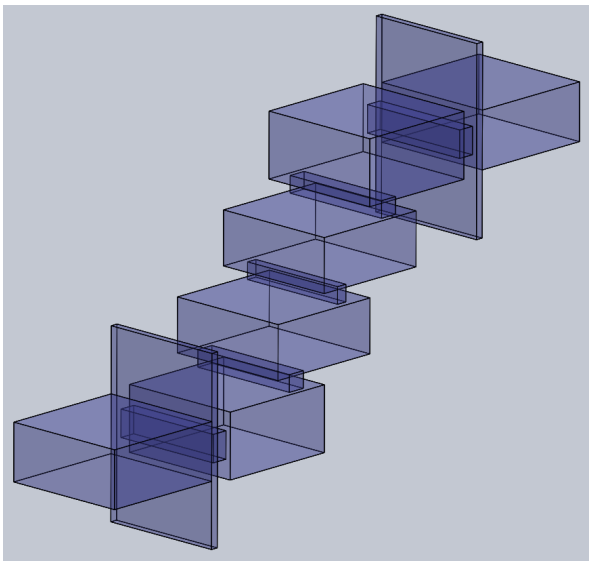

Figure 6.22: Structure of the dual-band RA staircase filter with capacitive stubs before the input and output RAs.

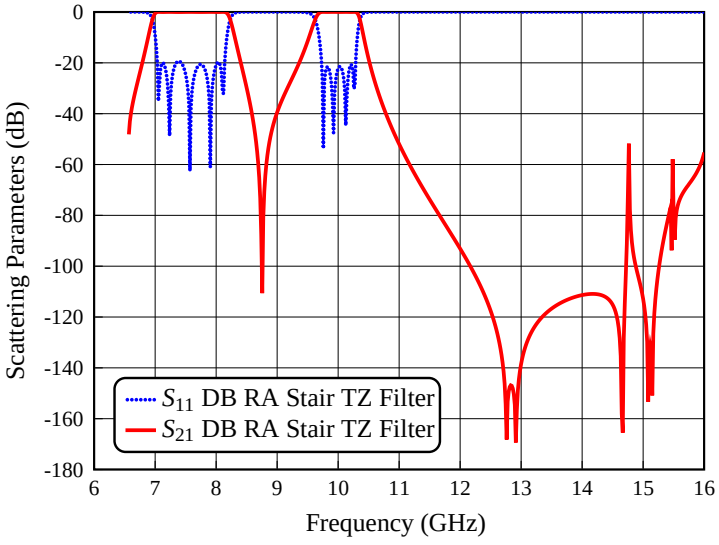

Figure 6.23: Simulated performance of the dual-band RA staircase filter with capacitive stubs before the input and output RAs (DB RA Stair TZ Filter).

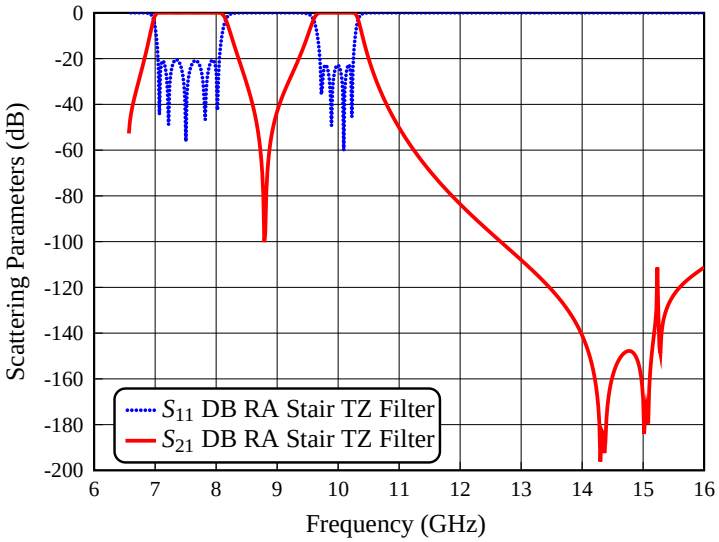

Figure 6.24: Simulated performance of the optimized dual-band RA staircase filter with capacitive stubs before the input and output RAs (DB RA Stair TZ Filter).

We can therefore conclude saying that the combined use of capacitive stubs, staircase configurations and width optimization in the resonators produce an improvement of both the selectivity and the out-of-band performance of the basic dual-band filter structure. Furthermore, depending on the symmetry and asymmetry of the capacitive stubs it is possible to implement more than one TZ, with the objective of further improving the rejection between the two pass-bands.

6.5 The First Prototype

The dual-band RA filter structures that we have designed and simulated so far, are very simple and compact, and have a very good out-of-band performance. Furthermore, for all designs performed we have used FEST3D directly in high accuracy mode, with the following set of parameters [103]:

- Accessible modes: 80
- Number of basis functions: 240
- Green's function terms: 2400

To validate our designs, we have decided to manufacture two prototypes. The first one with four TZs between the two pass-bands. The second one with only two TZs between the two pass-bands.

The first structure is shown in Fig. 6.25, where we have used two capacitive stubs before and after the input and output RAs. We have also optimized the widths of the dis-

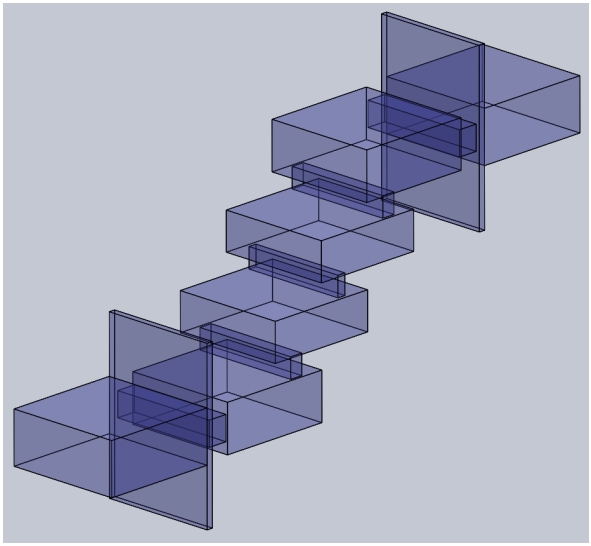

Figure 6.25: Structure of the first dual-band RA staircase filter with capacitive stubs before the input and output RAs.

tributed resonators. The location of the RAs along the resonators has also been optimized to produce the maximum spurious rejection.

Fig. 6.26 shows the simulated behavior of the structure of Fig. 6.25 (DB RA Stair TZ Filter I). As we can see, the structure shows a very significant attenuation of the harmonic resonances, with spurious response below -100 dB from 13 to 16 GHz, and a spike reaching -110 dB at 15.34 GHz. This filter shows also a strong rejection between the two pass-bands, which is below -40 dB, due to the four TZs introduced at 8.62, 8.72, 8.85 and 9.05 GHz, respectively.

It is now important to mention that, in order to facilitate manufacturing, we have also replaced all sharp concave corners in the distributed resonators with rounded corners with a radius equal to $r = 1.1$ mm. Fig. 6.27 shows the resulting structure.

To validate the high accuracy design obtained with FEST3D, we have next simulated the same structure with the full-wave electromagnetic simulator CST Studio Suite with the following settings:

- Solver: Frequency Domain Solver
- Frequency sweep: General Purpose
- Mesh refinement: 7.5, 8.75, 10.0 and 15.25 GHz
- Error threshold: 0.01
- Maximum number of iterations: 50

Fig. 6.28 shows a comparison of the simulated behavior of the first dual-band stair-

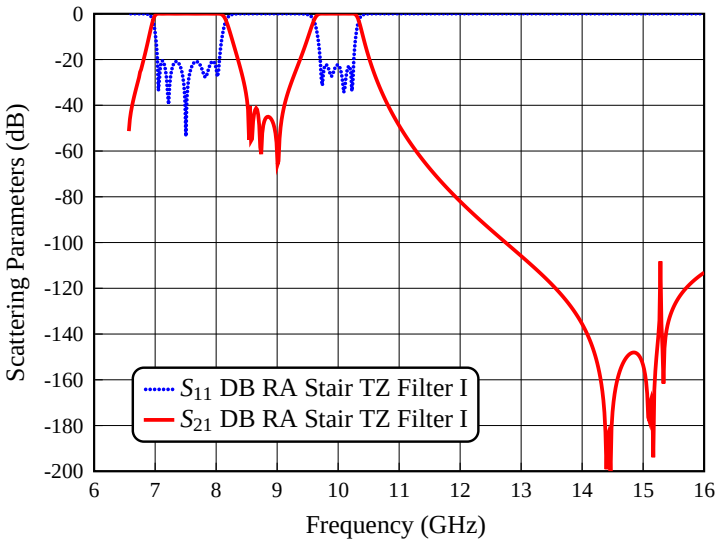

Figure 6.26: Simulated performance of the dual-band RA staircase filter with capacitive stubs before the input and output RAs (DB RA Stair TZ Filter I).

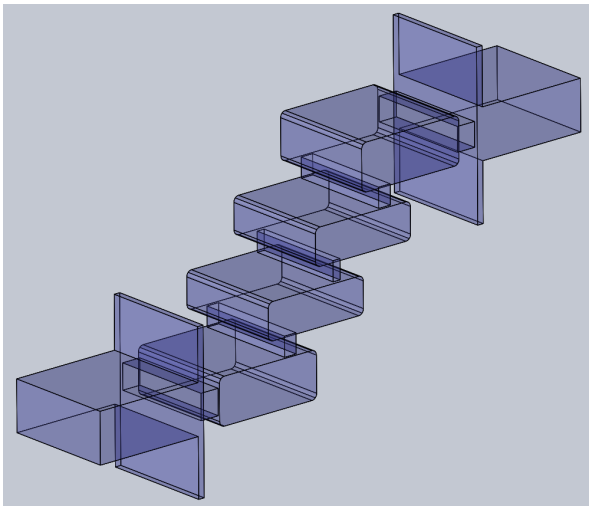

Figure 6.27: Structure of the first dual-band RA staircase filter with capacitive stubs before the input and output RAs of the filter (DB RA Stair TZ Filter I), designed with a radius equal to $r = 1.1$ mm in the distributed resonators.

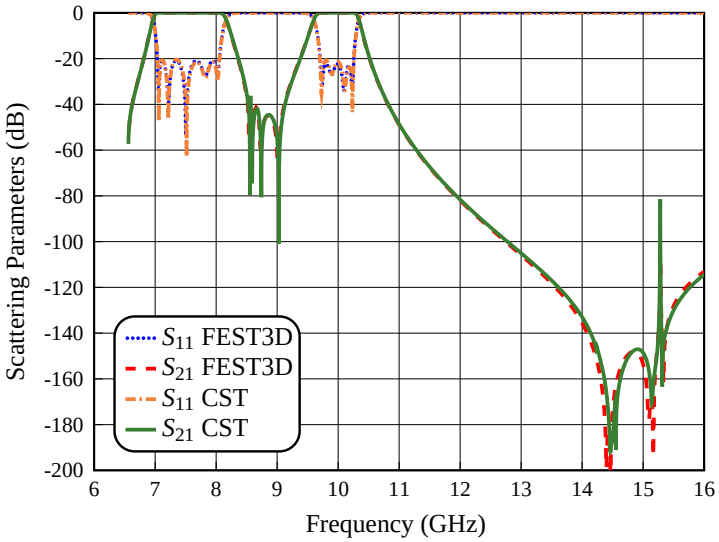

Figure 6.28: Full-wave simulated performance of the structure in Fig. 6.27 with rounded corners obtained using FEST3D and CST.

case RA filter structure obtained with the commercial tools FEST3D and CST Studio Suite. As we can see, the agreement both in the inter-band and out-of-band responses is generally very good. It is interesting to note that the CST simulation shows a spurious peak reaching -80 dB just above 15 GHz.

Finally, the values for all dimensions of the first dual-band RA staircase filter with capacitive stubs are shown in Table 6.1. The dimensions are given up to the center of the filter. This is because the whole filter is asymmetrical, in terms of dimension values, but the central part of the structure is symmetrical. The thickness of the RAs is t_i, and the capacitive stubs have the same width as the input waveguide.

6.5.1 Measurements

The first dual-band RA staircase filter prototype discussed in the previous section, has been manufactured in a clam-shell configuration using a combination of standard milling and spark erosion techniques, as shown in Fig. 6.29.

We have compared next the measured and simulated in-band responses, as displayed in Fig. 6.30. As we can see, the two pass-bands are centered at 7.5 and 10.0 GHz, respectively, all reflection zeros are clearly visible, and the agreement of measured and simulated results is excellent. We can also clearly see the four TZs introduced between the two pass-bands.

Fig. 6.31 shows the comparison between the measured and the simulated out-of-band

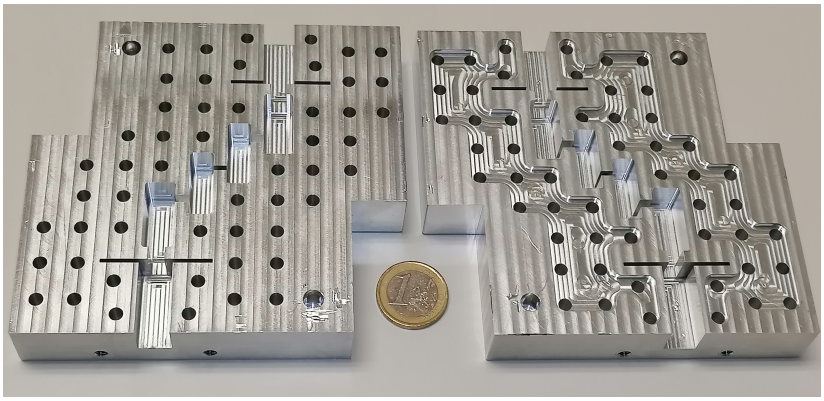

Figure 6.29: Manufactured prototype in aluminum of the first dual-band RA staircase filter (no silver plating).

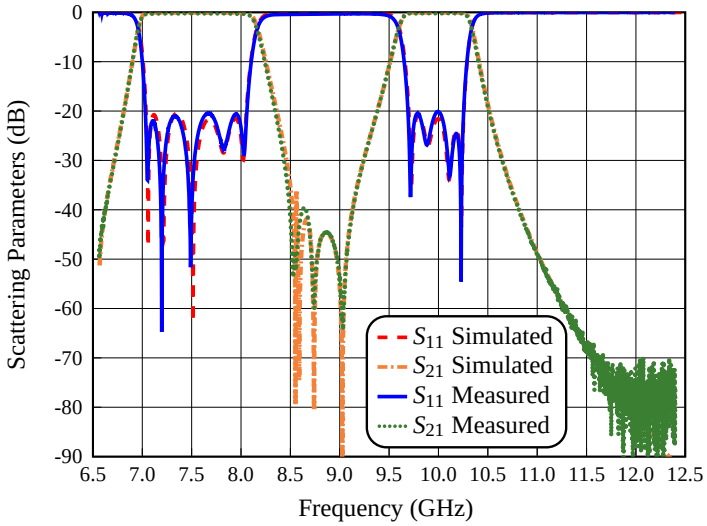

Figure 6.30: Measurement of the in-band performance compared with the EM simulation results (CST).

Table 6.1: Physical dimensions for the first DB RA Staircase Filter I with two stubs before of the RAs.

Section Type	Dimensions (mm)	
Input Waveguide	a =22.86 b =10.16 $L_{input} = L_{output}$ =22.86	
Capacitive stubs 1-2	l_{cs_1} =11.856 t_{cs_1} =1.282	l_{cs_2} =11.556 t_{cs_2} =1.282
Capacitive stubs 3-4	l_{cs_3} =11.856 t_{cs_3} =1.282	l_{cs_4} =10.556 t_{cs_4} =1.282
Resonant aperture 1-5	a_1 =21.433 b_1 =4.879 t_1 =4.0	a_5 =21.466 b_5 =5.169 t_5 =4.0
Resonator 1-4	w_1 =22.213 H_1 =9.408 L_1 =22.658	w_4 =22.213 H_4 =9.40 L_4 =22.637
Resonant aperture 2-4	a_2 =21.222 b_2 =2.688 t_2 =4.0	a_4 =21.222 b_4 =2.688 t_4 =4.0
Resonator 2-3	w_2 =22.344 H_2 =7.426 L_2 =22.176	w_3 =22.344 H_3 =7.426 L_3 =22.176
Resonant aperture 3	a_3 =20.775 b_3 =1.635 t_3 =4.0	

responses. To produce the measured result in Fig. 6.31, we have used three standard waveguide calibrations, namely WR-90, WR-75 and WR-62, with the TRL (Through, Reflection and Line) calibration method. The noise floor in each calibration was about -70 dB.

As we can see, the measured out-of-band performance shows good agreement with the simulation results, with spurious response below -50 dB from 13 to 16 GHz. However, there are spikes at the high frequency end. We believe that the spikes are due to higher

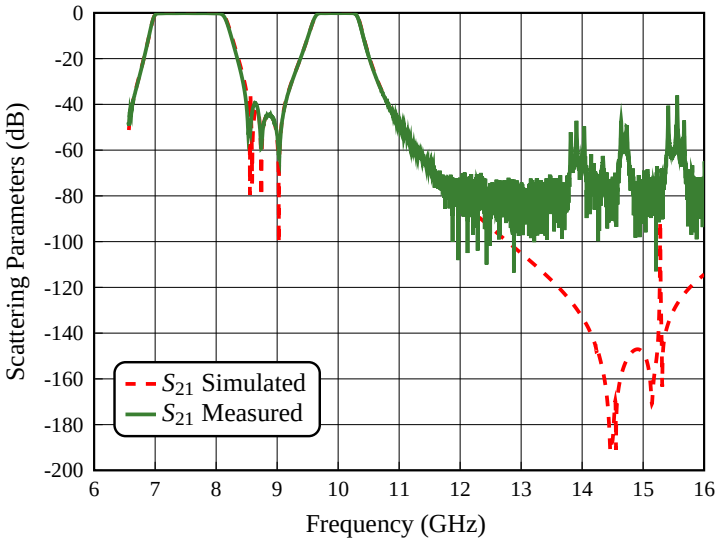

Figure 6.31: Measurement of the out-of-band performance compared with the EM simulation results (CST).

order modes that are excited by manufacturing errors.

6.6 The Second Prototype

The second structure that we will discus is shown in Fig. 6.32. It is important to mention that, following the advice of the company that manufactured the first prototype, we have redesigned the filter in Fig. 6.25 with wider, symmetric capacitive stubs in order to obtain a structure that can be easier to manufacture and provide, at the same time, a good out-of-band response.

Fig. 6.33 shows the simulated behavior of the structure in Fig. 6.32 (DB RA Stair TZ Filter II). As we can see, the second structure shows a very significant attenuation of the harmonic resonances, with spurious response below -120 dB from 14 to 16 GHz, and a spike reaching -110 dB at 15.32 GHz. This new filter shows also a strong rejection between the two pass-bands (below -60 dB) due to the two double TZs introduced at 8.73 and 8.93 GHz, respectively.

As we have already done in all the filters that we have manufactured, the sharp corners of the distributed resonators have been changed into rounded corners with a radius $r_1 = 1.1$ mm. The capacitive stubs end with a radius equal to $r_2 = 1.0$ mm, in order to facilitate the manufacturing. The final structure is shown in Fig. 6.34.

Fig. 6.35 shows a comparison of the simulated behavior of the second dual-band staircase RA filter structure obtained with the commercial tools FEST3D and CST, res-

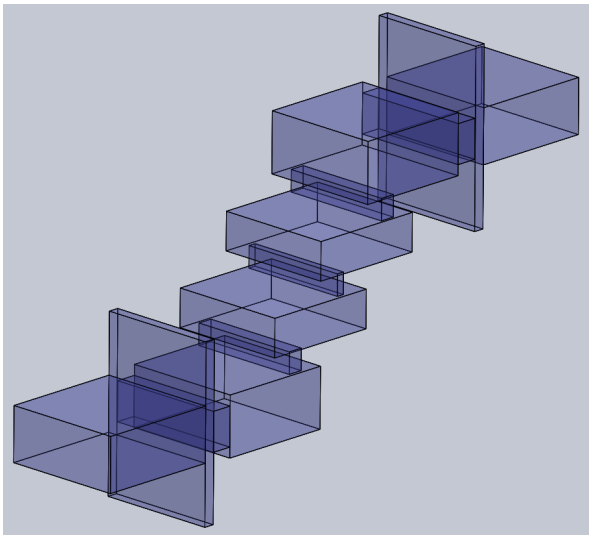

Figure 6.32: Structure of the second dual-band RA staircase filter with capacitive stubs before the input and output RAs.

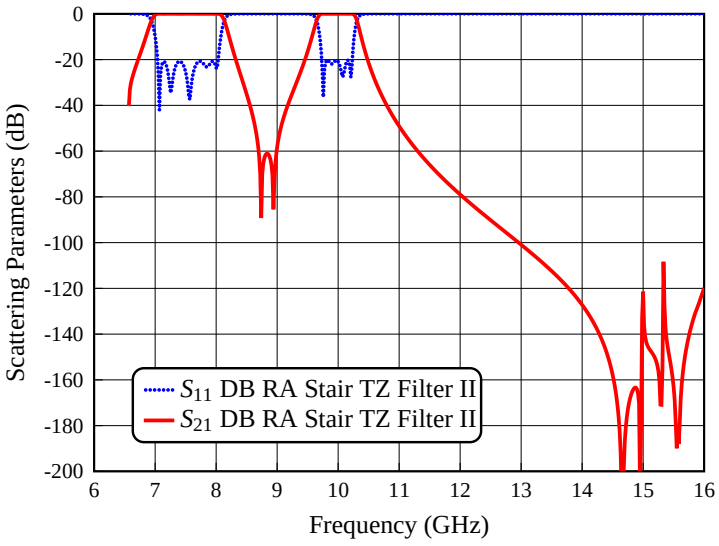

Figure 6.33: Simulated performance of the dual-band RA staircase filter with capacitive stubs before the input and output irises of the filter (DB RA Stair TZ Filter II).

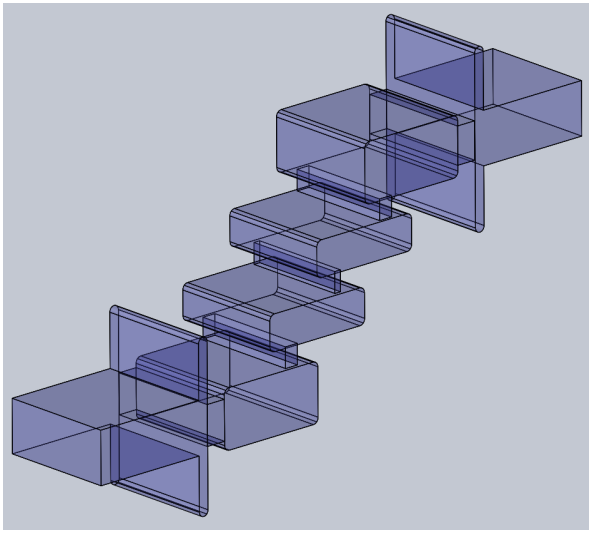

Figure 6.34: Structure of the second dual-band RA staircase filter with capacitive stubs before the input and output RAs of the filter (DB RA Stair TZ Filter II), designed with radius equal to $r_1 = 1.1$ mm in the distributed resonators and $r_2 = 1.0$ mm in the capacitive stubs, respectively.

pectively. As we can see, the agreement both in the inter-band and out-of-band frequency ranges is very good. The filter performance obtained with CST shows slightly higher spurious response reaching -80 dB above 15 GHz.

Finally, the values for all the dimensions of the second dual-band RA filter are shown in Table 6.2. The dimensions are given up to the center of the filter. This is because the whole filter is asymmetrical, but the central part of the structure is symmetrical. The thickness of the RAs is t_i, and the capacitive stubs have the same width as the input waveguide.

6.6.1 Measurements

The second dual-band staircase RA filter prototype has been manufactured in a clam-shell configuration using only standard milling, as shown in Fig. 6.36.

Next, we have performed the comparison between measured and simulated in-band responses, as shown in Fig. 6.37. As we can see, the in-band performance is centered at 7.5 and 10.0 GHz, where the five and four reflection zeros of the dual-band RA filter are clearly visible. The agreement with the simulation results is excellent. We can also clearly see the two TZs between the two pass-bands.

Fig. 6.38 shows the comparison between the measured and the simulated out-of-band responses. To produce the result in Fig. 6.38, we have employed the same measurement

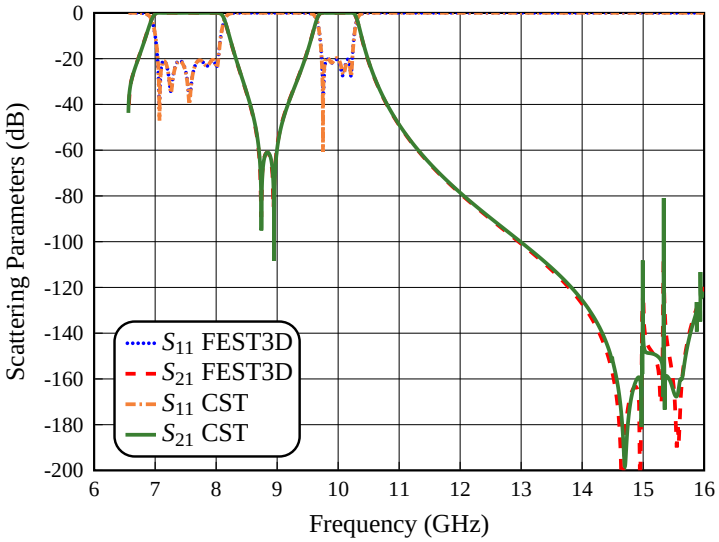

Figure 6.35: Full-wave simulated performance of the structure in Fig. 6.34 with rounded corners obtained using FEST3D and CST.

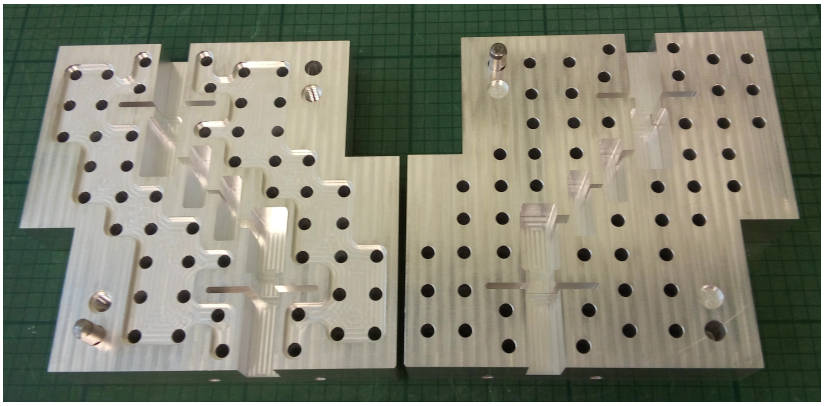

Figure 6.36: Manufactured prototype in aluminum of the second dual-band RA staircase filter (no silver plating).

Table 6.2: Physical dimensions for the second DB RA Staircase Filter II with two stubs before of the RAs.

Section Type	Dimensions (mm)	
Input Waveguide	a =22.86 b =10.16 $L_{input} = L_{output}$ =22.86	
Capacitive stubs 1-2	l_{cs_1} =11.896 t_{cs_1} =2.0	l_{cs_2} =11.896 t_{cs_2} =2.0
Capacitive stubs 3-4	l_{cs_3} =11.296 t_{cs_3} =2.0	l_{cs_4} =11.296 t_{cs_4} =2.0
Resonant aperture 1-5	a_1 =22.616 b_1 =7.187 t_1 =3.974	a_5 =22.720 b_5 =7.673 t_5 =4.005
Resonator 1-4	w_1 =22.747 H_1 =11.432 L_1 =21.655	w_4 =22.747 H_4 =11.432 L_4 =21.791
Resonant aperture 2-4	a_2 =21.257 b_2 =2.771 t_2 =3.955	a_4 =21.257 b_4 =2.771 t_4 =3.955
Resonator 2-3	w_2 =22.424 H_2 =6.914 L_2 =22.074	w_3 =22.424 H_3 =6.914 L_3 =22.074
Resonant aperture 3	a_3 =20.823 b_3 =1.326 t_3 =4.003	

and calibration procedures used for the first prototype.

As we can see, the out-of-band performance shows a good agreement between simulation and measurement, with spurious response below -40 dB from 13 to 16 GHz. However, there is a spike reaching -30 dB at about 13.5 GHz. The spike is probably due to higher order modes excited by manufacturing errors.

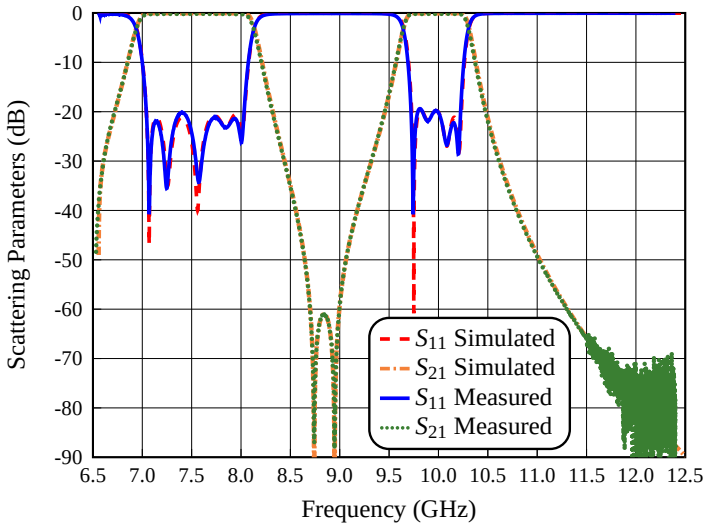

Figure 6.37: Measurement of the in-band performance compared with the EM simulation results (CST).

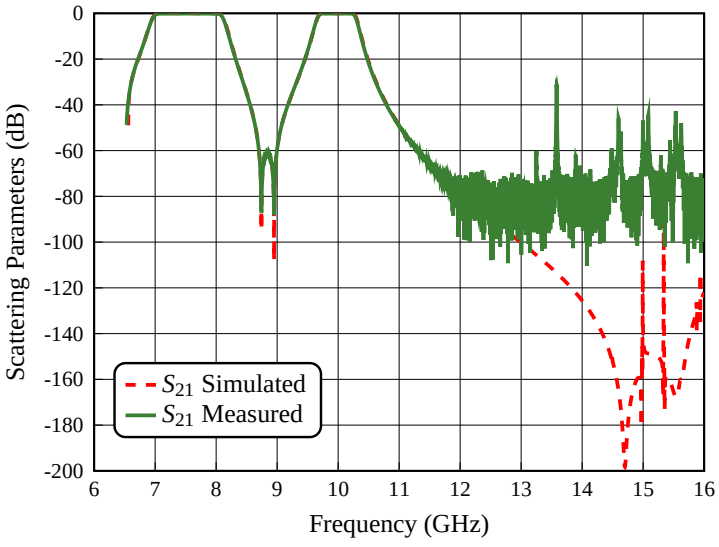

Figure 6.38: Measurement of the out-of-band performance compared with the EM simulation results (CST).

Table 6.3: Results of the tolerance analysis for the dual-band RA filters.

Filter Type	Yield of the Structure			
Tolerance	5 μm	10 μm	15 μm	20 μm
DB RA Filter I	95 %	84 %	52 %	32 %
DB RA Filter II	98 %	92 %	70 %	40 %

6.7 Tolerance Analysis

In this section we show the results of a yield analysis for the two dual-band filters designed in the previous sections. This analysis has been done in order to validate the choice of the manufacturing process. As we did in all other cases, we have used the commercial tool FEST3D to introduce a random error with a Gaussian distribution in all filters dimensions.

The sensitivity analysis for the DB RA filters structures, has been carried out with different values of the standard deviation, namely, $\pm$ 5, $\pm$ 10, $\pm$ 15 and $\pm$ 20 μm. Furthermore, since the filters have been designed with a return loss of 20 dB, the threshold value for the yield estimation has been set to 18 dB. Table 6.3 shows a summary of the results obtained for the two DB RA filters.

Fig. 6.39 and Fig. 6.40 show a number of simulations for several random errors. As we can see from both the simulations and the results in Table 6.3, with manufacturing errors between 10 and 15 μm, it should be possible to obtain an acceptable yield value. These results are indeed validated by the measured performance of the two prototypes that we have manufactured (see Fig. 6.30 and Fig. 6.37).

6.8 High Power Analysis

In this section we will show the results of the multipactor analysis for the two dual-band staircase filters that we have just designed. This analysis is done in order to identify the power (in W) where the multipactor effect can be initiated. For this purpose, we have chosen the frequencies where the group delay shows a maximum in the response of the dual-band filters (i.e f_1, f_3, f_4 and f_6) and at the center frequencies (f_2 and f_5). It is important to mention that the simulations have been carried out using FEST3D for the EM fields, and SPARK3D for the multipaction prediction, with the following set of parameters:

1. Initial power: 50 or 100 W
2. Maximum power: 1 MW
3. Growth factor of the power: 10^2

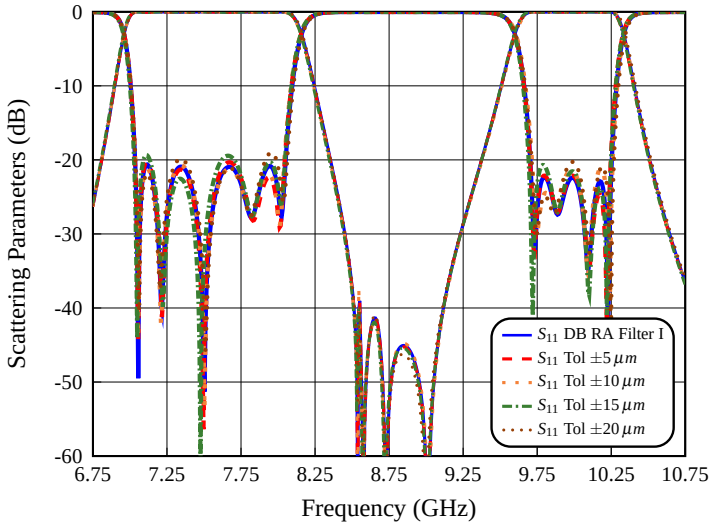

Figure 6.39: Tolerance analysis of the first dual-band RA filter.

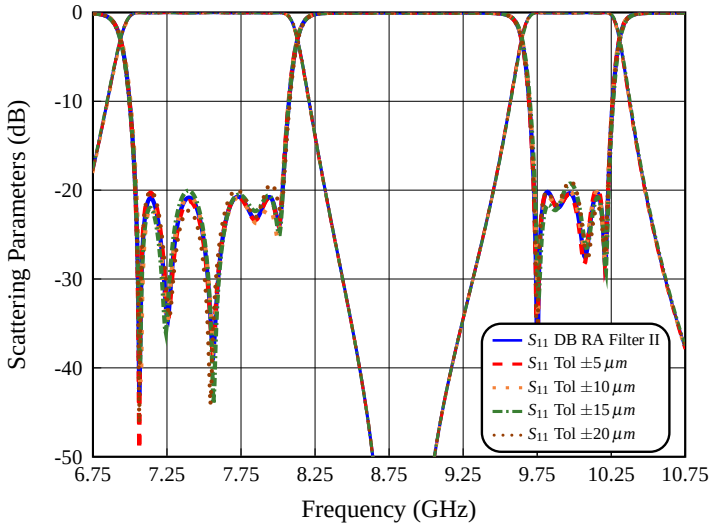

Figure 6.40: Tolerance analysis of the second dual-band RA filter.

Table 6.4: High power analysis of the first dual-band RA filter.

Structure	Power of the structure		
Frequency	$f_1 = 6.98$ GHz	$f_2 = 7.50$ GHz	$f_3 = 8.13$ GHz
RA_1	1175 W	3985 W	1785 W
$RA_2 = RA_4$	192 W	865 W	375 W
RA_3	119 W	315 W	207 W
RA_5	4785 W	4715 W	5725 W
Frequency	$f_4 = 9.65$ GHz	$f_5 = 10.0$ GHz	$f_6 = 10.31$ GHz
RA_1	14530 W	22450 W	24115 W
$RA_2 = RA_4$	7867 W	1325 W	1050 W
RA_3	4965 W	1815 W	631 W
RA_5	20520 W	27575 W	39877 MW

Table 6.5: High power analysis of the second dual-band RA filter.

Structure	Power of the structure		
Frequency	$f_1 = 6.97$ GHz	$f_2 = 7.50$ GHz	$f_3 = 8.11$ GHz
RA_1	4549 W	8899 W	3474 W
$RA_2 = RA_4$	234 W	931 W	404 W
RA_3	113 W	284 W	185 W
RA_5	13699 W	13099 W	13699 W
Frequency	$f_4 = 9.68$ GHz	$f_5 = 10.0$ GHz	$f_6 = 10.29$ GHz
RA_1	> 1 MW	> 1 MW	> 1 MW
$RA_2 = RA_4$	6749 W	3574 W	1137 W
RA_3	5249 W	1562 W	568 W
RA_5	> 1 MW	> 1 MW	> 1 MW

4. Frequencies of simulation: f_1, f_2, f_3, f_4, f_5 and f_6
5. Initial number of electrons: 10000

The power thresholds that we have obtained for the two filters are shown in Tables 6.4 and 6.5, respectively.

As expected, the resonant aperture RA_3 of the two dual-band RA filters shows the

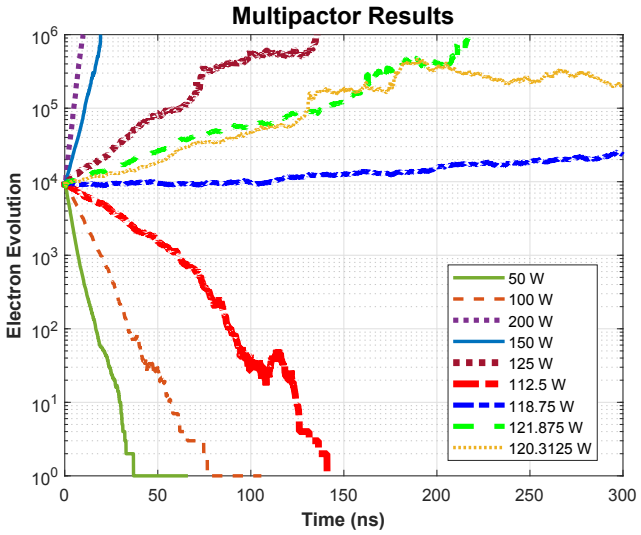

Figure 6.41: Multipactor simulation with discharges for the resonant aperture RA_3 at 6.98 GHz of the first dual-band RA filter.

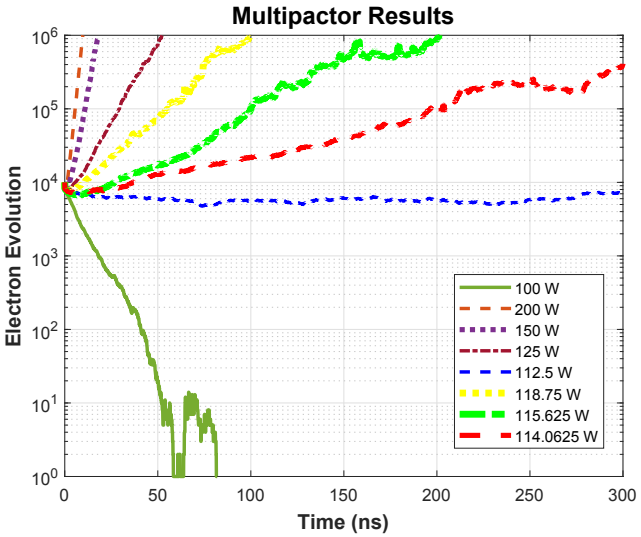

Figure 6.42: Multipactor simulation with discharges for the resonant aperture RA_3 at 6.97 GHz of the second dual-band RA filter.

Table 6.6: The higher order modes cut-off frequencies.

Mode	Cut-off frequency
Waveguide WR-90	a =22.86 mm b =10.16 mm
TE_{10}	f_c =6.557 GHz
TE_{20}	f_c =13.114 GHz
TE_{01}	f_c =14.753 GHz

lowest power threshold at 6.98 and 6.97 GHz with 119 and 113 W, respectively. Finally, the values obtained for each simulation in the resonant apertures of the two dual-band RA filters are shown in Fig. 6.41 and Fig. 6.42. The multipaction power levels obtained in the two dual-band filters are indeed remarkable, considering the significant size reduction that we have been able to obtain with the proposed filter topology.

6.9 Higher Order Modes Analysis

In this section we show the results of the higher order modes analysis for the two dual-band filters designed in this chapter.

It is important to note at this point that the measured performances of our two prototypes have been obtained using only the fundamental TE_{10} mode excitation. To complete our investigation, we now study the performance of our filters under higher order mode excitation. Table 6.6 shows the cut-off frequencies of the higher order modes that we have studied. Our investigation indicates that only the TE_{20} higher order mode needs to be studied in detail, as it causes a relevant spurious response in the out-of-band frequency range of interest.

As in the Chapter 5, if the higher order modes are present in the excitation, we can easily suppress the spurious responses generated by the TE_{20} higher order mode connecting the device shown in Fig. 6.43 at the output of our filters.

Table 6.7 shows the final values for all dimensions of the high-pass filter. The dimensions are given up to the center of the device, since it is a symmetric structure.

Fig. 6.44 and Fig. 6.45 show the comparison of the simulated performances (with CST) of the two dual-band RA filters, namely, DB RA Stair TZ Filter I and II, with and without the high-pass device. As we can see, we now have spurious responses below -30 dB from 13 to 16 GHz for both filters. This is indeed an important improvement.

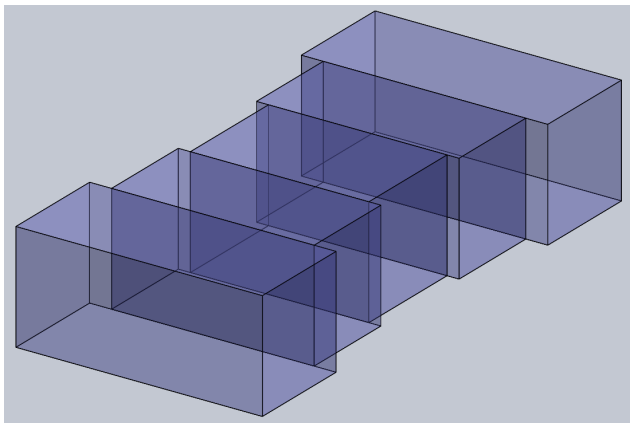

Figure 6.43: Structure of the H-plane transformer composed of rectangular waveguide sections of smaller width.

Table 6.7: Physical dimensions for the high-pass filter.

Section Type	Dimensions (mm)
Input Waveguide	$a = 22.86$ $b = 10.16$ $L_{input} = 10$
Section 1	$w_1 = 18.788$ $h_1 = 10.16$ $L_1 = 9.057$
Section 2	$w_2 = 16.556$ $h_2 = 10.16$ $L_2 = 10.604$

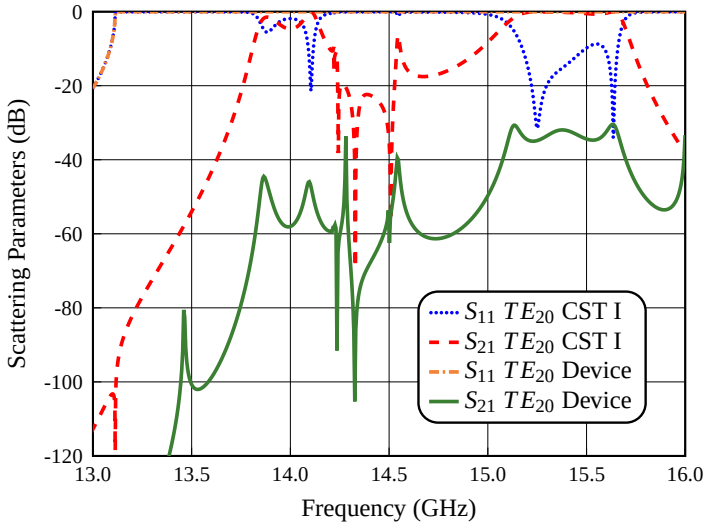

Figure 6.44: Simulated performance (using CST) of the first dual-band RA filter with TE_{20} excitation (TE_{20} CST I) compared to the performance of the filter plus high-pass device (TE_{20} Device).

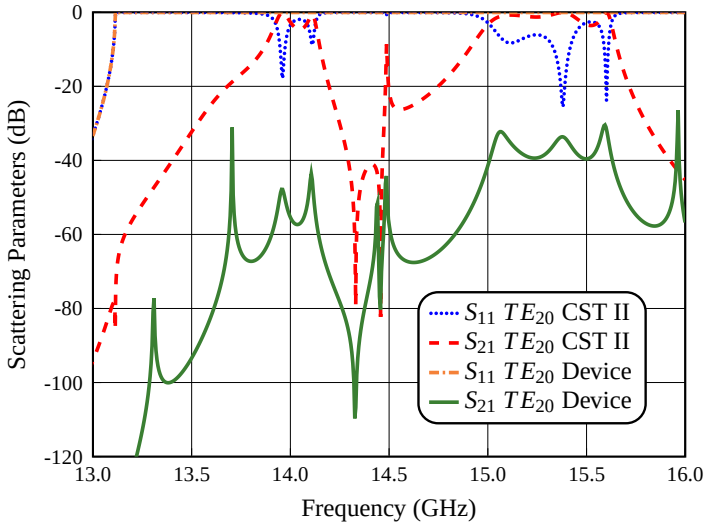

Figure 6.45: Simulated performance (using CST) of the second dual-band RA filter with TE_{20} excitation (TE_{20} CST II) compared to the performance of the filter plus high-pass device (TE_{20} Device).

We have therefore clearly demonstrated that, if it is necessary, we can use the simple device shown in Fig. 6.43 to reduce the spurious responses generated by the TE_{20} higher order mode.

6.10 Conclusions

In this chapter, we have discussed the design of dual-band waveguide filters based on resonant apertures. The results obtained indicate that the design procedure we have developed produces very compact structures, with a very good performance both inter-band and out-of-band. Furthermore, sensitivity, multipaction and higher order mode analyses have also been carried out.

Finally, we have also shown the experimental results for the two prototypes that we have manufactured, indicating very good agreement with simulations, thereby fully validating both the dual-band filters, and the corresponding procedure.

Chapter 7

Wideband Filters in Rectangular Waveguide Using Resonant Apertures

In this chapter, we describe a new family of microwave bandpass filters in rectangular waveguide based on resonant apertures that can be used to implement wideband filters. The use of capacitive stubs and a staircase configuration is also discussed in order to enhance the out-of-band response and the selectivity of the filter. In the following sections, we first describe the design procedure of the wideband filter, and we then discuss the simulated and manufactured performance of several prototypes.

As already discussed in the previous chapter, the results of our investigation in wideband waveguide filters based on resonant apertures have resulted in a publication that is currently under review:

- J.F Valencia Sullca, S. Cogollos, M. Guglielmi and V.E. Boria, "Compact dual-band and wideband filters with resonant apertures in rectangular waveguide," Under review in IEEE Transactions on Microwave Theory and Techniques.

The objective of this chapter is to extend the results in Chapter 6 for dual-band filters based on resonant apertures to the design of wideband filters with a single pass-band.

In this context, therefore, we discuss in this chapter a novel wideband waveguide filter based on resonant apertures with the following characteristics:

- The basic filter structure produces a single pass-band.
- The desired response is obtained optimizing the width a_1 and height b_1 of the RAs,

and the height b and length l of the distributed resonators.

- The out-of-band response and selectivity of the filter are strongly improved using the staircase configuration and capacitive stubs.
- The structure that we propose is mono-modal in the range of frequencies where the modes TE_{102} and TE_{103} are resonating. As a result, the negative effects of higher order modes are avoided.
- Due to the geometrical simplicity of the filter structure, we will be able to perform all simulations with FEST3D in the high accuracy mode.

7.1 Extended Bandpass RA Filter

An additional application of the RA concept is the design of bandpass filters with a single wide pass-band. The basic idea is to join the two pass-bands of the dual-band RA filter discussed in the previous chapter, thus obtaining a single, wide (or extended), pass-band. The electrical specifications that we will use for the extended bandpass RA filter design are as follow:

- Order $N = 9$
- Bandwidth $BW = 1400$ MHz
- In-band return loss $RL > 20$ dB
- Center frequency $f_0 = 7.55$ GHz
- Guided-wavelength fractional bandwidth $\mathcal{W}_\lambda = 105.041$ %
- Implementation of transmission zeros (TZs): Yes
- Input and output waveguide: WR-90 ($a = 22.86$ mm and $b = 10.16$ mm)

7.2 Design Procedure of Extended Bandpass RA Filter

The design procedure that we propose to use for the extended bandpass RA filter is detailed next.

We first obtain the normalized lumped element low-pass network (g_i values) of the (Chebyshev) filter from the specifications of the return loss (RL) and the order of the filter (N).

It is important to recall now that, in the low-pass network, the series components (with value g_i) are normalized inductors (L_n), and the shunt components (with value g_i) are normalized capacitors (C_n). Furthermore, we are free to choose between two different networks. One begins with series inductors and the other begins with shunt capacitors. In our work, we will implement the first element (g_1) as a shunt capacitor, as shown in Fig. 2.28.

Once the lumped low-pass model is obtained, we can perform a low-pass to bandpass transformation in order to obtain the bandpass network. The series inductors are then transformed into series resonant circuits with the following values:

$$L_{ri} = \frac{L_n}{\Delta\omega} \tag{7.1}$$

$$C_{ri} = \frac{\Delta\omega}{L_n\omega_0^2} \tag{7.2}$$

Similarly, the shunt capacitors are transformed into shunt resonant circuits with the following values:

$$L_i = \frac{\Delta\omega}{C_n\omega_0^2} \tag{7.3}$$

$$C_i = \frac{C_n}{\Delta\omega} \tag{7.4}$$

where $\Delta\omega$ corresponds to $2\pi BW$ (being BW the frequency bandwidth of the filter response). Before computing the real values of the lumped elements of the bandpass filter model, we must choose the impedance Z_0 to de-normalize the cited model (in this case Z_0 will be the characteristic impedance of the input waveguide, as defined next, and evaluated at the center frequency of the pass-band).

After that, we will proceed to transform the de-normalized lumped element model (Fig. 7.1) into a distributed bandpass filter of order $2N + 1$. For this purpose, we have implemented the $(N + 1)$ shunt resonators with RAs, and the (N) series resonators with sections of half-wavelength waveguide.

Next, the distributed bandpass model is built. For this purpose, it is necessary to calculate a set of parameters, namely, the slope parameter, the guided wavelength and the characteristic impedance of each series resonator.

The slope parameter of the LC resonators is given by:

$$\chi_{ri} = \omega_0 L_{ri} \tag{7.5}$$

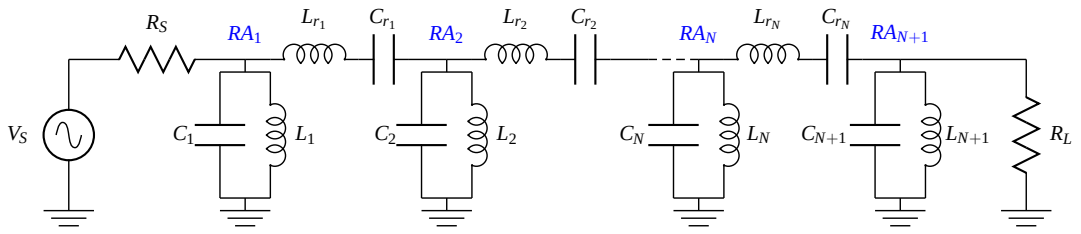

Figure 7.1: Circuital model of the extended bandpass RA filter.

The guided wavelength expression is given by:

$$\lambda_g = \frac{\lambda_0}{\sqrt{1 - \left(\frac{f_c}{f_0}\right)^2}} \tag{7.6}$$

where $\lambda_0 = c/f$ is the free-space wavelength, and $f_c = c/2a$ is the cutoff frequency.

The relation between the slope parameter (χ_{ri}) and the characteristic impedance of each waveguide (Z_{0_i}) is defined by the following expression [1]:

$$\chi_{ri} = Z_{0i}\frac{\pi}{2}\left(\frac{\lambda_{gi}}{\lambda_0}\right)^2 \tag{7.7}$$

All previous expressions can then be used to obtain the dimensions (a, b and length) of the waveguides that will replace the series resonators, after matching eqs. (7.5) and (7.7).

It is also possible to obtain the relation between the dimensions a and b (i.e. b/a) of each waveguide using the value of the corresponding characteristic impedance previously obtained, by using the following relationsip:

$$Z_{0i} = 2\frac{b}{a}\, Z_{TE} \tag{7.8}$$

where Z_{TE} is the frequency dependent modal impedance of the fundamental mode [2].

After that, we have all we need to substitute the series resonators with real waveguide sections with dimensions a, b and length equal to the half guided wavelength.

To continue, we model the half-wavelength waveguide lengths, near the resonance frequency, as a $\prod$-structure formed by one series and two shunt resonators, as shown in Fig. 7.2. Next, the values of the lumped elements of the model are obtained from the following expressions [3]:

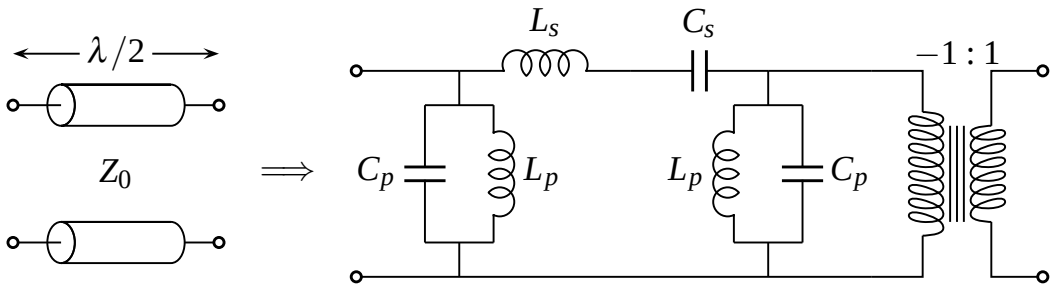

Figure 7.2: Circuital model based on a $\prod$ configuration.

$$L_s = \frac{\pi\ Z_0}{2\ \omega_0} \tag{7.9}$$

$$C_s = \frac{2\ Y_0}{\pi\ \omega_0} \tag{7.10}$$

$$C_p = \frac{\pi\ Y_0}{4\ \omega_0} \tag{7.11}$$

$$L_p = \frac{4\ Z_0}{\pi\ \omega_0} \tag{7.12}$$

It is important to mention that the series part of the $\prod$-structure can be identified with the series resonator elements, namely L_{ri} and C_{ri}, of the lumped elements model previously derived. It is important to note now that the parasitic capacitance and inductance connected in parallel, will change the behavior of the original de-normalized C_i and L_i (shunt resonators). For that reason, it is compulsory to design new shunt resonators that, including the parasitic elements, have responses as similar as possible to the original ones (C_i and L_i).

The new shunt resonators obtained from the $\prod$-model, provide the responses needed to create the resonant apertures. The next step that is required is a simple optimization to obtain the final distributed bandpass model that produces the desired response. Then, in order to obtain the real waveguide structure, we optimize the following variables: width, height and thickness of each RA, and a, b and the length of each waveguide resonator.

With the procedure just described, we can easily obtain a compliant extended bandpass RA filter of order $2N + 1$, with $(N + 1)$ RAs, and N distributed resonators.

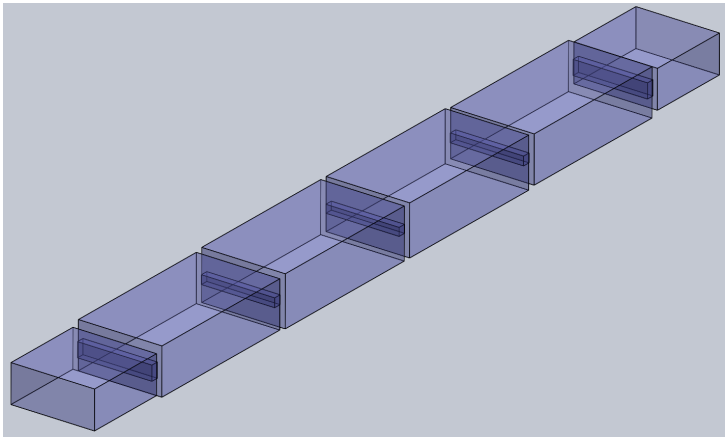

Figure 7.3: Structure of the extended bandpass RA filter.

7.2.1 Extended Bandpass RA Reference Filter

In this section, we have used the design procedure described in the previous section to obtain the waveguide structure of a RA filter with extended pass-band. Fig. 7.3 shows the structure of the filter. Fig. 7.4 shows the simulated behavior of the structure in Fig. 7.3 (EB RA Filter).

As we can see, this filter has a number of interesting features:

- The filter is a compact nine-pole filter, with only four distributed resonators.
- The spurious response of the filter at 10 GHz is only due to the four distributed resonators, since the other five poles (or reflection zeros) are due to lumped element resonators and are inherently non-periodic in nature.

We can conclude that the extended bandpass filter based on resonant apertures has been designed successfully starting from the electrical specifications, and using the procedure we have developed. In the next sections, we use again the capacitive stubs and the staircase configuration in order to improve both the out-of-band response and selectivity of the filter.

7.2.2 Capacitibe Stubs

To continue, we now use capacitive stubs in the extended bandpass RA filter, in order to suppress the spurious out-of-band response. Fig. 7.5 shows the structure of the extended bandpass filter with capacitive stubs. Fig. 7.6 shows a comparison between the simulated behavior of the structures in Fig. 7.3 (EB RA Filter), and Fig. 7.5 (EB RA TZ Filter), respectively.

As we can see, using four capacitive stubs in each of the RAs produces a reduction

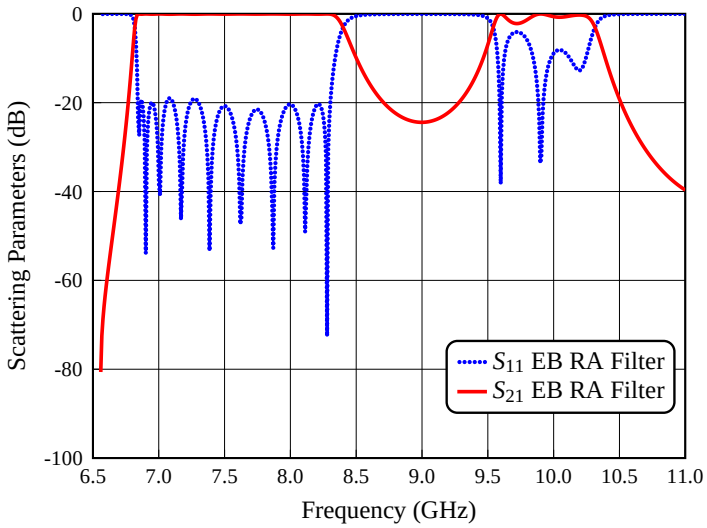

Figure 7.4: Simulated performance of the extended bandpass RA filter (EB RA Filter).

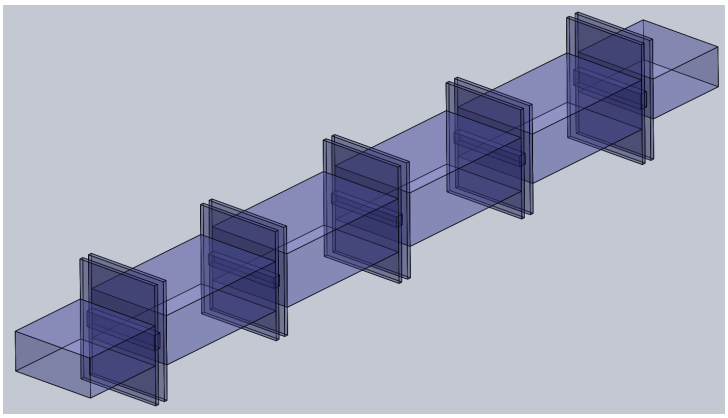

Figure 7.5: Structure of the extended bandpass RA filter with four capacitive stubs between all the RAs.

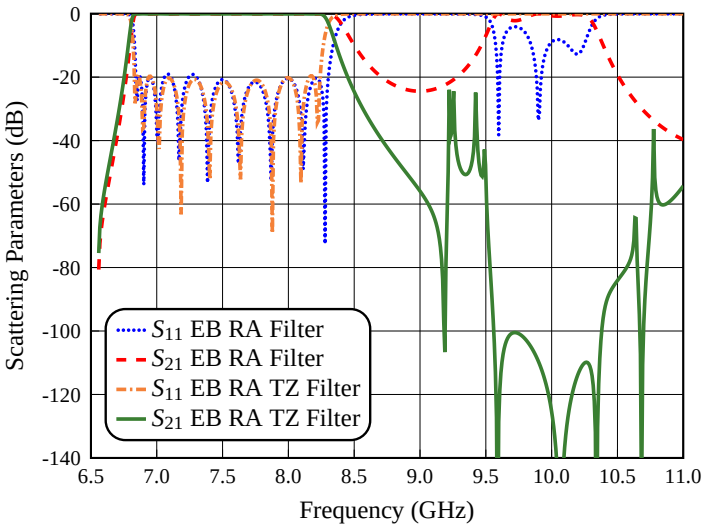

Figure 7.6: Simulated performance of the extended bandpass RA filter (EB RA Filter) and the EB RA Filter with four capacitive stubs between all the RAs (EB RA TZ Filter).

and attenuation of the spurious response below -40 dB, with spikes reaching -25 dB at 9.22 and 9.42 GHz, and -35 dB at 10.77 GHz, respectively.

7.2.3 Staircase Filter

In the previous chapters, we have used the staircase configuration to provide an important attenuation and reduction of the spurious response of a number of filters. For this reason, we now implement this configuration in the basic extended bandpass RA filter shown in Fig. 7.3. Fig. 7.7 shows the resulting structure. Fig. 7.8 shows a comparison of the simulated behavior of the structures in Fig. 7.3 (EB RA Filter) and Fig. 7.7 (EB RA Stair Filter I), respectively.

As we can see, the use of the staircase configuration does result into a significant reduction and attenuation of the spurious response. In addition, transmission zeros at 9.13, 9.37 and 9.78 GHz have also been generated. Unfortunately, however, there is still a spurious response at 10.25 GHz.

It is important to mention that the RAs have been placed at $l_s = 3l/4$ in the resonators (as illustrated in Fig. 6.17 of the previous chapter). A further improvement of the out-of-band response can be achieved, by optimizing the location of the RAs. Fig. 7.9 shows a comparison of the simulated behavior of the structure in Fig. 7.7 with the original staircase configuration (EB RA Stair Filter I) and with optimized RAs location (EB RA Stair Filter II), respectively.

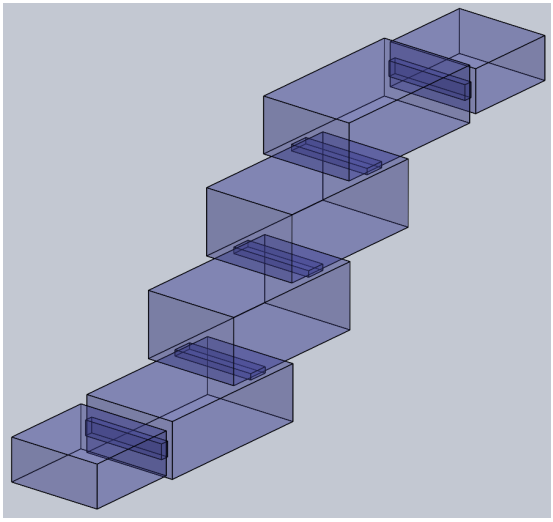

Figure 7.7: Structure of the extended bandpass RA staircase filter.

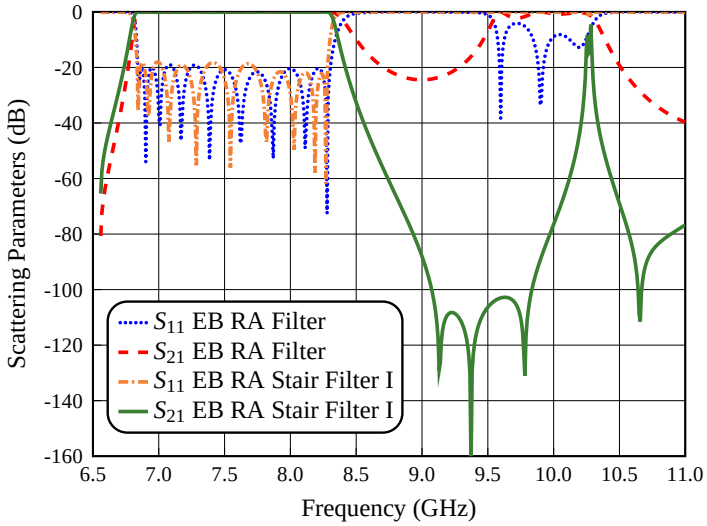

Figure 7.8: Simulated performance of the extended bandpass RA filter (EB RA Filter) and the EB RA Filter with the staircase configuration (EB RA Stair Filter I).

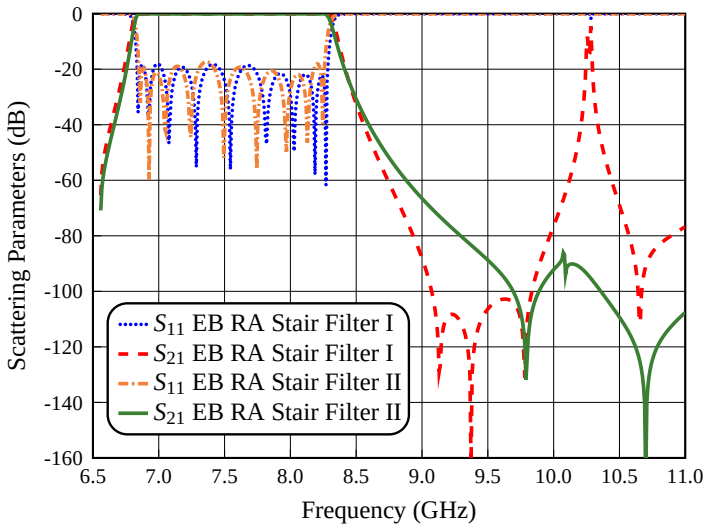

Figure 7.9: Simulated performance of the extended bandpass RA filter with the staircase configuration (EB RA Stair Filter I) and the EB RA Stair Filter I with the optimized change of the RAs location (EB RA Stair Filter II).

As we can see, with the implementation of this change of RAs location, we obtain a significant reduction and attenuation of the spurious response below -90 dB from 9.50 to 11.00 GHz.

7.2.4 Staircase Filter With TZs

The final improvement that we propose in this chapter, is to use both capacitive stubs and the staircase configuration to further improve the out-of-band performance and the filter selectivity. Fig. 7.10 shows the structure of the extended bandpass RA staircase filter with two stubs, located both before and after the input and output RAs. Fig. 7.11 shows a comparison of the simulated behavior of the structures in Fig. 7.7 (EB RA Stair Filter II) and Fig. 7.10 (EB RA Stair TZ Filter), respectively.

As we can see, an important reduction and attenuation of the spurious response below -75 dB from 9 to 11 GHz has been achieved. Transmission zeros at 8.89, 9.38 and 9.84 GHz have have been obtained, thereby increasing the filter selectivity.

The performances of the first EB RA Filter (see Fig. 7.3) and of the EB RA Stair TZ Filter (see Fig. 7.10) are compared in Fig. 7.12.

As we can clearly see, the last structure shows a very significant improvement of the out-of-band response in comparison with the first EB RA Filter. To conclude this section, we have extended the comparison to a wider frequency range, namely, from 6.5

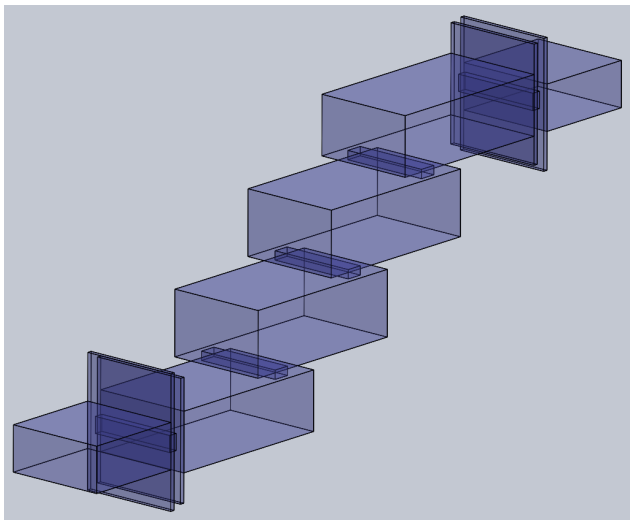

Figure 7.10: Structure of the extended bandpass RA staircase filter with two stubs both before and after of the input and output RAs.

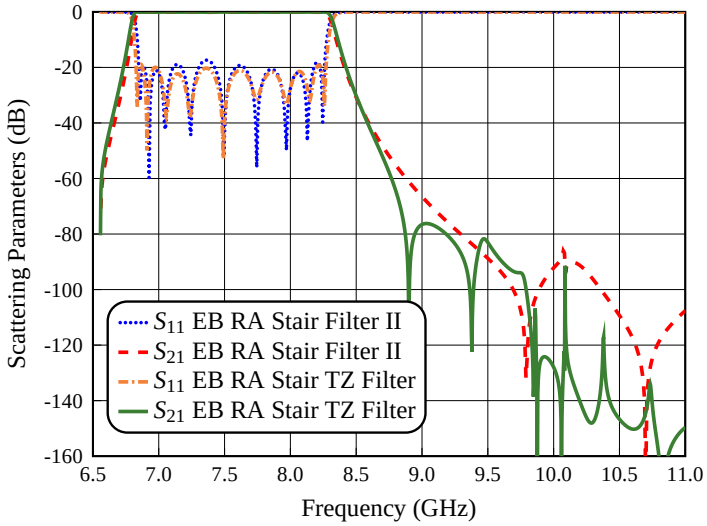

Figure 7.11: Simulated performance of the extended bandpass RA staircase filter (EB RA Stair Filter II) and the EB RA Stair Filter II with two stubs both before and after of the input and output RAs (EB RA Stair TZ Filter).

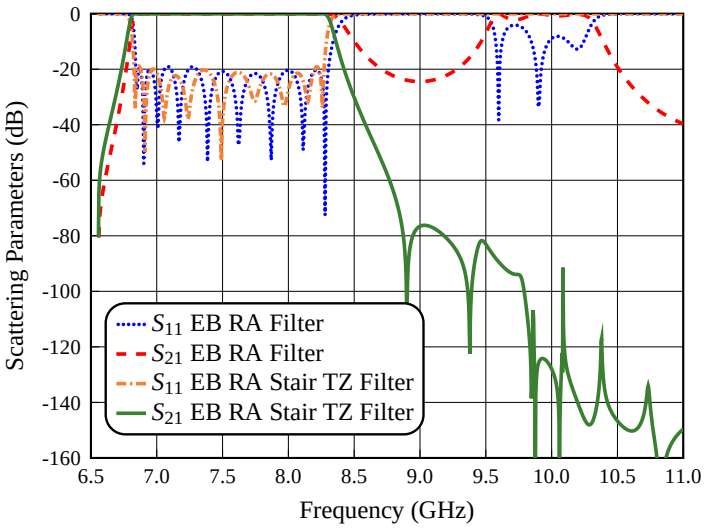

Figure 7.12: Simulated performance of the extended bandpass RA filter (EB RA Filter) and the EB RA Stair Filter II with two stubs both before and after of the input and output RAs (EB RA Stair TZ Filter).

to 13 GHz. Fig. 7.13 shows a comparison of the simulated behavior of the structures in Fig. 7.3 (EB RA Filter I) and Fig. 7.10 (EB RA Filter II), respectively. As we can see, our last filter does show a very significant improvement with respect to the first structure discussed in this chapter.

We can therefore conclude that, as expected, the combination of capacitive stubs with the staircase configuration, results into an important improvement of both the out-of-band response and the selectivity of the extended bandpass RA filters.

7.3 Extended Bandpass RA Prototype

To continue, it is important to mention that all structures discussed in this chapter have been simulated with FEST3D in high accuracy mode, with the following settings:

- Accessible modes: 120
- Number of basis functions: 360
- Green's function terms: 3600

However, all the structures designed so far have sharp corners (90°). As a consequence, we now need one more step before we can manufacture a prototype, namely, we need to replace all sharp concave corners in the cavities with rounded corners with a radius equal to r =1.1 mm. This will enable us to use a standard milling technique. The stubs, on the other hand, will remain as they are. They will be manufactured using spark

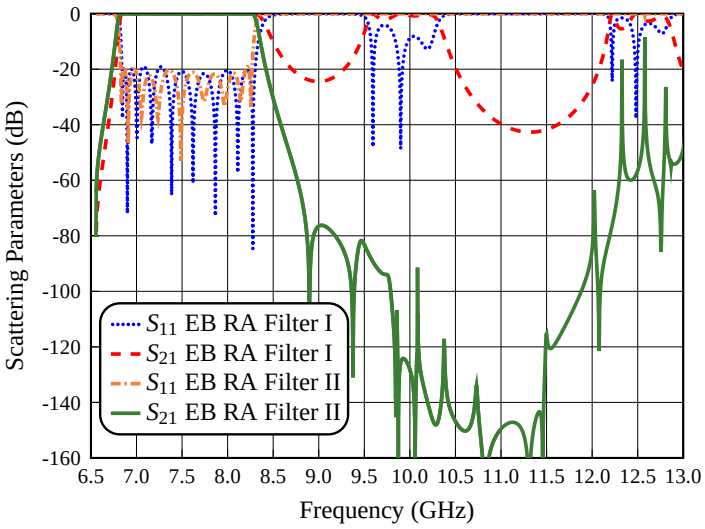

Figure 7.13: Simulated performance, in a wider frequency range (from 6.5 to 13 GHz), of the EB RA Filter (EB RA Filter I) and the EB RA Stair TZ Filter (EB RA Filter II).

erosion.

The final structure is shown in Fig. 7.14 (EB RA Stair TZ Filter). Fig. 7.15 shows the comparison of the simulated performances obtained with the software tools FEST3D and CST Studio Suite. To ensure the high accuracy of the results, CST Studio Suite has been used with the following settings:

- Solver: Frequency Domain Solver
- Frequency sweep: General Purpose
- Mesh refinement: 7.55 GHz
- Error threshold: 0.01
- Maximum number of iterations: 50

As we can see, the agreement is very good even at the high frequency end. The out-of-band response is also found to be very good, with spurious below -60 dB from 9 to 12 GHz, -40 dB from 12 to 13 GHz, with spikes reaching -7.78, -9.72 and -15.25 dB at 12.32, 12.58 and 12.80 GHz, respectively.

The final values for all dimensions of the extended bandpass RA staircase filter with capacitive stubs is shown in Table 7.1. The dimensions are given up to the center of the filter. This is because the whole structure is asymmetrical, but the central part of the filter is symmetrical. The thickness of the RAs is t_i, and all the resonators and capacitive stubs have the same width as the input waveguide.

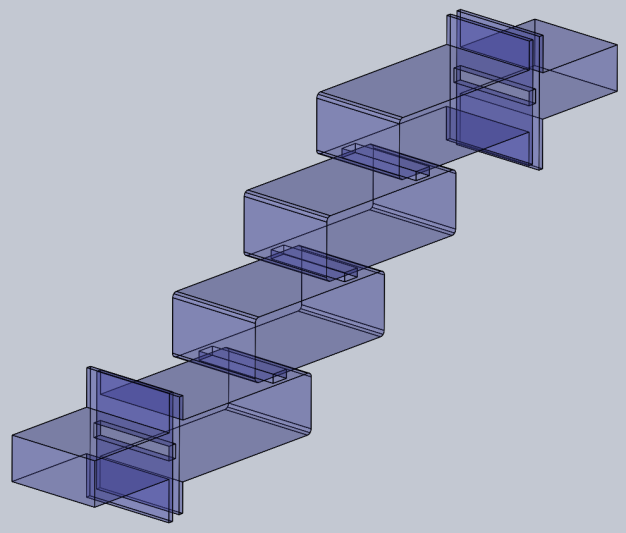

Figure 7.14: Structure of the extended bandpass RA filter with two stubs both before and after of the input and output RAs (EB RA Stair TZ Filter), designed with a radius equal to $r = 1.1$ mm in the distributed resonators.

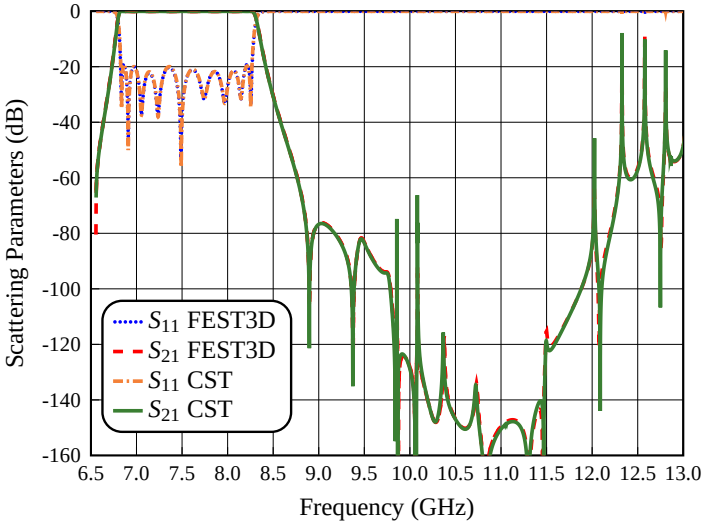

Figure 7.15: Simulated performance of the extended bandpass RA filter with two stubs both before and after of the input and output RAs (EB RA Stair TZ Filter) using FEST3D and CST.

Table 7.1: Physical dimensions for the EB RA Stair TZ Filter.

Section Type	Dimensions (mm)	
Input Waveguide	a =22.86 b =10.16 $L_{input} = L_{output}$ =22.86	
Capacitive stubs 1-2	l_{cs_1} =10.861 t_{cs_1} =1.1	l_{cs_2} =8.217 t_{cs_2} =1.1
Capacitive stubs 3-4	l_{cs_3} =7.343 t_{cs_3} =1.1	l_{cs_4} =6.352 t_{cs_4} =1.1
Capacitive stubs 5-6	l_{cs_5} =6.870 t_{cs_5} =1.1	l_{cs_6} =5.343 t_{cs_6} =1.1
Capacitive stubs 7-8	l_{cs_7} =9.510 t_{cs_7} =1.1	l_{cs_7} =8.658 t_{cs_8} =1.1
Resonant aperture 1-5	a_1 =20.814 b_1 =3.155 t_1 =2.0	a_5 =20.814 b_5 =3.203 t_5 =2.0
Resonator 1-4	w_1 =22.86 H_1 =13.550 L_1 =39.868	w_4 =22.86 H_4 =13.550 L_4 =39.415
Resonant aperture 2-4	a_2 =20.525 b_2 =4.095 t_2 =2.0	a_4 =20.525 b_4 =4.095 t_4 =2.0
Resonator 2-3	w_2 =22.86 H_2 =14.325 L_2 =39.633	w_3 =22.86 H_3 =14.325 L_3 =39.633
Resonant aperture 3	a_3 =20.392 b_3 =3.857 t_3 =2.0	

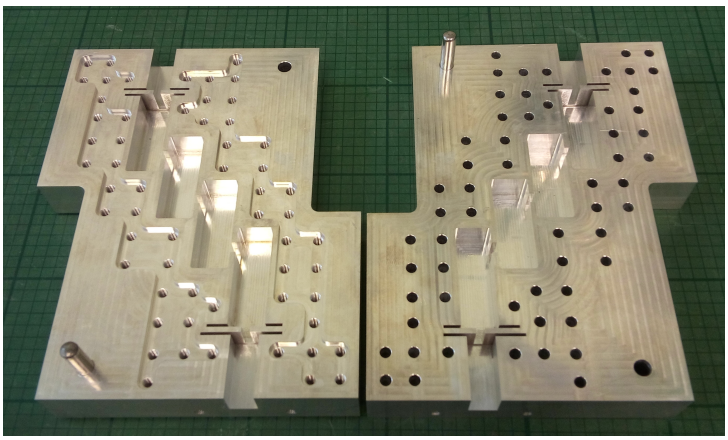

Figure 7.16: Manufactured extended bandpass RA prototype in aluminum (no silver plating).

7.3.1 Measurements

The filter prototype discussed in the previous section has been manufactured in a clam-shell configuration, using a combination of standard milling and spark erosion techniques, as shown in Fig. 7.16.

Next, we show in Fig. 7.17 the comparison between measured and simulated in-band responses. As we can see, the in-band performance is centered at 7.55 GHz, the nine reflection zeros of the filter are clearly visible, and the agreement with the simulation is excellent.

Fig. 7.18 shows the comparison between measured and simulated out-of-band responses. To produce the results shown in Fig. 7.18, we have used two standard waveguide calibrations, namely WR-90 and WR-75, with the TRL (Through, Reflection and Line) method. The noise floor in each calibration was about -70 dB.

As we can see, the out-of-band performance shows a good agreement between simulation and measurement results, with spurious below -75 dB from 9 to 12 GHz, and below -30 dB from 12 to 13 GHz, with spikes reaching -35, -25 and -27.5 dB at about 12.33, 12.58 and 12.80 GHz, respectively. However, a number of dips have appeared in the measured S_{11} results that are not present in the simulations.

To better understand this effect we have simulated the filter including losses. Fig. 7.19 shows a comparison of the simulated behavior of the extended bandpass RA filter including losses (aluminum), and the measured out-of-band response. As we can see in Fig. 7.19, the same dips are now clearly visible. Further investigations show that this behavior is due to the power dissipated in the filter structure, more specifically, in the capacitive stubs used to introduce transmission zeros. This is probably due to the fact that the height of the waveguide used to implement the stubs is only $t_s = 1.1$ mm. The resulting quality

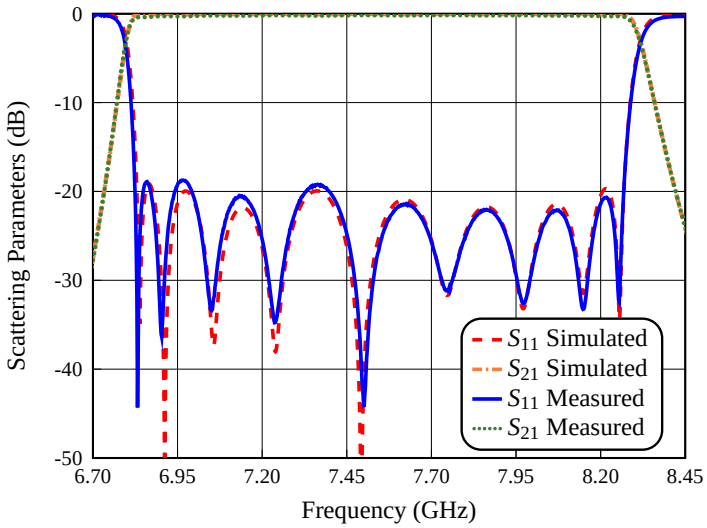

Figure 7.17: Measurement of the in-band performance of the extended bandpass RA filter compared with the EM simulation (CST).

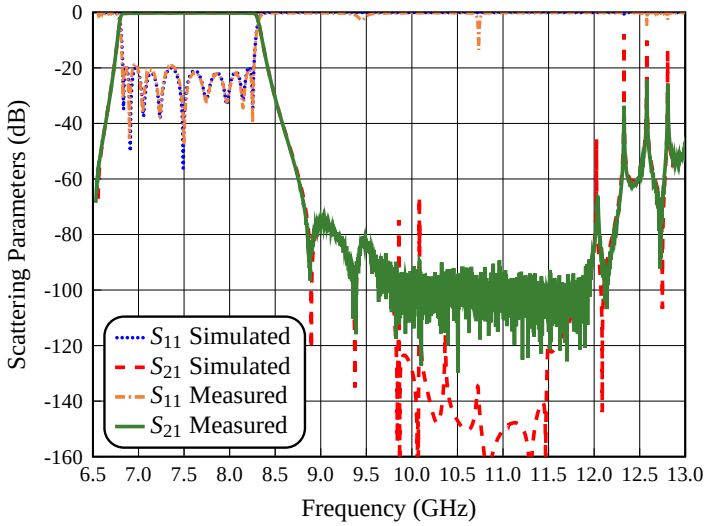

Figure 7.18: Measurement of the out-of-band performance of the extended bandpass RA filter compared with the EM simulation (CST).

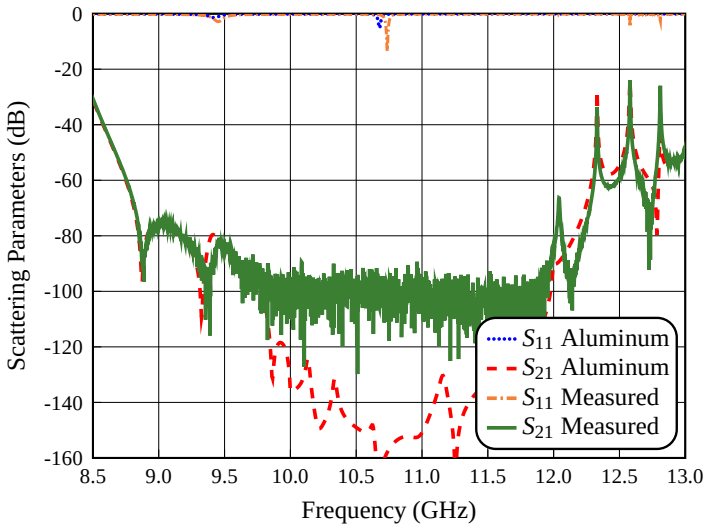

Figure 7.19: Measurement of the out-of-band performance of the extended bandpass RA filter compared with the EM simulation (CST) including losses (due to the finite conductivity of the aluminum).

Table 7.2: Results of the tolerance analysis for the extended bandpass RA filter.

Filter Type	Yield of the Structure			
Tolerance	5 μm	10 μm	15 μm	20 μm
EB RA Filter	78 %	54 %	38 %	14 %

factor of the stubs is therefore rather low, and absorption dips appear in the measured return loss.

7.4 Yield Analysis

In this section we show the results of a yield analysis for the extended bandpass RA filter just designed. For this purpose, we have used, as usual, the commercial tool FEST3D, introducing a random error with a Gaussian distribution in the filter dimensions.

The sensitivity analysis has been carried out with different values of the standard deviation, namely, $\pm$ 5, $\pm$ 10, $\pm$ 15 and $\pm$ 20 μm. Furthermore, since the filter has been designed with a return loss of 20 dB, the threshold value for the yield estimation has been set to 18 dB. Table 7.2 shows a summary of the results that we have obtained.

Fig. 7.20 shows a number of simulations using random errors. As we can see from both the simulations and the results in Table 7.2, with manufacturing errors between 5

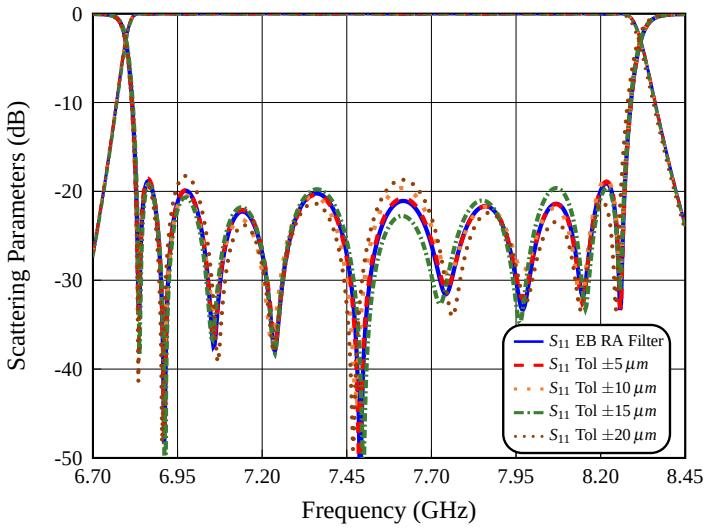

Figure 7.20: Tolerance analysis of the extended bandpass RA filter.

and 10 μm, it should be possible to obtain a very good yield value. This result is indeed validated by the measured results of the prototype (see Fig. 7.17).

7.5 High Power Analysis

In this section we show the results of a multipactor analysis for the filter designed in this chapter. This analysis has been done in order to identify the power (in W) where a multipactor effect can be initiated. For this purpose, we have chosen the frequencies where the group delay shows a maximum in the response (f_1 and f_3), and the center frequency (f_2). The simulations have been carried out using FEST3D for the EM fields, and SPARK3D for the multipaction prediction, with the following set of parameters:

1. Initial power: 100 W
2. Maximum power: 1 MW
3. Growth factor of the power: 10^2
4. Frequencies of simulation: f_1, f_2 and f_3
5. Initial number of electrons: 10000

In this case, the resonant aperture RA_2 shows the lowest power threshold at 6.81 GHz with 195 W. Finally, in Fig. 7.21 we show the values obtained with each simulation. It is important to note that the multipaction power levels obtained in the extended bandpass RA filer are indeed remarkable, considering the significant size reduction that we have been able to obtain with the proposed filter topology.

Table 7.3: High power analysis of the extended bandpass RA filter.

Structure	Power of the structure		
Frequency	$f_1 = 6.81$ GHz	$f_2 = 7.55$ GHz	$f_3 = 8.30$ GHz
RA_1	484 W	1875 W	1138 W
$RA_2 = RA_4$	195 W	1235 W	378 W
RA_3	204 W	1135 W	403 W
RA_5	1112 W	1887 W	2974 W

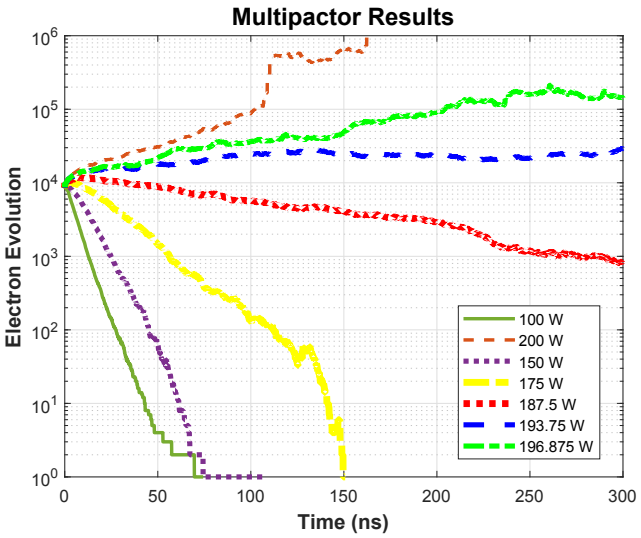

Figure 7.21: Multipactor simulation with discharges for the resonant aperture RA_2 at 6.81 GHz of the extended bandpass RA filter.

7.6 Higher Order Mode Analysis

In this section we show the results of the higher order mode analysis for the extended bandpass RA filter designed in this chapter. It is important to note at this point that the performance of our EB RA filter is mono-modal until 13.0 GHz. For that reason, we have compared the performance of the EB RA Filter (see Fig. 7.3) with the EB RA Stair TZ Filter (see Fig. 7.10), for a wide range of frequencies, namely, from 6.5 to 16.0 GHz.

Fig. 7.22 shows a comparison of the simulated behavior of the structures in Fig. 7.3 (EB RA Filter III) and Fig. 7.10 (EB RA Filter IV), from 6.5 to 16.0 GHz, where the modes TE_{102}, TE_{103} and TE_{104} appear at 10.0, 12.5 and 15.5 GHz, respectively.

As we can see, the mode TE_{102} shows an important attenuation of the spurious response below -70 dB from 9.0 to 11.5 GHz, whereas modes TE_{103} and TE_{104} show a

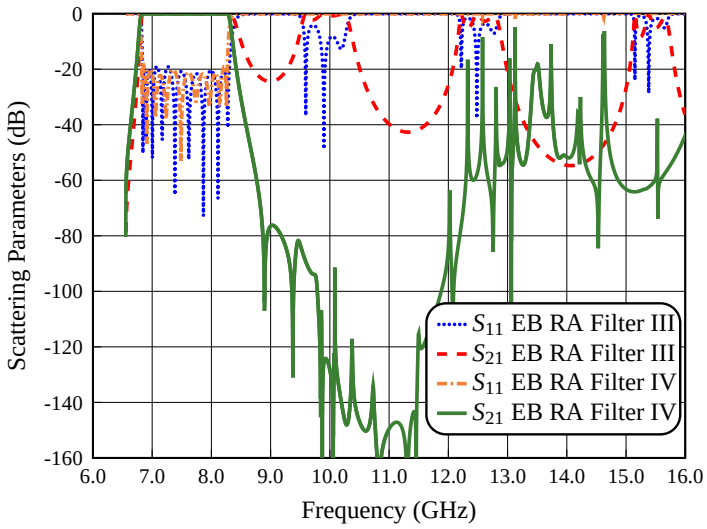

Figure 7.22: Simulated performance of the EB RA Filter (EB RA Filter III) and the EB RA Stair TZ Filter (EB RA Filter IV).

reduction of the spurious response from 11.5 to 16.0 GHz, respectively.

Next, we will study the performance of our EB RA filter under higher order mode excitation. As we already did in Chapter 6, only the TE_{20} higher order mode needs to be studied in detail for the range of frequencies up to 16.0 GHz. If the TE_{20} higher order mode is excited in our structure, the spurious responses generated can be very easily suppressed connecting the device shown in Fig. 6.43 of Chapter 6 at the output of our EB RA filter.

Fig. 7.23 shows the comparison of the simulated performances (with CST) of the extended bandpass RA filter, including the high-pass device. As we can see, we now have spurious responses below -30 dB from 13 to 16 GHz. This is indeed an important improvement.

We can therefore conclude that, using the device shown in Fig. 6.43 of Chapter 6, we can reduce the spurious responses generated by the TE_{20} higher order mode in our EB RA filter.

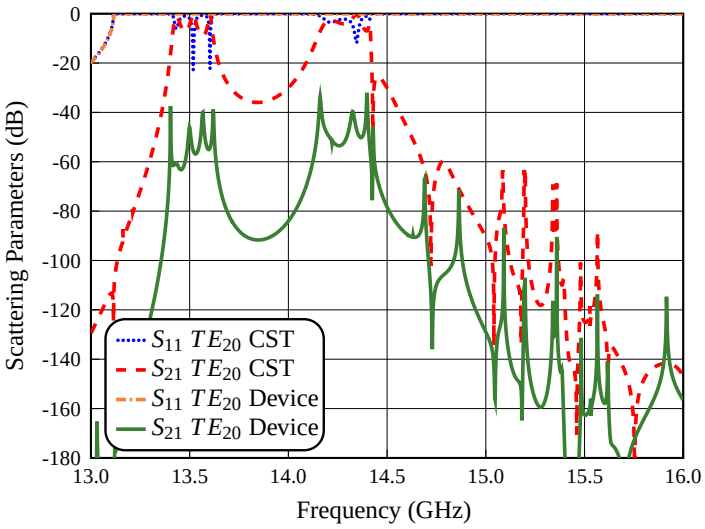

Figure 7.23: Simulated performance (using CST) of the extended bandpass RA filter with TE_{20} excitation (TE_{20} CST) compared to the performance of the filter plus high-pass device (TE_{20} Device).

7.7 Conclusions

In this chapter, we have discussed a novel structure for the implementation of wideband waveguide filters in rectangular waveguide, that is based on the mixed use of resonant apertures (RAs) and conventional distributed resonators. The new structure demonstrates an excellent performance and a very significant reduction of the filter dimensions with respect to the state-of-the-art. In addition, we have also described in detail a design procedure, that can be used very effectively to obtain the dimension of the filter from the set of desired performance specifications.

Furthermore, we have also shown how the performance of the extended bandpass RA filters can be significantly enhanced, both in the out-of-band response and in the selectivity, using a combination of the staircase configuration and capacitive stubs. In addition, the results of the detailed yield, high power and higher order mode analyses have also been discussed.

Finally, we have also shown experimental results demonstrating very good agreement with simulations, thereby fully validating both the new filter structure and the design procedure.

Chapter 8

Conclusions and Future Work

8.1 Conclusions

In this doctoral thesis, we have provided a number of practical contributions to the state-of-the-art of wide bandpass microwave filters for space or ground applications, that are manufactured in rectangular waveguide, and that have a spurious-free rejection band that is as large as possible. In this chapter, we provide a summary of all the contributions obtained in this doctoral thesis. The chapter is concluded outlining a number of possible future research areas.

The first topic that we have proposed is the complete design procedure of a wideband waveguide filter structure, based on the use of stepped impedance resonators (SIRs) in conjunction with capacitive and inductive coupling irises (hybrid filter), that provides a significant improvement in the out-of-band response of the filter with respect to the state-of-the-art. The key of the proposed design procedure is that the final structure is obtained using a very efficient combination of low accuracy and high accuracy simulations, thereby leading to a very accurate final filter design.

In addition to theory, we have also clearly demonstrated the advantages introduced by the new filter structure that we have proposed with the design, manufacture and measurement of an in-line eight-pole wideband hybrid SIR filter. The structure described shows a very significant rejection of the spurious responses in a wide stop-band and, at the same time, is suitable for implementations that require a wide pass-band.

The next contribution that we have proposed is the implementation of the in-line

hybrid SIR filter based on the H-plane and E-plane configurations. In particular, our approach allows us to obtain new structures that provide advantages both in the manufacturing process and in the reduction in the size of the filter. In particular, for the H-plane configuration, we have obtained an in-line hybrid SIR filter with tuning elements in the SIRs resonators. For the E-plane filter, the resulting structure is a very compact E-plane folded hybrid SIR filter.

Furthermore, the two configurations that we have proposed, have also been validated by designing, manufacturing and measuring two 8-pole hybrid SIR filter, namely, an H-plane in-line hybrid SIR filter with tuning screws, and an E-plane folded hybrid SIR filter. Several enhancements introduced in the final structures have also been discussed in order to obtain an important improvement of the out-of-band response of the filter.

The next contribution that we have discussed in this thesis is a new topology for wideband hybrid filters in rectangular waveguide based on the use of a staircase configuration in the resonators. This new configuration can be used to easily attenuate or reduce the higher order mode spurious responses of the resonators. Furthermore, an enhancement of the out-of-band response and selectivity of the filter have also been achieved by using both E-plane T-junctions and E-plane folded structures. The proposed topology has been validated by designing, manufacturing and measuring of an eight-pole hybrid wide-band staircase filter.

It is interesting to note that, the new staircase topology overcomes the limitations of the previous structures since the filter is more compact, due to the staircase configuration and the E-plane folding. Furthermore, the staircase filter is very easy to manufacture and does not require tuning screws.

The next contribution that we have discussed is the design of a new family of microwave bandpass filters in rectangular waveguide, based on resonant apertures, that can be used to implement both dual-band and wideband filters. The key feature of the novel filters that we propose is the use of coupling windows with a dual function, namely, resonant apertures (RAs) and impedance inverters. The benefits introduced by our contribution are that the filters obtained are extremely compact and provide, at the same time, an important improvement of the out-of-band response.

As a verification, we have designed, manufactured and measured two compact dual-band filters with two pass-bands, namely, the first one due to the resonant apertures (five-pole filter), and the second due to the distributed resonators (four-pole filter). In addition, we have also shown how important improvements in the out-of-band response, selectivity and inter-band rejection can be effectively obtained with the implementation of different techniques. Finally, the measured responses have been found to be in excellent agreement with the simulations, thereby fully validating the new dual-band filter topology.

Finally, the last contribution that we have discussed is the design procedure for wideband filters based on the use of resonant apertures, as mentioned in the previous paragraph. The key feature of the novel topology that we propose is the joining of the two pass-bands of the dual-band filter, in order to obtain a filter structure with a single wide pass-band. To further improve the out-of-band response and the selectivity, we have also used both the staircase configuration and a number of capacitive stubs. The proposed topology has been validated by designing, manufacturing and measuring of a compact nine-pole wideband filter.

8.2 Future work

The research work described in this thesis can effectively be used as a starting point for future research. Several areas could indeed be explored. In particular:

- **New Filter Structures**. Until now, in all the hybrid SIR filters described in this thesis, we have not used capacitive stubs in the sections where there are capacitive irises. The use of stubs could improve both the selectivity and spurious response of the filter and increase, at the same time, the height of the capacitive irises in order to avoid high power limitations. For the E-plane folded hybrid SIR filter, it may be beneficial to design alternative folded structures for the irises or resonators to reduce the footprint of the filter, and provide a further improvement of the out-of-band response. An additional benefit of the E-plane folded hybrid filter, is the increased selectivity that can be obtained with the use of cross-couplings between non-adjacent resonators to introduce transmissions zeros near the pass-band.
- **Hybrid Staircase Filter Tuning**. In our work, we have clearly shown that the implementation of the staircase configuration in wideband hybrid filters in rectangular waveguide can be used to reduce the harmonic resonances very efficiently. It would be interesting to implement tuning screws on the side walls of the filter, in order to design a structure with body and cover that is easy to manufacture at a lower cost. Additionally, we could also use tuning elements in the compact filters based on resonant apertures.
- **New Manufacturing Prototypes**. All filters based on resonant apertures have been manufactured using E-plane cuts. It would be interesting to redesign the dual-band and wideband RAs filters in order to manufacture these structures with an H-plane cut. For this purpose, we would redesign the in-line RAs filters, where a vertical offset is introduced in the RAs, so that the resulting structure could be built with body and cover. Additionally, the resulting structure could also use tuning screws on the cover of the filters.

- **RAs and Capacitive Stubs (RACS) Filters**. A further interesting extension of the work described in this thesis, could be the exploration of the RACS filters based on the use resonant apertures (RAs) in conjunction with capacitive stubs (CS). In this way, we obtain more compact and suitable structures for wideband applications, that could improve the out-of-band response and the filter selectivity, and provide a substantial reduction in filter length.
- **Dielectric Loading of the Capacitive Irises.** A final future line of investigation could be the use of a dielectric material with dielectric permittivity close to unity as a load for all the capacitive apertures. The expected result would be a very significant increase of the maximum power that each filter (with capacitive irises) can handle without triggering the multipaction phenomenon.

Appendix A

Manufacturing Plans With Solid Works

A.1 Objective

The objective of this appendix is to describe in detail all the steps that are necessary in order to obtain the 3D manufacturing plans with Solid Works for all filters manufactured in this doctoral thesis.

Since the filters have been designed and manufactured in different configurations, namely, E-plane and H-plane, we will propose for each of them a procedure that allows to obtain a geometry description of the filter that is suitable for manufacturing. For this purpose, we have used the following software tools:

- CST Studio Suite v.2021 for high precision EM simulations of the waveguide components.
- Solid Works v.2021 for all the graphic work of the 3D manufacturing plans.

A.2 Detailed Steps of the 3D Plans

In this section we will describe the procedure to be used in Solid Works (SW) to obtain the 3D plans for the structures we have designed.

A.2.1 Converting File Format

We first export the file format produced by CST, which could be .SAT or .STEP, with the objective to import this file in SW and next save as format normally used by SW, which is .SLDPRT. Once this is done, we are ready to draw the 3D plans in SW.

A.2.2 Designing the Outer Body

To draw the outer body of our structures, we first select the input or output face of the structure by applying the *Extrude Base operation*. For this purpose, we have used the dimensions of the waveguide flange of each filter in order to identify the height and width of the outer body. Also, depending on the symmetry of the structure, we need to implement the following steps:

- All in-line hybrid SIR filter have been designed with symmetry both in the H-plane and E-plane, except the in-line screw hybrid SIR filter, which is only symmetric in the H-plane. Therefore, we have only done an Extrude Base operation all through the structure in order to obtain the outer body.
- All other filters require additional dimensions to be added on both input and output to generate the outer body. This is because the structures are only symmetric in the H-plane.

It is important to mention that before we obtain the outer body, we should not merge the results of the box that contains the filter, and the filter itself.

A.2.3 Creating the Inside of the Filter

In this step, we will create the inside of the filter. For this purpose, we will subtract the inner body from the outer body we just created. The operation that we will do is *Insert*→*Features*→*Combine* from the top left menu in SW. Next, we will select the operation *Subtract* of the two objects. After that, we have correctly obtained the inside of the filter.

A.2.4 Input and Output Waveguide Flanges

Once we have identified the dimensions of the flanges of the waveguide, such as WR-90, we can then add holes for fastening the input and output flanges. The position of the holes is usually indicated as the X- and Y-coordinates from the center of the waveguide, as shown in Fig. A.1.

The dimensions of the waveguide flanges for the WR-90 are as follows:

- Dimensions of the height and width of the flanges are $A = 41.40$ mm

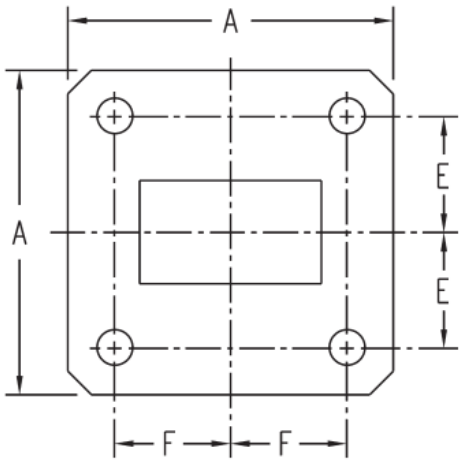

Figure A.1: Structure of the flanges for WR-90.

- Dimensions of the Y-coordinate of the holes are $E = 16.26$ mm
- Dimensions of the X-coordinate of the holes are $F = 15.49$ mm
- Dimensions of the M4 threaded holes are $\phi = 1.65$ mm

As already mentioned, we have used the dimensions of the waveguide flanges to design the outer body. Next, we will apply the *Extrude Cut operation*, where the threaded M4 screws are located both in the input and output surfaces of the structure. The depth of the holes in our designs is 10 mm.

A.2.5 Fixing Screws

The next step is to add the fixing screws to the outer body of our structures. For this purpose, we have chosen M4 through holes, which are in our case $\phi = 4.05$ mm. We have then selected along the structure a sufficient number of holes in order to ensure an adequate closing pressure. With this in mind, we use the *Extrude Cut operation* of the fixing screws through the whole outer body of the structure.

A.2.6 Alignment Pins

Since the filters have been designed using both H-plane and E-plane configurations, it is always a good idea to add alignment pins between body and cover. For that reason, we have decided to add two alignment pins of diameter equal to $\phi = 5.9$ mm in the outer body of the structure. To add alignment pins we have repeated the same procedure used for the fixing screws. Finally, we have used blind holes so that the pins will not fall off the outer body of our structure.

A.2.7 Real Tuning Screws

If the outer body of the structure has tuning elements, we need to change the tuning elements into real tuning screws. For this purpose, we only need to identify the positions of the center of the tuning elements. Then, we repeat the same procedure used for the closing screws and alignment pins, respectively.

It is important to note that commercial tuning elements have an inside radius of $r_1 = 0.9$ mm, and the outside part of the tuner has a radius of $r_2 = 1.35$ mm. In the manufacturing drawing, therefore, we have only used the dimension of the outside part of the tuner with a radius of 1.35 mm.

A.2.8 Body and Cover

The next step, is to cut the outer body of the structure in order to obtain two structures, namely, body and cover, this is achieved by applying the *Extrude Cut operation*. For this purpose, we have decided to split our structures as follows:

- If our structure is manufactured in the H-plane (in-line screw hybrid SIR filter), the cover will be composed of the part that we have cut off from the structure from the height of the input of the WR-90 waveguide, and the body will be composed of the remaining part of the structure.
- If our structure is manufactured in the E-plane (all other filters), the structure will be split vertically in two identical halves.

A.2.9 Pressure Wells

Once we have obtained the body and cover of our structure, it is necessary to ensure that the top is in very good electrical contact with the body. For this purpose, we have created two *pressure wells* in the body, so that the contact pressure is higher in the close vicinity of the walls of the filter. To do this, we have used again the *Extrude Cut operation*.

It is important to mention that the drawing of the pressure wells depends on the specific geometry of the structure. Naturally, we will include inside the pressure well all the holes of the fixing screws of the body. Finally, we have used in all designs a pressure wells depth equal to 2 mm.

A.2.10 Assembly of the Body and Cover

To validate the procedure described in the previous paragraphs, we need to join the two parts of the filter structure. For this purpose, we select in SW *File/Make Assembly for part* in order to automatically assemble the two parts.

A.2.11 Generate Drawings

Once the 3D plans of the body and cover have been obtained and validated, we are ready to send the 3D plans to manufacture. In some cases, it is also necessary to obtain the drawings of the two pieces. For this purpose, we select *File/Generate (or Make) Drawing from Part* in order to generate the drawings. Finally, a number of details must also be defined, namely:

- The views that we want to show in the drawing, for instance, top, bottom, etc.
- The metric of the pieces generated, for instance, length, height and width of the pieces. Also, we can add the dimensions of the screws and pins.
- Finally, we can include all annotations that can be needed to better understand what needs to be manufactured.

A.3 3D Manufacturing Plans of the Filters

We conclude this appendix showing all the 3D manufacturing plans of the filters designed and manufactured in our research.

- Fig. A.2 shows the 3D plans of the in-line hybrid SIR filter.
- Fig. A.3 shows the 3D plans of the in-line screw hybrid SIR filter.
- Fig. A.4 shows the 3D plans of the E-plane folded hybrid SIR filter.
- Fig. A.5 shows the 3D plans of the E-plane folded hybrid staircase filter.
- Fig. A.6 shows the 3D plans of the first dual-band RA staircase filter.
- Fig. A.7 shows the 3D plans of the second dual-band RA staircase filter.
- Fig. A.8 shows the 3D plans of the extended bandpass RA staircase filter.

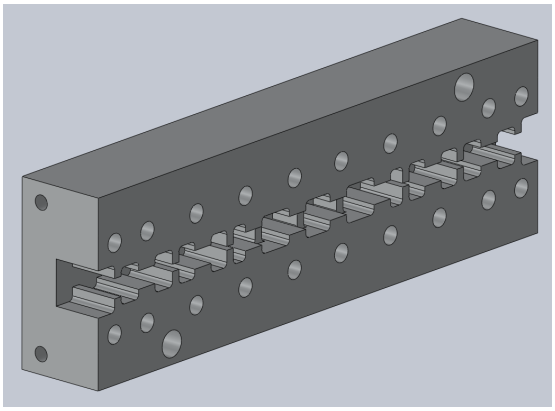

(a) First half of the filter.

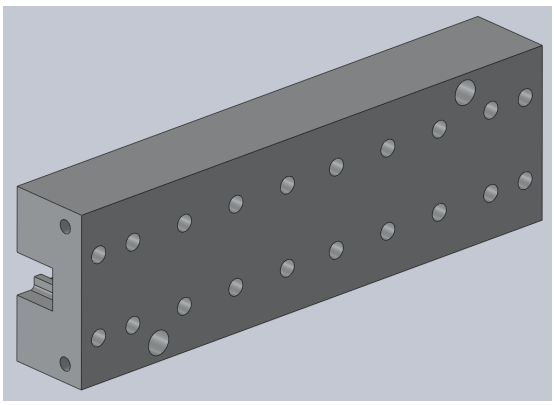

(b) Second half of the filter.

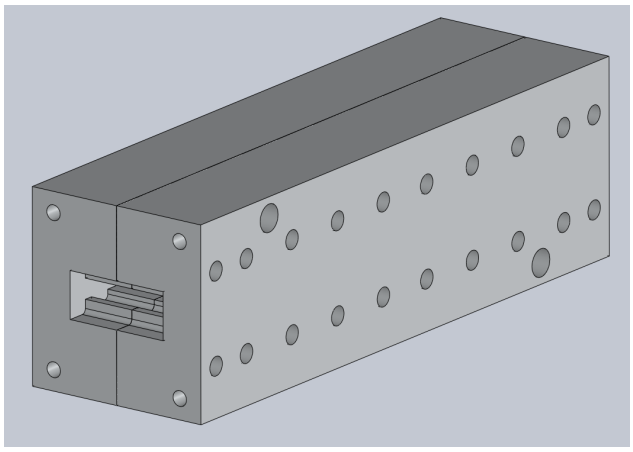

(c) Assembly of the two halves of the filter.

Figure A.2: 3D manufacturing plans of the in-line hybrid SIR filter.

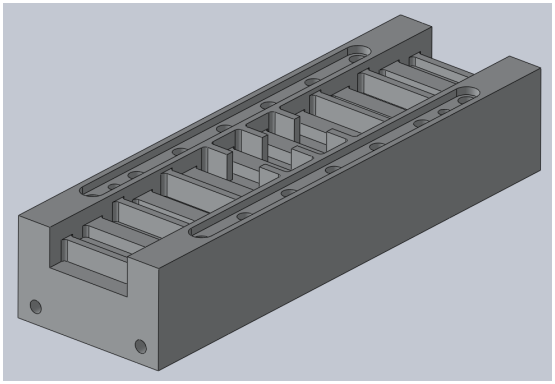

(a) Body of the filter.

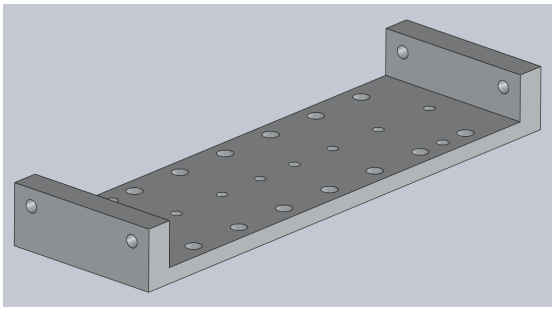

(b) Cover of the filter.

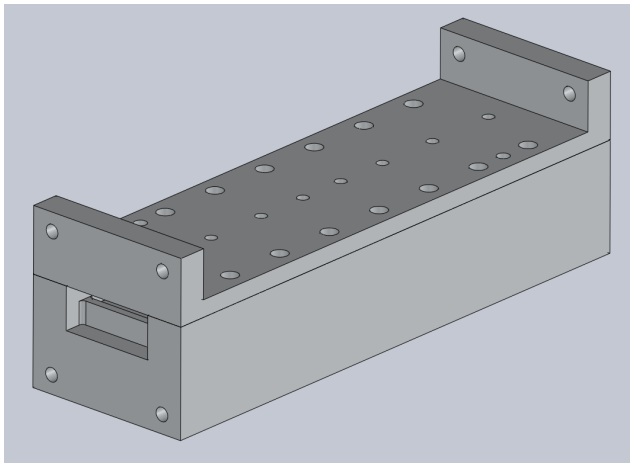

(c) Assembly of the body and cover of the filter.

Figure A.3: 3D manufacturing plans of the in-line screw hybrid SIR filter.

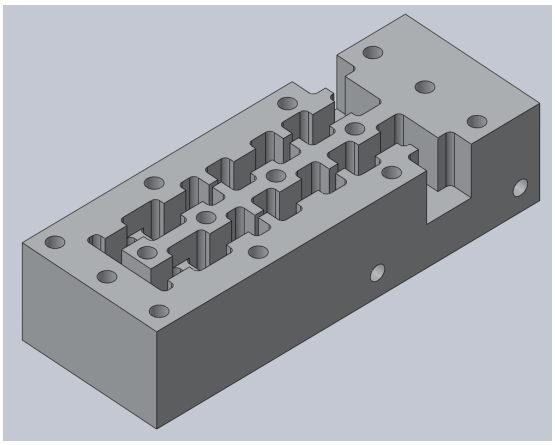

(a) First half of the filter.

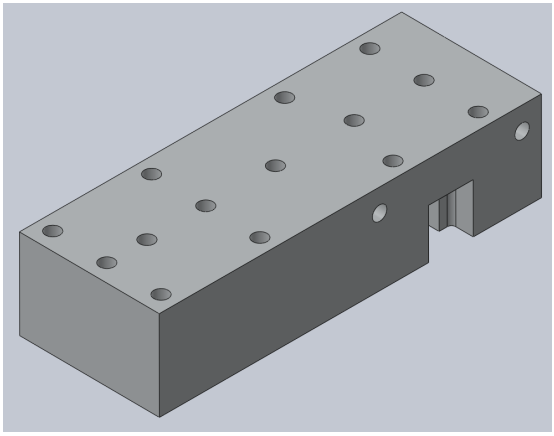

(b) Second half of the filter.

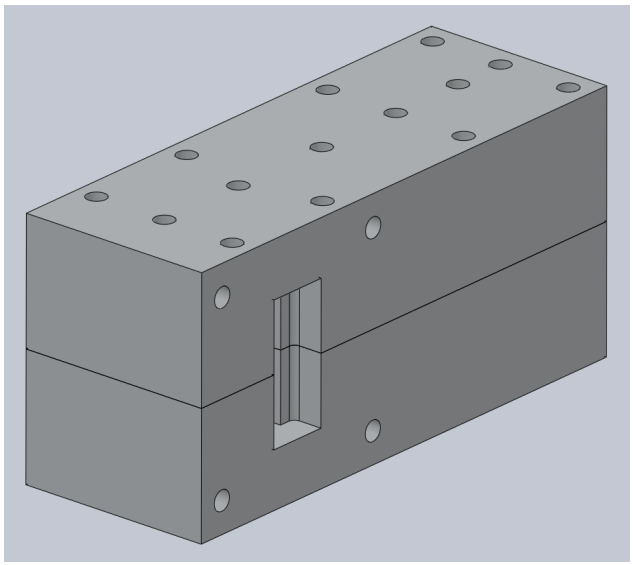

(c) Assembly of the two halves of the filter.

Figure A.4: 3D manufacturing plans of the E-plane folded hybrid SIR filter.

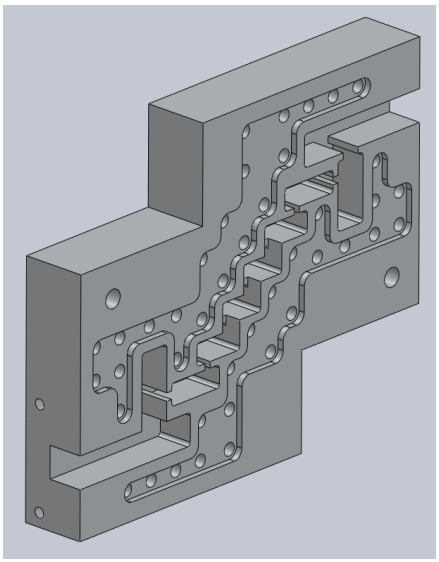

(a) First half of the filter.

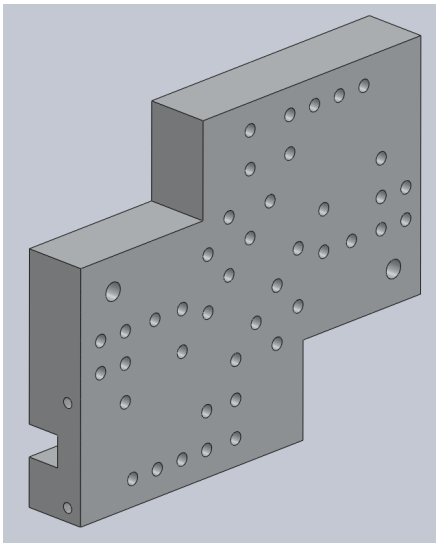

(b) Second half of the filter.

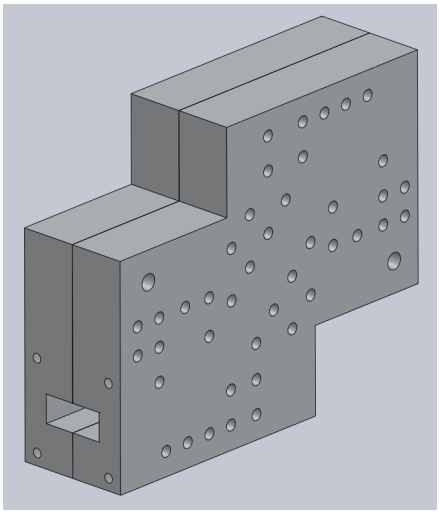

(c) Assembly of the two halves of the filter.

Figure A.5: 3D manufacturing plans of the E-plane folded hybrid staircase filter.

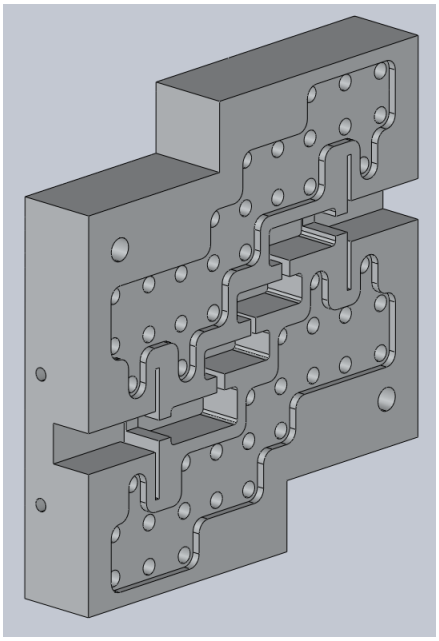

(a) First half of the filter.

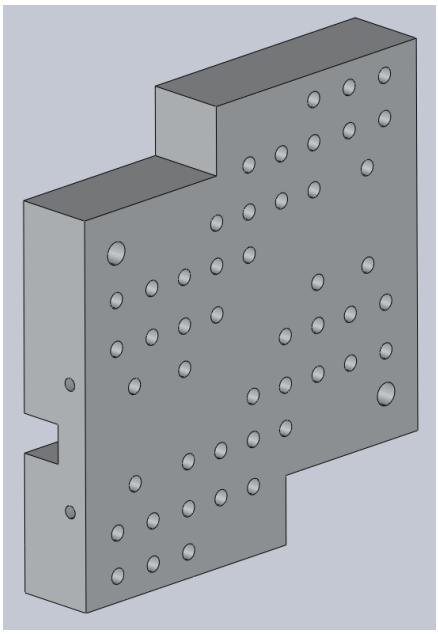

(b) Second half of the filter.

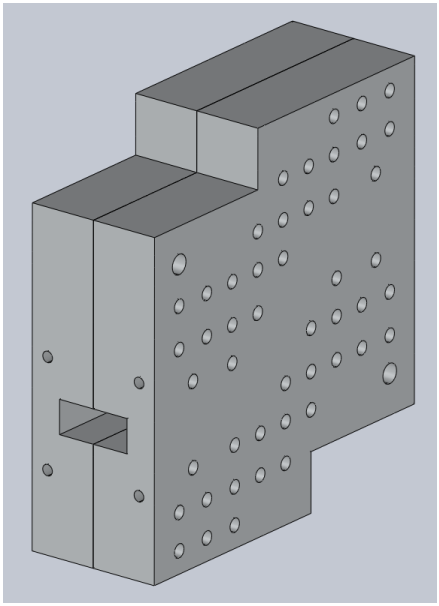

(c) Assembly of the two halves of the filter.

Figure A.6: 3D manufacturing plans of the first dual-band RA staircase filter.

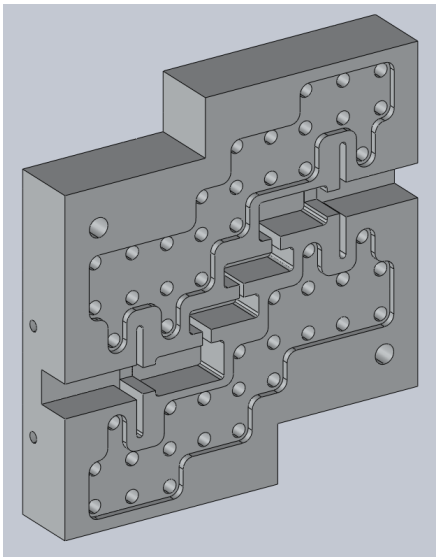

(a) First half of the filter.

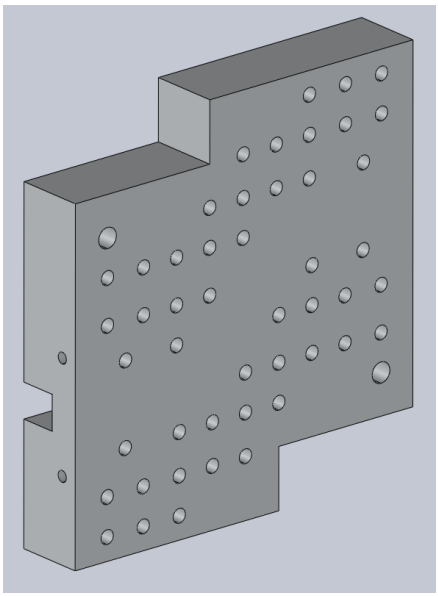

(b) Second half of the filter.

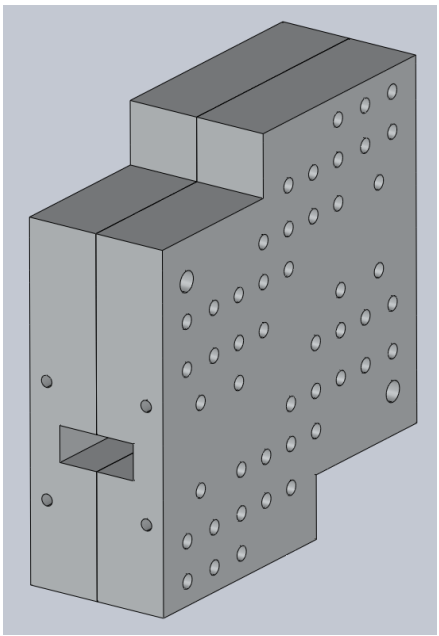

(c) Assembly of the two halves of the filter.

Figure A.7: 3D manufacturing plans of the second dual-band RA staircase filter.

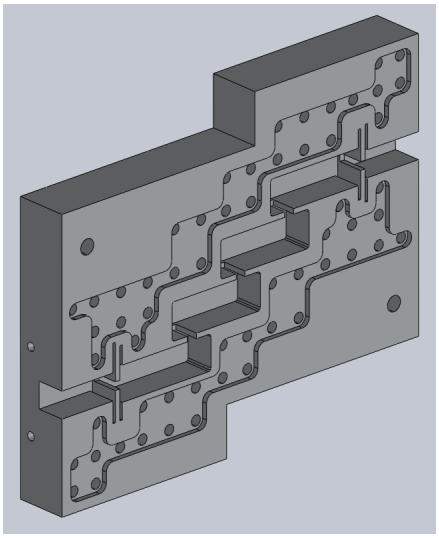

(a) First half of the filter.

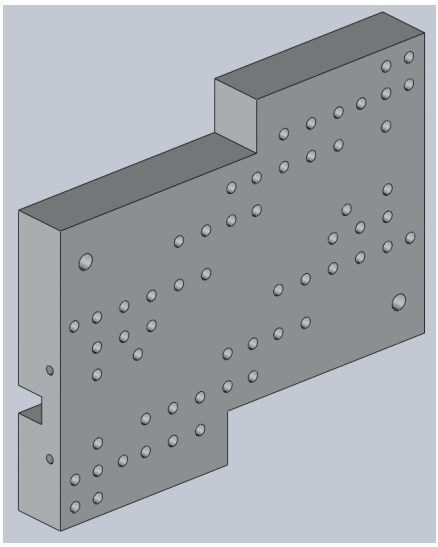

(b) Second half of the filter.

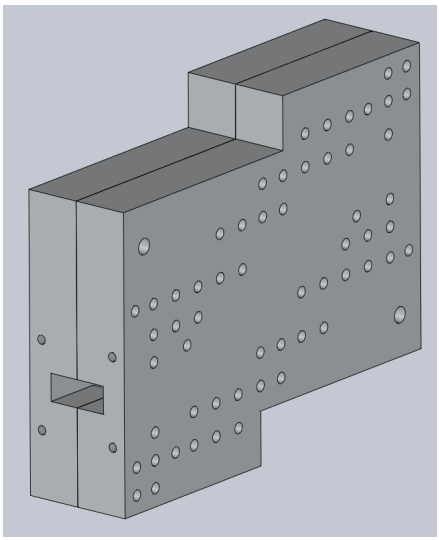

(c) Assembly of the two halves of the filter.

Figure A.8: 3D manufacturing plans of the extended bandpass RA staircase filter.

Appendix B

Publications

The novel contributions discussed in this doctoral thesis have resulted into a total number of five scientific publications. They are two journal papers and three contributions to international conferences, as detailed next. There is also another journal article (describing the novel results of Chapters 6 and 7) that is currently under review.

B.1 Journal Publications

- J. Valencia, V.E. Boria, M. Guglielmi and S. Cogollos, "Compact wideband hybrid filters in rectangular waveguide with enhanced out-of-band response", in IEEE Transactions on Microwave Theory and Techniques, vol. 68, no. 1, pp. 87-101, Jan. 2020. 2019.
- J.F Valencia Sullca, M. Guglielmi, S. Cogollos and V.E. Boria, "Hybrid wideband staircase filters in rectangular waveguide with enhanced out-of-band response", in IEEE Transactions on Microwave Theory and Techniques, vol. 69, no. 8, pp. 3783-3796, Aug. 2021.

B.2 Conference Publications

- J. Valencia, M. Guglielmi, S. Cogollos, J. Vague and V.E. Boria, "Enhancing the performance of stepped impedance resonator filters in rectangular waveguide", in *2017 47th European Microwave Conference (EuMC)*, Oct. 2017, pp. 989-992.
- J. Valencia, M. Guglielmi, S. Cogollos and V.E. Boria, "Enhancing the out-of-band response of hybrid wide-band filters in rectangular waveguide", in *2020 50th*

European Microwave Conference (EuMC), Jan. 2021, pp. 747-750.

- J.F Valencia Sullca, S. Cogollos, M. Guglielmi and V.E. Boria, "Dual-band filters in rectangular waveguide based on resonant apertures," in *2021 IEEE MTT-S International Microwave Symposium Digest*, Atlanta, GA, USA, 2021, pp. 1-4.

Bibliography

[1] G.L. Matthaei, L. Young, and E.M.T. Jones, *Microwave Filters, Impedance-Matching Networks, and Coupling Structures*. Norwood, MA: Artech House, 1980.

[2] N. Marcuvitz, *Waveguide Handbook*, ser. IEE Electromagnetic Waves Series, vol. 21. Stevenage, UK: Peter Peregrinus Ltd., 1986.

[3] D. M. Pozar, *Microwave Engineering*. John Wiley & Sons, 2012.

[4] M. Morelli, I. Hunter, R. Parry, and V. Postoyalko, "Stopband performance improvement of rectangular waveguide filters using stepped-impedance resonators," *IEEE Transactions on Microwave Theory and Techniques*, vol. 50, no. 7, pp. 1657–1664, Jul. 2002.

[5] Q. Wu, F. Zhu, Y. Yang, and X. Shi, "An effective approach to suppressing the spurious mode in rectangular waveguide filters," *IEEE Microwave and Wireless Components Letters*, vol. 29, no. 11, pp. 703–705, Nov. 2019.

[6] R.J. Cameron, C.M. Kudsia, and R.R. Mansour, *Microwave Filters for Communication Systems: Fundamentals, Design and Applications*, 2nd ed. Hoboken, NJ, USA: John Wiley & Sons, 2018.

[7] T.S. Chen, "Characteristics of waveguide resonant-iris filters (correspondence)," *IEEE Transactions on Microwave Theory and Techniques*, vol. 15, no. 4, pp. 260–262, Apr. 1967.

[8] R.V. Snyder, "Filter design for modern communication systems," in *2012 Asia-Pacific Microwave Conference Proceedings*, Dec. 2012, pp. 673–675.

[9] R.V. Snyder, A. Mortazawi, I. Hunter, S. Bastioli, G. Macchiarella, and K. Wu, "Present and future trends in filters and multiplexers," *IEEE Transactions on Microwave Theory and Techniques*, vol. 63, no. 10, pp. 3324–3360, Oct. 2015.

[10] R. Levy, R.V. Snyder, and G. Matthaei, "Design of microwave filters," *IEEE Transactions on Microwave Theory and Techniques*, vol. 50, no. 3, pp. 783–793, Mar. 2002.

[11] I.C. Hunter, L. Billonet, B. Jarry, and P. Guillon, "Microwave filters-applications and technology," *IEEE Transactions on Microwave Theory and Techniques*, vol. 50, no. 3, pp. 794–805, Mar. 2002.

[12] V. E. Boria, P. Soto, and S. Cogollos, "Distributed models for filter synthesis," *IEEE Microwave Magazine*, vol. 12, no. 6, pp. 87–100, Oct. 2011.

[13] H. Wang, L. Zhu, and W. Menzel, "Ultra-wideband bandpass filter with hybrid microstrip/CPW structure," *IEEE Microwave and Wireless Components Letters*, vol. 15, no. 12, pp. 844–846, Dec. 2005.

[14] V. E. Boria and B. Gimeno, "Waveguide filters for satellites," *IEEE Microwave Magazine*, vol. 8, no. 5, pp. 60–70, Oct. 2007.

[15] L. Zhu, R. R. Mansour, and M. Yu, "Compact triple-band bandpass filters using rectangular waveguide resonators," in *2016 IEEE MTT-S International Microwave Symposium Digest*, May 2016, pp. 1–3.

[16] R.V. Snyder, "Evolution of passive and active microwave filters," in *2012 IEEE MTT-S International Microwave Symposium Digest*, Jun. 2012, pp. 1–3.

[17] J.F. Liang, K.A. Zaki, and A.E. Atia, "Mixed modes dielectric resonator loaded cavity filters," in *1994 IEEE MTT-S International Microwave Symposium Digest*, vol. 2, May 1994, pp. 731–734.

[18] J.F. Liang, K.A. Zaki, and A.E. Atia, "Mixed modes dielectric resonator filters," *IEEE Transactions on Microwave Theory and Techniques*, vol. 42, no. 12, pp. 2449–2454, Dec. 1994.

[19] H.W. Yao, K.A. Zaki, A.E. Atia, and R. Hershtig, "Generalized slot coupled combline filters," in *1995 IEEE MTT-S International Microwave Symposium Digest*, vol. 2, May 1995, pp. 395–398.

[20] J.A. Ruiz-Cruz, K.A. Zaki, J.R. Montejo-Garai, and J.M. Rebollar, "Rectangular waveguide elliptic filters with capacitive and inductive irises and integrated coaxial

excitation," in *2005 IEEE MTT-S International Microwave Symposium Digest*, Jun. 2005, pp. 269–272.

[21] A.R. Weily and A.S. Mohan, "Mixed combline and HE_{11} mode dielectric resonator filter with improved spurious performance," in *1997 Asia-Pacific Microwave Conference Proceedings*, vol. 2, Dec. 1997, pp. 805–808.

[22] S. Yuan, X. Wei, G. Yue, and M. Zhang, "Cascaded fourth-order mixed-coupled bandpass filter with good frequency selectivity," in *2013 International Workshop on Microwave and Millimeter Wave Circuits and System Technology*, Oct. 2013, pp. 229–232.

[23] P. Chu, W. Hong, L. Dai, H. Tang, J. Chen, Z. Hao, X. Zhu, and K. Wu, "A planar bandpass filter implemented with a hybrid structure of substrate integrated waveguide and coplanar waveguide," *IEEE Transactions on Microwave Theory and Techniques*, vol. 62, no. 2, pp. 266–274, Feb. 2014.

[24] C. Tomassoni, S. Bastioli, and R.V. Snyder, "Mixed-mode resonator using TE_{101} cavity mode and $TE_{01\delta}$ dielectric mode," in *2016 IEEE MTT-S International Microwave Symposium Digest*, May 2016, pp. 1–3.

[25] C. Tomassoni, S. Bastioli, and R.V. Snyder, "Compact mixed-mode filter based on TE_{101} cavity mode and $TE_{01\delta}$ dielectric mode," *IEEE Transactions on Microwave Theory and Techniques*, vol. 64, no. 12, pp. 4434–4443, Dec. 2016.

[26] K. Li, D. Qu, and X. Zhong, "Novel filters based on hybrid structure of coaxial resonator and evanescent mode waveguide with loaded posts," in *2017 IEEE 9th International Conference on Communication Software and Networks (ICCSN)*, May 2017, pp. 771–774.

[27] Z. He, Z. Shao, C.J. You, Y.M. Huang, and X. Li, "Design of compact bandpass filter based on quarter-mode substrate integrated waveguide with mixed coupling," in *2015 Asia-Pacific Microwave Conference Proceedings*, vol. 3, Dec. 2015, pp. 1–3.

[28] Z. He, C.J. You, S. Leng, X. Li, and Y. Huang, "Compact bandpass filter with high selectivity using quarter-mode substrate integrated waveguide and coplanar waveguide," *IEEE Microwave and Wireless Components Letters*, vol. 27, no. 9, pp. 809–811, Sep. 2017.

[29] W.M. Fathelbab, R.V. Snyder, and K.G. Keck, "Wide bandpass filters with wide upper stopbands for high power system applications," in *2011 41st European Microwave Conference (EuMC)*, Oct. 2011, pp. 361–364.

[30] S. Bastioli and R.V. Snyder, "Ultra-compact evanescent mode filter using inhomogeneous semi-lumped capacitive elements," in *2014 20th International Conference on Microwaves, Radar and Wireless Communications (MIKON)*, Jun. 2014, pp. 1–4.

[31] T. Kuo, S. Lin, and C.H. Chen, "Compact ultra-wideband bandpass filters using composite microstrip-coplanar-waveguide structure," *IEEE Transactions on Microwave Theory and Techniques*, vol. 54, no. 10, pp. 3772–3778, Oct. 2006.

[32] V. Gholipour, S.M.M. Moshiri, A. Alighanbari, and A. Yahaghi, "Highly selective wideband bandpass filter using combined microstrip/coplanar waveguide structure," *Electronics Letters*, vol. 52, no. 13, pp. 1145–1147, Jun. 2016.

[33] V. Bagheri, M. Mansouree, K. Mohammadpour-Aghdam, and R. Faraji-Dana, "Design, construction and measurement of a millimeter-wave filter with 40-60 GHz passband," in *2014 Third Conference on Millimeter-Wave and Terahertz Technologies (MMWATT)*, Dec. 2014, pp. 1–4.

[34] F. Teberio, P. Soto, I. Arregui, T. Lopetegi, S. Cogollos, I. Arnedo, P. Martin-Iglesias, V. E. Boria, and M. A. G. Laso, "Waveguide band-pass filter with reduced sensitivity to fabrication tolerances for Q-band payloads," in *2017 IEEE MTT-S International Microwave Symposium Digest*, Jun. 2017, pp. 1464–1467.

[35] L. Miranda, F. Teberio, P. Martin-Iglesias, I. Calero, I. Arregui, I. Arnedo, J. M. Percaz, D. Santiago, T. Lopetegi, and M. A. G. Laso, "Stepped-impedance band-pass filters with improved selectivity," in *2019 IEEE MTT-S International Microwave Symposium Digest*, Jun. 2019, pp. 1198–1200.

[36] S.B. Cohn, "Analysis of a wide-band waveguide filter," *Proceedings of the IRE*, vol. 37, no. 6, pp. 651–656, Jun. 1949.

[37] S.B. Cohn, "Design relations for the wide-band waveguide filter," *Proceedings of the IRE*, vol. 38, no. 7, pp. 799–803, Jul. 1950.

[38] S.B. Cohn, "Direct-coupled-resonator filters," *Proceedings of the IRE*, vol. 45, no. 2, pp. 187–196, Feb. 1957.

[39] G.L. Matthaei, "Design of wide-band (and narrow-band) band-pass microwave filters on the insertion loss basis," *IRE Transactions on Microwave Theory and Techniques*, vol. 8, no. 6, pp. 580–593, Nov. 1960.

[40] L. Young, "Direct-coupled cavity filters for wide and narrow bandwidths," *IEEE Transactions on Microwave Theory and Techniques*, vol. 11, no. 3, pp. 162–178, May 1963.

[41] R. Levy, "Theory of direct-coupled-cavity filters," *IEEE Transactions on Microwave Theory and Techniques*, vol. 15, no. 6, pp. 340–348, Jun. 1967.

[42] R. Levy, "A generalized design technique for practical distributed reciprocal ladder networks," *IEEE Transactions on Microwave Theory and Techniques*, vol. 21, no. 8, pp. 519–526, Aug. 1973.

[43] I. Arregui, F. Teberio, I. Arnedo, A. Lujambio, M. Chudzik, D. Benito, R. Jost, F.-J. Görtz, T. Lopetegi, and M. A. G. Laso, "High-power low-pass harmonic waveguide filter with TE_{n0} -mode suppression," *IEEE Microwave and Wireless Components Letters*, vol. 22, no. 7, pp. 339–341, Jul. 2012.

[44] F. Teberio, I. Arregui, A. Gomez-Torrent, I. Arnedo, M. Chudzik, M. Zedler, F.-J. Görtz, R. Jost, T. Lopetegi, and M. A. G. Laso, "Chirping techniques to maximize the power-handling capability of harmonic waveguide low-pass filters," *IEEE Transactions on Microwave Theory and Techniques*, vol. 64, no. 9, pp. 2814–2823, Sep. 2016.

[45] F.M. Vanin, D. Schmitt, and R. Levy, "Dimensional synthesis for wideband waveguide filters," in *2004 IEEE MTT-S International Microwave Symposium Digest*, vol. 2, Jun. 2004, pp. 463–466.

[46] F.M. Vanin, D. Schmitt, and R. Levy, "Dimensional synthesis for wide-band waveguide filters and diplexers," *IEEE Transactions on Microwave Theory and Techniques*, vol. 52, no. 11, pp. 2488–2495, Nov. 2004.

[47] M. Guglielmi, "Accurate CAD of integrated band-pass and second harmonic band-reject microwave filters," in *1998 IEEE MTT-S International Microwave Symposium Digest*, vol. 2, Jun. 1998, pp. 813–816.

[48] V.E. Boria, M. Bozzi, D. Camilleri, A. Coves, H. Esteban, B. Gimeno, M. Guglielmi, and L. Polini, "Contributions to the analysis and design of all-inductive filters with dielectric resonators," in *2003 33rd European Microwave Conference (EuMC)*, vol. 3, Oct. 2003, pp. 1247–1250.

[49] M. Morelli, I. Hunter, R. Parry, and V. Postoyalko, "Stop-band improvement of rectangular waveguide filters using different width resonators: selection of resonator widths," in *2001 IEEE MTT-S International Microwave Sympsoium Digest*, vol. 3, May 2001, pp. 1623–1626.

[50] N. Yildirim and A. Hizal, "Waveguide filters with ridged and unequal width resonators," in *2005 IEEE MTT-S International Microwave Symposium Digest*, Jun. 2005, pp. 1259–1262.

[51] Y. Li, Q. Wang, and C. Wang, "Rectangular waveguide band-pass filter with harmonic suppression," in *2013 International Workshop on Microwave and Millimeter Wave Circuits and System Technology*, Oct. 2013, pp. 251–253.

[52] P. Soto, E. Tarín, V.E. Boria, C. Vicente, J. Gil, and B. Gimeno, "Accurate synthesis and design of wideband and inhomogeneous inductive waveguide filters," *IEEE Transactions on Microwave Theory and Techniques*, vol. 58, no. 8, pp. 2220–2230, Aug. 2010.

[53] P. Zhao, X. Wang, and C. Chen, "Rectangular waveguide band-pass filter with high power harmonic suppression," in *2014 15th International Conference on Electronic Packaging Technology*, Aug. 2014, pp. 1327–1328.

[54] J.M. Perez Escudero, D. Martinez Martinez, A. Pons Abenza, J.A. Lorente Acosta, A. Alvarez-Melcon, and M. Guglielmi, "Enhancing the spurious free range in inductive rectangular waveguide filters," in *2015 45th European Microwave Conference (EuMC)*, Sep. 2015, pp. 678–681.

[55] S. Afridi, M. Sandhu, and I. Hunter, "Mixed non-uniform width/evanescent mode ceramic resonator waveguide filter with wide spurious free bandwidth," in *2016 IEEE MTT-S International Conference on Numerical Electromagnetic and Multiphysics Modeling and Optimization (NEMO)*, Jul. 2016, pp. 1–3.

[56] S. Afridi, M. Sandhu, N. Somjit, and I. Hunter, "Monolithic ceramic waveguide filter with wide spurious free bandwidth," in *2016 46th European Microwave Conference (EuMC)*, Oct. 2016, pp. 241–244.

[57] S. Afridi, I. Hunter, and M.Y. Sandhu, "Spurious free non uniform width dielectric loaded filters," in *2018 48th European Microwave Conference (EuMC)*, Sep. 2018, pp. 85–88.

[58] I. Hunter, S. Afridi, and M. Sandhu, "Integrated ceramic waveguide filters with improved spurious performance," in *2015 45th European Microwave Conference (EuMC)*, Sep. 2015, pp. 674–677.

[59] S. Li, J. Fu, and X. Wu, "Analysis of high-power rectangular waveguide filter with capacitive coupling iris for satellite," in *2009 Asia-Pacific Power and Energy Engineering Conference*, Mar. 2009, pp. 1–4.

[60] S. Li, J. Fu, and X. Wu, "Rectangular waveguide band pass filter with capacitive coupling iris," in *2008 Progress in Electromagnetics Research Symposium (PIERS)*, Mar. 2008, pp. 337–341.

[61] W. Menzel, A. Muller, and F. Bogelsack, "A capacitively coupled waveguide filter with wide stop-band," in *2003 33rd European Microwave Conference (EuMC)*, Oct. 2003, pp. 1239–1242.

[62] M.S. Mahani and M. Tayarani, "Solving complex wave guide structures using hybrid modes and its application in analysis of a wide reject band waveguide iris filter," in *2007 IEEE Applied Electromagnetics Conference (AEMC)*, Dec. 2007, pp. 1–4.

[63] S. Upadhyay, C. Panchal, P.K. Atrey, and R. Singh, "Development of narrowband microwave bandpass filter for Ku band," in *2016 International Conference on Wireless Communications, Signal Processing and Networking (WiSPNET)*, Mar. 2016, pp. 893–895.

[64] S. Akatimagool, N. Intarawiset, and S. Inchan, "Design of waveguide bandpass filter using cascade inductive and capacitive irises," in *2016 IEEE 5th Asia-Pacific Conference on Antennas and Propagation (APCAP)*, Jul. 2016, pp. 387–388.

[65] A. Kirilenko, L. Mospan, and V. Tkachenko, "Capacitive iris bandpass filters with spurious harmonic modes suppression," in *International Conference on Mathematical Methods in Electromagnetic Theory*, vol. 2, Sep. 2002, pp. 532–534.

[66] M. Guglielmi, F. Montauti, L. Pellegrini, and P. Arcioni, "Implementing transmission zeros in inductive-window bandpass filters," *IEEE Transactions on Microwave Theory and Techniques*, vol. 43, no. 8, pp. 1911–1915, Aug. 1995.

[67] S. Cogollos, P. Soto, M. Brumos, V. E. Boria, and M. Guglielmi, "Novel rectangular waveguide structures for advanced filter characteristics," in *2014 IEEE MTT-S International Microwave Symposium Digest*, Jun. 2014, pp. 1–4.

[68] P. Soto, V. Boria, C. Carceller, S. Cogollos, M. Guglielmi, and D. Smacchia, "Practical design of rectangular waveguide filters with a capacitive building block providing an extra transmission zero," in *2015 IEEE MTT-S International Microwave Symposium Digest*, May 2015, pp. 1–4.

[69] C. Carceller, P. Soto, V.E. Boria, M. Guglielmi, and D. Raboso, "New folded configuration of rectangular waveguide filters with asymmetrical transmission zeros," in *2014 44th European Microwave Conference (EuMC)*, Oct. 2014, pp. 183–186.

[70] C. Carceller, P. Soto, V.E. Boria, and M. Guglielmi, "Design of hybrid folded rectangular waveguide filters with transmission zeros below the passband," *IEEE Transactions on Microwave Theory and Techniques*, vol. 64, no. 2, pp. 475–485, Feb. 2016.

[71] C. Carceller, P. Soto, V.E. Boria, and M. Guglielmi, "Capacitive obstacle realizing multiple transmission zeros for in-line rectangular waveguide filters," *IEEE Microwave and Wireless Components Letters*, vol. 26, no. 10, pp. 795–797, Oct. 2016.

[72] T.E. Rozzi and M.S. Navarro, "Propagation in a rectangular waveguide periodically loaded with resonant irises," in *1976 IEEE MTT-S International Microwave Symposium Digest*, Jun. 1976, pp. 359–361.

[73] M.S. Navarro, T.E. Rozzi, and Y.T. Lo, "Propagation in a rectangular waveguide periodically loaded with resonant irises," *IEEE Transactions on Microwave Theory and Techniques*, vol. 28, no. 8, pp. 857–865, Aug. 1980.

[74] G. Craven and C. Mok, "The design of evanescent mode waveguide bandpass filters for a prescribed insertion loss characteristic," *IEEE Transactions on Microwave Theory and Techniques*, vol. 19, no. 3, pp. 295–308, Mar. 1971.

[75] M. Piloni, R. Ravenelli, and M. Guglielmi, "Resonant aperture filters in rectangular waveguide," in *1999 IEEE MTT-S International Microwave Symposium Digest*, vol. 3, Jun. 1999, pp. 911–914.

[76] M. Capurso, M. Piloni, and M. Guglielmi, "Resonant aperture filters: Improved out-of-band rejection and size reduction," in *2001 31st European Microwave Conference (EuMC)*, Sep. 2001, pp. 1–4.

[77] Y. Wu, Q. Zeng, and Y. Shang, "A low-insert loss and high-return loss bandpass filter based on cut-off rectangular waveguide for satellite communication application," *International Journal of RF and Microwave Computer-Aided Engineering*, vol. 31, no. 2, pp. 1–8, Feb. 2021.

[78] F. Arndt, T. Duschak, U. Papziner, and P. Rolappe, "Asymmetric iris coupled cavity filters with stopband poles," in *1990 IEEE MTT-S International Microwave Symposium Digest*, vol. 1, May 1990, pp. 215–218.

[79] F. Arndt and T. Sieverding, "The rigorous CAD of aperture-coupled T-junction bandstop-filters, E-plane circuit elliptic-function filters, and diplexers," in *1991 IEEE MTT-S International Microwave Symposium Digest*, vol. 3, Jul. 1991, pp. 1103–1106.

[80] T. Sieverding and F. Arndt, "Field theoretical CAD of open or aperture matched T-junction coupled rectangular waveguide structures," *IEEE Transactions on Microwave Theory and Techniques*, vol. 40, no. 2, pp. 353–362, Feb. 1992.

[81] A. Kirilenko, L. Mospan, and V. Tkachenko, "Extracted pole bandpass filters based on the slotted irises," in *2002 32nd European Microwave Conference (EuMC)*, Sep. 2002, pp. 1–4.

[82] U. Rosenberg, S. Amari, and J. Bornemann, "Mixed-resonance compact in-line pseudo-elliptic filters," in *2003 IEEE MTT-S International Microwave Symposium Digest*, vol. 1, Jun. 2003, pp. 479–482.

[83] U. Rosenberg, S. Amari, and J. Bornemann, "Inline TM_{110}-mode filters with high-design flexibility by utilizing bypass couplings of nonresonating $TE_{10/01}$ modes," *IEEE Transactions on Microwave Theory and Techniques*, vol. 51, no. 6, pp. 1735–1742, Jun. 2003.

[84] U. Rosenberg, S. Amari, J. Bornemann, and R. Vahldieck, "Compact pseudo-highpass filters formed by cavity and iris resonators," in *2004 34th European Microwave Conference (EuMC)*, vol. 2, Oct. 2004, pp. 985–988.

[85] S. Bastioli, "Nonresonating mode waveguide filters," *IEEE Microwave Magazine*, vol. 12, no. 6, pp. 77–86, Oct. 2011.

[86] L. Pelliccia, C. Tomassoni, F. Cacciamani, P. Vallerotonda, R. Sorrentino, J. Galdeano, and C. Ernst, "Very-compact waveguide bandpass filter based on dual-mode TM cavities for satellite applications in Ku-band," in *2018 48th European Microwave Conference (EuMC)*, Sep. 2018, pp. 93–96.

[87] P. Vallerotonda, L. Pelliccia, C. Tomassoni, F. Cacciamani, R. Sorrentino, J. Galdeano, and C. Ernst, "Compact waveguide bandpass filters for broadband space applications in C- and Ku-bands," in *2019 European Microwave Conference in Central Europe (EuMCE)*, May 2019, pp. 116–119.

[88] R. Barrio-Garrido, S. Llorente-Romano, and M. Salazar-Palma, "Design of Ka-band highly selective wideband band-pass filters using directly coupled resonant irises," in *2003 IEEE AP-S (Antennas and Propagation Society) International Symposium Digest*, vol. 2, Jun. 2003, pp. 1161–1164.

[89] R. Barrio-Garrido, S. Llorente-Romano, A. Garcia-Lamperez, and M. Salazar-Palma, "Design of broadband directly coupled non-centred resonant irises filters," in *2003 33rd European Microwave Conference (EuMC)*, Oct. 2003, pp. 219–222.

[90] R. Barrio-Garrido, S. Llorente-Romano, M. Salazar-Palma, A. Onoro-Navarro, and I. Hidalgo-Carpintero, "Design, construction and experimental characterization of a broadband highly selective filter in waveguide technology in Ka-band," in *2006 IEEE MTT-S International Microwave Symposium Digest*, Jun. 2006, pp. 250–253.

[91] C. Zong-Tao and L. Sheng-Xian, "Design of microwave filter with resonant irises of resonant windows at different location," in *2011 IEEE International Conference on Microwave Technology Computational Electromagnetics*, May 2011, pp. 156–159.

[92] R. Yang and A. S. Omar, "Investigation of multiple rectangular aperture irises in rectangular waveguide using TE^{x}_{mn}-modes," *IEEE Transactions on Microwave Theory and Techniques*, vol. 41, no. 8, pp. 1369–1374, Aug. 1993.

[93] A. A. Kirilenko and L. P. Mos'pan, "Reflection resonances of two-aperture irises in rectangular waveguide," in *1999 29th European Microwave Conference (EuMC)*, vol. 1, Oct. 1999, pp. 28–31.

[94] C. A. Leal-Sevillano, J. R. Montejo-Garai, J. A. Ruiz-Cruz, and J. M. Rebollar, "Wideband equivalent circuit for multi-aperture multi-resonant waveguide irises," *IEEE Transactions on Microwave Theory and Techniques*, vol. 64, no. 3, pp. 724–732, Mar. 2016.

[95] R. Rodriguez-Berral, F. Mesa, and F. Medina, "Resonant modes of a waveguide iris discontinuity: Interpretation in terms of canonical circuits," *IEEE Transactions on Microwave Theory and Techniques*, vol. 66, no. 5, pp. 2059–2069, May 2018.

[96] M. Tsuji, H. Deguchi, and M. Ohira, "A new frequency selective window for constructing waveguide bandpass filters with multiple attenuation poles," *Progress in Electromagnetics Research C*, vol. 20, pp. 139–153, 2011.

[97] S. Amari and J. Bornemann, "Using frequency-dependent coupling to generate finite attenuation poles in direct-coupled resonator bandpass filters," *IEEE Microwave and Guided Wave Letters*, vol. 9, no. 10, pp. 404–406, Oct. 1999.

[98] L. Chen, Q. Wang, and C. Wu, "A compact filter with resonating-irises and shorting stubs," in *2011 China-Japan Joint Microwave Conference*, Apr. 2011, pp. 1–3.

[99] J. Cano, A. Mediavilla, and A. Tazón, "On the use of a new class of simplified multi-window iris notch in the design of ultra-compact high-rejection waveguide filters for satellite links," *Electronics*, vol. 9, p. 1221, Jul. 2020.

[100] S. Cogollos, *Fundamentos de la Teoría de Filtros.* Universitat Politècnica de València, 2016.

[101] M. Guglielmi and A.A. Melcon, "Novel design procedure for microwave filters," in *1993 23rd European Microwave Conference (EuMC)*, Sep. 1993, pp. 212–213.

[102] J.W. Bandler, R.M. Biernacki, R.H. Hemmers, and K. Madsen, "Electromagnetic optimization exploiting aggressive space mapping," *IEEE Transactions on Microwave Theory and Techniques*, vol. 43, no. 12, pp. 2874–2882, Dec. 1995.

[103] G. Conciauro, M. Guglielmi, and R. Sorrentino, *Advanced Modal Analysis*. Wiley, 2000.

[104] E. Sorolla, S. Anza, B. Gimeno, A. M. Perez, C. Vicente, J. Gil, F. J. Perez-Soler, F. D. Quesada, A. Alvarez, and V. E. Boria, "An analytical model to evaluate the radiated power spectrum of a multipactor discharge in a parallel-plate region," *IEEE Transactions on Electron Devices*, vol. 55, no. 8, pp. 2252–2258, Aug. 2008.